Revolution in large-area curved surface lithography: Nanofilm sculpting by thermocapillary modulation

Thesis by
Soon Wei Daniel Lim

In Partial Fulfillment of the Requirements for the
degree of
Bachelor of Science

CALIFORNIA INSTITUTE OF TECHNOLOGY
Pasadena, California

2017
Defended May 22, 2017

Soon Wei Daniel Lim
ORCID: 0000-0003-1689-6860

ACKNOWLEDGEMENTS

Firstly, I will like to thank my mentor, Professor Sandra Troian, for her support in all matters experimental, theoretical, or administrative. Thank you for challenging me to dream big and to aspire towards continuous improvement, and for patiently guiding me through the process of finding loopholes in my crazy ideas, instead of providing the answer outright. I am also grateful to my graduate student mentor, Kevin Fiedler, who taught me the intricacies of wet-lab fabrication, lithography, and optics, and who never hesitated to share his immense repository of theoretical and experimental knowledge with me. I am also thankful for Chengzhe Zhou and his invaluable assistance in performing finite element and raytracing simulations of the various TCL systems. Thank you also for indulging me in our spontaneous scientific and culinary explorations around the conference cities. Particular thanks also goes out to Dr Peter Thompson, whose expertise with computing systems kept the project humming smoothly and twice saved my work from annihilation. To the members of the {LIS^{2}T} group, Yanbing Zhu, Theodore Albertson, and Nicholas White, thank you for your willingness to teach me concepts I had difficulty with, listening to and improving on new ideas, and above all for your friendship.

The research I performed would not have been possible without the technical support and generosity of several other Caltech laboratories. I am grateful to Mr. Frank Rice, manager of the Sophomore Physics Laboratories, who, through his year-long course of excellent skill-building experiments and generous lending of laboratory equipment afterwards, instilled in me the confidence to tackle complex systems armed with little more than a curious mind and a willingness to crunch through reams of datapoints. I am also thankful to Mr. Alireza Ghaffari, who granted me access to the Micro Nano Fabrication Laboratory. Dr. Yunbin Guan and Professor John Eiler, of the Caltech Microanalysis Center, made the Zygo NewView 600 equipment and calibration standards available for my use, and Professor Rustem Ismagilov provided me access to his cleanroom and the Zemetrics Zegage scanning white light interferometer. These instruments form the key analytical technique used in this thesis. I am also thankful to Dr. Chi Ma and the Caltech Geological and Planetary Sciences (GPS) Division Analytical Facility for providing support and access to the Cressington sputter coater and sputter targets.

This research has been supported by two Caltech Summer Undergraduate Research Fellowships (SURFs), the 2015 Toshi Kubota Aeronautics SURF and the 2016 Kiyo

and Eiko Tomiyasu SURF. I have also been generously afforded the privilege of presenting this project in two conferences by the George W. Housner fund, which funded my 2016 American Physical Society (APS) Division of Fluid Dynamics (DFD) conference attendance, and the Caltech Y Patrick Hummel and Harry Gray Travel Fund, which supported my 2017 APS March Meeting attendance.

Finally, this thesis is dedicated to the one who timed the two major breakthroughs in 2015 and 2017 to occur precisely at the lowest, most helpless points in my research journey, and thereby upended the way I viewed the relationship between human effort and results. To the God that uses the foolish things in this world to shame the wise and the weak things to shame the strong (1 Corinthians 1:27), who constructed all these beautiful complexities out of simple nonlinearities, and whose answers to prayer exceeded every expectation, be all glory and honor.

ABSTRACT

Conventional lithography excels in producing blocky structures but has difficulty producing out-of-plane curvature. Such curvature is necessary for optical elements such as microlens arrays. Spatiotemporal control of the surface tension of liquid films offers a powerful method for sculpting myriad 3D shapes, thereby meeting this deficiency. In the Thermocapillary Lithography (TCL) project, we modulate thermocapillary forces by local control of surface temperature to deform a flat nanofilm into a variety of structures, which are then solidified *in situ*. In this thesis, we present two facile means of projecting the required temperature field, which we call Conduction TCL and Laser-induced TCL. In the former, which is a detailed expansion of the work performed in this group, the Laboratory of Interfacial and Small Scale Transport {LIS^{2}T}, we place an array of chilled, prefabricated pins in close proximity to the film to provide precise thermal control via conduction. In the latter, which is new and has not been realized in literature yet, we project a spatially-modulated laser light field onto a horizontal heated fluid to achieve the same film deformation. Laser-induced TCL is shown to be a fully non-contact means of fabrication that admits real-time monitoring of the film profile. We demonstrate that the resultant temperature gradient field is capable of sculpting complex structures such as refractive optical elements, multiscale protrusions and depressions, arbitrary 2D images, as well as waveguides. By varying the pattern width, pitch and evolution time, we have also fabricated plano-convex, plano-concave, *caldera-like*, and hierarchical Microlens Arrays (MLAs) with ultrasmooth surfaces. As a proof of concept, the diverging arrays were incorporated in an adaptive optics component for wavefront sensing. This is the first functional optical device fabricated by modulation of the thermocapillary instability. Furthermore, the ultrasmooth out-of-plane curvature accessible through TCL is ideal for fabricating curved mirrors at the microscale. We exploit this property to fabricate the first large-scale optical microcavity array with curved mirrors for optical filtration. In the process, we developed a conformal, room-temperature metallization protocol for thermosensitive surfaces. In all, TCL is shown to be a facile, single-step means of fabricating complex ultrasmooth topologies, and opens up the possibility of printing planar optical circuit elements and beam shaping topologies on demand.

TABLE OF CONTENTS

LIST OF ILLUSTRATIONS

LIST OF TABLES

NOMENCLATURE

Symbol	Description	Dimensions	Units
α	Extinction coefficient in bulk materials	L^{-1}	m^{-1}
α_1	First aspheric coefficient	L^{-3}	m^{-3}
AR	Asphericity ratio	–	–
Bo	Bond (Eötvös) number	–	–
$\overline{Ca}$	Capillary number	–	–
D	Diameter of circular pin	L	m
$\overline{d}_0$	Normalized air and film gap thickness	–	–
d_0	Photoresist spacer thickness	L	m
d_1	Photoresist pin pillar thickness (for pin arrays) or block pattern thickness (for depression arrays)	L	m
δh	Small nondimensional perturbation used in linear stability analysis	–	–
ΔT	Vertical temperature jump across nanofilm thickness and air gap	T	K
$D_{\mathbf{lens}}$	Characteristic diameter of fitting domain	L	m
$\overline{\overline{E}}$	Local strain rate tensor	$Mt^{-2}L^{-1}$	Pa
ϵ	Aspect ratio h_0/P	–	–
f	Lens focal length	L	m
$\boldsymbol{g}$	Uniform gravitational acceleration	Lt^{-2}	$m\,s^{-2}$
γ	Surface tension	Mt^{-2}	Nm^{-1}
$\overline{\gamma}$	Nondimensional surface tension	–	–

γ_H	Film surface tension evaluated at T_H	T	K
γ_T	First temperature derivative of surface tension $d\gamma/dT$	$Mt^{-2}T^{-1}$	$Nm^{-1}K^{-1}$
$\overline{h}$	Non-dimensional film height	–	–
h_0	Unperturbed nanofilm thickness	L	m
h_T	Convective heat transfer coefficient	$Mt^{-3}K^{-1}$	$Wm^{-2}K^{-1}$
$\overline{\overline{I}}$	Identity tensor	–	–
$\overline{\boldsymbol{K}}$	Dimensionless wavenumber	–	–
k	Spatial wavenumber	L^{-1}	m^{-1}
$k_{\mathbf{air}}$	Air thermal conductivity	$MLt^{-3}T^{-1}$	$Wm^{-1}K^{-1}$
κ	Ratio of air to film thermal conductivity ($k_{\text{air}}/k_{\text{film}}$)	–	–
$k_{\mathbf{film}}$	Film thermal conductivity	$MLt^{-3}T^{-1}$	$Wm^{-1}K^{-1}$
l	Lateral length scale	L	m
λ_{max}	Most unstable spatial mode wavelength	L	m
$\overline{Ma}$	Marangoni number	–	–
μ	Viscosity	L^2t^{-1}	$Pa \cdot s$
$\hat{n}$	Normal unit vector	–	–
∇_S	Local plane gradient operator	L^{-1}	m^{-1}
ω	Angular frequency	t^{-1}	s^{-1}
$\mathcal{P}$	Pressure	$Mt^{-2}L^{-1}$	Pa
$\overline{\mathcal{P}}$	Non-dimensional fluid overpressure	–	–
P	Pin pitch (center-to-center spacing)	L	m
$\mathcal{P}_c$	Characteristic pressure scale	$Mt^{-2}L^{-1}$	Pa

Φ	Velocity Potential	L^2t^{-1}	m^2s^{-1}
$Pow_{\mathbf{lens}}$	Effective power per lens incident on sample surface	ML^2t^{-3}	W
R_1, R_2	Radii of curvature along the paraboloid principal axes	L	m
ρ	Density	ML^{-3}	$kg\,m^{-3}$
$\overline{\overline{T}}$	Stress tensor	$Mt^{-2}L^{-1}$	Pa
$\bar{t}$	Non-dimensional time	–	–
T	Temperature	T	K
t	Time	t	s
$\overline{\overline{\tau}}$	Deviatoric stress tensor	$Mt^{-2}L^{-1}$	Pa
τ	Dimensionless time, normalized to viscous-capillary timescale t_{VC}	–	–
T_C	Temperature of the cooler heat reservoir	T	K
t_c	Characteristic timescale	t	s
$T_{\mathbf{amb}}$	Ambient temperature, 23°C unless otherwise stated.	T	K
T_H	Temperature of the warmer heat reservoir	T	K
θ	Angle between the paraboloid principal axes and the raw data axes	–	rad
t_{VC}	Characteristic viscous-capillary timescale $\mu P/\epsilon^3\gamma_H$	t	s
u_c	Characteristic horizontal velocity scale	Lt^{-1}	$m\,s^{-1}$
$\boldsymbol{v}$	Eulerian fluid velocity field	Lt^{-1}	$m\,s^{-1}$
$\overline{v}_{\parallel}$	Non-dimensional velocity along the lateral plane	–	–
$\overline{v}_z$	Non-dimensional vertical velocity	–	–

w	Beam waist diameter after focusing	L	m
w_c	Characteristic vertical velocity scale	Lt^{-1}	$m\,s^{-1}$
$\overline{\boldsymbol{x}}_{\parallel}$	Non-dimensional position along the lateral plane	–	–
(x_o, y_o)	Position of the paraboloid geometrical center	L	m
$\overline{z}$	Non-dimensional vertical position	–	–
$z_{\mathbf{max}}$	Vertical height of the paraboloid vertex	L	m

Part I

Theoretical Background

Chapter 1

INTRODUCTION AND OVERVIEW

1.1 The value of controlling surface tension

The classical forces we are accustomed to in daily life operate in bulk. As physicists trained in the classical tradition, we push blocks and cylinders up inclined planes with inexplicable delight, summing vectors about an invisible center of mass. Surface tension stands alone as a force that cannot operate within the bulk and that is only found at the interfaces of bulk components. It arises due to an imbalance of the attractive forces between liquid molecules at the interface of the liquid. We may consider a simple isothermal liquid-gas interface to develop intuition regarding the action of surface tension. Liquid molecules at the liquid-gas interface have far more attractive interactions between liquid molecules from the fluid bulk than they have attractive interactions pointing into the gas bulk, simply by virtue of the number of liquid molecules close to them in the direction of the liquid bulk. The net result of these interactions is that the liquid molecules at the liquid-gas interface experience an inward attraction normal to the interface. This net inward attraction causes the interface to behave in a manner similar to that of an elastic membrane under tension, so that the surface constantly seeks to contract and decrease the interfacial area, subject to the geometrical constraints of the total liquid volume [1]. We account for this surface behavior by introducing a force per unit length acting along the interface that points from regions of higher curvature (proportional to the second spatial derivative at a point) to regions of lower curvature. Since this surface tension force acts in the plane of the surface, it is a shear stress, in comparison to pressure, which acts normal to the interface. The combined effects of pressures and shears can be summarized in the fluid stress tensor, which accounts not only for the vector directions that these act along, but also for the vector normals representing the surfaces that these act upon.

Despite operating in the margins of space, surface tension can induce highly non-intuitive phenomena at the large scale. A glass of wine exhibits the “tears of wine” when swirled, forming droplets of wine that spontaneously rise up the side of the glass and fall back. In proposing a mechanism linking surface tension and alcohol concentration for this dinner curiosity in 1855, Thomson became the first to investi-

gate mass transfer due to surface tension [2]. The modern explanation bears a close resemblance to Thomson's proposal. The cyclic behavior of the wine droplets arises because surface tension increases as the concentration of aqueous alcohol decreases. Evaporating alcohol at the margins of the wine meniscus increase the local surface tension due to the reduced alcohol concentration there, inducing the flow of wine up the sides of the glass. The wine then falls back into the bulk as droplets after it gets too heavy for surface tension to overcome gravity.

Apart from alcohol concentration, surface tension depends on a whole host of external parameters. In extremely thin films on the order of tens to hundreds of nanometers thick, surface tension overwhelms all other body forces and governs all film evolution. Whoever gains control over the parameters upon which surface tension depends exerts indirect control over it, and hence exercises complete control over all nanofilm dynamics.

In this thesis, we use temperature fields to control surface tension and fabricate complex surfaces. We call this the Thermocapillary Lithography (TCL) project. Virtually all materials exhibit a monotonic increase in surface tension with decreasing temperature, so cooler regions pull harder along the interface as compared to warmer regions. While there are very few materials that exhibit an increase in surface tension with temperature, such as some liquid metals (e.g. Cadmium) near their melting points [3] and some multicomponent aluminosilicates [4], they also obey the same physical principles of thermocapillary flow that will be described in the following sections. The only difference for these positive temperature coefficient materials will be that material flow will proceed from cooler regions (with weaker surface tension) to warmer regions (with stronger surface tension). By projecting a temperature field on a polymer film, we will show that we are able to control film deformation and feature formation in a deterministic fashion so as to produce film evolution that results in ultrasmooth curved surfaces. These curved surfaces can be sculpted in the form of optical elements, micro-cavities, waveguides, and arbitrary 2D topologies, provided the appropriate temperature field is applied. The results of this thesis indicate that TCL has immense potential in complementing existing established techniques in lithography. While conventional lithography is capable of fabricating blocky structures, TCL excels at producing smooth and continuous surfaces at a high throughput. We hence expect that TCL will play a critical role in contributing to the achievement of arbitrary surface patterns on demand, placing precision-engineered custom optical surfaces and metasurfaces within easy reach.

1.2 Organization of thesis

This thesis is divided into four major parts. In the first part, we deal with the theoretical aspects of fluid dynamics under thermocapillary forces. We derive the thermocapillary equation of motion in the limit of ultrathin films and discuss the role of fluid instabilities in existing nanofilm fabrication techniques. In the second part, we introduce the concept and implementation of Conduction TCL, in which the requisite temperature field is achieved by air conduction from a 3D distribution of pillars or depressions. We describe how Conduction TCL is able to achieve high quality large-scale microlens arrays and provide a complete characterization of these micro-optical structures. For the third part, we detail an alternative means of projecting the fabrication temperature field: Laser-induced TCL. We show how Laser-induced TCL successfully circumvents the key limitations of Conduction TCL by performing fabrication in a fully non-contact fashion with real-time film monitoring. Finally, in the last part of this thesis, we use TCL to fabricate optical devices. We describe how the fabricated microlens arrays can be integrated into a functional Shack-Hartmann wavefront sensor, and how the thermosensitive TCL samples can be coated with a conformal metallic coating in order to produce an optical microcavity array.

Chapter 2

INTRODUCTION TO FLUID INSTABILITIES

2.1 Motivation for studying fluid instabilities

In this Part, we discuss thermocapillary flow, which is the fundamental mechanism allowing us to pattern surfaces in the TCL project. Thermocapillary flow is a specific form of Marangoni flow. In Marangoni flow, material is transported by gradients in surface tension. Thermocapillary flow results when these gradients are set up through the temperature dependence of surface tension. In TCL, we control this mass transport by imposing a highly nonlinear stimulus on a fluid film in the form of a controllable temperature field. To understand what a nonlinear stimulus refers to, we first have to study the linear regime of film evolution under thermocapillary stresses, focusing in particular on the thermocapillary instability. As we will derive later, the thermocapillary instability is a natural phenomenon occurring in fluid layers that are subject to a transverse (normal to the flat layer interface) thermal gradient. The fluid interface spontaneously deforms into an undulating surface with a characteristic feature spacing.

2.2 Organization of Part I: Theoretical Background

We will approach the thermocapillary instability in a tangential manner, first beginning with a simplified model of the more familiar Rayleigh-Taylor instability in Section 2.4, which forms when a more dense fluid layer is placed above a less dense layer. The Rayleigh-Taylor instability model will be used to provide intuition for the thermocapillary instability and also introduce linear stability analysis in Section 2.5. The latter is critical to the understanding the fluid instabilities in general and the implication of the stability analysis will be discussed in Section 2.6.

In Chapter 3 and Section 3.2, we will derive the equation of motion for an ultrathin film subject to a transverse temperature gradient. We will show that in the limit of extreme transverse temperature gradients, the film evolution is dominated by capillary and thermocapillary forces alone. We will apply linear stability analysis to the thermocapillary equation of motion in Section 3.3 and exhibit the existence of a characteristic instability mode, then discuss experimental observations of such surface perturbations in Section 3.4.

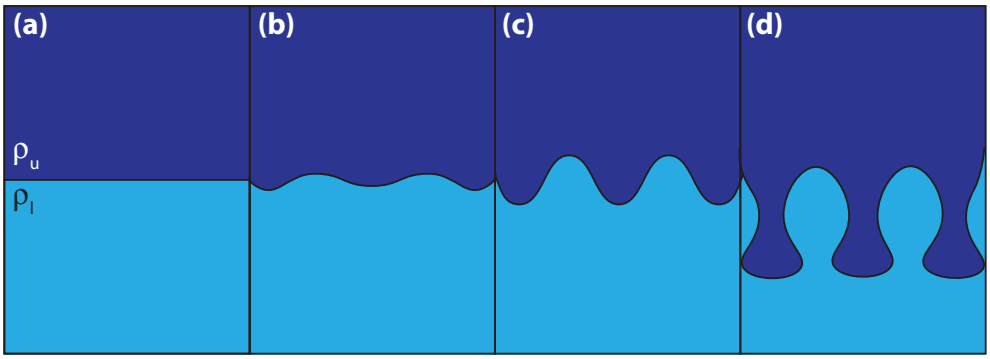

Figure 2.1: Sketch of the time evolution of the Rayleigh-Taylor instability. A denser darker blue fluid with density ρ_u sits on top of a less denser light blue fluid with density $\rho_l < \rho_u$. (a) The initial interface is flat. (b) At early times, we let the interface deforms into an approximately sinusoidal shape. (c) The perturbation amplitude grows exponentially in time. (d) At late times, the denser fluid forms plumes which sink into the less dense fluid below.

In Chapter 4, we then turn to survey various fabrication techniques which exploit fluid instabilities in ultrathin films to achieve surface patterns. We will address the key limitations of these existing techniques in Section 4.4 and use these concepts to motivate the development of the central fabrication technique of this thesis: Thermocapillary Lithography. Finally, we will detail the previous studies into TCL performed by the {LIS^{2}T} group in Section 4.8, and identify how this thesis stands in relation to these developments.

2.3 What is a fluid instability?

Fluid instabilities are characterized by perturbations that grow exponentially away from an initial state. In the canonical Rayleigh-Taylor instability, for instance, one layer of denser fluid sits on top of another less-dense fluid layer. This system is unstable to interfacial perturbations since tiny deviations from perfect flatness will result in that deviation being further accelerated by the difference in density. Figure 2.1 exhibits a sketch of this instability, where a darker blue denser fluid sits above a lighter blue less dense fluid. The initially flat interface (Figure 2.1(a)) that is perturbed by a sinusoidal perturbations in early times (Figure 2.1(b)) produces fluctuations which exponentially increase in amplitude (Figure 2.1(c)). At late times, these perturbations form complex fingering instabilities in which narrow plumes, or "fingers" of denser fluid sink into the less dense fluid below (Figure 2.1(d)) [5, 6]. This instability can be analytically treated using linear stability theory, which examines early time perturbations of the surface (Figure 2.1(a-c)) by linearizing the

differential equations describing the surface about the initial flat condition. It is instructive to examine the main features of linear stability theory in the context of the simple inviscid incompressible Rayleigh-Taylor instability before tackling the more complex thermocapillary instability.

2.4 Derivation of the Rayleigh-Taylor instability

Consider two semi-infinite fluids with the less dense fluid of constant density ρ_l bounded above by the plane $z = 0$ and the more dense fluid of constant density ρ_u bounded below by $z = 0$. Let gravity $\boldsymbol{g}$ be constant in the $-\hat{z}$ direction. For simplicity, we consider one lateral dimension in the plane of the interface, which we denote by the $\hat{x}$ direction. In the limit of slow fluid velocities, the fluid can be treated as incompressible and the Navier-Stokes equation in each layer (assuming uniform viscosity μ) can be written as:

$$\frac{\partial \boldsymbol{v}}{\partial t} + (\boldsymbol{v} \cdot \nabla)\boldsymbol{v} - \frac{\mu}{\rho}\nabla^2 \boldsymbol{v} = \boldsymbol{g} - \nabla\left(\frac{\mathcal{P}}{\rho}\right) \tag{2.1}$$

where $\boldsymbol{v}(\boldsymbol{x}, t)$ is the fluid velocity field in the Eulerian picture and $\mathcal{P}$ is the pressure. We make the additional assumptions that the fluids are inviscid (uniform viscosity $\mu = 0$) and irrotational ($\nabla \times \boldsymbol{v} = 0$). The latter assumption allows us to write the velocity field of each fluid layer as the gradient of a velocity potential Φ:

$$\boldsymbol{v} = \nabla\Phi, \tag{2.2}$$

The incompressibility of the fluid and the lack of any sources or sinks in the fluids imply that the fluid velocity field must be divergenceless:

$$\nabla \cdot \boldsymbol{v} = 0 \implies \nabla^2\Phi = 0 \tag{2.3}$$

Using the vector calculus identity $(\boldsymbol{v} \cdot \nabla)\boldsymbol{v} = \frac{1}{2}\nabla(\boldsymbol{v} \cdot \boldsymbol{v}) - \boldsymbol{v} \times (\nabla \times \boldsymbol{v})$, assuming a constant gravitational field $\boldsymbol{g} = -g\hat{z}$, and implementing the previous assumptions, we may simplify the Navier-Stokes equation:

$$\nabla\mathcal{P} + \rho\frac{\partial \boldsymbol{v}}{\partial t} + \frac{1}{2}\rho\nabla(\boldsymbol{v} \cdot \boldsymbol{v}) = -\rho g\hat{z} \tag{2.4}$$

and substituting the velocity potential while assuming all derivatives are well-behaved,

$$\nabla \mathcal{P} + \nabla \left(\rho \frac{\partial \phi}{\partial t} \right) + \frac{1}{2} \rho \nabla [(\nabla \phi)^2] = -\rho g \hat{z} \tag{2.5}$$

This equation can be projected along $\hat{z}$ and immediately integrated once with respect to z to yield Bernoulli's equation:

$$\mathcal{P} + \rho \left(\frac{\partial \phi}{\partial t} + \frac{1}{2} |\nabla \phi|^2 + gz \right) = \text{constant} \tag{2.6}$$

Since the fluid layers are initially stationary, the velocity potentials are initially constants in their respective domains. We may pick this constant to be zero. We now introduce a small perturbation in the interface, parametrized by $z = h(x, t)$. The corresponding perturbation in the velocity field can be captured by adding a small nonzero term (with vanishing Laplacian) in the velocity potential:

$$\Phi(x, z, t) = \begin{cases} \phi_u(x, z, t), & z > 0 \\ \phi_l(x, z, t), & z \leq 0 \end{cases} \tag{2.7}$$

We will like to examine the dynamics near the interface and at short times (where the velocity and position perturbations are small), hence we require that the velocity potentials vanish far from the interface. We evaluate the total derivative of the interface equation to relate the derivatives of the velocity potential and the height perturbation at the interface:

$$\frac{Dz}{Dt} = \frac{Dh(x, t)}{Dt} = \frac{\partial h(x, t)}{\partial x} \frac{Dx}{Dt} + \frac{\partial h(x, t)}{\partial t} \tag{2.8}$$

We will like to express the total derivatives Dz/Dt and Dx/Dt in terms of derivatives of the velocity potential ϕ_j in each of the upper and lower domains. By definition, the spatial derivative of the velocity potential is the velocity field itself. Replacing the total derivatives, we hence obtain:

$$\frac{\partial \phi_j}{\partial z} = \frac{\partial h}{\partial x} \frac{\partial \phi_j}{\partial x} + \frac{\partial h}{\partial t}, \quad j = u, l \tag{2.9}$$

The first term on the right hand side is the product of two infinitesimal perturbations and hence may be neglected to first order to yield:

$$\frac{\partial \phi_j}{\partial z} = \frac{\partial h}{\partial t}, \quad j = u, l \tag{2.10}$$

We now implement the Bernoulli equation derived earlier and compare the perturbed system parameters (evaluated at the interface position $z = h(x,t)$) to that of the stationary initial condition (evaluated at the initial interface $z = 0$).

$$\mathcal{P}_j + \rho_j \left(\frac{\partial \phi_j}{\partial t} + \frac{1}{2} \left| \nabla \phi_j \right|^2 + gz \right) = \mathcal{P}_{\text{initial}}, \quad j = u, l \tag{2.11}$$

This comparison allows us to equate the equations for the initial pressure above and below the perturbed interface:

$$\mathcal{P}_u + \rho_u \left(\frac{\partial \phi_u}{\partial t} + \frac{1}{2} \left| \nabla \phi_u \right|^2 + gh \right) = \mathcal{P}_l + \rho_l \left(\frac{\partial \phi_l}{\partial t} + \frac{1}{2} \left| \nabla \phi_l \right|^2 + gh \right) \tag{2.12}$$

In the absence of surface tension, the only forces acting on the fluid interface are due to normal pressure. Force balance over the interface (which has zero mass and hence must experience zero net force) hence requires that the pressures immediately above and below the perturbed interface are equal $\mathcal{P}_u = \mathcal{P}_l$. Furthermore, the velocity squared term is second order and hence can be neglected to first order:

$$\rho_u \left(\frac{\partial \phi_u}{\partial t} + gh \right) = \rho_l \left(\frac{\partial \phi_l}{\partial t} + gh \right) \tag{2.13}$$

2.5 Linear stability analysis of the Rayleigh-Taylor instability

We may study the time-dependence of the Rayleigh-Taylor system using a technique known as Linear Stability Analysis. In the context of fluid dynamics, Linear Stability Analysis is the examination of the short time behavior of a system through the study of the time-dependence of simple growth modes. The outcome of these analyses provide information on the susceptibility of a system to spontaneous irreversible change, as well as the characteristic geometric properties of such changes. For the Rayleigh-Taylor system, we substitute a single Fourier mode ansatz for the height perturbation, where $k > 0$ is the spatial wavenumber of the lateral (x) oscillation,

and examine the short time behavior of the system under such a perturbation. Symbolically, we write the height perturbation ansatz as:

$$h(x,t) = h_0 e^{i(kx-\omega t)} \tag{2.14}$$

Substituting this ansatz into equation 2.13, we notice that ϕ_u and ϕ_l must also have a similar exponential dependence when evaluated at the interfacial position. We hence also write a Fourier mode ansatz for the velocity potential perturbations, allowing the mode amplitude to vary as a function of vertical position z away from the interface:

$$\phi_j(x,z,t) = \phi_j^0(z) e^{i(kx-\omega t)}, \quad j = u, l \tag{2.15}$$

Since the velocity potential has a vanishing Laplacian (Equation 2.3), we require that:

$$\frac{\partial^2 \phi_j^0(z)}{\partial z^2} - k^2 \phi_j^0(z) = 0, \quad j = u, l \tag{2.16}$$

This second order ordinary differential equation immediately has solutions for the amplitude function of the Fourier mode ansatz:

$$\phi_j^0(z) = A e^{\pm kz} \tag{2.17}$$

Since we require that the velocity potential vanish far away from the interface, we pick the appropriate sign of k for the potentials above and below the interface so that ϕ_j^0 vanishes exponentially away from $z = 0$:

$$\phi_u^0(z) = C_u e^{-kz}, \quad z > 0 \tag{2.18}$$

$$\phi_l^0(z) = C_l e^{kz}, \quad z < 0 \tag{2.19}$$

Substituting the ansatz equations for ϕ_j and h into equations 2.10 and 2.13, we obtain:

$$-C_u k e^{-kh(x,t)} e^{i(kx-\omega t)} = -i\omega h_0 e^{i(kx-\omega t)} \tag{2.20}$$

$$C_l k e^{kh(x,t)} e^{i(kx-\omega t)} = -i\omega h_0 e^{i(kx-\omega t)} \tag{2.21}$$

$$\rho_u \left(-i\omega C_u e^{-kh(x,t)} e^{i(kx-\omega t)} + g h_0 e^{i(kx-\omega t)}\right) = \rho_l \left(-i\omega C_l e^{kh(x,t)} e^{i(kx-\omega t)} + g h_0 e^{i(kx-\omega t)}\right)$$

We observe that since both C_j, $j = u, l$ and $h(x,t)$ are small, we may evaluate $e^{\pm kh(x,t)}$ to zeroth order (thereby requiring $e^{\pm kh(x,t)} \approx 1$) and obtain:

$$-C_u k = -i\omega h_0 \tag{2.22}$$

$$C_l k = -i\omega h_0 \tag{2.23}$$

$$\rho_u \left(-i\omega C_u + g h_0\right) = \rho_l \left(-i\omega C_l + g h_0\right) \tag{2.24}$$

Substituting the expressions for C_j into equation 2.24, and requiring that $h_0 \neq 0$ so that the perturbations are nontrivial,

$$\rho_u \left(-i\omega \frac{i\omega h_0}{k} + g h_0\right) = \rho_l \left(-i\omega \frac{-i\omega h_0}{k} + g h_0\right) \implies \rho_u \left(\frac{\omega^2}{k} + g\right) = \rho_l \left(-\frac{\omega^2}{k} + g\right)$$

Rearranging, we obtain the dispersion relation:

$$\implies \omega^2 = kg \frac{\rho_l - \rho_u}{\rho_l + \rho_u} \tag{2.25}$$

2.6 Analysis of the Rayleigh-Taylor dispersion relation

Since the upper fluid layer is denser than the lower fluid layer, $\rho_u > \rho_l$, and the right hand side of the dispersion relation in Equation 2.25 is strictly negative. This means that ω is purely imaginary, and since the time dependence is contained in the exponential term $e^{i(kx-\omega t)}$, there are Fourier mode solutions (parametrized by k) which grow exponentially in time. In fact, for every value of $k > 0$, there exist solutions with negative imaginary part of ω which exhibit this exponential blow-up. Since a true surface contains perturbations with nonzero spatial wavenumber, the interface between the fluid bilayer is unstable and will always exhibit an early time exponential amplification of the perturbation. This is the essence of the Rayleigh-Taylor instability: since there exist evolution solutions with exponential dependence

on time in the form $e^{i\omega t}$, where the imaginary part of the angular frequency is negative $\Im(\omega) < 0$, the surface is unstable to perturbations and will exhibit spontaneous interface deformation that deviates exponentially from the initial condition.

The Rayleigh-Taylor instability exists because of the gradient in fluid density. Similarly, other fluid instabilities exist that are associated with gradients in other physical parameters. If a sufficiently strong electric field (electric potential gradient) is applied across a flat thin polymeric film so that it overcomes stabilization due to capillary (surface tension) forces, it spontaneously forms undulating surface patterns [7]. This instability is known as the electrohydrodynamic (EHD) instability. Unlike the Rayleigh-Taylor instability, in which the exponential growth rate (controlled by the imaginary part of ω) is a monotonically increasing function of wavenumber k, the dispersion relation for the EHD instability exhibits a global maximum for growth rate against wavenumber. The wavenumber corresponding to the maximum growth rate k_{max} is known as the most unstable mode, and is associated with a spatial wavelength $\lambda_{\max} = 2\pi/k_{\max}$ that sets the characteristic length scale of the instability [8]. The structures formed by the EHD instability over a flat liquid film in a uniform transverse electric field are self-assembled hexagonally packed undulations with characteristic sizes on the order of the wavelength of the most unstable mode.

Chapter 3

THE THERMOCAPILLARY INSTABILITY

3.1 A quick history of thermocapillarity applied to thin films

In this chapter, we derive the equation of motion of an incompressible, Newtonian thin film with a temperature-dependent surface tension. The evolution of liquid films through surface tension forces in response to heating or cooling has been studied for over a century, beginning perhaps with Bénard's 1901 observation of convective cells in a heated thin liquid film that could not be explained by density variations [9]. These features would later be correctly ascribed by Block in 1956 as due to thermocapillarity: the dependence of surface tension on temperature [10]. Since then, the evolution of liquids under thermocapillary forces has been studied theoretically and experimentally under virtually every possible system geometry. However, one regime was neglected until only recently. Over 2009-2010, Dietzel and Troian showed that in the previously unexplored limit of ultrathin films and ultrahigh temperature gradients transverse to a liquid film, a film should form spontaneous thickness perturbations with a characteristic lengthscale [11, 12]. This thermocapillary mechanism was found to explain experimental observations of spontaneous periodic nanofilm perturbations in this regime better than competing acoustic phonon or electrostatic theories [13]. The regime of ultrathin films is important because of its ubiquity in natural phenomena (e.g., in biological membranes) and in industrial processes (e.g., adhesives and boundary flows). Understanding these flows in response to ever-present temperature fluctuations is essential to controlling them and the more complex systems dependent on these boundary conditions. It is for this reason that we will specialize this study of thermocapillary flows to that which occurs in ultrathin films. We will follow in the convention of Oron *et al.* and examine the long-scale behavior of these films (for slow spatial variations in the plane of the film as compared to that of transverse variations normal to it), developing a highly nonlinear differential equation of motion in terms of a single dynamic parameter: the local film thickness [14]. The following derivation reproduces the major results of Dietzel and Troian [12] with a similar analytical strategy.

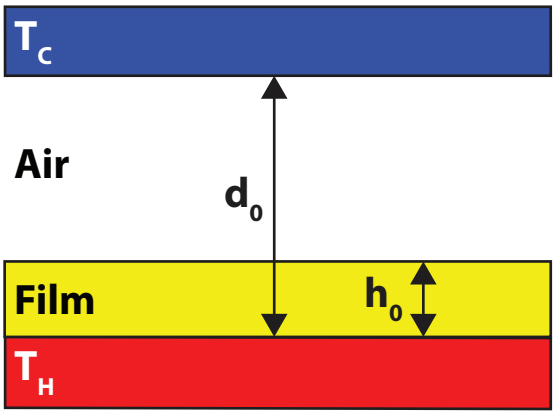

Figure 3.1: Geometry of the parallel-plate system used in the derivation of the thermocapillary equation of motion in the ultrathin film and ultralarge thermal gradient limit. Two parallel plates are held at fixed temperatures T_H and T_C, where $T_H > T_C$, and are separated by a distance d_0. A nanofilm of thickness h_0 rests on the lower hotter plate.

3.2 Derivation of the thermocapillary equation of motion

System geometry

Figure 3.1 exhibits the geometry of the system we will use to derive the thermocapillary equation of motion. Consider two parallel horizontal heat reservoirs placed d_0 apart, with the lower reservoir held at a fixed temperature of T_H and the upper reservoir held at a cooler temperature $T_C < T_H$. Let there be a liquid nanofilm of thickness $h_0 < d_0$ on the surface of the lower reservoir. Let the viscosity be approximately constant throughout each fluid layer. We may treat the horizontal dimensions x and y on par with each other and keep the vertical dimension z separate. We hence separate positions, velocities and gradients into the lateral components (x and y, parallel to the reservoir plates) and the transverse component (z, perpendicular to the reservoir plates), writing $\boldsymbol{x} = (\boldsymbol{x}_\parallel, z), \boldsymbol{v} = (\boldsymbol{v}_\parallel, v_z), \nabla = \nabla_\parallel + \frac{\partial}{\partial z}\hat{z}$. As in the derivation of the Rayleigh-Taylor instability, we parametrize the film-air interface with the function $z = h(\boldsymbol{x}_\parallel, t)$.

Boundary Conditions and Assumptions

We begin again with the Navier-Stokes equation:

$$\frac{\partial \boldsymbol{v}}{\partial t} + (\boldsymbol{v} \cdot \nabla)\boldsymbol{v} - \frac{\mu}{\rho}\nabla^2 \boldsymbol{v} = \boldsymbol{g} - \nabla\left(\frac{\mathcal{P}}{\rho}\right) \tag{3.1}$$

and the equation for continuity:

$$\nabla \cdot \boldsymbol{v} = 0 \tag{3.2}$$

We may separate the Navier-Stokes equation into the lateral and transverse components:

$$\frac{\partial \boldsymbol{v}_\parallel}{\partial t} + (\boldsymbol{v}_\parallel \cdot \nabla_\parallel)\boldsymbol{v}_\parallel + v_z \frac{\partial \boldsymbol{v}_\parallel}{\partial z} - \frac{\mu}{\rho}\nabla_\parallel^2 \boldsymbol{v}_\parallel - \frac{\mu}{\rho}\frac{\partial^2 \boldsymbol{v}_\parallel}{\partial z^2} = -\nabla_\parallel \frac{\mathcal{P}}{\rho} \tag{3.3}$$

$$\frac{\partial v_z}{\partial t} + (\boldsymbol{v}_\parallel \cdot \nabla_\parallel)v_z + v_z \frac{\partial v_z}{\partial z} - \frac{\mu}{\rho}\nabla_\parallel^2 v_z - \frac{\mu}{\rho}\frac{\partial^2 v_z}{\partial z^2} = -g - \frac{\partial}{\partial z}\frac{\mathcal{P}}{\rho} \tag{3.4}$$

We will be incorporating surface tension effects into this system by examining the stress balance at the film-air interface. In the regime under study, the effects of body forces (due to gravity) are negligible compared to that of surface tension. The relative strength of body forces to that of surface tension can be estimated by calculating the dimensionless Bond number (also known as the Eötvös number):

$$Bo = \frac{\Delta\rho g L^2}{\gamma} \tag{3.5}$$

where $\Delta\rho$ is the difference in density between two phases, g is the gravitational acceleration, L is a characteristic lengthscale for the system, and γ is the surface tension under consideration. Small Bond numbers mean that surface tension dominates body forces, and vice versa. For a typical low-molecular weight polymeric nanofilm melt, $\Delta\rho \sim 10^3$ kg m^{-3}, L is the film thickness of around 100 nm, and $\gamma \sim 10^{-2}$ N/m. These parameter values yield a Bond number estimate of 10^{-8}, indicating that surface tension effects are on the order of 100 million times stronger than that of gravitational effects. We may hence safely neglect gravity in the examination of this surface-tension dominated system. However, we will keep g in the following Navier-Stokes analysis for the time being. The influence of gravitational forces will be naturally removed later when we move into the thin film regime.

The liquid boundary conditions consist of the no-slip boundary condition at the lower interface:

$$\boldsymbol{v}(z = 0) = 0 \tag{3.6}$$

the kinematic boundary condition (in 2D now) relating the velocities at the air-film interface:

$$\frac{Dz}{Dt} = \frac{Dh(\boldsymbol{x}_\parallel, t)}{Dt} = \nabla_\parallel h(\boldsymbol{x}_\parallel, t) \cdot \boldsymbol{v}_\parallel + \frac{\partial h(\boldsymbol{x}_\parallel, t)}{\partial t} \tag{3.7}$$

along with a force balance condition at the air-film interface (which has zero thickness, and hence must experience precisely zero net force) [15]:

$$\left(\overline{\overline{T}}_{\text{air}} - \overline{\overline{T}}_{\text{film}}\right) \cdot \hat{n} + \nabla_S \gamma - \gamma \hat{n}(\nabla \cdot \hat{n}) = 0 \tag{3.8}$$

where $\hat{n}$ is the local normal vector, $\nabla_S = \nabla - \hat{n}(\hat{n} \cdot \nabla)$ is the local plane gradient operator, $\overline{\overline{T}}$ is the stress tensor, and γ is the surface tension.

The stress tensor for a fluid can be written as the sum of a diagonal pressure contribution (multiplied by the identity tensor $\overline{\overline{I}}$) and the deviatoric stress $\overline{\overline{\tau}}$:

$$\overline{\overline{T}} = -\mathcal{P}\overline{\overline{I}} + \overline{\overline{\tau}} \tag{3.9}$$

For a Newtonian fluid, the deviatoric stress is linearly related to the local strain rate $\overline{\overline{E}}$ (making the incompressible assumption that the trace $\text{tr}\,\overline{\overline{E}} = \nabla \cdot \boldsymbol{v} = 0$):

$$\overline{\overline{\tau}} = 2\mu\overline{\overline{E}} \tag{3.10}$$

where μ is the shear viscosity (also known as the dynamic viscosity) of the fluid.

The local strain rate can be written as the symmetric sum (noting that the gradient operator now acts on a vector quantity $\boldsymbol{v}$ to yield a tensor $\nabla\boldsymbol{v}$), where the superscript T refers to the transpose:

$$\overline{\overline{E}} = \frac{\nabla\boldsymbol{v} + \nabla\boldsymbol{v}^T}{2} \tag{3.11}$$

In the air layer, we may take the stress tensor to have the form $\overline{\overline{T}}_{\text{air}} = -\mathcal{P}_{\text{air}}\overline{\overline{I}}$, thereby neglecting deviatoric stresses in the air. This assumption is justified since the shear viscosity of air is much smaller than that of the liquid layer. For instance, the viscosity of air at 127°C is 23.1×10^{-6} Pa·s [16] while the viscosity of low molecular weight polystyrene melt is around 32.5 Pa·s at 100°C (from private communication

with the authors of Urakawa *et al.* [17]), a difference of six orders of magnitude. We may take the dot product of the stress balance equation, 3.8, with $\hat{n}$ and $\hat{t}$, the outward normal and tangential unit vectors (of which there are two orthogonal tangential unit vectors), respectively, to yield the normal and tangential equations (all evaluated at the air-film interface):

$$-\mathcal{P}_{\text{air}} + \mathcal{P}_{\text{film}} - \hat{n} \cdot \mu \left[\left(\nabla \boldsymbol{v} + \nabla \boldsymbol{v}^T \right) \cdot \hat{n} \right] - \gamma (\nabla \cdot \hat{n}) = 0 \tag{3.12}$$

$$\mu \hat{t} \cdot \left[\left(\nabla \boldsymbol{v} + \nabla \boldsymbol{v}^T \right) \cdot \hat{n} \right] - \hat{t} \cdot \nabla_S \gamma = 0 \tag{3.13}$$

Observe that the normal equation does not contain the surface tension gradient term because $(\nabla_S \gamma) \cdot \hat{n} = (\nabla \gamma) \cdot \hat{n} - \hat{n} \cdot \nabla \gamma = 0$. Since surface tension depends on temperature (and we neglect the dependence of surface tension on other external parameters), we may used the chain rule to write the surface gradient of surface tension $\nabla_S \gamma$ as:

$$\nabla_S \gamma = \frac{\partial \gamma}{\partial T} \nabla_S T \tag{3.14}$$

For small lateral changes in temperature, we may linearize the dependence of surface tension on temperature and write it as:

$$\gamma(T) = \gamma_H - \gamma_T (T - T_H) \tag{3.15}$$

where γ_T is the linear coefficient for temperature dependence and T_H is the temperature of the lower thermal reservoir. γ_H is the surface tension of the film evaluated at the lower heated stage temperature T_H. We have chosen a negative coefficient for the linear term because most materials exhibit a decrease in surface tension with increasing temperature, so $\gamma_T > 0$. The same formalism is appropriate for materials which exhibit an increase in surface tension with temperature, albeit with $\gamma_T < 0$.

Nondimensionalization in the thin film regime

We now examine the regime in which the distance between the fluid boundaries (heated reservoir below and the free air-film surface above) is small compared to its lateral extent. This is known as the long wavelength limit or lubrication approxi-

mation. Formally, we introduce a lateral length scale l and define a dimensionless quantity ϵ:

$$\epsilon \equiv \frac{h_0}{l} \tag{3.16}$$

We may use this lateral length scale and ϵ to non-dimensionalize the Cartesian positions (non-dimensional quantities will be labelled with an overline if there is an ambiguity):

$$\overline{\boldsymbol{x}}_{\parallel} \equiv \frac{\boldsymbol{x}_{\parallel}}{l}, \quad \overline{z} \equiv \frac{z}{h_0} = \frac{z}{\epsilon l} \tag{3.17}$$

The non-dimensional film thickness is normalized to the initial film height:

$$\overline{h} \equiv \frac{h}{h_0} \tag{3.18}$$

We also introduce a characteristic horizontal velocity scale u_c and characteristic vertical velocity scale w_c to non-dimensionalize the fluid velocities:

$$\overline{\boldsymbol{v}}_{\parallel} \equiv \frac{\boldsymbol{v}_{\parallel}}{u_c}, \quad \overline{v}_z \equiv \frac{v_z}{w_c} \tag{3.19}$$

The characteristic velocity scale u_c is introduced simply for clarity. We will show later that the time evolution equation of motion does not depend on u_c, but we will keep u_c for the time being to show how the various nondimensional fluid parameters relate to that of classical fluidic systems. The characteristic timescale $t_c \equiv l/u_c$ can be used to non-dimensionalize the time:

$$\bar{t} \equiv \frac{t}{l/u_c} = \frac{t}{t_c} \tag{3.20}$$

Substituting these velocity scales into the equation for continuity, and requiring that the partial derivatives involving dimensionless quantities be of order unity,

$$\nabla \cdot \boldsymbol{v} = 0 \implies \frac{w_c}{\epsilon l}\frac{\partial \overline{v}_z}{\partial \overline{z}} = -\frac{u_c}{l}\left(\frac{\partial \overline{v}_x}{\partial \overline{x}} + \frac{\partial \overline{v}_y}{\partial \overline{y}}\right) \implies w_c = \epsilon u_c \tag{3.21}$$

We hence non-dimensionalize the vertical fluid velocity by replacing w_c:

$$\overline{v}_z = \frac{v_z}{\epsilon u_c} \tag{3.22}$$

The dimensionless continuity equation is hence (defining the non-dimensional in-plane gradient $\overline{\nabla}_{\parallel} \equiv (1/l)\nabla_{\parallel}$):

$$\overline{\nabla}_{\parallel} \cdot \overline{\boldsymbol{v}}_{\parallel} + \frac{\partial \overline{v}_z}{\partial \overline{z}} = 0 \tag{3.23}$$

We also introduce the characteristic pressure scale $\mathcal{P}_c$ to achieve the non-dimensional overpressure:

$$\overline{\mathcal{P}} \equiv \frac{\mathcal{P} - \mathcal{P}_{\text{air}}}{\mathcal{P}_c} \tag{3.24}$$

which, when substituted into equations 3.3 and 3.4, yields:

$$\frac{u_c^2}{l}\frac{\partial \overline{\boldsymbol{v}}_{\parallel}}{\partial \overline{t}} + \frac{u_c^2}{l}(\overline{\boldsymbol{v}}_{\parallel} \cdot \overline{\nabla}_{\parallel})\overline{\boldsymbol{v}}_{\parallel} + \frac{u_c^2}{l}\overline{v}_z\frac{\partial \overline{\boldsymbol{v}}_{\parallel}}{\partial \overline{z}} - \frac{\mu u_c}{\rho l^2}\overline{\nabla}_{\parallel}^2\overline{\boldsymbol{v}}_{\parallel} - \frac{\mu u_c}{\rho \epsilon^2 l^2}\frac{\partial^2 \overline{\boldsymbol{v}}_{\parallel}}{\partial \overline{z}^2} = -\frac{\mathcal{P}_c}{l\rho}\overline{\nabla}_{\parallel}\overline{\mathcal{P}} \tag{3.25}$$

$$\frac{\epsilon u_c^2}{l}\frac{\partial \overline{v}_z}{\partial \overline{t}} + \frac{u_c^2 \epsilon}{l}(\overline{\boldsymbol{v}}_{\parallel} \cdot \overline{\nabla}_{\parallel})\overline{v}_z + \frac{\epsilon u_c^2}{l}\overline{v}_z\frac{\partial \overline{v}_z}{\partial \overline{z}} - \frac{\mu \epsilon u_c}{\rho l^2}\overline{\nabla}_{\parallel}^2\overline{v}_z - \frac{\mu u_c}{\rho \epsilon l^2}\frac{\partial^2 \overline{v}_z}{\partial \overline{z}^2} = -g\hat{z} - \frac{\mathcal{P}_c}{\epsilon l \rho}\frac{\partial \overline{\mathcal{P}}}{\partial \overline{z}} \tag{3.26}$$

Rearranging,

$$\epsilon^2 \mathcal{P}_c \overline{\nabla}_{\parallel}\overline{\mathcal{P}} = -\epsilon^2 \rho u_c^2\left(\frac{\partial \overline{\boldsymbol{v}}_{\parallel}}{\partial \overline{t}} + (\overline{\boldsymbol{v}}_{\parallel} \cdot \overline{\nabla}_{\parallel})\overline{\boldsymbol{v}}_{\parallel} + \overline{v}_z\frac{\partial \overline{\boldsymbol{v}}_{\parallel}}{\partial \overline{z}}\right) + \frac{\epsilon^2 \mu u_c}{l}\overline{\nabla}_{\parallel}^2\overline{\boldsymbol{v}}_{\parallel} + \frac{\mu u_c}{l}\frac{\partial^2 \overline{\boldsymbol{v}}_{\parallel}}{\partial \overline{z}^2} \tag{3.27}$$

$$\mathcal{P}_c\frac{\partial \overline{\mathcal{P}}}{\partial \overline{z}} = -\rho \epsilon^2 u_c^2\left(\frac{\partial \overline{v}_z}{\partial \overline{t}} + (\overline{\boldsymbol{v}}_{\parallel} \cdot \overline{\nabla}_{\parallel})\overline{v}_z + \overline{v}_z\frac{\partial \overline{v}_z}{\partial \overline{z}}\right) + \frac{\mu \epsilon^2 u_c}{l}\overline{\nabla}_{\parallel}^2\overline{v}_z + \frac{\mu u_c}{l}\frac{\partial^2 \overline{v}_z}{\partial \overline{z}^2} - \epsilon l \rho g \tag{3.28}$$

We observe that there are two possible scalings for $\mathcal{P}_c$ by balancing each of Equations 3.27 and 3.28 above. Since $\epsilon < 1$, the lowest order term in ϵ on the right hand side of equation 3.28 is the zeroth order second-to-last term, which leads to a characteristic pressure scaling of $\mathcal{P}_c = \frac{\mu u_c}{l}$. However, the choice of this pressure scaling, when substituted into equation 3.27, will leave a single term (the last term) in 3.27 with zeroth order dependence on ϵ. All other terms will have second

order or higher dependence on ϵ. In the limit as ϵ vanishes, we will obtain an underdetermined system since the horizontal pressure gradient term (term left of the equality) vanishes. This approximation does not leave a physically valid set of equations.

We are hence restricted to using equation 3.27 to balance the parameter scaling relations. This yields the characteristic pressure scaling:

$$\mathcal{P}_c = \frac{\mu u_c}{l\epsilon^2} \tag{3.29}$$

We may now implement the lubrication or long-wavelength approximation, where the transverse length scales are much smaller than the lateral length scales. We explore the regime where $\epsilon^2 \ll 1$, and remove terms of order ϵ^2 and higher. In this low-order model, the Navier-Stokes equations in the fluid bulk 3.27-3.28 yield:

$$\overline{\nabla}_\parallel \overline{\mathcal{P}} = \frac{\partial^2 \overline{\boldsymbol{v}}_\parallel}{\partial \overline{z}^2} \tag{3.30}$$

$$\frac{\partial \overline{\mathcal{P}}}{\partial \overline{z}} = 0 \implies \overline{\mathcal{P}} = F_1(\overline{\boldsymbol{x}}_\parallel) \tag{3.31}$$

The invariance of the pressure in the vertical direction is a common characteristic of thin film systems. Since $\overline{\mathcal{P}}$ (and hence $\overline{\nabla}_\parallel \overline{\mathcal{P}}$) does not depend on $\overline{z}$, we may integrate equation 3.30 twice to obtain:

$$\overline{\boldsymbol{v}}_\parallel = \frac{\overline{z}^2}{2}\overline{\nabla}_\parallel \overline{\mathcal{P}} + \overline{z}\boldsymbol{F}_2(\overline{\boldsymbol{x}}_\parallel) = \frac{\overline{z}^2}{2}\overline{\nabla}_\parallel F_1(\overline{\boldsymbol{x}}_\parallel) + \overline{z}\boldsymbol{F}_2(\overline{\boldsymbol{x}}_\parallel) \tag{3.32}$$

where F_1 and $\boldsymbol{F}_2$ are unknown scalar-valued and vector-valued functions, respectively. We suppress the time dependence in these functions for the time being in pursuit of clarity. Knowing $\overline{\boldsymbol{v}}_\parallel$ allows us to construct $\overline{v}_z$ using the dimensionless continuity equation 3.23:

$$\frac{\partial \overline{v}_z}{\partial \overline{z}} = -\left[\frac{\overline{z}^2}{2}\overline{\nabla}_\parallel^2 F_1(\overline{\boldsymbol{x}}_\parallel) + \overline{z}\overline{\nabla}_\parallel \cdot \boldsymbol{F}_2(\overline{\boldsymbol{x}}_\parallel)\right] \tag{3.33}$$

$$\implies \overline{v}_z = -\frac{\overline{z}^3}{6}\overline{\nabla}_\parallel^2 F_1(\overline{\boldsymbol{x}}_\parallel) - \frac{\overline{z}^2}{2}\overline{\nabla}_\parallel \cdot \boldsymbol{F}_2(\overline{\boldsymbol{x}}_\parallel) \tag{3.34}$$

We have used the no-slip conditions from equation 3.6 to write the dimensionless form and eliminate the constants from the integration of $\overline{\boldsymbol{v}}_{\parallel}$ and $\overline{v}_z$:

$$\overline{v}_z(\overline{z}=0)=0\,,\quad \overline{\boldsymbol{v}}_{\parallel}(\overline{z}=0)=0 \tag{3.35}$$

To solve for F_1 and $\boldsymbol{F}_2$, we have to incorporate the pressure balance boundary conditions at the film-air interface. Equations 3.12 and 3.13 can be nondimensionalized and reduced to order ϵ to yield:

$$\left[\overline{\mathcal{P}}+\frac{\overline{\nabla}_{\parallel}^2\overline{h}}{\overline{Ca}}\right]_{\overline{z}=\overline{h}}=0 \tag{3.36}$$

$$\left[\frac{\partial\overline{\boldsymbol{v}}_{\parallel}}{\partial\overline{z}}-\overline{Ma}\,\overline{\nabla}_{\parallel}\overline{\gamma}\right]_{\overline{z}=\overline{h}}=0 \tag{3.37}$$

where the nondimensional Capillary number for this system is given as:

$$\overline{Ca}\equiv\frac{\mu u_c}{\epsilon^3\gamma_H} \tag{3.38}$$

and the nondimensional Marangoni number is:

$$\overline{Ma}\equiv\frac{\epsilon\gamma_T(T_H-T_C)}{\mu u_c}=\frac{\epsilon\gamma_T\Delta T}{\mu u_c} \tag{3.39}$$

with γ_H being the initial surface tension of the base of the film in thermal contact with the hotter reservoir at temperature T_H, and $\Delta T = T_H - T_C$ being the temperature difference across the combined air and film gap. The algebraic details of the calculation are tedious and are omitted for brevity. $\overline{\gamma}$ is the nondimensional surface tension with scaling:

$$\overline{\gamma}\equiv\frac{\gamma}{\gamma_T\Delta T} \tag{3.40}$$

The Capillary and Marangoni numbers have the same form as that in common fluid dynamics systems with the addition of the dimensionless ϵ terms. Equation 3.36 immediately yields the pressure, since the pressure is a constant in the $\hat{z}$ direction:

$$\overline{\mathcal{P}}=F_1(\overline{\boldsymbol{x}}_{\parallel})=-\frac{\overline{\nabla}_{\parallel}^2\overline{h}}{\overline{Ca}} \tag{3.41}$$

Comparing equations 3.32 and 3.37, we also obtain an expression for $\boldsymbol{F}_2$, evaluating at $\overline{z} = \overline{h}$:

$$\boldsymbol{F}_2(\overline{\boldsymbol{x}}_\parallel) = \overline{Ma}\,\overline{\nabla}_\parallel\overline{\gamma} + \overline{h}\,\overline{\nabla}_\parallel\left(\frac{\overline{\nabla}_\parallel^2\overline{h}}{\overline{Ca}}\right) \tag{3.42}$$

$$\overline{\boldsymbol{v}}_\parallel(\overline{z} = \overline{h}) = -\frac{\overline{h}^2}{2}\overline{\nabla}_\parallel\frac{\overline{\nabla}_\parallel^2\overline{h}}{\overline{Ca}} + \overline{h}\left[\overline{Ma}\,\overline{\nabla}_\parallel\overline{\gamma} + \overline{h}\,\overline{\nabla}_\parallel\left(\frac{\overline{\nabla}_\parallel^2\overline{h}}{\overline{Ca}}\right)\right] \tag{3.43}$$

$$\overline{v}_z(\overline{z} = \overline{h}) = \frac{\overline{h}^3}{6}\overline{\nabla}_\parallel^2\frac{\overline{\nabla}_\parallel^2\overline{h}}{\overline{Ca}} - \frac{\overline{h}^2}{2}\overline{\nabla}_\parallel\cdot\left[\overline{Ma}\,\overline{\nabla}_\parallel\overline{\gamma} + \overline{h}\,\overline{\nabla}_\parallel\left(\frac{\overline{\nabla}_\parallel^2\overline{h}}{\overline{Ca}}\right)\right] \tag{3.44}$$

These expressions for $\overline{\boldsymbol{v}}_\parallel$ and $\overline{v}_z$ can be substituted into the non-dimensional kinematic boundary condition from equation 3.7:

$$[\overline{v}_z]_{\overline{z}=\overline{h}} = \left[\overline{\nabla}_\parallel\overline{h}\cdot\overline{\boldsymbol{v}}_\parallel + \frac{\partial\overline{h}}{\partial\overline{t}}\right]_{\overline{z}=\overline{h}} \tag{3.45}$$

to yield the thin-film equation of motion in terms of the surface tension gradient $\overline{\nabla}_\parallel\overline{\gamma}$:

$$\frac{\partial\overline{h}}{\partial\overline{t}} + \overline{\nabla}_\parallel\cdot\left[\overline{Ma}\frac{\overline{h}^2}{2}\overline{\nabla}_\parallel\overline{\gamma} + \frac{\overline{h}^3}{3\overline{Ca}}\overline{\nabla}_\parallel\left(\overline{\nabla}_\parallel^2\overline{h}\right)\right] = 0 \tag{3.46}$$

It is instructive to note that the second term (containing the Marangoni number and the lateral surface tension gradient) represents the thermocapillary term, while the third term (containing the Capillary number and the curvature of the film $\overline{\nabla}_\parallel^2\overline{h}$) represents the capillary (surface tension) term. We hence see that in the thin film regime, the nanofilm evolution is entirely dominated by thermocapillary and capillary effects. In the absence of thermocapillary effects, the capillary term, which is proportional to the curvature of the system, will seek to reduce the interfacial area and produce a flat film. It is the thermocapillary term that will produce a counteracting effect to achieve a non-flat interface.

Incorporating the temperature dependence of surface tension

In order to produce the final nonlinear equation of motion in a single dynamical height parameter alone, we seek to express the surface tension gradient $\overline{\nabla}_{\|}\overline{\gamma}$ in terms of the film height. We proceed by relating the temperature of the film surface to the local height and substituting the linearized form of the surface tension temperature dependence from equation 3.15.

In the thin film limit, thermal transport is dominated by conduction. Convection is suppressed and radiative effects are negligible. We may also take the timescale of conductive transport to be much shorter than the timescale of fluid flow and let the height vary slowly as a function of lateral position. This allows us to solve the steady state heat equation $\nabla^2 T = 0$ at each instance in time to find the temperature of the film as a function of the local film height, which we can take to be practically flat in a domain much narrower than the characteristic lateral lengthscale. This allows us to neglect the horizontal terms $\partial^2_{x,y} T$ and just solve for the vertical temperature dependence $\partial^2_z T = 0$. We hence write the temperature with a linear ansatz:

$$T(z) = \begin{cases} A + Bz, & z \leq h \\ C + Dz, & z > h \end{cases} \tag{3.47}$$

The temperature and heat flux must be continuous across the film-air interface:

$$T(h^-) = T(h^+), \quad k_{\text{film}} \left.\frac{\partial T}{\partial z}\right|_{z=h^-} = k_{\text{air}} \left.\frac{\partial T}{\partial z}\right|_{z=h^+} \tag{3.48}$$

and are subject to the heat reservoir boundary conditions:

$$T(0) = T_H, \quad T(d_0) = T_C \tag{3.49}$$

This yields the temperature distribution:

$$T(z) = \begin{cases} T_H + \dfrac{k_{\text{air}}(T_C - T_H)}{h(k_{\text{air}} - k_{\text{film}}) + k_{\text{film}} d_0} z, & z \leq h \\ \dfrac{k_{\text{film}} d_0 T_H + h T_C (k_{\text{air}} - k_{\text{film}})}{h(k_{\text{air}} - k_{\text{film}}) + k_{\text{film}} d_0} + \dfrac{k_{\text{film}}(T_C - T_H)}{h(k_{\text{air}} - k_{\text{film}}) + k_{\text{film}} d_0} z, & z > h \end{cases} \tag{3.50}$$

The film surface temperature is hence:

$$T(h) = T_H + \frac{k_{\text{air}}(T_C - T_H)}{h(k_{\text{air}} - k_{\text{film}}) + k_{\text{film}} d_0} h = T_H + \frac{\kappa(T_C - T_H)}{h(\kappa - 1) + d_0} h \tag{3.51}$$

where we introduce $\kappa \equiv k_{\text{air}}/k_{\text{film}}$ to be the relative thermal conductivity.

We may now write the surface tension and its normalized form:

$$\gamma(h) = \gamma_H - \gamma_T \left[T_H + \frac{\kappa(T_C - T_H)}{h(\kappa - 1) + d_0} h - T_H \right] \tag{3.52}$$

$$\overline{\gamma}(h) = \frac{\gamma(h)}{\gamma_T(T_H - T_C)} = \frac{\gamma_H}{\gamma_T(T_H - T_C)} + \frac{\kappa}{h(\kappa - 1) + d_0} h \tag{3.53}$$

The first term on the right hand side is a constant which vanishes when the lateral gradient is taken. We may call it a constant C. We may now write the normalized surface tension in terms of dimensionless parameters alone, where $\overline{d}_0 \equiv d_0/h_0$ is the normalized gap width:

$$\overline{\gamma}\left(\overline{h}\right) = C + \frac{\kappa \overline{h}}{\overline{h}(\kappa - 1) + \overline{d}_0} \tag{3.54}$$

$$\implies \overline{\nabla}_{\parallel} \overline{\gamma}\left(\overline{h}\right) = \frac{\kappa \overline{d}_0}{\left[\overline{h}(\kappa - 1) + \overline{d}_0\right]^2} \overline{\nabla}_{\parallel} \overline{h} \tag{3.55}$$

Substituting the surface tension gradient into the thin-film equation of motion 3.46, we have the completed thermocapillary equation of motion in terms of the film height:

$$\frac{\partial \overline{h}}{\partial \overline{t}} + \overline{\nabla}_{\parallel} \cdot \left\{ \overline{Ma} \frac{\overline{h}^2}{2} \frac{\kappa \overline{d}_0}{\left[\overline{h}(\kappa - 1) + \overline{d}_0\right]^2} \overline{\nabla}_{\parallel} \overline{h} + \frac{\overline{h}^3}{3\overline{Ca}} \overline{\nabla}_{\parallel} \left(\overline{\nabla}_{\parallel}^2 \overline{h} \right) \right\} = 0 \tag{3.56}$$

If, however, the gap height $\overline{d}_0$ is not a constant value due to a non-uniform patterned surface above the nanofilm, Equation 3.46 (thermocapillary evolution equation with surface tension dependence $\overline{\nabla}_{\parallel}\gamma$) does not simplify to Equation 3.56 (thermocapillary equation in terms of $\overline{h}$ alone). Instead, we need to return to Equation 3.54

to take the spatial dependence of $\overline{d}_0$ into account (this time with explicit spatial dependence and assuming that the gap profile is fixed in time):

$$\overline{\gamma}(\boldsymbol{x}_\parallel) = C + \frac{\kappa\overline{h}(\boldsymbol{x}_\parallel)}{\overline{h}(\boldsymbol{x}_\parallel)(\kappa-1) + \overline{d}_0(\boldsymbol{x}_\parallel)} \tag{3.57}$$

$$\implies \overline{\nabla}_\parallel\overline{\gamma}(\boldsymbol{x}_\parallel) = \frac{\kappa\overline{d}_0}{\left[\overline{h}(\kappa-1)+\overline{d}_0\right]^2}\overline{\nabla}_\parallel\overline{h} - \frac{\kappa\overline{h}}{\left[\overline{h}(\kappa-1)+\overline{d}_0\right]^2}\overline{\nabla}_\parallel\overline{d}_0 \tag{3.58}$$

We hence re-write the thermocapillary evolution equation allowing for a variation in gap height (now suppressing the spatial dependence of the height $\overline{h}$ and gap profile $\overline{d}_0$):

$$\overline{Ca}\frac{\partial\overline{h}}{\partial\overline{t}} + \overline{\nabla}_\parallel\cdot\left\{\overline{Ca}\,\overline{Ma}\frac{\overline{h}^2}{2}\overline{\nabla}_\parallel\left[\frac{\kappa\overline{h}}{\overline{h}(\kappa-1)+\overline{d}_0}\right] + \frac{\overline{h}^3}{3}\overline{\nabla}_\parallel\left(\overline{\nabla}_\parallel^2\overline{h}\right)\right\} = 0 \tag{3.59}$$

Observe that we have multiplied the equation by the capillary number. This step explicitly exhibits that the equation does not depend on the characteristic lateral velocity u_c since:

$$\frac{t_c}{\overline{Ca}} = \frac{l}{u_c}\frac{\mu u_c}{\epsilon^3\gamma_H} = \frac{\mu l}{\epsilon^3\gamma_H}, \quad \overline{Ca}\,\overline{Ma} = \frac{\mu u_c}{\epsilon^3\gamma_H}\cdot\frac{\epsilon\gamma_T\Delta T}{\mu u_c} = \frac{\gamma_T\Delta T}{\epsilon^2\gamma_H} \tag{3.60}$$

Hence we introduce the characteristic viscous-capillary timescale:

$$t_{VC} \equiv \frac{t_c}{\overline{Ca}} = \frac{\mu l}{\epsilon^3\gamma_H}, \quad \tau \equiv \frac{t}{t_{VC}} \tag{3.61}$$

and write the thermocapillary evolution equation in manifestly u_c-independent form:

$$\frac{\partial\overline{h}}{\partial\tau} + \overline{\nabla}_\parallel\cdot\left\{\overline{Ca}\,\overline{Ma}\frac{\overline{h}^2}{2}\overline{\nabla}_\parallel\left[\frac{\kappa\overline{h}}{\overline{h}(\kappa-1)+\overline{d}_0}\right] + \frac{\overline{h}^3}{3}\overline{\nabla}_\parallel\left(\overline{\nabla}_\parallel^2\overline{h}\right)\right\} = 0 \tag{3.62}$$

where τ is the dimensionless time normalized to the viscous-capillary timescale. We have hence achieved a highly nonlinear 4th order differential equation in terms of a single dynamical parameter, the film height.

3.3 Linear stability analysis of thermocapillary equation of motion

We now examine the thermocapillary equation of motion under the condition of a constant gap height $\nabla_{\parallel} d_0 = 0$. The relevant equation of motion is hence Equation 3.56. In a similar fashion to the Rayleigh-Taylor height perturbation in equation 2.14, we make an exponential ansatz for the film thickness in two lateral dimensions:

$$h(\overline{\boldsymbol{x}}_{\parallel}, \bar{t}) = 1 + \delta h e^{\omega(|\overline{\boldsymbol{K}}|)\bar{t}} e^{i\overline{\boldsymbol{K}}\cdot\overline{\boldsymbol{x}}_{\parallel}} \tag{3.63}$$

where $\delta h \ll 1$ is a small dimensionless perturbation amplitude and $\overline{\boldsymbol{K}}$ is the dimensionless wavenumber normalized to the characteristic length l.

Substituting this ansatz into the thermocapillary equation of motion for a constant gap height 3.56 yields the dispersion relation [12]:

$$\omega(|\overline{\boldsymbol{K}}|) = \left[\frac{\kappa \bar{d}_0 \overline{Ma}}{2\left(\bar{d}_0 + \kappa - 1\right)^2} - \frac{\left|\overline{\boldsymbol{K}}\right|^2}{3\overline{Ca}} \right] |\overline{\boldsymbol{K}}|^2 \tag{3.64}$$

The dispersion relation has one maximum with positive growth rate $\omega > 0$ located at [12]:

$$|\overline{\boldsymbol{K}}|_{\max} = \sqrt{\frac{3\kappa \bar{d}_0 \overline{Ca}\,\overline{Ma}}{2\left(\bar{d}_0 + \kappa - 1\right)^2}} \tag{3.65}$$

Since the dispersion relation is a continuous function of $|\overline{\boldsymbol{K}}|$, and $|\overline{\boldsymbol{K}}|_{\max} > 0$, there exists a finite range of wavenumbers with positive growth rate. The presence of these unstable wavenumbers with positive growth rates implies that any initially flat nanofilm will exhibit an early-stage instability where it spontaneously deforms to form features with characteristic spacing on the order of the maximally unstable wavelength. The dimensional form of the maximally unstable wavelength $\lambda_{\max}$ can be extracted from the nondimensional wavenumber through the characteristic lateral length [12]:

$$\lambda_{\max} = \frac{2\pi l}{|\overline{\boldsymbol{K}}|_{\max}} = 2\pi h_0 \sqrt{\frac{4\gamma_H h_0}{3\kappa d_0 \gamma_T (T_H - T_C)}} \left[\frac{d_0}{h_0} + \kappa - 1 \right] \tag{3.66}$$

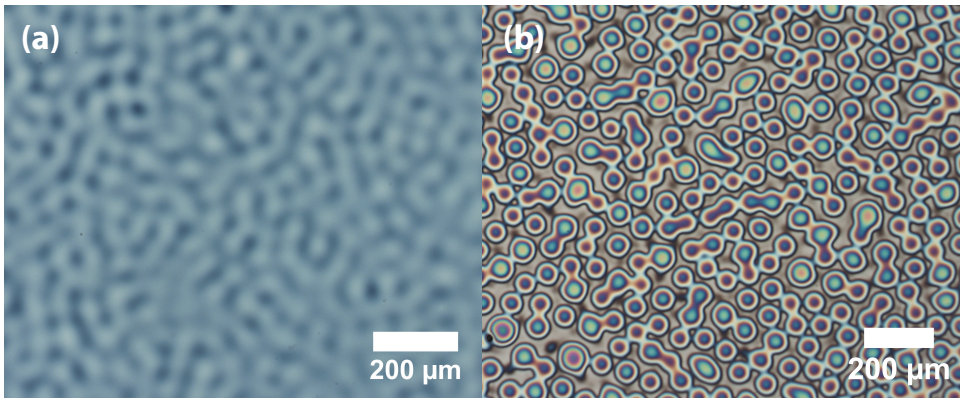

Figure 3.2: Microscope image of the native thermocapillary instability in polystyrene-on-silicon. Samples courtesy of {LIS^{2}T} group member Kevin Fiedler. (a) The early-stage thermocapillary instability is barely visible. These height perturbations are on the order of 10 nm. (b) The late-stage thermocapillary instability shown exhibits isolated peaks with multiple colorful interference fringes, indicating that these peaks are at least several hundred nanometers tall. These features in (b) do not come from the same samples as (a) but were achieved under similar conditions.

For a nanofilm of thickness $h_0 = 228$ nm made of low molecular weight polystyrene, sandwiched between two heat reservoirs with $\Delta T = 7.2°$C, and with a gap thickness of around $d_0 = 2435$ nm, the maximally unstable spatial wavelength is 65 μm.

3.4 Observation of thermocapillary instabilities

Thermocapillary instabilities in thin films appear as undulating perturbations in the early stage, which grow in the vertical direction until they either deplete the film material locally (thereby forming an isolated peak) or touch a surface above (thereby forming a nanopillar). Figure 3.2 exhibits light microscope images of the thermocapillary instability in a polystyrene-on-silicon system. Figure 3.2(a) shows the early stage instability, in which the polystyrene film perturbations are only barely visible in the form of shading differences in the microscope image. The height deviations are on the order of 1 to 10 nm at this stage. Figure 3.2(b) shows the late-stage form of the instability where the film dewets in between peaks due to local material depletion. The peaks have not touched the upper surface and hence remain rounded and ultrasmooth.

The first discovery of the features obtained under the thermocapillary instability was provided by Chou *et al.* in 1999 [18, 19]. By heating and then cooling a system containing a polymethylmethacrylate (PMMA) film and air layer sandwiched between a patterned mask above and a silicon substrate below (in effect implementing

the experimental geometry described in Section 3.2 with $T_C = T_H$ and a time-varying temperature), Chou *et al.* observed that the polymer film spontaneously formed periodic arrays of pillars that bridged the lower and upper stages. Although Chou *et al.* ascribed the effect to a related electrohydrodynamic (EHD) instability induced by charge redistribution in the polymer film and patterning template, Dietzel, McLeod and Troian later showed that the predominant mechanism was thermocapillary in nature [12, 13]. The micropillars formed when the thermocapillary perturbations grew sufficiently large to touch the patterned template above to form the flat-topped narrow arrays of pillars.

The early-stage behavior of the thermocapillary instability was more recently studied and modeled by Fiedler and Troian, who measured the fastest growing instability wavelength and demonstrated that it agreed well with the thermocapillary model described in the previous section [20].

Chapter 4

PATTERNING USING FLUID INSTABILITIES IN ULTRATHIN FILMS

4.1 Overview of ultrathin film patterning

The Rayleigh-Taylor instability and thermocapillary instability described in the previous chapters are only two of many fluid instabilities. The spontaneous and self-assembling nature of these instabilities make them attractive for patterning repeating arrays of features over a surface. In this chapter, we survey existing efforts to fabricate microstructures and compare their respective capabilities. We begin with an overview of the motivation for patterning nanofilms using fluid instabilities in Section 4.2, then go on to describe existing techniques and the various instabilities used in Section 4.3. Next, we identify the key challenges of existing techniques and introduce the possibility of performing fabrication in a non-contact fashion in Section 4.4. We then turn to the concept of Thermocapillary Lithography itself in Section 4.5 and distinguish between its two forms in Section 4.6. We review the advantages of TCL in Section 4.7. Finally, in Section 4.8, we describe how the techniques and results presented in this thesis fits in with the existing work published by {LIS^{2}T}.

4.2 Why use fluid instabilities?

With the maturation of nanofabrication technology, complex optical devices have become increasingly dependent on micro-optical components to shape, filter, and steer light at the microscale. Traditional grinding and polishing techniques are incapable of achieving the fine resolution and optical quality demanded by such applications, thereby necessitating the use of complex multi-step fabrication processes. Conventional photolithography and scanning beam lithography are commonly used and well-established in manufacturing processes, but typically require expensive advanced equipment, multiple post-processing steps, and are limited to producing two-dimensional surface structures [21]. Fluid instabilities meet several of these needs at once. Instabilities arising from electrohydrodynamic effects, demixing, dewetting, in addition to the Bénard-Marangoni (thermocapillary) flows already described, become dominant when thin film systems experience external perturbations such as electric potential gradients and surface tension gradients. Under appropri-

ate experimental geometries, these linear instabilities self-assemble into undulating arrays of protrusions exhibiting a characteristic spatial wavelength. By fixing these natural instability features in place (by curing with actinic light, for instance), these spontaneous, self-assembled fluid features can be used to form microscopic periodic surface patterns in a simple process. For instance, in 2011, McLeod and Troian showed that the thermocapillary instability can be exploited to form polymer microlens arrays, the archetypal micro-optical device comprising periodically spaced micro-lenses arranged on a two-dimensional plane, in a one-step process [22].

Micro-optical devices represent only one domain that would stand to benefit from a complete mastery of precision, large-scale fluid patterning. Fluid instabilities can be directed by imposing a strong stimulus with a non-uniform template, thereby overwhelming the natural linear instabilities and inducing pattern replication of that template. This opens up the possibility of using directed fluid instability formation to produce complex planar structures such as waveguides, photonic circuits and surfaces with tunable geometric or thermodynamic properties. Importantly, this fabrication process can be performed in parallel, as opposed to serial forms of production such as 3D additive printing or femtosecond laser micromachining. This characteristic greatly increases the potential throughput and scalability (in terms of the area that can be patterned simultaneously) of such techniques. To perform this template-guided fabrication, one may induce a non-uniform electric field using a pre-patterned electrode [7, 8, 23–29], direct flow using different materials deposited on that surface [30–35], or impose temperature gradients using a surface relief structure [36]. These methods generally assume a one-to-one correspondence between the imposed template pattern and the corresponding thin film response, so that the fabricated film structure exhibits the same spatial distribution of features as in the template design, up to lateral scaling.

4.3 Existing techniques for ultrathin film patterning

Table 4.1 provides a summary of the key features of each technique used in patterning ultrathin films. Particular attention was paid to the minimum feature sizes and minimum feature separations (pitch) achieved in each technique, as well as to the materials used in the fluid and substrate layers. Specifically, the fluid layer refers to the layer patterned using the fluid instability, while the underlying substrate layer remains flat and unpatterned.

Year	Ref	Mechanism	Fluid	Substrate	Min. lateral feature size (μm)	Min. feature separation (μm)
1998	[37, 38]	Demixing instability, on a substrate with regions of self-assembled monolayer	PS/PVP mixture	Gold	0.75	2.4
1999	[39]	Dewetting fingering instability over uniform surface	PS	Glass, mica or silicon	0.3	1
1999	[18]	TC instability, pattern replication and eventual contact to a very large upper mask	PMMA	Silicon	1.6	3
2000	[7]	EHD/TC instability, pattern replication and eventual contact to a structured electrode	Brominated polystyrene	Silicon	0.14	0.2
2003	[36]	TC instability, pattern replication and eventual contact to a patterned upper template	PS	Silicon with oxide layer	0.5	2
2006	[23]	EHD instability, unpatterned and patterned electrodes with eventual contact	Photocurable polymers	Doped silicon	17.8 (unpatterned), 50 (patterned)	30 (unpatterned), 100 (patterned)
2010	[40]	EHD instability, patterned electrode with eventual contact	Photothermal-curing silsesquioxane	Metal sheet	50	250
2011	[24]	EHD instability, patterned electrode with eventual contact and reflow	UV-curved reactive mesogen	ITO glass	50	~ 60
2013	[26]	EHD instability, patterned electrode with eventual contact	UV-curable prepolymer	ITO glass	100	104
2013	[27]	EHD instability, patterned electrode with eventual contact	UV-curable resist mr-NIL 6000E	Conductive substrate	5	20
2015	[29]	EHD/TC instability, on a periodic pyroelectric substrate	PDMS	Lithium Niobate	25	25
2016	[41]	TC instability on bilayer film	UV-curable paint and silicone oil	Silicon	~ 1000	~ 1500

Table 4.1: Survey of fabrication techniques exploiting fluid instabilities. Estimates that are not specifically stated in the reference text are indicated with a tilde (~).

Thermocapillary (TC) instability patterning

The earliest use of the thermocapillary instability to pattern a surface, though inadvertent, was reported by Chou *et al.* in 1999 [18, 19]. In the technique, which was called "Lithographically induced self-assembly", or LISA, Chou *et al.* coated a silicon wafer with a PMMA nanofilm ($h_0 \sim 95$ nm) and placed a non-uniform patterned mask above the nanofilm, maintaining a constant separation between the nanofilm and the mask by use of spacer elements between the two. The system was then heated as a whole to around 130°C for 5 to 80 minutes, which was above the glass transition temperature of the polymer. This resulted in the formation of narrow hexagonally-packed pillars (which were much smaller than the patterned mask feature size) of PMMA bridging the silicon substrate and the mask pattern above. The pillars exhibited good short range order but poor long-range order. The resulting patterns did not need to be cured since they solidified once the temperature was brought below the polymer glass transition temperature. Chou *et al.* attributed the fabrication mechanism to an electrohydrodynamic instability, where electrostatic forces between charges in the nanofilm and image charges in the mask above overwhelmed the stabilizing capillary forces in a positive-feedback mechanism, amplifying the small initial perturbations in film thickness until contact with the mask above occurs. Further theoretical and experimental studies of the setup geometry by Dietzel, McLeod and Troian [12, 13] later determined that the characteristic spatial wavelength produced by the instability exhibited a dependence on the temperature drop across the nanofilm, which was consistent with the behavior expected of the thermocapillary instability and not of the surface charge explanation.

In 2003, Schäffer *et al.* performed a similar experiment to that of Chou *et al.* with significantly smaller and closer-spaced template patterns [36]. This change allowed Schäffer *et al.* to control the spatial positioning of the nanopillar formations to achieve large area periodic and aperiodic patterns, whereas Chou *et al.* exerted control only over the general area in which hexagonally-packed nanopillar arrays could form. However, this positional control still required the polymer film to make contact with the template pattern above to replicate the fine template structures. Schäffer *et al.* also imposed a transverse temperature gradient across the nanofilm by holding the two stages at different temperatures, in contrast to Chou *et al.*, who tried to perform fabrication with an isothermal system. Schäffer *et al.* explained the formation of the instability on the basis of coherent reflections of acoustic phonons which exert a destabilizing radiation pressure. However, this mechanism demonstrated poor correspondence to the experimental observations of the instability wavelength

as a function of the gap size. These observations were better explained by a thermocapillary instability mechanism, indicating that the features Schäffer *et al.* observed were most likely thermocapillary instabilities [13].

Since these early experiments, there has not been significant interest in thermocapillary instability patterning outside {LIS^{2}T}, although multiple experimental studies may have been heavily influenced by thermocapillary effects. Experiments involving the EHD instability, for instance, use thermal means to affix the deformed fluid in position [7, 29], which establishes a transverse thermal gradient through the fluid layer and thereby destabilizes it to thermocapillary flow. Since the EHD and thermocapillary instabilities are eventually overwhelmed by the template pattern at late times, the end result still remains the same: tall and narrow nanopillars connecting the substrate to the template patterns above. For more detailed descriptions of the various fabrication techniques which use thermocapillarity, the reader is directed to the recent review article by Singer [42].

Electrohydrodynamic (EHD) instability patterning

While a transverse thermal gradient induces the thermocapillary instability, a transverse electric potential gradient (that is, an electric field) applied to an initially flat fluid surface also induces an instability. This is known as the electrohydrodynamic (EHD) instability. While the interaction of electrostatic pressure on deformations in a fluid dielectric has been studied for a long time [43, 44], the first application of this instability to surface fabrication was performed by Schäffer *et al.* in 2000. Schäffer *et al.* spin-coated a polystyrene (and PMMA or PBrS in later reports) nanofilm ($h_0 \sim 93$ nm) onto a flat lower electrode, then placed a patterned electrode above the nanofilm to establish an air gap of around $d_0 \sim 100 - 1000$ nm. They then applied a small voltage across the electrodes to achieve a transverse electric field on the order of $10^7 - 10^8$ Vm^{-1}. They then heated the system up to beyond the glass transition temperature of the polymer to allow flow, and cooled it back down to allow the fabricated structures to solidify. The polymer melt is drawn towards the protruding electrode patterns and makes contact with the electrode above to form steep nanopillars replicating the imposed pattern of the electrode template [7, 8]. While the electric field does induce self-amplifying perturbations as a result of the EHD instability, the authors did not account for the thermocapillary instability which was also present in the heated system. In the regime studied, the combined EHD and thermocapillary analysis would also have resulted in the same nanostructures being formed, but the theoretical justification would become vastly more complex,

as analyzed by Corbett and Kumar [45].

Since 2000, the EHD instability has received much attention in view of the speed of fabrication (on the order of minutes or less with large electric fields) and its generalizability (most template patterns can be fabricated by established techniques such as photolithography). A key improvement was made in 2006 by Dickey *et al.*, who replaced the thermal means of affixing patterns (heating beyond the glass transition temperature to allow flow and then letting the sample cool and solidify) with a more rapid ultraviolet (UV) curing process [23]. This removed the need for the setup to be heated, which also greatly reduced the influence of the thermocapillary instability in these later EHD experiments.

Demixing instability patterning

The demixing instability was exploited by Böltau *et al.* in 1998 to achieve pattern replication of self-assembled monolayer patterns on a gold substrate [38]. Two incompatible polymers spontaneously phase-separate when spin-coated onto a substrate. The nature of the phase-separation depends strongly on the interaction energies between the substrate and the polymer species. In the experiment, the gold substrate exhibited a preferential absorption to polyvinylpyridine (PVP) over that of polystyrene (PS), thereby inducing the polymer mix to form a bilayer with PVP closer to the gold surface upon demixing. On a self-assembled monolayer substrate that did not exhibit preferential absorption for either species, the PVP/PS mixture demixed into a complex corrugated surface involving both polymer species. The demixing distribution was controlled by strategic placement of gold and self-assembled monolayer regions, so that PVP was preferentially deposited onto the gold surfaces and PS was pushed to the adjacent surfaces covered by the monolayer. Either species could then be removed by dissolution using the appropriate polar or nonpolar solvent.

Dewetting instability patterning

A volatile solvent on a surface can produce fingering instabilities at the edge of the droplet (the three-phase line) as the solvent edge recedes. In 1999, Karthaus *et al.* showed that these dewetting instabilities in a polymer-carrying solvent could be tuned to produce regular arrays of smaller droplets. This self-organizing process was driven by periodic features which formed along the three-phase line, creating periodic fluctuations in polymer concentration along the interface to produce the ordered arrays of droplets observed.

4.4 Exploring a non-contact fabrication TC instability fabrication technique

A common thread through the EHD and TC instability fabrication techniques is that they require the fluid to make contact with the upper template in order to achieve the small features sizes reported. This is necessary because the characteristic wavelength of the instabilities (and hence characteristic spacing of the fluid deformations prior to contact) is much larger than the template feature size. Fabrication techniques which require contact with the template are described as exhibiting "eventual contact" in Table 4.1.

On the other hand, techniques which do not involve direct contact with another surface are largely restricted by the size of the characteristic wavelength, which is large for thick films. Nejati *et al.* achieve ultrasmooth protrusions in a UV-curable paint by modulating the surface with a thicker perfluorinated hydrocarbon layer placed above the lower paint layer [41]. A temperature gradient is enforced in a non-contact fashion with parallel thermal reservoirs across the perfluorinated hydrocarbon to produce Bénard-Marangoni cells, and the resulting hydrocarbon fluid motion deforms the paint layer interface to produce a periodic array of protrusions. Since the hydrocarbon layer is thick (> 500 μm), the characteristic size of the Bénard-Marangoni cells is also large, which sets the characteristic spacing for the paint layer protrusions ($\sim$ 1500 nm). It is hence difficult to achieve small feature sizes without resorting to physical contact with a templating surface.

The key advantage to a non-contact means of fabrication is the preservation of the ultra-smooth nature of the surface throughout the fabrication process. Capillary forces work to minimize the surface energy of a deformed surface, which ensure that the fluid interface remains smooth in the absence of physical contact with external objects. Physical contact imparts the roughness of the external surfaces to the solidified fluid-air interface, which introduces surface defects detrimental to sensitive applications such as micro-optical devices.

4.5 Overview of thermocapillary lithography operation

In this thesis, we develop a cost-efficient, scalable, and highly generalizable fabrication technique to sculpt curved surfaces by means of imposing surface tension gradients in a non-contact manner. This technique is called Thermocapillary Lithography (TCL), in accordance with previous {LIS^{2}T} work.

TCL operates by modulating thermocapillary forces. It overrides the natural thermocapillary instability by imposing a strong stimulus in the form of a non-uniform

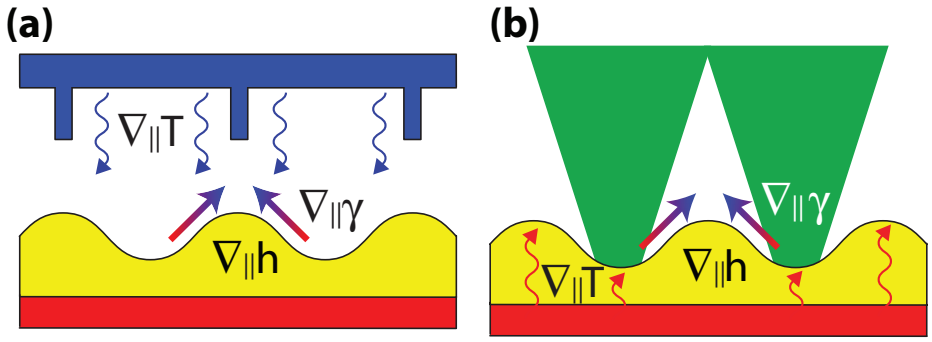

Figure 4.1: Depiction of the differences between Conduction TCL and Laser-induced TCL. (a) In Conduction TCL, a cooled patterned relief structure placed above the heated nanofilm projects a temperature gradient field ($\nabla_{\|}T$) by conduction, setting up surface tension gradients ($\nabla_{\|}\gamma$) that sculpt the surface into an ultrasmooth profile ($\nabla_{\|}h$) with protrusions under the chilled pins. (b) In Laser-induced TCL, a laser is used to project the temperature gradient field. The nanofilm substrate absorbs the laser energy and heats the nanofilm surface by conduction through the film itself. Protrusions are formed in regions not irradiated by the laser.

temperature field over the fluid-air interface. The operation of TCL can be summarized symbolically to show the flow of logic as follows:

$$\nabla_{\|}T(\boldsymbol{x}_{\|},t) \rightarrow \nabla_{\|}\gamma(\boldsymbol{x}_{\|},t) \rightarrow \nabla_{\|}h(\boldsymbol{x}_{\|},t) \tag{4.1}$$

Since surface tension γ in most materials exhibits an increase with decreasing temperature, the non-uniform temperature field ($\nabla_{\|}T$) induces surface tension gradients ($\nabla_{\|}\gamma$) along the interface. The difference in surface tension results in thermocapillary flow along the fluid interface, which drags along the bulk fluid to produce a sculpted ultrasmooth surface ($\nabla_{\|}h$). The sculpted surface can then be fixed in place by either curing using actinic light or by decreasing the temperature of the system below the glass transition temperature of the polymer melt used.

4.6 The two forms of Thermocapillary Lithography: Conduction and Laser-induced

In this thesis, we introduce two distinct ways of projecting the required non-uniform temperature field $T(\boldsymbol{x}_{\|},t)$ onto a fluid surface. Figure 4.1 illustrates the main differences between the two methods. The first uses air conduction from a cooled photoresist structure placed very close to (but not touching) the fluid surface. We will call this technique Conduction TCL (Figure 4.1(a)). The second projects a temperature field by means of focusing a laser light field onto a target surface. We

call this Laser-induced TCL (Figure 4.1(b)). Each of these two techniques will be described and implemented in separate Parts within this thesis.

In Conduction TCL, when a non-uniform template is placed over the nanofilm, the gap distance is no longer a constant, and $\overline{d}_0(\boldsymbol{x}_\parallel)$ picks up a spatial dependence. A non-uniform temperature field is projected onto the fluid surface by air conduction, and surface tension gradients are introduced in accordance with the imposed template geometry. Lateral fluid redistribution from warmer regions towards cooler regions occurs as a result of the thermocapillary forces induced at the surface, forming ultra-smooth peaks and depressions at cooler and warmer regions, respectively. This technique uses a similar geometry to that of Schäffer *et al.* [36], in that we use surface relief structures between two parallel thermal reservoirs. However, the key difference is that in Conduction TCL, we halt fabrication before the nanofilm protrusions make contact with the upper surface, avoiding film breakup and maintaining an ultrasmooth continuous film surface throughout. The connectivity of the nanofilm across surface features also allows us to exploit wave-like interference between adjacent structures, affording us the opportunity to fabricate highly complex multiscale structures simultaneously, as will be described in the Conduction TCL Part of this thesis.

Laser-induced TCL was developed after Conduction TCL and addresses many of the key challenges of Conduction TCL. Instead of using air conduction from a template, which requires proximity to physical structures, Laser-induced TCL uses a spatially-modulated laser to project a temperature field onto a fluid surface from a distance. This fully non-contact means of fabrication greatly increases the throughput and scalability of fabrication and allows for real-time monitoring and control feedback of the evolving nanofilm. Laser-induced TCL is better suited for larger scale industrial applications as a result.

4.7 Key advantages of Thermocapillary Lithography

Both forms of TCL are cost efficient and scalable since they do not require specialized materials and allow the same fabrication setup to be reused repeatedly. They rely solely on the variation of material surface tension with temperature and hence are applicable to virtually all material surfaces once they are molten. The materials do not need to be cured separately since surface features are affixed in position once the heat source is removed.

Most importantly, TCL is generalizable to achieve a wide variety of curved surfaces.

Since no material is added or removed, but is instead redistributed, mass conservation requires that local protrusions are formed with material from nearby interstitial depressions and vice versa. This feature allows one to achieve highly nontrivial topologies even with simple templates by controlling feature overlap. While pattern replication methods seek to form a replica of the template (up to overall scaling), TCL draws upon the physical principles of thermocapillary flow to interrupt fluid redistribution at various stages of feature growth and thereby achieve multiscale patterns that differ significantly from the imposed template temperature pattern if so desired.

4.8 Previous studies of TCL in the {LIS^{2}T} group

Early theoretical and experimental studies of Conduction TCL (when it was just known as thermocapillary lithography) have been reported by Dietzel, McLeod and Troian in the the {LIS^{2}T} group [22, 46] and the general concept for performing fabrication through thermocapillary means is described in a patent by Troian [47]. However, thus far, only one topology (slender template pin array producing periodic strictly convex protrusions) has been fabricated and studied [22], and the experimental samples were not used in any application. The sample also could not be applied to refractive visible-light micro-optics since the substrate used was silicon, which is opaque in the visible spectrum. In this thesis, we pick up where these experiments left off using an improved setup with greater reproducibility. We perform Conduction TCL fabrication on transparent polymers over a transparent substrate so that the resultant arrays are immediately available for use as transmissive Microlens Arrays (MLAs). We also study the effect of allowing overlap between adjacent surface features, halting film evolution at various times, and inverting the height profile of the templating pattern (replacing pins with depressions and vice versa). Finally, we incorporate the fabricated arrays in a functional wavefront sensor device.

A Laser-based system, on the other hand, has only been mentioned as a possibility in the patent by Troian [47] and has not been implemented experimentally before. In this thesis, we perform the first large-scale nanofilm patterning using a laser-induced setup designed built from scratch and demonstrate that it is possible to perform laser-induced thermocapillary fabrication using even a weak laser. We also exhibit real-time monitoring of the fabricated sample, and describe a roadmap for TCL to be adopted as a precision yet low-cost industrial technique for the arbitrary patterning of films.

Part II

Conduction Thermocapillary Lithography

Chapter 5

ORGANIZATION OF PART II: CONDUCTION THERMOCAPILLARY LITHOGRAPHY

In this thesis Part, we implement and characterize the Conduction TCL technique. Conduction TCL is named as such because it draws upon air conduction from a patterned template to project the necessary temperature field for thermocapillary flow, and to distinguish it from the newer laser-induced TCL process to be described in a later thesis part. We begin with a complete description of the various optimized experimental techniques, materials, and processes involved in taking a clean substrate to a finished device known as a Microlens Array (MLA) in Chapter 6. Particular attention will be paid to the numerical processing techniques used to quantify the lens parameters and non-idealities of the resultant structure. We then evaluate the resultant fabricated MLAs and study the focusing properties of the new *caldera-like* lens arrays in Chapter 7. Finally, we conclude with a discussion of the outlook of Conduction TCL in Chapter 8.

Chapter 6

MATERIALS AND METHODS

6.1 Overview of Materials and Methods

The Conduction TCL experimental setup is sketched in Figure 6.1. This chapter provides the detailed fabrication protocol for each element within the setup. In this experiment, we seek to fabricate microlens arrays using a transparent nanofilm made of polystyrene (PS) on a transparent fused quartz substrate through the Conduction TCL process. We refer to these samples as polystyrene-on-quartz.

We begin with the measurement of the refractive index of PS through Abbe Refractometry in Section 6.2. The refractive index of the PS used is essential for ellipsometric measurements of PS film thicknesses and for calculating the focusing characteristics of the fabricated samples. We then describe the photomasks used to produce the patterns on the sapphire window in Section 6.3. The sapphire window patterning process is then described in Section 6.4. Following this, we describe the protocol for achieving high-quality defect-free polystyrene-on-quartz samples in Section 6.5. The actual Conduction TCL step performed on the polystyrene-on-quartz samples using the patterned sapphire window stages is described in Section 6.6.

In the following sections, we turn to the techniques used to analyze the fabricated samples from the Conduction TCL step. In Section 6.7, we describe the numerical fitting routines used to quantify the lens parameters of the fabricated arrays within our custom MATLAB function suite that we unofficially call “Zygocruncher”. In the next Section 6.8, we describe the protocol used to capture the transmitted light profile for the fabricated microlens arrays.

The next two sections deal with the computational simulation of the nanofilm evolution under thermocapillary forces, specific to the equipment geometry used in our experimental setup. Section 6.9 lists the sources and numerical estimates for the necessary material parameters and Section 6.10 describes the configuration used to perform finite element simulation of the nanofilm evolution.

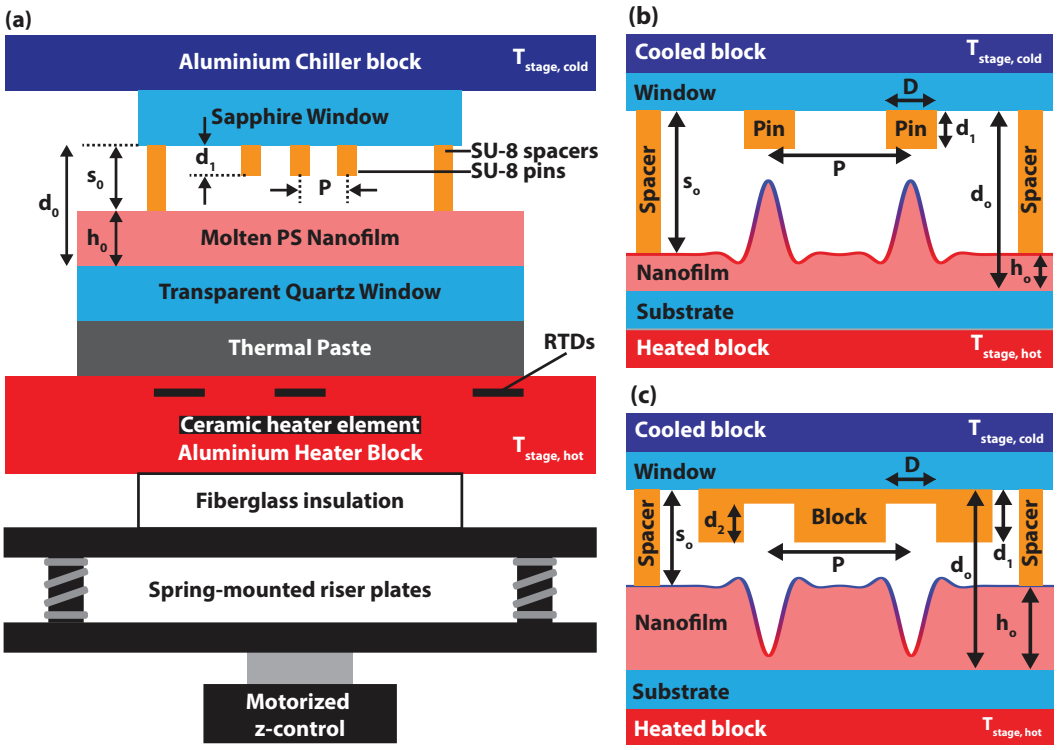

Figure 6.1: The TCL experimental setup displayed in full (a) and focusing on the photoresist pin pattern for fabricating (b) convex and (c) concave microlens arrays. The ranges of parameters used are 20 μm $\leq D \leq$ 50 μm, 50 μm $\leq P \leq$ 150 μm, 0.7 μm $\leq d_1 \leq$ 1.1 μm, 1.3 μm $\leq s_0 \leq$ 1.8 μm and 228 μm $\leq h_0 \leq$ 288 μm. The reservoir block temperatures were held constant at $T_{\text{stage, hot}} = 180°\text{C}$ and $T_{\text{stage, cold}} = 60°\text{C}$. The photoresist block depressions in (c) are at least 360 μm away from the block edges. The nanofilm evolves continuously in response to the applied temperature field; the film topologies shown in (b-c) are representative late-stage geometries.

6.2 Abbe Refractometry

The refractive index of the polystyrene used in the ellipsometric measurements was measured using an Abbe refractometer operating at laser wavelengths of 405 nm, 532 nm and 632.8 nm. The refractometer was calibrated using liquid standards of known refractive indices at those wavelengths - water, toluene [48] (EMD), acetone [49] (BDH), and ethylene glycol [50] (Mallinckrodt). The 405 nm operating wavelength was calibrated using water and ethylene glycol alone due to measurement range limitations. The refractive index of the PS was measured to be 1.5894 ± 0.008 at 532 nm and 1.5800 ± 0.0005 at 632.8 nm, where the errors represent one standard deviation.

6.3 Photomasks

Chrome-on-glass photomasks were obtained from the University of California, Los Angeles (UCLA) Nanolab Mask Shop and HTA Photomask. The patterns within the photomask were indexed using the nomenclature [Name] [Coordinate], where [Name] represented the name of each photomask and [Coordinate] represented the Cartesian position of the pattern within the photomask. The photomask patterns (and relevant geometrical parameters) used in this project are listed in Table 6.1. The patterns are either opaque (and surrounded by a transparent background) or transparent (and surrounded by an opaque background).

Pattern name	Description	Diameter (um)	Pitch (um)
20131105 A1	Square array of transparent circles	20	100
20131105 A2	Square array of transparent circles	5	50
20131105 A3	Square array of transparent circles	50	100
20131105 A4	Square array of transparent circles	25	50
20131105 B1	Hexagonal array of transparent circles	20	100
20131105 B2	Hexagonal array of transparent circles	10	50
20131105 B3	Hexagonal array of transparent circles	50	100
20131105 B4	Hexagonal array of transparent circles	25	50
20140826 E4	Five-fold quasicrystal array	10	-
20140826 F1	Six transparent circles in a ring	1000	3000
20140826 H4	Ten-fold quasicrystal array	5	-
20150721 B1	Square array of opaque circles	50	100
20150721 B2	Square array of opaque circles	50	75
20150721 B3	Square array of opaque circles	50	150
20150721 B4	Square array of opaque circles	50	60
20150721 D3	Six transparent circles in a ring	1000	3000

Table 6.1: Description and geometry of photomask patterns used in Conduction TCL

6.4 Photoresist patterning of sapphire window cold stages

The equipment-specific protocol for performing the sapphire window patterning process is included in Appendix C.

The sapphire window cold stages comprised c-axis sapphire windows (MSW 037/040, Meller Optics) with cylindrical SU-8 photoresist patterns deposited onto it. Each sapphire window had exactly two photoresist patterns: a central pin pattern to project a thermal map during thermocapillary fabrication (20 μm $\leq D \leq$ 50 μm, 50 μm $\leq P \leq$ 150 μm, 0.7 μm $\leq d_1 \leq$ 1.1 μm), and an outer ring of six thicker spacer elements (diameter = 1000 μm, 1.3 μm $\leq s_0 \leq$ 1.8 μm) to hold the window at a fixed

distance away from the nanofilm surface being fabricated. The spacer elements were deposited before the central pin patterns. Before any deposition, the sapphire windows were cleaned in piranha solution (sulfuric acid and 30% hydrogen peroxide in a 3:1 ratio by volume) for at least 15 minutes, rinsed in deionized water (18.2 MΩ cm resistivity, Milli-Q Gradient A10) and acetone, and dried using nitrogen. The photoresist patterns were deposited onto the window by spin-coating with SU-8 2010 (Microchem) diluted with cyclopentanone (Alfa Aesar), then cured with UV for 60 seconds through a chrome-on-glass patterned mask (fabricated by the University of California, Los Angeles Nanolab Mask Shop) on a Karl Suss MJB3 mask aligner. The photoresist structures were stabilized before and after UV exposure by a soft bake (1 minute at 65°C and 2 minutes at 95°C). The patterns were further stabilized after development by a hard bake at 200°C for 120 minutes. The central pin patterns were deposited after the hard bake for the spacer elements was completed.

The completed window (central pin pattern and spacers) was subjected to molecular vapor deposition in an evacuated desiccator with five drops of Trichloro(1H,1H,2H,2H-perfluorooctyl)silane (PFOTS) in an adjacent beaker (CAS: 78560-45-9, Sigma) to form a silanized surface monolayer and reduce polymer adhesion to the spacer elements. The spacer and pattern heights were measured directly before and after each TCL fabrication run using a Stylus Profilometer (Ambios Technologies XP2) to ensure uniformity. The value of d_0 was taken to be the arithmetic mean of the six spacer element maximum heights.

6.5 Preparation of polystyrene-on-quartz samples

Polystyrene (PS, M_w = 1100 g/mol, M_n = 990 g/mol, Scientific Polymer Products Inc.) was dissolved to 2% by mass in toluene (EMD) and was sonicated for 2 minutes to ensure complete dissolution. To minimize the variation of PS concentration in the solution due to toluene evaporation, more than 3 times the required volume of PS solution was made each time. The toluene was filtered once (EMD Millipore, 20 nm pore size) before dissolving the PS into it. The PS solution was filtered once more upon spin-coating. PS solution was dripped onto fused quartz windows or silicon wafers (diameter 50.8 mm, 279 ± 25 μm thickness, boron doped, ⟨100⟩ orientation, Silicon Materials Inc.) until the surface was fully covered with solution. The films were then spin-coated (Cee 100 spin-coater, Brewer Science) at 1000 RPM for 30 seconds with an acceleration of 1000 RPM/s. To ensure that the nanofilms were deposited under identical conditions, a graduated glass syringe was used to control the volume deposited. The syringe was rinsed and then refilled with fresh

PS solution in between depositions.

The film thicknesses on the transparent quartz samples were measured indirectly by spinning the same PS solution onto a silicon wafer immediately before and after spin-coating the quartz samples, and then measuring the PS-on-silicon film thicknesses using ellipsometry (Rudolph Auto EL III). Ellipsometry was also performed on the as-spun films on quartz but it did not yield reliable results due to measurement interference from additional reflections off the base of the quartz substrate. Film thicknesses were measured at nine positions in a 3×3 grid near the center of the silicon sample using the 632.8 nm source wavelength. The thickness ambiguity was resolved by additional ellipsometric measurements using 546.1 nm and 405.0 nm source wavelengths. The PS-on-quartz film thickness was taken to be the arithmetic mean of the eighteen measurements made on the "before" and "after" PS-on-Silicon film thickness measurements, and the error was taken to be the standard deviation of the eighteen measurements.

6.6 Conduction Thermocapillary Lithography fabrication process

The equipment-specific protocol for Conduction TCL is included in Appendix D.

Convex and Concave structures use the same setup

Figure 6.1 exhibits the Conduction TCL setup in full (6.1(a)) and zooming in on the nanofilm region (6.1(b-c)). Figure 6.1(b) exhibits the photoresist pin configuration for the fabrication of convex MLAs, and Figure 6.1(c) exhibits the configuration for concave MLAs. The same experimental setup is used in both convex and concave MLA fabrications, with the exception of the photoresist pattern. By inverting the polarity of the photoresist patterns — replacing pins with depressions and vice versa — we are able to invert the sign of the temperature gradient field, which in turn inverts the sign of the induced thermocapillary flow velocity. This inversion creates the possibility of fabricating surfaces reflected in the vertical direction simply by inverting the polarity of the templating structure.

It is important to note that the temperatures $T_{\text{stage, hot}}$ and $T_{\text{stage, cold}}$ are distinct from the temperatures T_H and T_C used in the derivation of the thermocapillary instability. In the theoretical derivation, T_H and T_C represent the temperatures at the bottom of the nanofilm and top of the air gap, respectively. In the experimental setup, $T_{\text{stage, hot}}$ and $T_{\text{stage, cold}}$ represent the set temperatures of the heating element in the hot stage (below the fused quartz substrate) and the set temperature of the cooling stage (above the sapphire window upon which the photoresist patterns are mounted). These stage

temperatures are the temperatures that we can directly control and measure; we do not have direct control or measurements of T_H and T_C in the experimental setup. Nevertheless, we may deduce the corresponding values of T_H and T_C by finite element modeling of the experimental geometry.

Another distinction between the theoretical geometry and the experimental geometry is the introduction of s_0 for the spacer heights. We have defined $d_0 = s_0 + h_0$ to be the sum of the spacer and initial film heights. d_0 hence corresponds to the distance between the nanofilm base and the air gap, in accordance with that of the theoretical geometry. In experimental studies, we did observe a small amount of subsidence when the spacer elements sank into the polymer melt, thereby making the effective d_0 smaller than the sum of the spacer and film heights. However, this subsidence is small for most samples, and we will take $d_0 = s_0 + h_0$ to hold.

Fabrication protocol

The patterned sapphire window (i.e. the cold stage) was maintained at a fixed temperature ($T_{\text{stage, cold}}$) by thermal contact with a custom-machined water-cooled aluminum thermal reservoir driven by a Fisher Scientific Model 910 cooler pump. The cold stage was placed above the polystyrene-on-silicon sample. The quartz substrate was placed on a hot stage (custom-built cylindrical aluminum block with a 2.54 cm square 5.2 Ω alumina metallic ceramic heating element from Induceramic, powered by a Keithley 2200-30-5 150 W DC Power Supply) held at a fixed temperature ($T_{\text{stage, hot}}$) through active PID feedback implemented using a custom Matlab GUI controller (named tempController). The design documents for the hot stage are displayed in Appendix A. The power supply was controlled using GPIB through an ICS Electronics Model 488-USB2 USB to GPIB controller. The settling time to heat to within 1°C of the target temperature was 5.3 ± 0.4 min for the $T_{\text{stage, hot}} = 180$°C, $T_{\text{stage, cold}} = 60$°C fabrication runs. A drop of thermal paste (approximately 150 mg of Aremco Heat-Away 638, corresponding to a 130 μm thick layer) was placed between the heater block and the lower face of the quartz window to ensure good thermal contact and even heating. The heater block was bolted onto a set of four spring-mounted riser plates supported from below by a motorized vertical translator (16618, Oriel) to ensure that all the surfaces were flat relative to the cooler block. Platinum resistance temperature detectors (RTD-3-F3105-36-T, Omega, monitored with an Omega PT-104A RTD data acquisition module) were placed immediately below the quartz window, at the half-radius, and at the outer edge of the heater block to monitor the heating process. The temperature just below the cylindrical axis of

the heating block was fed back to the Matlab PID controller to modulate the power supply voltage. After a pre-determined length of time (t = 5 min to 120 min), the heating element below the quartz window was automatically turned off to allow the PS film to cool and solidify in place. The setup was allowed to cool to a central temperature within 10°C of $T_{\text{stage, cold}}$ before the sample was removed. The surface topology of the MLAs was analyzed in a non-contact fashion using scanning white light interferometry (Zygo NewView 600 and Zemetrics Zegage) and the resultant height profiles were analyzed quantitatively using our custom-built Zygocruncher MATLAB package, which is described in the next section. The usage instructions for the Zemetrics Zegage is included in Appendix E.

6.7 Zygocruncher MATLAB package

Zygocruncher overview

The Zygocruncher package was a custom-built MATLAB graphical user interface (GUI) I developed to serve as a wrapper for the exported output from scanning white light interferometry (ASC files from MetroPro, Zygo Corporation and SDF files from ZeMaps, Zygo Corporation) and atomic force microscopy (ITX files from Igor Pro, WaveMetrics), and to provide the computational tools specific to the analysis of microlenses and optical elements.

The Zygocruncher GUI provides a range of surface manipulation tools. It is able to perform thresholding in the three Cartesian coordinates, select contiguous islands of data points, fit planes and quadratic surfaces to the data in order to remove an overall tilt or curvature, and smooth a surface using a cubic spline. It is also able to calculate the surface mean curvature using the cubic spline, and select points which correspond to either positive or negative curvature. Most importantly, it performs 1D and 2D fits on the microlens surfaces obtained.

Leveling

The GUI offers two leveling options: tilt removal or curvature removal. These functions compensate for sample tilts and deformations during the scanning white light interferometry measurement. In tilt removal, the best fit plane passing through the surface is calculated and then subtracted from the data. This removes the overall tilt of the surface. In particular, the best-fit coefficients $c_x, c_y, c_{\text{const}}$ of the plane equation:

$$z(x, y) = c_x x + c_y y + c_{\text{const}} \tag{6.1}$$

were calculated by linear least squares regression, then the fitted function $z(x, y)$ was subtracted from the original surface. The tilt removal tool was essential in compensating for the overall sample tilt at all magnifications when evaluated using the white light interferometer.

In curvature removal, the best fit quadratic passing through the surface is calculated and subtracted from the data. The best fit coefficients of the generalized quadratic surface:

$$z(x, y) = c_x x + c_y y + c_{xx} x^2 + c_{yy} y^2 + c_{xy} xy + c_{\text{const}} \tag{6.2}$$

were calculated by linear least squares regression, then the fitted function was subtracted from the original surface. In this process, the overall tilt of the surface (first order terms) was removed as well. The curvature removal function was found to be relevant only at low scanning white light interferometer magnifications (2.5x) where a large field of view was scanned.

Lens characterization

The Zygocruncher GUI-specific instructions for the following fitting procedures are included in Appendix F.

The 2D surface profile obtained from scanning white light interferometry was used to characterize the optical and geometrical properties of the fabricated MLAs. The domain assigned to each individual lens surface was defined by the sign of the mean curvature. That is, contiguous pixels (in all eight directions around a pixel) corresponding to negative (positive) mean curvature were determined to be part of the same convex (concave) lens. Prior to calculating the mean curvature of each surface, we removed the high frequency spatial noise by smoothing the raw data using a cubic spline (`csaps` in MATLAB, smoothing parameter = 10^{-4}). The cubic spline is then used to calculate the mean curvature at all points. The raw unsmoothed data points corresponding to the appropriate sign of mean curvature were then grouped together to define a lens. The lens characteristic diameter D_{lens} was calculated by taking the area occupied by the lens domain and equating it to $\pi D_{\text{lens}}^2/4$. The fill factor of the lens array was calculated by taking the area occupied by the lens domain and dividing it by the area of a unit cell.

The focal length of the fabricated microlenses were estimated by fitting the lens domain to that of a rotated paraboloid using the MATLAB `NonLinearModel.fit`

function:

$$z(x, y) = z_{\max} - \frac{(x')^2}{2R_1} - \frac{(y')^2}{2R_2} \tag{6.3}$$

$$\begin{pmatrix} x' \\ y' \end{pmatrix} = \begin{pmatrix} \cos\theta & -\sin\theta \\ \sin\theta & \cos\theta \end{pmatrix} \begin{pmatrix} x - x_o \\ y - y_o \end{pmatrix} \tag{6.4}$$

where $R_{1,2}$ is the radius of curvature along the lateral principal axes x', y', which are rotated by an angle θ with respect to the raw data axes x, y. (x_o, y_o) is the coordinate of the lens vertex in the raw data coordinates, and $z_{\max}$ is the height of the lens at its vertex. Two focal lengths are fitted to account for astigmatism. The focal length f of the resultant plano-convex (or plano-concave) microlens can be estimated using the lensmaker's equation for thin lenses of refractive index n, taking one face of the lens to be flat (infinite radius of curvature):

$$\frac{1}{f_{1,2}} = \frac{n-1}{R_{1,2}} \tag{6.5}$$

The larger of the focal lengths calculated (in terms of the magnitude of the focal length) was defined to be f_1 and the smaller was defined to be f_2.

The RMS residual of the 2D surface fit has two main contributions: the non-conformity of the microlens geometry to the paraboloid shape and the high spatial frequency surface roughness contribution. The RMS residual hence provides an upper bound to the surface roughness of the fabricated surfaces. We hence used the RMS residual as a proxy for quantifying the quality of the fabricated surfaces.

The asphericity of each lens was quantified by fitting the lens cross-sections along its principal axes (defined by the angle θ from the 2D paraboloidal fit) to an aspheric profile (Equation (6.6)):

$$z(r) = h - \left[\frac{r^2}{R\left(1 + \sqrt{1 - r^2/R^2}\right)} + \alpha_1 r^4 \right] \tag{6.6}$$

The aspheric profile comprises a vertical offset (first term), a spherical sag (second term) and a perturbing even polynomial (third term). In the general aspheric profile, there are higher order terms in the perturbing even polynomial, but we have retained only the most important lowest order r^4 term for this analysis. Before fitting the 1D cross-section, each convex (concave) cross-section was displaced so that its

minimum (maximum) point was located at zero. $|h|$ hence represented the height of the lens. R is the radius of curvature of the spherical sag, and α_1 is the first aspheric correction. We defined a dimensionless parameter, the aspheric ratio, to compare the degree of asphericity across lenses of different sizes. We converted α_1 to a characteristic lengthscale for the correction polynomial by evaluating the perturbing polynomial $\alpha_1 r^4$ at the characteristic radius $r = D_{\text{lens}}/2$, then normalizing it to the lens height by dividing the lengthscale by z_{max}, the fitted height of the microlens from the 2D paraboloidal fitting step:

$$AR \equiv \left| \frac{\alpha_1 (D_{\text{lens}}/2)^4}{z_{\text{max}}} \right| \tag{6.7}$$

The larger the value of AR, the greater the contribution of the lowest order polynomial correction term, and hence the larger the degree of asphericity.

6.8 Transmitted intensity measurements

The Conduction TCL process was able to produce MLAs in which the central vertex exhibited the opposite curvature to that of the larger lens structure. These lens structures were coined *caldera-like* MLAs. The focusing characteristics (under transmission) of the *caldera-like* MLAs were recorded by placing the MLAs lens-side up on an optical microscope (Olympus BX60 with Olympus UMPlanFL 5x, 0.15 NA, 20.0 mm working distance objective) configured for transmitted light illumination from a halogen bulb. The vertical position of the MLAs was controlled to an accuracy of 1 μm using the microscope fine adjust knob and the resulting transmitted light images were captured at various vertical distances using a high resolution monochrome CMOS camera (Basler acA2500-14gm, 2592×1944 pixels, 2.2 μm $\times$ 2.2 μm pixel size) with a fixed exposure time set to avoid pixel saturation at any pixel in the stack. The zero of the vertical displacement was taken to be at the position where the surfaces of the lenses were in focus. The images were aligned in ImageJ (Template matching and Slice alignment plugin) [51–53] and were imported into MATLAB for radial averaging of the pixel intensities to be performed around each lens focus position. The radial averaging process identified the central locations of each focusing feature, then measured the average pixel intensities around each point as a function of distance from that central point. Only points that lay within a square of size length 53 μm centered at each central point were included in the radial averaging process. This distance was chosen so that pixels corresponding to adjacent focusing features would be excluded while maximizing the number of

pixels assigned to each focusing feature. The averaging was performed by dividing the radial distance into 45 bins of equal radial lengths and calculating the arithmetic average of pixel intensities that fell within each binned radius range. The radial averaged intensity distributions for each of 53 lens positions were averaged to obtain the radial intensity distribution for a single cross-sectional slice.

6.9 Numerical estimation of material thermodynamic parameters

The surface tension, temperature dependence of surface tension, thermal conductivity and viscosity of the polystyrene melt were obtained from experimental literature values. These values were incorporated in numerical simulations and the computation of derived quantities such as the characteristic thermocapillary instability wavelength. The temperature distribution across the polystyrene melt was calculated by solving the steady state heat distribution of the experimental setup computationally in COMSOL, which is separately described by Fiedler and Troian [20]. In brief, the TCL setup was modeled as a two-dimensional axisymmetric system in COMSOL (Version 4.3a, Heat Transfer in Solids package). The system was surrounded by an air domain with an outer boundary held at a constant ambient temperature of 23°C. The heat energy introduced into the system was represented by a uniform cylindrical volumetric heat source located at the position of the ceramic heating element emitting a constant total power. The total power used in each calculation was obtained by taking the product of the experimental steady-state heating voltage and current at the timestep just before the heating element was switched off at the end of a fabrication run.

The steady-state simulation yielded that the nanofilm base temperature range across the four experimental conditions in Table 1 was (99.4°C, 101.3°C), and the nanofilm surface temperature range was (99.1°C, 101.0°C). The temperature drop across the nanofilm layer ranged from 0.24°C to 0.31°C, which is small. We hence evaluated all film thermodynamic parameters at 100°C.

We evaluated the surface tension of polystyrene melt by interpolation. The liquid surface tension of M_v = 44000 g/mol polystyrene was cited to be γ = 40.7 mN/m at 20°C with a temperature dependence of $\gamma_T = d\gamma/dT = -0.072$ mN/m [54]. The temperature of the upper surface of the nanofilm was calculated using the steady-state temperature simulation of the experimental setup. We took the temperature dependence to be constant at $d\gamma/dT = -0.072$ mN/m and extrapolated the surface tension to be γ = 35 mN/m at 100°C.

The thermal conductivity of air was also evaluated through interpolation. The thermal conductivity was evaluated at the temperature of the nanofilm surface obtained through the steady-state temperature simulation. At 23°C , the thermal conductivity of air at one atmosphere is 26.4 mW/mK and at 123°C, it is 33.5 mW/mK [16]. Linearizing in this range, we obtain that the estimated thermal conductivity of air at 100°C is 31.6 mW/mK.

We obtained numerical measurements of the viscosity of M_w = 1900 g/mol PS as a function of temperature through private communication with the authors of Urakawa *et al.* [17]. We obtain the viscosity at 100°C by taking the viscosity variation to be exponential and interpolating between the two closest (temperature, log (viscosity/Pa·s)) data points, which were (98.3°C, 3.63) and (108°C, 2.78). This yielded a log-viscosity estimate of 3.48 at 100°C and thereby a viscosity estimate of 32.5 Pa·s.

6.10 Computational simulation of nanofilm evolution

The computational simulation in this section was constructed and performed by Chengzhe Zhou, who was a graduate student in {LIS^{2}T} at the time. The thermocapillary evolution equation (Equation 3.62) was solved using finite element analysis on the COMSOL Multiphysics 4.3a platform. The independent variables and their numerical values are listed in Table 6.2. The experimental parameters used was that which fabricated the caldera-like array in Figure 7.1(d). We used a minimal representation of the experimental geometry for the computational simulation, and this is displayed in Figure 6.2. The domain was a square box [0,2]×[0,2] with periodic boundary conditions in the x and y directions. The characteristic horizontal length scale in this periodically repeated case is naturally $l = P$, the pitch between the pin elements in the upper cold stage array. The constituent elements are P2 Lagrange triangular elements. Four pins arranged in a 2×2 array (blue surface in Figure 6.2) were contained in the computational domain. The temperature jump across the polystyrene nanofilm and the air gap immediately above, ΔT, was calculated by solving the steady state heat distribution computationally in COMSOL as described earlier.

The dependent variables were $\overline{h}(\overline{x}, \overline{y}, \tau)$ for the film height and $C(\overline{x}, \overline{y}, \tau) = \overline{\nabla}_{\|}^2 \overline{h}(\overline{x}, \overline{y}, \tau)$ for the in-plane curvature. Rearranging the thermocapillary evolution equation with variable gap height (Equation 3.62) in terms of $\overline{h}$ and C, we obtain the matrix evolution equation used in the simulation:

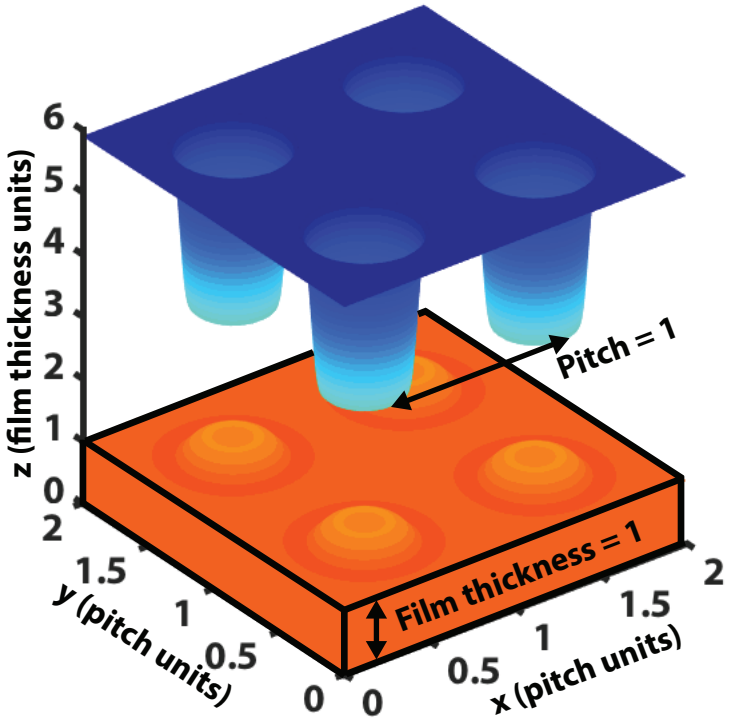

Figure 6.2: COMSOL simulation geometry of a 2×2 array of pins above a molten polymer surface.

$$\frac{\partial}{\partial \tau}\begin{bmatrix} \overline{h} \\ 0 \end{bmatrix} + \overline{\nabla}_{\parallel} \cdot \begin{bmatrix} \frac{1}{3}\overline{h}^3 \overline{\nabla}_{\parallel} C \\ \overline{\nabla}_{\parallel}\overline{h} \end{bmatrix} + \overline{\nabla}_{\parallel} \cdot \begin{bmatrix} \frac{\kappa\overline{\mathrm{CaMa}}}{2} \frac{\overline{d}_0 \overline{h}^2}{\left[\overline{h}(\kappa-1)+\overline{d}_0\right]^2} \overline{\nabla}_{\parallel}\overline{h} \\ 0 \end{bmatrix}$$
$$-\overline{\nabla}_{\parallel} \cdot \begin{bmatrix} \frac{\kappa\overline{\mathrm{CaMa}}}{2} \frac{\overline{h}^3}{\left[\overline{h}(\kappa-1)+\overline{d}_0\right]^2} \overline{\nabla}_{\parallel}\overline{d}_0 \\ 0 \end{bmatrix} = \begin{bmatrix} 0 \\ C \end{bmatrix} \tag{6.8}$$

The surface relief pattern of the cold stage mask is captured in the protrusion function $f(\overline{x}_{\parallel})$ contained within the normalized gap height $\overline{d}_o(\overline{x}_{\parallel}) = (d_0/h_0)[1 - \delta \cdot f(\overline{x}_{\parallel})]$, which was taken to be a periodic extension of COMSOL's built-in rectangle function over the [0,2]× [0,2] computational domain:

$$f(\overline{x}_{\parallel}) = \mathrm{rect}\left[\sqrt{(\overline{x} - 0.5)^2 + (\overline{y} - 0.5)^2}\right] \tag{6.9}$$

The rectangle function was set to have an upper and lower limit of ±0.25 and a transition zone width of 0.1. $\delta = \frac{d_1}{d_0}$ is the pin height normalized to the sum of the spacer height and initial film thickness.

We started the simulation with the initial film height being unity plus small random noise and plotted the surface profile and diagonal cross-sections at various timesteps. The initial height was set at:

$$\overline{h}(\overline{x}, \overline{y}, \tau = 0) = 1 + 0.1 \cdot rn(\overline{x}, \overline{y}) \tag{6.10}$$

where $rn(\overline{x}, \overline{y})$ is a two-dimensional random number generator, in which each argument is sampled from a normal distribution with $\mu = 0$ and $\sigma = 0.05$. The model is not sensitive to the initial random height function because the capillary term in the thin-film model automatically damps out high spatial frequency components, while the time-dependent COMSOL computation is based on an implicit backward differentiation solver. These two factors guarantee the numerical stability of the solution system and eliminate the high frequency components after the first computation timestep.

Table 6.2: List of independent parameter values used in the computational simulation of microlens evolution. All temperature-dependent parameters are computed at 100°C, the estimated film temperature.

Parameter	Formula	Value	Reference
h_0	-	288 nm	-
s_0	-	1410 nm	-
d_1	-	730 nm	-
P	-	100 μm	-
D	-	50 μm	-
ΔT	-	6.27°C	-
γ_H	-	3.5×10^{-2} Nm^{-1}	[54]
γ_T	-	7.2×10^{-5} Nm^{-1} K^{-1}	[54]
k_{air}	-	0.032 Wm^{-1}K^{-1}	[16]
k_{film}	-	0.128 Wm^{-1}K^{-1}	[54]
μ	-	32.5 Pa·s	[17]
ϵ	$\frac{h_0}{P}$	0.00288	-
$\overline{\text{Ca}}\,\overline{\text{Ma}}$	$\frac{\gamma_T \Delta T}{\epsilon^2 \gamma_H}$	1490	-
$\frac{d_0}{h_0}$	-	5.90	-
δ	$\frac{d_1}{h_0}$	0.430	-
κ	$k_{\text{air}}/k_{\text{film}}$	0.247	-
t_{VC}	$\frac{\mu P}{\gamma_H \epsilon^3}$	3.89×10^6 s	-

Chapter 7

RESULTS AND DISCUSSION

7.1 Microlens Array topologies achieved

Figure 7.1 exhibits four representative MLA topologies achieved through Conduction TCL fabrication, imaged using scanning white light interferometry. The fabrication parameters and surface characteristics for each of the topologies in Figure 7.1 are listed in Table 7.1 and representative cross-sectional plots are exhibited in Figure 7.2. Conduction TCL has successfully achieved both convex (converging, Figure 7.1(a)) and concave (diverging, Figure 7.1(b)) MLAs. Simple topologies are formed when the pin diameter D is much larger than the center-to-center pitch P, creating isolated lenses surrounded by a flat plane. When D is around the size of P, the concave ridges around convex microlenses (formed from local material depletion/accumulation to form protrusions/depressions) overlap to form smaller interstitial lens arrays. This achieves a hierarchical MLA structure where a smaller array of lenslets is formed in the interstitial region of the larger lens array (Figure 7.1(c)). Hierarchical MLAs exhibit two distinct length scales, corresponding to the lateral size of the two lens arrays. We also report the fabrication of a lens structure with a central depression at the vertex of each microlens (Figure 7.1(d)), which we call the *caldera-like* structure. This name was inspired by the summit caldera, a geological feature that forms when the top of a volcano collapses into an empty magma chamber below. While we were preparing these findings, we discovered that the *caldera-like* microlens structure bears much resemblance to the microdonut topology fabricated by Vespini *et al.* through spin-coating polymer onto a patterned pyroelectric substrate [29]. While Vespini *et al.* attributes the central depression formation to a slump of material away the protrusion vertex during spin-coating, we will show through first-principles computational simulation that our *caldera-like* arrays evolve from the bottom-up and outside-in. The technique investigated by Vespini *et al.* has only achieved convex *caldera-like*/"microdonut" structures, whereas Conduction TCL has achieved concave *caldera-like* topologies as well and hence has access to a larger variety of curved topologies.

Table 7.1: Parameter values for the four microlens arrays imaged in Figure 7.1. Uncertainties are one standard deviation. t is the fabrication time for which the heating elements were active. d_2 is the depth of the photoresist depression in a block and is only applicable to concave microlens array fabrication (experimental setup in Figure 6.1(c) and MLA in Figure 7.1(b)). Lens parameters were measured for at least 10 lenslets randomly selected over the array. The fastest-growing unstable wavelength $\lambda_{\max}$ and viscous-capillary timescale t_{VC} was computed based on numerical simulation results. †Parameter was calculated at the Helium-Neon laser wavelength $\lambda = 632.8$ nm.

	Simple Convex	Simple Concave	Hierarchical (interstitial array)	*Caldera-like* (central depression)
Sample name	Q0051	Q0046	Q0039	Q0043
Cold stage name	S0047	S0039	S0035	S0035
Photomask pattern	20131105 B1	20150721 B2	20131105 A3	20131105 A3
t (min)	30	60	15	45
T_{cold} (°C)	60	60	60	60
T_{hot} (°C)	180	180	180	180
s_0 (nm)	1630 ± 40	1430 ± 50	1400 ± 30	1410 ± 20
d_1 (nm)	805 ± 7	880 ± 10	730 ± 10	730 ± 10
d_2 (nm)	-	320 ± 20	-	-
D (μm)	20	50	50	50
P (μm)	100	75	100	100
h_0 (nm)	228 ± 2	288 ± 4	288 ± 4	288 ± 4
ΔT (°C)	7.20	6.34	6.17	6.27
$\lambda_{\max}$ (μm)	65.4	69.5	69.5	69.2
$t_{\mathrm{VC}} \times 10^{-6}$ (s)	7.85	1.23	3.89	3.89
D_{lens} (μm)	29.4 ± 0.5	51.3 ± 0.6	71 ± 2 (30 ± 2)	71.0 ± 0.4 (21.6 ± 0.8)
Fill factor (%)	7.9 ± 0.3	36.7 ± 0.8	39 ± 2 (7.2 ± 0.7)	39.6 ± 0.4 (3.7 ± 0.3)
f_1 (mm)	6.2 ± 0.7	−23 ± 2	38 ± 9 (70 ± 10)	(−34 ± 6)
f_2 (mm)	5.4 ± 0.3	−22 ± 2	29 ± 7 (47 ± 7)	(−23 ± 3)
RMS residual (nm)	1.3 ± 0.5	0.7 ± 0.1	1.4 ± 0.6 (0.49 ± 0.04)	(0.44 ± 0.02)
AR	0.5 ± 0.2	0.12 ± 0.03	0.5 ± 0.5 (0.5 ± 0.3)	(0.4 ± 0.2)
$F_{\mathrm{lens}} \times 10^{3\dagger}$	59 ± 5	46 ± 4	63 ± 14 (7 ± 2)	(7 ± 2)
$F_{\mathrm{array}} \times 10^{3\dagger}$	687 ± 67	98 ± 8	127 ± 31 (72 ± 4)	(148 ± 36)

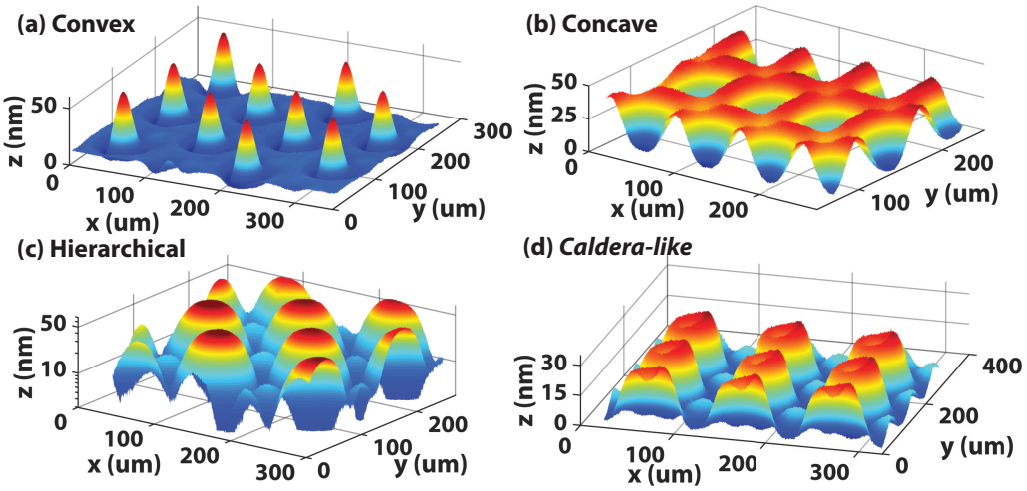

Figure 7.1: Surface topologies of representative fabricated microlens arrays imaged using scanning white light interferometry. Note that the vertical axis has units of nanometers and the horizontal axes has units of micrometers; all microlenses shown here are wide and shallow. (a) The convex microlens array has converging lenslets. (b) The concave microlens array has diverging lenslets. (c) The hierarchical compound microlens array is formed from two overlapping periodic arrays of lenslets. The vertical scale is logarithmically plotted to accentuate the visibility of the shorter secondary array between the main peaks.(d) The *caldera-like* microlens array has a central depression at the vertex of each lens. An additional array of smaller lenslets is also visible in the interstitial region.

7.2 Microlens parameters

The fabricated MLAs have continuous ultrasmooth surfaces and hence lack a boundary separating distinct microlenses. We hence define the region occupied by each lens based on the sign of the mean curvature at each point. For instance, a convex microlens comprises the approximately circular region of all contiguous points with a negative mean curvature. The MLAs attained thus far have characteristic diameters D_{lens} ranging from 29 μm to 71 μm, as calculated by taking the horizontal lens area (including the central region of opposite mean curvature in *caldera-like* topologies) to be $\pi D_{\text{lens}}^2/4$. The height of the microlenses, as defined by the vertical distance of the lens vertex above the boundary of the lens with zero mean curvature, ranges from 8 nm to 160 nm. These characteristic dimensions are three orders of magnitude smaller than that of the range of focal lengths achieved so far: 2 mm to 83 mm for convex MLAs and −22 mm to −53 mm for concave MLAs. TCL is not limited to these small aspect ratios; we deliberately chose to work on ultrathin films to operate in the long-wavelength limit where gravity plays a negligible effect

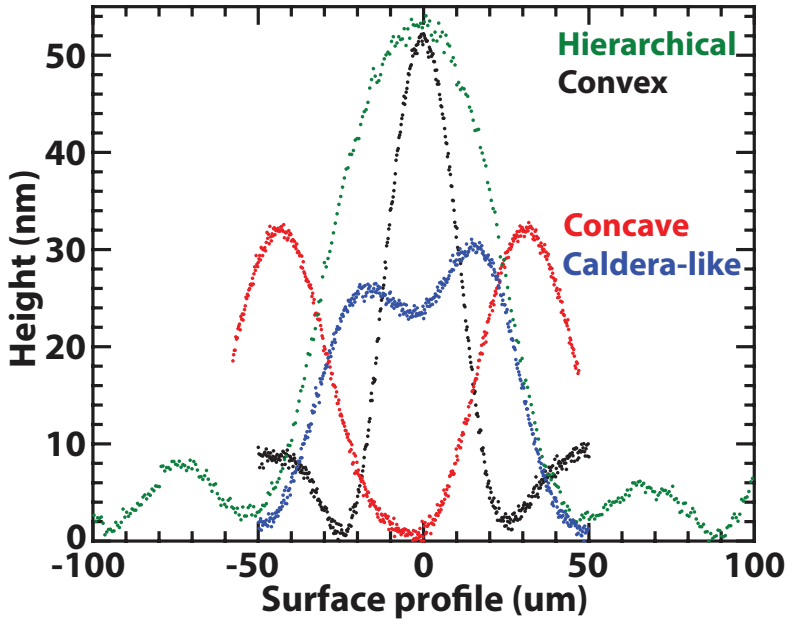

Figure 7.2: Representative cross-sectional plots of the fabricated microlens arrays in Figure 7.1. Note that the convex (black) microlens was fabricated with a smaller $D = 20$ μm and hence appears narrower than the other cross-sections, which were fabricated with $D = 50$ μm.

to obtain correspondence to computational simulations based on the equation of motion (3.56). On thick films where gravity and density variations play a significant role, the thermocapillary evolution equation is much more complex, but the surface can still be sculpted using the same physical principles of thermocapillary flow.

7.3 Axisymmetry and geometrical properties of the lens profile

The fabricated microlenses exhibit an aspheric, non-axisymmetric, paraboloidal profile. The non-axisymmetry results in astigmatic lenses, where the lens exhibits two focal lengths in orthogonal axes. To account for this astigmatism, two radii of curvature parameters R_1 and R_2 were used in the fitting of individual 2D lenslet surface profiles to the rotated paraboloidal surface in Equations 6.3-6.4. The fitted radii of curvature was then substituted into the lensmaker's equation (Equation 6.5) for thin plano-convex (or plano-concave) lenses to obtain the corresponding lens focal lengths.

R_1 and R_2 are generally slightly different, indicating that the MLAs formed are not axisymmetric and are compressed in a preferential direction. This is likely due to unintended lateral flow of the lens material, when the spacer heights are not completely even and the stage surfaces are slightly tilted. The lenses are hence

compressed in the direction of the tilt by the bulk motion of polymer melt and exhibit the observed asymmetry. This asymmetry is not an inherent limitation of Conduction TCL, and can be eliminated by better parallelism between the warmer and cooler stages. One way to improve this parallelism is to use multiple narrower spacer elements that push through the polymer melt and make physical contact with the substrate below, as opposed to the current spacer elements which sit on the surface of the polymer melt.

The fabricated microlenses operate in the Fraunhofer regime where diffraction is important. The Fresnel numbers of the individual microlenses $F_{\text{lens}} = D_{\text{lens}}^2/4\lambda f$ evaluated one focal length away at the Helium-Neon wavelength of $\lambda = 632.8$ nm is on the order of 10^{-3} to 10^{-2}, and hence is small compared to unity. The generalized Fresnel number [21] corresponding to the spatial period Λ of the array, $F_{\text{array}} = \Lambda^2/4\lambda f$ is also smaller than unity, indicating significant overlap between diffraction patterns from adjacent lenslets. MLAs fabricated by Conduction TCL are not restricted to the Fraunhofer regime; by increasing the aspect ratio of the lenslets, it is possible to decrease the lens Fresnel number and enter the Fresnel far field regime. Our fabricated MLAs have small aspect ratios as a direct consequence of performing fabrication on an ultrathin film; one may perform TCL fabrication on a thicker film to achieve greater deformations and hence larger lens aspect ratios.

To justify the selection of a paraboloidal geometry over a spherical geometry and quantify the degree of asphericity, we define a new dimensionless parameter which we call the asphericity ratio. We define the aspheric ratio (AR) to be:

$$AR \equiv \left| \frac{\alpha_1 (D_{\text{lens}}/2)^4}{z_{\text{max}}} \right| \tag{7.1}$$

where α_1 is obtained from 1D lens cross-sectional fits to an aspheric profile (Equation 7.2), D_{lens} is the characteristic diameter of the microlens and z_{max} is the lens height obtained from the parabolic fit. The aspheric profile comprises a spherical sag plus a perturbing even polynomial:

$$z(r) = h - \left[\frac{r^2}{R\left(1 + \sqrt{1 - r^2/R^2}\right)} + \alpha_1 r^4 \right] \tag{7.2}$$

The lens profiles are displaced vertically so that the minimum (maximum) of the fitted convex (concave) lens lies at zero height and h corresponds to the height of the

lens. Note that h is not necessarily equal to $z_{\max}$, though the two are only slightly different due to the different fitting domain (1D vs 2D). The first aspheric coefficient α_1 hence quantifies the degree of asphericity: the larger its value, the less spherical the 1D lens profile. To allow comparison of this asphericity over different lens sizes, we defined the asphericity ratio in (Equation 7.1) to be the ratio of the contribution due to α_1, relative to the lens height, evaluated one characteristic radius away from the lens vertex.

The AR values calculated are mostly on the order of unity, indicating that the contribution due to the perturbing polynomial is large compared to that of the spherical geometry. As a comparison to a figure of merit, a commercial spherical microlens array (Thorlabs MLA150-5C-M) evaluated using the same process yields an AR value of 0.04 ± 0.03 and a commercial parabolic microlens array (Thorlabs MLA300-14AR-M) yields a larger AR value of 0.13 ± 0.02. This result corroborates with the excellent fits obtained by the 2D paraboloidal surface in Equations 6.3-6.4 over the lens surface. The majority of the microlens fits achieve an RMS residual of less than 2 nm, which also provides an upper bound to the low surface roughness of the ultrasmooth lenslets.

7.4 *Caldera-like* array focusing

The *caldera-like* microlens array (Figure 7.1(d)) is characterized by a central depression of the opposite curvature as the lenslet and is an early stage topology. Computational finite-element simulations solving the thermocapillary evolution equation and incorporating the experimental dimensions of the *caldera-like* array setup demonstrate that at early times, nanofilm protrusions begin forming directly under the edges of the cylindrical chilled pins, forming a shallow ring (Figure 7.3(b) red line). The circular protrusions grow and migrate towards the center, forming the *caldera-like* microlenses (green line). At late times, the protrusions merge into a single convex peak (blue line), which continues growing towards the chilled pins above (purple line). Two distinct regimes are observed in this evolution when the maximum lens height and central lens height are plotted on the same axes (Figure 7.3(a)). There is an early time *caldera-like* regime when the central height is below the lens maximum height (left of Figure 7.3(a), before 6.0 minutes), and the late-time convex regime when the central height becomes the tallest point on the lenslet (right of Figure 7.3(a), after 6.0 minutes). *Caldera-like* arrays are hence formed when thermocapillary fabrication is halted by removing the heat source during the *caldera-like* regime.

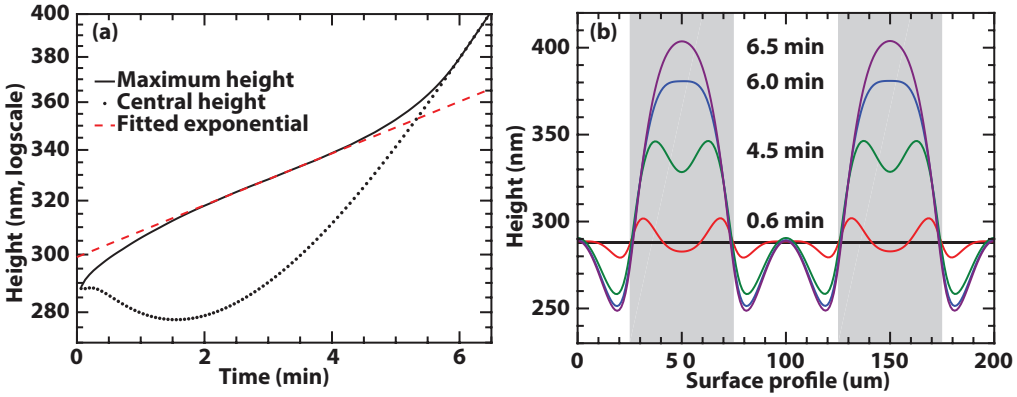

Figure 7.3: (a) Time dependence of the maximum height of a single microlens and central height of the microlens. The central region is initially lower than the maximum height, indicating that the microlens formed a *caldera-like* geometry with a concave top. At late times the central region becomes the highest point, indicating a transition from a *caldera-like* regime to a simple convex regime. The plot is semilogarithmic to exhibit the exponential growth of the lens maximum height. The red line is an exponential fit for the data points from $t = 2$ min to $t = 4$ min. The fitted time constant is 1.3×10^8 seconds. (b) Cross-sections in the computational simulation of convex microlens array evolution at four representative times. The grey shaded region represents the points directly under the photoresist pins (placed further above the film surface). Polymer begins accumulating below the edges of the chilled pins to form a ring-like protrusion (0.6 minutes), then forms a *caldera-like* lens with a wide central depression (4.5 minutes). At late times, the central depression vanishes (6.0 minutes) and the microlenses form simple convex topologies (6.5 minutes).

It is interesting to note that the maximum height of the *caldera-like* structure grows approximately exponentially, thereby forming a straight line between 2 and 4 minutes in the semilogarithmic growth plot in Figure 7.3(a). We fitted the data points between 2 and 4 minutes to an exponential (red dotted line in Figure 7.3(a)) and obtained a fitted time constant of 1.3×10^8 seconds, which is two orders of magnitude larger than the visco-capillary timescale of $t_{VC} = 3.89 \times 10^6$ s for this system. The exponential growth of the thermocapillary protrusions implies that it is easier (and more precise) to arrest film evolution at earlier times as compared to late times, where the uncertainty in the film height will be larger.

Convex *caldera-like* arrays focus normally incident collimated light into arrays of annuli. The transmitted light relative intensity distribution as a function of vertical displacement above the lens surface and radial position is plotted in Figure 7.4(a). Due to the presence of the central depression of the opposite curvature, a

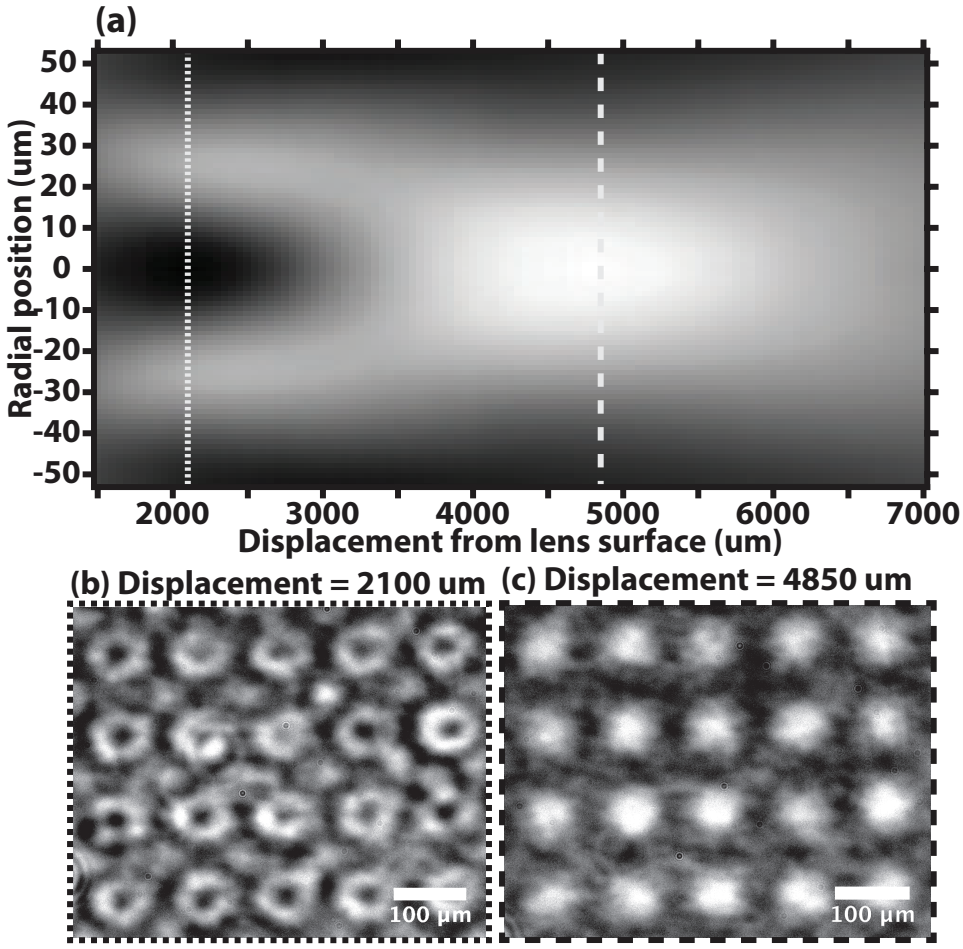

Figure 7.4: Transmitted light images captured through microlens arrays. (a) Radial intensity of transmitted light through *caldera-like* array shown in Figure 7.1(d) as a function of vertical displacement from the lens surface. The plot is azimuthally symmetric about the optical axis (radial position zero). (b) Transmitted light image captured 2100 μm from the surface of the *caldera-like* MLA, corresponding to the dotted line position in (a). Annular focusing with a central minima is observed due to the central *caldera* lens depression. (c) Transmitted light image captured 4850 μm from the surface of the *caldera-like* MLA, corresponding to the dashed line position in (a). Approximately Gaussian focusing is observed due to the convex portion of the lens.

central minimum occurs in the transmitted intensity pattern for distances close to the lens surface, resulting in annular focusing (Figure 7.4(a) left dotted line and Figure 7.4(b)). Further away from the surface, the *caldera-like* MLA behaves as an ordinary converging MLA. The convex portion of the lens around the central depression focuses incident light into an approximately Gaussian point and the effect of the central depression is not apparent (Figure 7.4(a) right dashed line and Figure 7.4(c)).

One possible application of *caldera-like* array focusing may be in Stimulated-Emission-Depletion (STED) fluorescence microscopy [55]. In STED microscopy, an annular depletion laser spot is used in conjunction with a gaussian excitation laser spot to selectively de-excite fluorescence in the outer regions of the gaussian excitation laser spot. This enhances the contrast for fluorescence from the central region of the excitation laser spot and decreases the effective area illuminated by the excitation laser. This technique affords resolution below the diffraction limit. The *caldera-like* array can be used to focus the depletion laser light into an array of annuli to perform simultaneous super-resolution microscopy on an array of points.

Chapter 8

CONCLUSION AND OUTLOOK

At present, our Conduction TCL setup is not suitable for fabricating closely spaced structures less than 10 μm apart due to overlapping of the interstitial features that form. The largest fill factor obtained thus far is 47.0%, which is significantly smaller than the complete packing achievable by fully packed square or hexagonal arrays [21]. We expect this limit to decrease as further numerical and experimental studies are performed to determine how one may minimize the extent of these interstitial features or compensate for their formation by appropriate tuning of fabrication parameters. We anticipate that Conduction TCL with a temporally varying temperature field or sloping templating arrays may be able to achieve these effects and open a new range of topologies.

Conduction TCL thermocapillary fabrication has been shown to be a viable, single-step means of fabricating convex and concave microlens topologies by projecting a temperature field onto a polymer surface using thermal conduction from photoresist patterns. A wide range of topologies and tunable parameters are available. Several unconventional fabrication regimes are also accessible: one may use feature overlap to achieve multiscale hierarchical arrays and halt film evolution during the transitory stage to yield *caldera-like* arrays.

Part III

Laser-induced Thermocapillary Lithography

Chapter 9

ORGANIZATION OF PART III: LASER-INDUCED THERMOCAPILLARY LITHOGRAPHY

In this Part, we introduce the second form of thermocapillary lithography, which we call Laser-induced TCL. As its name suggests, this technique uses a laser to project the required temperature field for thermocapillary flow. We will motivate the development of Laser-induced TCL by first discussing the limitations of Conduction TCL in Section 10.1 and how these can be addressed by moving to a laser-induced system in Section 10.2. We then exhibit the preliminary computational and experimental proof-of-concept runs that first proved that the technique was viable in Chapter 11. Following this, we examine the main features of Laser-induced TCL in Section 12.2 and how it compares to current methods in laser patterning in Section 12.3. Next, we detail the equipment and protocol used in the technique in Chapter 13. Finally, we discuss the fabrication results in Chapter 14 and posit possible improvements for the next generation of Laser-induced TCL in Chapter 15.

Chapter 10

MOTIVATING LASER-INDUCED THERMOCAPILLARY LITHOGRAPHY

10.1 Limitations of Conduction Thermocapillary Lithography

Conduction TCL in its present stage of development faces several key challenges due to its use of physical contact in peripheral regions, limited spatiotemporal modulation of parameters, and lack of *in situ* monitoring of fabrication progress. Firstly, in order to maintain ultrahigh thermal gradients across a micron-scale gap, the existing Conduction TCL setup uses tall photoresist spacer elements that make contact with the nanofilm below and the patterned surface above. This physical contact limits the usable lifetime of each patterned stage due to accumulated deformation or contamination due to dust on the stage surface. Furthermore, even though the spacers make physical contact far away from the pattern of interest so as to make the Conduction TCL process non-contact for most practical purposes, the presence of any physical contact at all makes it difficult for one to automate Conduction TCL. Much care had to be taken to slowly remove the upper sapphire window upon completion of fabrication so as to minimize the risk of tearing the nanofilm from the spacer contacts.

Secondly, Conduction TCL is not ideal for the spatiotemporal modulation of fabrication parameters. Spatiotemporal control over thermocapillary fabrication is essential because it will lead to fine control over fabricated surface topologies and greater pattern resolution. However, the large heat capacities of the cooling and heating systems make it difficult for fabrication temperatures to be varied on timescales shorter than several minutes, and the physical contact of the photoresist pattern stage with the nanofilm below makes relative horizontal translations exceedingly difficult.

Thirdly, it is difficult for one to view the results of the fabrication process while Conduction TCL is proceeding. Although the cooled stage above the nanofilm is transparent so that the nanofilm can be viewed from above through a hole in the cooler stage (as was done previously in {LIS^{2}T} by McLeod *et al.* [13]) , the presence of the photoresist elements on the underside of the stage distorts the transmitted image of the nanofilm below. The experimenter can only accurately monitor fabrication progress outside the regions obstructed by the photoresist edges.

Furthermore, placing the sapphire window beneath a hole in the cooled stage results in non-uniform thermal contact of the window with the stage itself and leads to non-uniformities in the pattern temperature. These temperature non-uniformities in turn translate into non-uniform features in the fabricated array. In addition, *in situ* white light interferometry of the nanofilm (in order to perform height measurements) is exceedingly difficult to perform due to the presence of the nonuniform transparent stage located above the nanofilm, which cannot be easily compensated for through programmatic means.

Finally, it is difficult to scale Conduction TCL up for industrial production. The reproducibility of Conduction TCL hinges on one's ability to maintain perfect parallelism between the heated and cooled stages during fabrication. Slight tilts can lead to lateral fluid flow and hence inhomogeneities in the fabricated patterns. It is generally difficult to maintain perfect parallelism between the stages over large spatial scales due to the natural warping of stage material under its own weight and due to the inherent curvature of the surface.

10.2 Benefits of laser heating

Projecting a temperature field onto a target surface using a laser instead of relying on air conduction from photoresist patterns allows for a truly non-contact means of thermocapillary fabrication, fine spatiotemporal modulation of the projected temperature field, and the possibility of monitoring the fabrication results in real time.

Firstly, lasers are the natural means of projecting thermal influences over macroscopic distances. Unlike the photoresist patterns used in Conduction TCL, the laser beam profile can be shaped by optical elements placed away from the target surface. This distance affords true non-contact thermocapillary patterning of the sample surface; no part of the exposed sample surface needs to come into contact with a physical surface. This allows for rapid loading and unloading of samples with virtually no risk of film disruption, making the laser-induced system more favorable for large-scale high-throughput industrial fabrication.

Secondly, the possibility of performing laser beam shaping away from the target sample provides fine and rapid spatiotemporal control of the projected temperature field. For instance, the laser beam position can be shifted as a whole using a scanning mirror, the laser power can be modulated by adjusting the power source output, and the spatial pattern of the laser can be changed rapidly by placing a phase modulator

or photomask in the beam's path. These changes can be made over a timescale of seconds, which is two orders of magnitude more rapid than that which can be achieved by Conduction TCL. In fact, this flexibility can be exploited to pattern multiple different structures onto a single surface by swapping laser patterns in the middle of fabrication.

Thirdly, the single-wavelength nature of laser-induced patterning opens the possibility of monitoring fabrication in real time. This can be accomplished by use of dichroic beamsplitters, which have well-defined wavelength ranges of high reflectivity (and hence low transmission) and low reflectivity (and hence high transmission). One may then monitor the sample surface using a different wavelength (lying within the low-reflectivity high-transmission region of the beamsplitter) by looking towards the sample surface through the beamsplitter. In fact, it may even be possible to perform scanning white light interferometry (also known as coherent scanning microscopy) [56] by viewing the transmitted (i.e., non-laser) light through a Mirau microscope objective mounted on a piezo-electric stage, as described de Groot *et al.* [57].

Finally, the laser system is highly scalable. Given a laser with sufficient power and beam homogeneity, the patterned area can be made arbitrarily large. Furthermore, one may increase the rate of fabrication by increasing the laser power and sample temperature.

Chapter 11

DEMONSTRATING THE VIABILITY OF A LASER-INDUCED SYSTEM

11.1 Overview

The main point of concern for a laser-induced patterning system was that of the required laser power. Previous studies of laser-induced patterning through dewetting or rupture [58–62] have used high powered lasers (>3 W continuous wave power) focused to single spots. These extreme conditions heated the target sample surface to an excess of several hundred degrees Celsius, ablating the sample surface in some cases, to achieve the desired pattern. Instead of performing point-wise patterning, as was commonly proposed in literature, we sought to perform fabrication over a large area simultaneously, thereby achieving a scalable means of thermocapillary fabrication. We realized that we could greatly reduce the power required for laser-induced patterning by using the laser beam to induce thermal gradients and not heat the surface as a whole. That is, we sought to heat the sample surface uniformly using an external non-laser means, such as through placing the target sample on a uniformly-heated hotplate. This brings the target surface to a temperature closer to (or just exceeding) the glass transition temperature of the polymeric surface. The laser light field just needs to exhibit spatial variations in intensity so that sample regions are heated differentially, thereby establishing temperature gradients that induce thermocapillary flow. We hence do not use laser heating to heat the sample from room temperature, but to establish surface temperature gradients. In principle, this should reduce the laser power required and allow us to perform large-scale patterning without the need to scan the laser spot around. However, as this had not been attempted before to our knowledge, we sought to prove that this technique would work on the small scale before scaling up to a complete setup.

This chapter is split into two major sections. First, we examine the finite element simulations performed to solve for the steady-state heat distribution of a target sample under laser irradiation. The surprisingly favorable results from the finite element simulations were corroborated by the experimental results from a proof-of-concept setup incorporating a low-powered 30 mW laser. The experimental setup and results are described in the second section. The combined computational and experimental

results proved that laser-induced TCL was not only feasible, but could achieve lateral thermal gradients orders of magnitude larger than that achieved through Conduction TCL, and hence would be able to access a large area of parameter space inaccessible to Conduction TCL.

11.2 Computational simulation of laser heating

We implemented a simple model of laser heating in a steady-state finite element simulation within COMSOL 4.3a using the Heat Transfer in Solids package in a 2D geometry. The model was designed to simulate the steady-state temperature profile of laser focusing through a single microlens of diameter D_{lens} (which was part of a microlens array of period P) onto a polystyrene film (of thickness t_{PS}) over a thick silicon wafer (of thickness t_{Si}). The constituent elements were rectangular mapped elements. The base of the silicon wafer was held at a fixed temperature T_H, representing the effect of an external heat source (such as a hotplate) holding the system at a uniform temperature from the bottom. The T_H in this system is distinct from the T_H in the theoretical geometry from Part I in that the T_H here refers to a controllable temperature — the set temperature of the hotplate below the silicon substrate. The domain was P wide with periodically repeated boundary conditions along the leftmost and rightmost boundaries to simulate the effect of a large periodic array of lenses. The uppermost boundary condition (top surface of the nanofilm) was set to be convectively cooled with a heat transfer coefficient h_T towards an external ambient temperature T_{amb}. The laser was assumed to be incident in the downward direction at the central horizontal position at the top of the nanofilm. Since the extinction coefficient of visible light in polystyrene is three orders of magnitude smaller than that of silicon (since polystyrene is transparent in the visible), and the polystyrene layer is much thinner than the silicon layer ($\sim$ 300 nm as compared to 279 μm), virtually all the laser power absorption occurs within the silicon layer. For instance, the extinction coefficient of Silicon with 620 nm light is 0.022 [16], while that of polystyrene is estimated to be smaller than 10^{-5} at that wavelength [63], a difference of three orders of magnitude. The polystyrene nanofilm layer above the silicon wafer is heated by conduction from the silicon. We hence modeled the laser power input as a volumetric heat source within the silicon wafer which exponentially decayed into the silicon with extinction coefficient α_{Si}. The beam was assumed to be Gaussian with one spatial standard deviation equal to the beam waist diameter w after focusing through a lens of focal length f. The beam waist diameter was calculated using Self's Gaussian beam propagation formulae

[64], which also took the collimated beam divergence into account.

Two parameter sets were examined in this finite element simulation, corresponding to two different commercial microlens arrays used. The first set (known as Parameter Set 1) incorporated the geometric parameters of the plano-convex parabolic microlens array MLA300-14AR-M from Thorlabs. The second set (known as Parameter Set 2) incorporated the geometric parameters from another plano-convex spherical microlens array, MLA150-5C-M, also from Thorlabs. Both parameter sets assumed that the incident laser was centered at 532 nm, had a total power of 1.5 W, and emerged from a Thorlabs fixed focus collimation package (F240FC-532). The effective power absorbed per lens Pow_{lens} was computed by taking the average power per area of the outgoing laser beam multiplied by the lens area, accounting for losses due to reflection at transmitted interfaces (using the normal incident Fresnel equations) and finally calculating the transmitted power for laser light incident on the polystyrene-on-silicon sample using Fresnel transfer matrices. Table 11.1 lists the geometric and material parameters used for both parameter sets in the simulation.

Table 11.1: List of independent parameter values used in the finite element simulation of the steady-state temperature profile of a polystyrene-on-silicon sample under laser irradiation through a single microlens.

Parameter	Value for Parameter Set 1	Value for Parameter Set 2	Reference
MLA used	MLA300-14AR-M	MLA150-5C-M	-
f	18.6 mm	5.2 mm	-
P	300 μm	150 μm	-
t_{PS}	80 nm	80 nm	-
t_{Si}	279 μm	279 μm	-
T_H	100°C	100°C	-
α_{Si}	7.85×10^3 cm^{-1}	7.85×10^3 cm^{-1}	[65]
Pow_{lens}	56.7 mW	0.64 mW	-
T_{amb}	23°C	23°C	-
h_T	1.5 Wm^{-2}K^{-1}	1.5 Wm^{-2}K^{-1}	-
w	9 μm	1 μm	-

The steady state temperature profiles are exhibited in Figure 11.1. In addition to the full 2D plots ((a) and (d)), we exhibit the 1D temperature profiles along the vertical direction at the leftmost boundaries ((b) and (e)) and along the top of the nanofilm ((c) and (f)). The vertical temperature profiles exhibit a linear increase from the base of the silicon wafer (where the fixed temperature hotplate boundary is located) to the top of the wafer, with the exception of a small region on the order of 30 μm thick, where the rate of increase tapers off. Along the upper surface of the

nanofilm, the temperature profile is highly spiked, with the maximum temperature reaching 120°C above the hotplate temperature in Parameter Set 1 and reaching 20°C above the hotplate temperature in Parameter Set 2. The latter results (especially in Parameter Set 2, with $Pow_{\text{lens}} = 0.64$ mW) were not expected since the associated power per lens was small as compared to conventional laser pointers, which achieve a maximum output power of 5 mW and cannot be felt on bare skin.

The sharply peaked temperature profile of the horizontal plots (Figure 11.1) admits a very large horizontal (lateral) thermal gradient. The maximum temperature gradient along the horizontal interface was calculated to be 2.9×10^6 Km^{-1} for Parameter Set 1 and 1.2×10^6 Km^{-1} for Parameter Set 2. These gradients are extremely large; in finite element constructions of Conduction TCL using the model described in Fiedler and Troian [20], the maximum horizontal thermal gradient in a deformed interface was on the order of 300 Km^{-1}. Since the lateral thermal gradient sets up corresponding lateral surface tension gradients, we expected that the laser-induced model used would be able to induce thermocapillary flow at the rate of Conduction TCL or better.

The model was constructed to give the best possible focusing conditions given the equipment and material constraints and hence was certainly an overly optimistic estimate of the actual laser heating parameters. However, the extreme conditions observed in the simulation indicate that these focusing constraints can be relaxed and still yield large lateral gradients to achieve thermocapillary microfabrication. Specifically, the model predicted that even a low-powered laser with a total output power on the order of 10 mW, focused through a microlens array (so that each lens would only be focusing a small fraction of the total output power), would be able to deform a polystyrene surface into an array of laser-heated depressions. Since surface tension decreases with temperature, the laser-heated polystyrene surface would experience a locally weaker surface tension, allowing the peripheral regions to pull material away from that spot and thereby forming an ultrasmooth depression. This hypothesis was tested in the proof-of-concept experiment described in the next Section, 11.3.

11.3 Proof-of-concept experiment

The proof-of-concept experiment was set up to test the result from finite element simulations that even a low-powered laser would be able to induce thermocapillary flow and deform a heated polystyrene surface. The setup for this experiment is

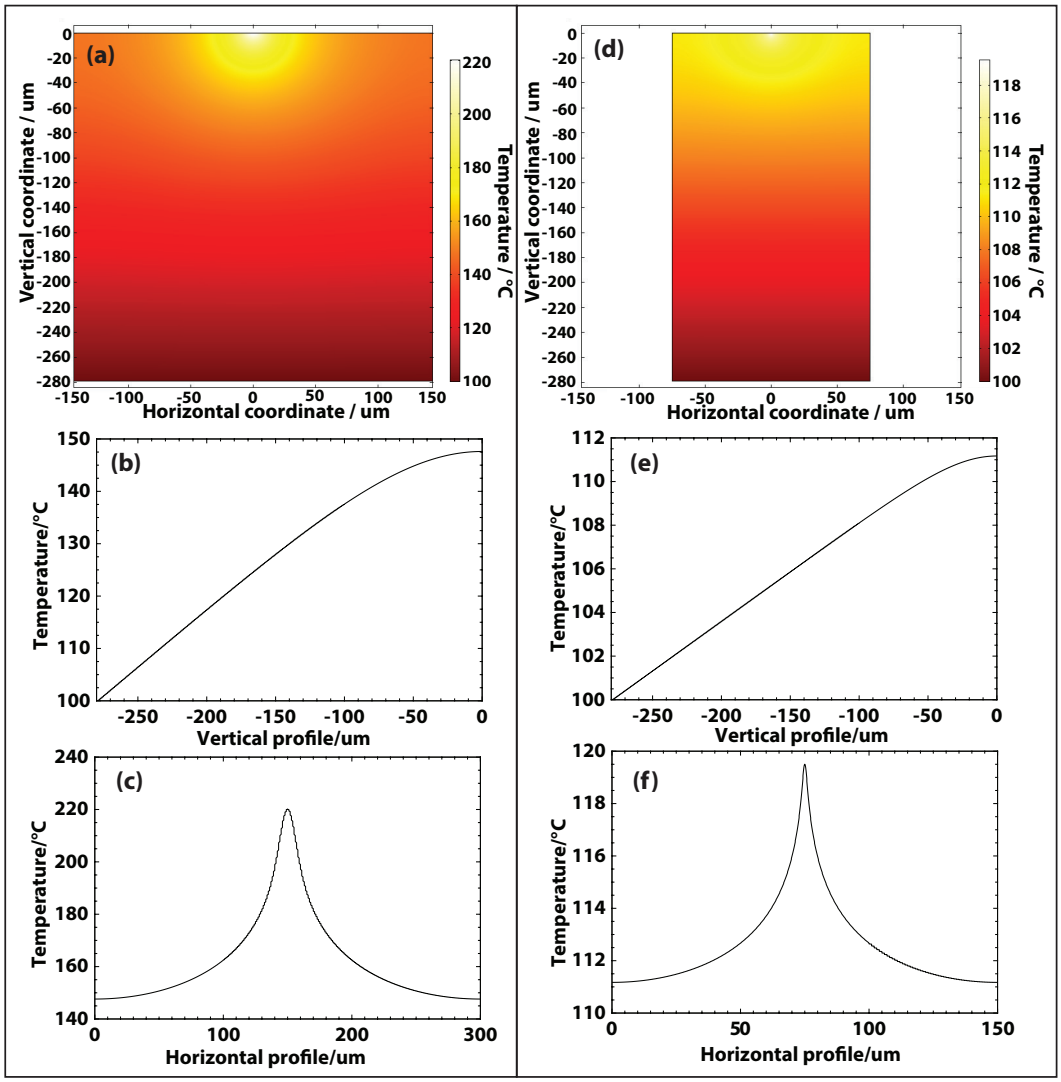

Figure 11.1: Steady-state temperature profiles from finite element simulation of laser heating model. The left column contains plots using a power per lens of 56.7 mW and a lens pitch of 300 μm (also known as Parameter Set 1), and the right column contains plots from a power per lens of 0.64 mW and a lens pitch of 150 μm (also known as Parameter Set 2). Note that the polystyrene nanofilm at the top of the domain is not visible since it is much thinner than the silicon wafer. (a) and (d) are the 2D cross-sectional heatmaps for the entire domain in Parameter Sets 1 and 2 respectively. (b) and (e) are the temperature profiles along the vertical direction at the leftmost boundary. The zero vertical position is at the top of the nanofilm, and the position at $y = -279$ μm is the hotplate position (held at 100°C). (c) and (f) are the temperature profiles along the horizontal direction at the top of the nanofilm. The laser spot is incident at the center of the horizontal profile.

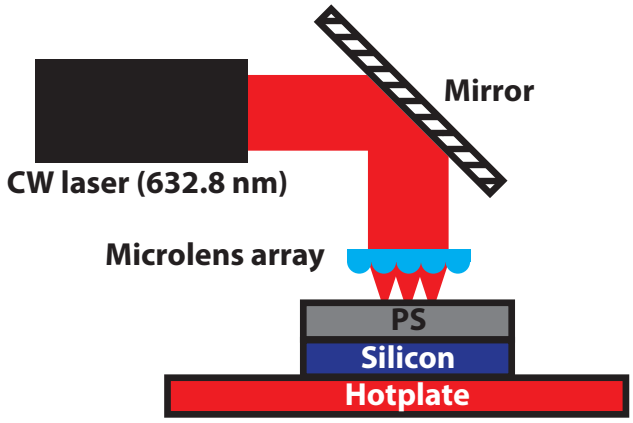

Figure 11.2: Proof of concept experimental setup. A Helium-Neon laser is focused through a microlens array onto polystyrene-on-silicon surface heated from below using a digital hotplate.

exhibited in Figure 11.2. A horizontal 30 mW Helium-Neon laser (λ = 632.8 nm, Melles-Griot 25-LHP-991, $1/e^2$ diameter 0.65 mm) was reflected by 90° using a metallic mirror to be incident normally on a digital hotplate (Dataplate PMC 720 Series Hotplate). The metallic mirror was adjusted by replacing the target polystyrene-on-silicon sample with another metallic mirror before fabrication, and adjusting the first mirror so that the laser beam was incident normally onto the second metallic mirror and retraced its path subsequently. The vertical laser beam was focused using a microlens array (Thorlabs MLA150-5C-M, f = 5.2 mm, P = 150 μm, convex side down). The microlens array was secured at a height equal to the focal length of the microlenses by use of two metallic washers to act as spacer elements between the microlens array mount and the hotplate surface.

A polystyrene-on-silicon sample (the coating protocol for sample preparation is detailed later in Section 13.2) was placed polystyrene-side-up on the digital hotplate while the hotplate was still at room temperature. The thickness of the polystyrene layer t_{PS} we chosen to minimize reflectivity at the Helium-Neon wavelength. In normal incidence thin film interference, the first interference minimum is expected to occur at a film thickness of $\lambda/4n$, where λ is equal to the wavelength of the incident light in vacuum and n is the refractive index of the thin film. We hence calibrated the spin-coating parameters to achieve this thickness, which was around 100 nm for λ = 632.8 nm Helium-Neon laser light. The Helium-Neon laser was switched on at the same time as the hotplate. After a fixed length of time, the hotplate was switched off. The laser was kept on during the time where the hotplate was cooling

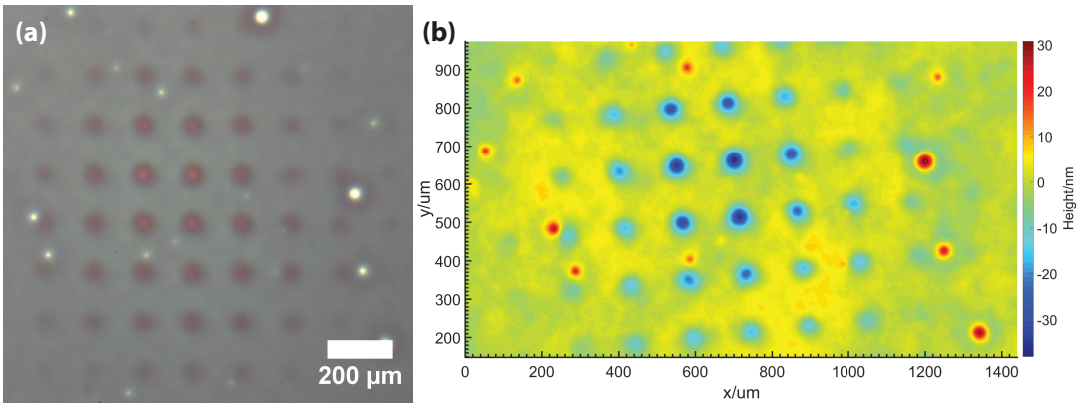

Figure 11.3: Sample L0014, fabricated in the proof-of-concept laser-induced experimental setup. (a) Light microscope image and (b) Scanning white light interferometry profile.

back to room temperature. This step prevented the sample from relaxing back to a flat film during the cooling-down process. The sample was removed once the hotplate readout temperature dropped below 60°C. The entire fabrication process was performed outside of a cleanroom in a conventional laboratory setting.

Two samples (called L0014 and L0015) were prepared using this experimental setup. Table 11.2 lists the fabrication parameters for each experiment.

Table 11.2: List of experimental parameters used to fabricate the laser-induced proof-of-concept samples L0014 and L0015.

Parameter	L0014 value	L0015 value
t_{Si}	279 ± 25 μm	279 ± 25 μm
t_{PS}	100.7 ± 0.4 nm	100.8 ± 0.4 nm
T_H	120°C	140°C
Heating time	76 min	110 min
Laser irradiation time	139 min	187 min

In accordance with the computational predictions, L0014 and L0015 exhibited deformations (Figures 11.3 and 11.4) with the periodicity of the focusing microlens array (P = 150 μm). The polystyrene film was imaged using light microscopy (Figures 11.3(a) and 11.4(a)) and using scanning white light interferometry to obtain the relative height profiles (Figures 11.3(b) and 11.4(b)). The resultant films exhibited a large number of dewetting defects, which show up as white spots in the light microscope images and either as sharp protrusions or depressions in the scanning white light interferometry images. The defects show up as sharp protrusions if

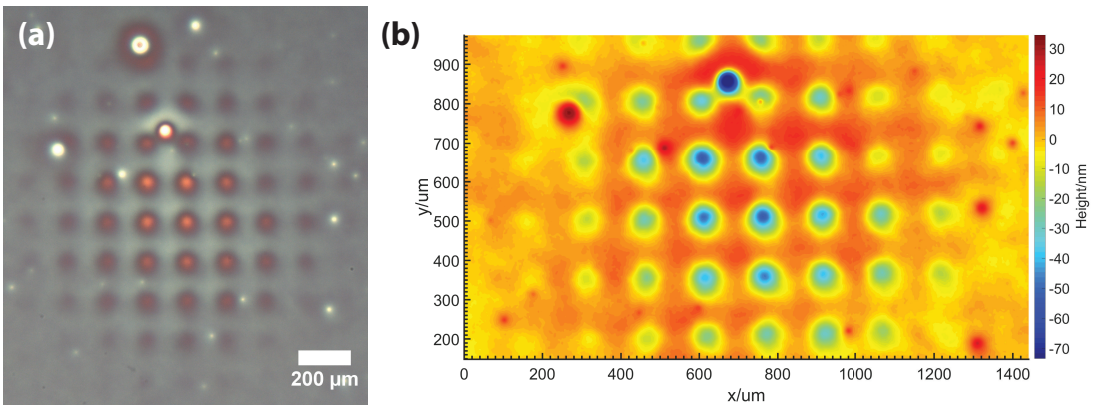

Figure 11.4: Sample L0015, fabricated in the proof-of-concept laser-induced experimental setup. (a) Light microscope image and (b) Scanning white light interferometry profile.

the white light interferometry system picks up the tall ring of material that forms around a dewetting defect, and show up as depressions if the defect is large enough so that the exposed silicon surface beneath the polystyrene nanofilm contributes to the interferometry signal.

In both samples, the central region of the deformation pattern exhibits deeper depressions because the laser beam intensity was stronger towards the beam axis. L0015 exhibits a wider area of deformation and deeper depressions because it was fabricated for a longer time at a higher temperature, thereby allowing thermocapillary flow to proceed to a greater extent. However, as a direct result of this extended heating process, L0015 exhibited a greater number of larger dewetting defects than did L0014. There are two primary forms of dewetting defects: those that appear spontaneously due to the nanofilm being unstable to perturbations, and those that arise due to external defects such as dust particles or film inhomogeneities. We hypothesized that we could reduce the incidence of the former spontaneous dewetting defects by holding the sample at a lower temperature (reducing the hotplate temperature setting) and increasing the incident laser power (so that the irradiated region evolves much more rapidly as compared to the rest of the nanofilm). The latter dewetting defects can be eliminated by performing fabrication in an enclosed area or in a cleanroom, and by optimizing the polymer coating process to achieve uniform films.

In conclusion, the proof-of-concept experimental setup showed that laser-induced thermocapillary deformation was feasible even with a low power laser, and that the quality of the resultant features might be further improved by using a higher-powered

laser beam and a lower hotplate temperature. A lower hotplate temperature ensures that minimal film evolution takes place outside of the laser-irradiated area, while slowing down the fabrication process so that a greater degree of reproducibility and accuracy can be achieved. Taken in context, these results indicated that even a handheld presenter laser pointer (with beam powers < 5 mW) can achieve deformations in this laser-induced fabrication process. The laser beam just needs to set up temperature gradients to induce thermocapillary flow; it does not need to melt the target surface as this role is performed by an external hotplate.

Chapter 12

DESIGN OF LASER-INDUCED THERMOCAPILLARY LITHOGRAPHY

12.1 Overview

In view of the positive results from the proof-of-concept experiment, we designed and implemented a laser-induced thermocapillary fabrication setup that would be able to project arbitrary temperature fields onto a target surface and modulate these temperature fields spatiotemporally at a position away from the target surface. In this chapter, we discuss the key features of this system, which we call Laser-induced TCL. We then examine published techniques of laser-induced patterning, and discuss the implications of the differences between Laser-induced TCL and these techniques.

12.2 Design choices in Laser-induced Thermocapillary Lithography

Fiber-coupled diode laser for flexibility

We chose a $\lambda = 532$ nm fiber-coupled diode laser for flexibility in positioning the laser source. The laser used was a Civillaser LSR532H-FC-1.5W, which had a maximum listed continuous wave output power of 1500 mW and a continuously adjustable power supply. The system was also controllable using a TTL input, opening the possibility of controlling the laser intensity in realtime by varying the switching duty-cycle into the TTL input.

Spatial modulation using photomask

We chose to modulate the laser beam by transmission through a pre-fabricated chrome-on-quartz photomask. By choosing the transparent and opaque regions on the photomask, we effectively choose the illuminated and non-illuminated regions on the target surface. Photomasks are also easily obtainable from commercial sources, and can be fabricated with excellent precision down to micron-scale features. We chose a robust fused quartz substrate for the photomask to minimize damage due to laser heating on the photomask itself. Laser-induced TCL does not necessarily need to be performed with a photomask for spatial modulation; numerous other alternatives exist, such as phase-shift masks and grayscale masks. However, we believe that opaque photomasks represent the simplest and most established means of controlling a light field, in view of its essential role in conventional photolithography.

Bare-board camera sensor for light field visualization

A key challenge in laser-induced TCL is verifying that the desired laser light field is actually achieved at the target surface itself. To do this, we placed a bare-board camera sensor at the location of the target surface before each fabrication run in order to capture the light field that would be incident on the target surface. This camera sensor was mounted onto a precision-machined custom holder that held it at the level of the upper surface of the target (inclusive of the silicon wafer thickness) to within 0.1 mm. This technique allowed us to tune the laser optics and focus the laser field while monitoring the actual projected intensity distribution before each run.

Future iterations of the laser-induced system may incorporate onpower-stabilization by feeding the measured intensity back to a variable duty cycle switching circuit to modulate the time-averaged power output of the laser source.

Beam sampling for realtime power monitoring

The Civilaser laser setup was not power-stabilized and did not exhibit a one-to-one correspondence between the supply current and laser output power due to equipment heating effects. We hence had to actively monitor the laser power without disrupting the laser beam used for projecting the temperature field. We performed this by introducing a beam sampler in the laser beam path before incidence on the photomask. The beam sampler reflected a small fraction of the incident beam power towards a photodiode power sensor and transmitted most of the beam power. The sampled beam was modulated with a beam chopper before being captured by the photodiode power sensor and demodulated using a lock-in amplifier in order to minimize measurement noise due to ambient light.

Rapid heating and quenching of sample for reproducibility

The proof-of-concept experimental setup allowed the target sample to heat up from room temperature and slowly cool back down later while remaining on the hotplate. This was done because we wanted to minimize rapid surface heating or cooling, which might induce buckling or wrinkles on the thermosensitive polystyrene surface. Polystyrene, as with most polymers, exhibits a large thermal expansion coefficient, and this large coefficient might result in differential expansion of the polymer layer over the silicon surface (which has a smaller expansion coefficient), thereby inducing delamination or wrinkling defects.

While testing the laser-induced TCL setup, we observed that polystyrene-on-silicon

samples did not exhibit any form of wrinkling or quality degradation if the heating-up and cooling-down phases were performed rapidly. That is, a room temperature sample could be placed onto a heated plate and a heated sample could be placed onto a room temperature plate to cool rapidly without loss in fabricated feature quality. We hence removed the heating-up and cooling-down steps in favor of direct heating on a pre-heated hotplate surface. After the requisite time had elapsed, the sample was removed from the hotplate surface and placed onto a room temperature copper plate to rapidly bring the sample temperature below the glass transition temperature and thereby quench film evolution. This choice of heating protocol improved the fabrication reproducibility and greatly reduced the length of time necessary for fabrication to occur.

12.3 Comparison to prior work in laser-induced patterning

Current literature in laser-induced patterning can be broadly categorized into two major categories: techniques which rely on chemical modifications to the substrate itself and techniques which rely on physical modifications. Within the category of physical modifications, we may further identify techniques which are subtractive (e.g., ablation), additive (e.g., material deposition), and redistributive. Laser-induced TCL falls into the redistributive physical modification category since it operates by redistributing material through thermocapillary flow and involves insufficient laser intensities for ablation. In this section, we will provide an overview of the techniques in each category, but will focus primarily on the redistributive physical modification category, since these fabrication techniques are the closest in concept to Laser-induced TCL.

Laser-induced patterning by chemical modifications

Laser-induced chemical modifications can be used to change the surface tension of the target surface, thereby inducing flow along surface tension gradients from regions of weaker surface tension to regions of stronger surface tension. One such modification was observed in 1995 by two independent groups led by Kumar [66] and Natansohn [67]. They illuminated azoaromatic thin films (made of organic materials containing the N=N double bond) with laser light fields at a wavelength near the absorption maxima of these thin films. Both groups observed that the azo films spontaneously deformed to match the spatial pattern of the laser light fields. By projecting laser interference patterns with alternating light and dark fringes onto the thin film surface, the groups were able to achieve periodic surface relief

gratings. The exact mechanism behind this spontaneous deformation remained disputed until 2016, when Kim *et al.* exhibited strong evidence to indicate that the laser light induced a *cis-trans* isomerization reaction of the azo groups which in turn changed the surface tension of the azo compound. The laser light illumination thus created surface tension pattern onto the azo film surface corresponding to the laser light field pattern, which induced flow along these gradients to achieve the spontaneous deformation features observed [68]. The laser light thus induced a chemical modification of the material to induce feature formation.

Intense laser light can also be focused to small points in order to anneal and crosslink specific positions within a photosensitive block in 3D, thereby rendering these points insoluble to later development. This technique is called Focused Laser Spike Annealing (FLaSK), which was introduced by Singer *et al.* in 2011 [69]. In effect, FLaSK acts as a 3D direct writing tool, defining a structure in a point-by-point fashion. Untreated material surrounding the treated structure can then be removed by development steps later.

Laser-induced patterning by subtractive physical modifications

Laser-induced patterning is most strongly associated with the selective removal of surface material using high-powered laser systems. Indeed, the main challenge in using lasers to deterministically subtract material is the exertion of precise control over the damaged region so as to achieve the desired surface features without introducing additional structural damage in the surrounding region. Femtosecond laser fabrication is one very common technique used to achieve this degree of control. The basic idea behind femtosecond laser patterning is to use very short laser pulses (of timescales shorter than 1 ps = 10^{-12} s) with high intensities to introduce micro-scale changes to a target surface without allowing the peripheral region to heat up substantially. This technique, which appears to be first used for optical device fabrication in 1996 by Davis *et al.* [70], and for sharp relief patterns by Chichkov *et al.* also in 1996 [71], has developed very rapidly over the past two decades and has found extensive applications in micromachining 2D and 3D nanostructures, optical components, sensors (see Correa *et al.* for an extensive survey of the techniques and manufacturing capabilities of femtosecond lasers [72]) and has even been rendered safe for use in the human eye to perform surgery in procedures such as LASIK (Laser-Assisted *in situ* Keratomileusis) [73, 74].

Laser-induced patterning by additive physical modifications

Lasers play an essential role in additive manufacturing, where a desired part or device is built up progressively from an unordered stream of material. The high intensities achievable through laser heating have made it feasible to perform additive manufacturing with metals. This is known as Laser Additive Manufacturing (LAM). In LAM, a high-intensity laser is used to melt a metallic powder at specific locations so as to achieve a contiguous metallic structure. The two main LAM techniques involve either melting a continuous stream of metallic powder using a guided nozzle (called Laser Metal Deposition), or selectively melting regions in a bed of metallic powder (called Selective Laser Melting). In both cases, the structure is built up layer-by-layer to create full 3D components [75, 76].

Laser-induced patterning by redistributive physical modifications

Fabrication techniques drawing upon laser sources to induce redistribution of material generally rely on establishing surface tension gradients as a result of differential surface heating under laser irradiation. The surface may be deformed transiently (only deformed while the laser heating is proceeding and relaxing back to a flat surface subsequently) [77–79] or fixed in position after deformation (usually through cooling) [60, 80]. The surface can also be deformed until the film layer breaks and dewets from the substrate beneath [59, 62, 81, 82]. These techniques share one thing in common: the laser fabrication is performed one spot at a time. That is, it is necessary to focus all the laser energy into a single spot to achieve the high temperatures necessary to melt the sample and induce large surface tension gradients.

Laser-induced TCL differs significantly from laser heating for solid surface deformation or dewetting purposes in that it does not use the laser to heat the surface beyond the glass transition or melting temperatures to allow flow to occur. Instead, the bulk heating is performed by a resistive heating element that heats the entire nanofilm and its substrate from below. The laser is only responsible for the creation of temperature gradients along the air-film interface; the raising of the sample temperature is performed by the hotplate element beneath the sample. This greatly reduces the laser output power needed, and allows fabrication to proceed on a much larger lateral scale since the laser beam (or multiple laser beams) can be expanded and spatially modulated to pattern a large-area surface.

Chapter 13

MATERIALS AND METHODS

13.1 Overview

In this chapter, we detail the materials and protocols used in Laser-induced TCL. The chapter begins with a description of the coating protocol used to obtain the polystyrene-on-silicon samples used as target surfaces in the fabrication process in Section 13.2. We then turn to the two iterations of experimental setups developed. The first iteration, called Experimental Setup Alpha (Sections 13.3 and 13.4), operated in a geometry similar to that of photomask lithography: the photomask was placed immediately above the target surface to produce the required temperature field beneath the photomask. In the later iteration, called Experimental Setup Beta (Sections 13.5 and 13.6), I improved upon the shortcomings of Experimental Setup Alpha to develop a setup that projected a sharp image of the photomask pattern onto the target surface from a greater distance.

13.2 Polystyrene-on-silicon Sample preparation

The experimental samples were polystyrene spin-coated onto silicon wafers. Narrow distribution polystyrene (M_w = 1100 g/mol, M_n = 990 g/mol from Scientific Polymer Products, Inc.) was dissolved in toluene and spin-coated onto silicon wafers (diameter 50.8 mm, $\langle 100 \rangle$, thickness 279 ± 25 μm, Boron doped, from Silicon Materials Inc.). The clean silicon wafer was rinsed in dry nitrogen immediately before spin-coating to remove any dust particles. The fresh toluene was filtered through a 20 nm pore-sized membrane (Anodisc 13, Whatman) before being used to dissolve the polystyrene, and the polystyrene solution was filtered a second time through another Anodisc 13 membrane onto the silicon wafer surface for spin-coating.

The polystyrene film thickness was measured using an ellipsometer (Rudolph Auto EL III) operating at a wavelength 632.8 nm. The thicknesses were also measured using a source wavelength of 546.1 nm to break the ambiguity in measured film thicknesses. The refractive index of the polystyrene used was 1.5800 ± 0.0005 at 632.8 nm. The film thicknesses were measured in a 3×3 grid of points centered on the wafer and were averaged to obtain an estimate of the overall film thickness with uncertainty.

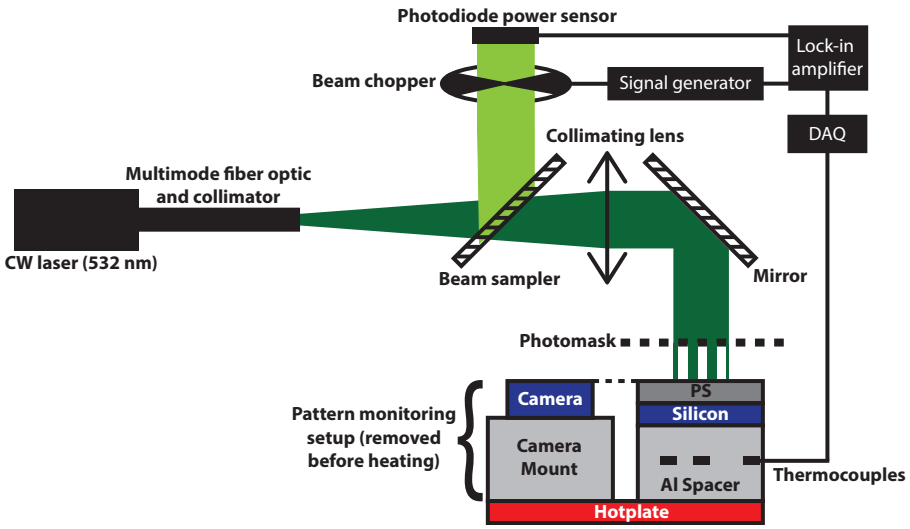

Figure 13.1: Experimental Setup Alpha fabrication setup.

13.3 Experimental Setup Alpha: Fabrication Setup

Experimental Setup Alpha was the first iteration in the laser-induced TCL setup that incorporated a moderately high power (1500 mW) laser. The setup is sketched in Figure 13.1. The output fiber from a fiber coupled laser (Civillaser LSR532H-FC-1.5W, λ = 532 ± 1 nm, 1500 mW maximum output power, fiber core diameter 400 μm, FC/PC interface, powered by an LSR-PS-FA variable power supply) was coupled to a step-index multimode fiber patch cable (Thorlabs M74L05, core diameter 400 μm, NA = 0.39) through an FC/APC fiber optic mating sleeve (Thorlabs ADAFC3). The output from the fiber patch cable was collimated using a fixed fiber collimation package (Thorlabs F240FC-532, f = 7.86 mm, NA = 0.51) mounted on a kinematic pitch/yaw adapter (Thorlabs KAD12NT).

The collimated laser output was split through non-normal incidence on a beam sampler (Thorlabs BSF10-A) mounted on a pivoting optic mount (Thorlabs CP360R) into a stronger transmitted beam and a weaker reflected beam. The reflected beam was used to monitor the beam power in real-time during the fabrication. The reflected beam was focused through a plano-convex lens (Thorlabs LA1433-A, f = 150 mm) and attenuated through a neutral density filter (ND1.3, Thorlabs NE13B). The absorptive neutral density filter was used to minimize heating effects and damage to the sensing elements at high beam powers. The attenuated beam was chopped at 1000 RPM with a beam chopper (50% duty cycle, EG&G Instruments Model 651 Light chopper powered by an EG&G Instruments Model 650 Light Chopper Controller) and incident on a switchable gain photodiode (Thorlabs PDA100A). The modulated

photodiode voltage output was demodulated using a lock-in amplifier (Thorlabs LIA100) synchronized with the beam chopper controller. The demodulated voltage output was monitored and recorded with a data acquisition module (Data Translation DT9805 controlled by QuickDAQ 3.7.0.40 software). The photodiode, light chopper controller, and data acquisition module were connected by 50 Ω-terminated BNC cables.

The powers of the main transmitted and reflected beams were measured using the switchable gain photodiode at five different laser intensities to obtain the multiplicative coefficient relating the beam powers. The photodiode voltage output (after demodulation through the lock-in amplifier) was recorded using a HP34401 multimeter connected through a 50 Ω impedance BNC cable. The voltage offset from the lock-in amplifier was adjusted to yield zero output voltage when the photodiode sensor was covered. To reduce the effect of laser heating on the sensor, the photodiode sensor was exposed to the laser beam for around one second, after which a single measurement of the photodiode voltage was taken using the multimeter. The photodiode was then blocked with a laser beam block (Thorlabs LB1) and allowed to cool for one minute before the next reading was taken. The ratio of the reflected beam power and the transmitted beam power was $(9.4 \pm 0.3) \times 10^{-3}$ where the error is one standard deviation. This calibration ratio was used to calculate the transmitted beam power based on power measurements performed on the reflected beam.

The main transmitted beam was focused and collimated a second time through a converging plano-convex lens (Thorlabs LA1979-A, f = 200 mm) and reflected by 90° on a metallic mirror to be incident normally onto an aluminum sample holder mounted on a digital hotplate surface (Dataplate PMC 720 Series Hotplate).

The aluminum sample holder was a cylindrical block of solid aluminum (diameter = 4", thickness = 25.0 ± 0.1 mm) with three 1/8" diameter holes drilled into the curved face (12.7 mm below the upper face) with varying depths (equal to one radius, half a radius, and one-quarter of a radius). The lower face of the sample holder was placed onto the digital hotplate surface. Thermocouples (J-type Omega 5TC-TT-J-40-36) were inserted into the holes and were held in place with thermal paste (Aremco Heat-Away 638) injected into the base of each hole. The thermocouples were used to monitor the temperature at the various radial distances of the sample holder and were monitored using a data acquisition module (Data Translation DT9805). For Experimental Setup Alpha, only two thermocouples (placed at the central position and at the half-radius point) were used.

The downward-oriented main beam was modulated before reaching the aluminum sample holder by either a patterned photomask ($3'' \times 3'' \times 0.060''$ chrome-on-quartz mask fabricated by HTA Photomask) mounted horizontally (right reading down, chrome face underneath) on a rectangular optic mount (Thorlabs XYFM1), or a converging microlens array (Thorlabs MLA300-14AR-M, f = 18.6 mm, pitch = 300 μm, mounted with the convex side down) mounted horizontally on a threaded kinematic mount. The leveling of these elements with respect to the horizontal was verified using a liquid level.

The spatially modulated main beam pattern was visualized by placing a camera sensor at the position of the sample. A bare-board camera (Basler dart daA2500-14um, pixel size 2.2 μm $\times$ 2.2 μm, sensor size 5.70 mm $\times$ 4.28 mm, controlled by Basler's pylon software) was mounted onto a custom precision-machined camera holder (height = 17.4 $\pm$ 0.1 mm; design drawing is included in Appendix B) with steel standoffs (Wurth Electronics 9774060243R, 6 mm height). The camera holder height was chosen so that the mounted camera sensor would be at the same height as a silicon wafer placed onto the surface of the aluminum sample holder. Before each fabrication run, the laser was attenuated with a neutral density filter (ND2.0, Thorlabs NE20B) to protect the camera sensor, and the aluminum sample holder on the hotplate was replaced with the mounted camera sensor. This allowed the experimenter to monitor and capture the incident laser light field in real time while performing adjustments to the focusing optics. The exposure time of the sensor was adjusted so that the captured pixels were not saturated.

The entire fabrication setup was mounted on an optical table, enclosed with laser safety screens (Thorlabs TPS6) from the sides, and covered with a laser safety curtain from above. The laser safety curtain was fastened to the sides of the laser safety screens using velcro during fabrication to prevent laser light from escaping.

The laser was aligned by placing a mirror on the surface of the aluminum sample holder to reflect the downward beam back towards the fiber optic collimator. The tip/tilt of the metallic mirror mount and the position of the Thorlabs LA1433-A plano-convex lens were adjusted so that the reflected beam retraced the path taken by the incoming beam. This process ensured that the downward beam was normally incident onto the aluminum sample holder surface.

13.4 Experimental Setup Alpha: Experimental Protocol

The equipment-specific instructions to perform fabrication using Experimental Setup Alpha are listed in Appendix G. The first step in the fabrication was to capture an image of the laser light field used to irradiate the sample surface. The laser power supply was turned to 1.5 A, a low current that produces a weak visible laser spot. The laser beam was further attenuated with an ND2.0 neutral density filter placed between the fiber collimator and the beam sampler. The laser beam diameter on the sample holder was measured using vernier calipers, following which the sample holder block on the digital hotplate was then removed and replaced with the mounted Basler dart camera and chrome mask or the microlens array was mounted above the camera sensor. The chrome mask and microlens array were leveled by use of a liquid level. The height of these elements above the sample holder surface was also measured using vernier calipers. The camera sensor was placed at the center of the laser spot passing through the chrome mask or microlens array and the exposure time was adjusted so that the brightest pixels were just below the saturation threshold. The camera image was saved as an uncompressed TIFF file.

Next, the sample holder block was replaced on the hotplate surface and the hotplate was set to the desired temperature (ranging from 80°C to 140°C). The system was allowed to heat up until the thermocouple temperatures stabilized. This stable temperature was usually 3°C below the target hotplate temperature. The polystyrene-on-silicon sample was then flushed with dry nitrogen and placed onto the heated sample holder. The setup was then covered from above with an opaque laser curtain. The recording of the lock-in amplifier output voltage and thermocouple voltages was started once the laser curtain was securely fastened around the experimental setup with velcro. The laser supply current was then ramped up to the target current, and this time point represented the start of the fabrication time.

After a pre-determined length of time, the laser supply current was ramped down to zero and the laser was switched off. This time represented the end of the fabrication time. The polystyrene-on-silicon sample was removed from the sample holder and immediately placed onto a copper plate at room temperature. This process rapidly cooled the sample down and let the surface features solidify in place.

The fabricated structures were imaged using scanning white light interferometry (Zemetrics Zegage, calibrated using an 88 nm VLSI SHS-880 QC step height standard) to obtain a 2D relative height profile.

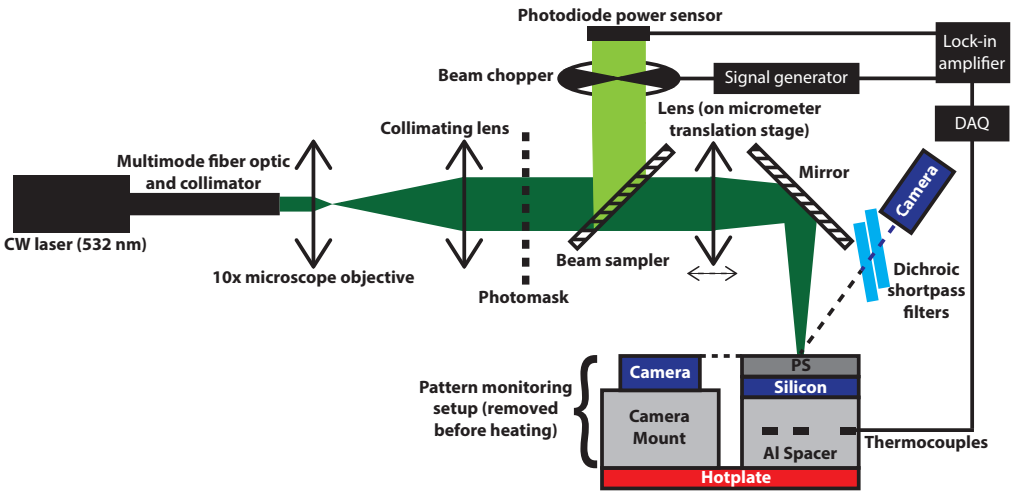

Figure 13.2: Experimental Setup Beta fabrication setup

The relative height profiles obtained from scanning white light interferometry were imported into Zygocruncher (Section 6.7) for analysis. Features with circular features (both depressions and protrusions) were processed quantitatively using the same protocol as in the microlens array analysis of Conduction TCL (Appendix F).

The surface temperature of the polystyrene during fabrication was estimated in post-processing by assuming that there was a linear drop in temperature from the hotplate surface through to the middle (in the vertical dimension) of the sample holder (where the thermocouple leads were placed) to the top of the sample holder, upon which the silicon wafer was placed. The polystyrene temperature was hence estimated as:

$$T_{\text{film}} = T_{\text{thermocouple}} - \left(T_{\text{hotplate}} - T_{\text{thermocouple}}\right) \tag{13.1}$$

13.5 Experimental Setup Beta: Fabrication Setup

Experimental Setup Beta was an improved version of Experimental Setup Alpha. The experimental geometry is exhibited in Figure 13.2. The main differences between the Alpha and Beta experimental setups was in the position of the photomask and in the use of a camera to view the film deformation in real time. In the Alpha setup, the mask was placed just above the target sample surface, thus reducing the quality of the projected laser image due to diffractive effects. In the Beta setup, the mask was placed in the path of a collimated laser beam, and the beam was later focused using an additional plano-convex lens so that the real image plane coincided

with the sample surface. This preserved the quality of the projected image. The lack of any elements immediately above the polystyrene nanofilm surface allowed the film surface to be imaged using a camera. The scattered and reflected light from the high-intensity laser beam was filtered out by the use of two dichroic shortpass filters, which transmitted light with wavelengths shorter than that of the sculpting laser wavelength.

The beam path was identical to that of the Alpha setup up to the fiber collimation package. The collimated laser output was focused using a microscope objective (Newport M-20X, NA = 0.4) and then collimated again using a plano-convex lens (Thorlabs LA1805-A, f = 30 mm). An iris placed after the plano-convex lens removed the stray light from the edges of the central peak. This central peak was then incident onto a beam sampler (Thorlabs BSF10-A), which split the beam into a stronger transmitted beam and a weaker reflected beam. The reflected beam was attenuated using a neutral density filter (ND1.3, Thorlabs ND13B) and focused to a smaller spot size using a plano-convex lens (Thorlabs LA1484-A, f = 300 mm). The attenuated beam was chopped at 1000 RPM with a beam chopper (50% duty cycle, EG&G Instruments Model 651 Light chopper powered by an EG&G Instruments Model 650 Light Chopper Controller) and incident on a switchable gain photodiode (Thorlabs PDA100A). The modulated photodiode voltage output was demodulated using a lock-in amplifier (Thorlabs LIA100) synchronized with the beam chopper controller. The demodulated voltage output was monitored and recorded with a data acquisition module (Data Translation DT9805 controlled by QuickDAQ 3.7.0.40 software). The photodiode, light chopper controller, and data acquisition module were connected by 50 Ω-terminated BNC cables.

The main transmitted beam was then incident on the vertical quartz face of the same patterned chrome-on-quartz photomask used in the Alpha experimental setup. The photomask was mounted vertically on a rectangular optic mount (Thorlabs XYFM1) and two orthogonally-oriented horizontal translation stages to provide full precision 3D positioning control.

The spatially-modulated beam was then focused using a plano-convex lens (Thorlabs LA1608-A, f = 75 mm) and reflected by 90° to point downward using a laser line mirror (Thorlabs NB1-K13). The downward beam was then incident on the same custom aluminum sample holder placed on top of the digital hotplate. All three drilled holes in the aluminum sample holder (at the center, half radius, and 1/4 radius from the circumference) were filled with thermal paste (Aremco Heat-Away 638)

and each contained one thermocouple (J-type Omega 5TC-TT-J-40-36) monitored by a data acquisition module (Data Translation DT9805). The surface of the silicon wafer on top of the sample holder was set to be the image plane of the photomask pattern by adjusting the horizontal position of the photomask using the translation stages that the photomask was mounted upon, while monitoring the image plane using the bare-board camera mounted onto the same custom precision-machined camera holder as in Experimental Setup Alpha.

The powers of the main transmitted and reflected beams were measured to obtain the multiplicative coefficient relating the beam powers. Instead of using the same switchable gain photodiode to monitor the transmitted and reflected beams sequentially, as done in the Alpha experimental setup, a second factory-calibrated power meter was used in the Beta experimental setup. The switchable gain photodiode (Thorlabs PDA100A) was fixed in position to monitor the reflected beam (through the ND1.3 filter and plano-convex lens), and an energy meter sensor (Thorlabs S120C sensor with PM100D controller, attenuated with a Thorlabs NE20B ND2.0 neutral density filter) was placed after the laser line mirror to monitor the downward beam. This sensor position allowed us to account for power losses due to the imaging lens and mirror. These factors were not accounted for in Experiment setup Alpha because the sensor was placed before the mirror and the collimating lens in that setup. An additional plano-convex lens (Thorlabs LA1401-A, $f = 60$ mm) was placed above the main transmitted beam sensor to reduce the beam diameter to fit that of the sensor. The reflected and transmitted beam powers were captured simultaneously when the power meter indicated that the beam power was stable to three significant figures. These readings were recorded for the full range of laser output powers and for each of the gain settings on the switchable gain photodiode. Using the 10 dB setting on the photodiode, which was the setting used for all fabrication runs in Experimental Setup Beta, the ratio of the reflected beam power to the transmitted beam power was $(1.16 \pm 0.01) \times 10^{-2}$.

The film was imaged in real-time during laser fabrication using a camera (called the sample-viewing camera) placed at an angle of approximately 14° with respect to the sample normal. A CMOS color camera (Basler acA2500-14gc, 2590 × 1942 pixels) was coupled to a fixed focal length lens (EdmundOptics 85-868, 35.0 mm focal length, $f/1.8$-$f/16$, 12.6° field of view) and was mounted pointing at the focused laser spot on the sample holder surface. Two dichroic shortpass filters (EdmundOptics 69-202, 500 nm cut-off wavelength, 520 nm - 610 nm reflection

wavelength with > 97% unpolarized reflectance, 325 nm - 480 nm transmission wavelength) were placed between the camera and the sample surface to filter out the green laser light used to sculpt the polystyrene surface. The dichroic filters were held at an approximately 45° angle to the line connecting the focused laser spot and the camera and were mounted back-to-back with the coated side facing outwards. The laser spot was not visible through the dichroic filters as viewed by the camera even at maximum laser power. The sample holder surface was illuminated by a fluorescent table lamp.

13.6 Experimental Setup Beta: Experimental Protocol

The equipment-specific instructions to perform fabrication using Experimental Setup Beta are listed in Appendix H. The first step in the fabrication was to capture an image of the laser light field and adjust the photomask position to bring the image into focus on the sample surface. The laser power supply was turned to a current of 1.45 A (out of a maximum of 7 A) to produce a weak laser beam. The aluminum sample holder was removed from the hotplate surface and replaced with the mounted camera. The horizontal position of the photomask was then adjusted to produce a focused image of the mask pattern on the camera sensor. The exposure time of the camera was adjusted so that the brightest pixels were just below the saturation threshold, and the image was saved as an uncompressed TIFF file. For short exposure times, there were visible periodic lines in the captured image due to camera processing artifacts. When these lines were visible, multiple images in the form of an uncompressed video were captured and later averaged on a pixel-by-pixel basis using ImageJ (Stack Z-projection) [51] to remove the effect of these lines.

The camera mount was then replaced with the aluminum sample holder. The digital hotplate was switched on and allowed to heat up and stabilize at the target temperature (ranging from 110°C to 130°C). A nitrogen-rinsed polystyrene-on-silicon sample was then placed on the hotplate. Temperature logging, laser beam intensity logging and sample-viewing camera capture was started at this time. The setup was then covered with opaque laser curtain material and securely fastened around the experiment perimeter with velcro. The laser supply current was then ramped up to the target current manually. This time point represented the start of the fabrication duration.

At the end of the target fabrication time, the laser current was ramped down to zero and the data logging was stopped. The sample was removed from the sample holder

surface and immediately placed onto a copper plate to cool the sample down and halt film evolution. The fabricated sample was then imaged using scanning white light interferometry (Zemetrics Zegage).

The surface temperature of the polystyrene during fabrication was estimated in the same way as in the Alpha protocol. The polystyrene temperature was hence estimated as (assuming a linear drop in temperature from the hotplate to the polystyrene-on-silicon sample):

$$T_{\text{film}} = T_{\text{thermocouple}} - \left(T_{\text{hotplate}} - T_{\text{thermocouple}}\right) \tag{13.2}$$

The relative height profiles obtained from scanning white light interferometry were imported into Zygocruncher (Section 6.7) for analysis. Features with circular features (both depressions and protrusions) were processed quantitatively using the same protocol as in the microlens array analysis of Conduction TCL (Appendix F).

Chapter 14

RESULTS AND DISCUSSION

14.1 Correspondence between laser light field and fabricated patterns

The samples from Laser-induced TCL were indexed using the notation "L00xx", where the last two digits represent a unique numeric reference assigned to each polystyrene-on-silicon sample. Figure 14.1 exhibits several laser light fields used and the topologies resulting from these light fields. The full list of samples, their fabrication parameters, and the resultant topologies are contained in Appendix I. Laser-induced TCL was successful in achieving a wide variety of periodic and aperiodic patterns, such as arrays of depressions (Figure 14.1(b)) from a light field consisting of an array of focused laser dots from a microlens array (Figure 14.1(a)), features of varying size (Figure 14.1(d)) from a light field image of a progression of hole diameters (Figure 14.1(c)), and linear features (Figure 14.1(f)) from a light field image of lines (Figure 14.1(e)). In addition to inducing depressions through laser illumination, laser-induced TCL was capable of inducing protrusions by inducing fluid flow towards intentionally darker (and hence less-illuminated) regions. Figure 14.2 exhibits one such protrusion pattern in the shape of the word "CALTECH". Upon superimposing the dark pattern outline from the laser light field capture in Figure 14.2(a) on the light microscope image of the post-fabrication film in Figure 14.2(b), we observe that the fabricated features match very closely to the templating light field patterns. The fabricated pattern is slightly larger than the templating light field patterns, possibly due to lateral heat conduction in silicon which induces a small amount of lateral "smearing" of the effective temperature field. Improved lateral resolution may be achieved by using substrates with lower thermal conductivity.

14.2 Real-time monitoring of laser-induced deformation

A key advantage of Experimental Setup Beta over Experimental Setup Alpha is the lack of any components immediately above the target polystyrene surface. This afforded us the ability to view the nanofilm evolution in real-time by simply placing a camera above the film surface. The laser light used for thermocapillary lithography was easily filtered out by use of two dichroic shortpass filters, which reflected the green laser light (which had a wavelength $\lambda = 532$ nm, longer than the shortpass cut-off wavelength of 500 nm) scattered and reflected off the target sample and

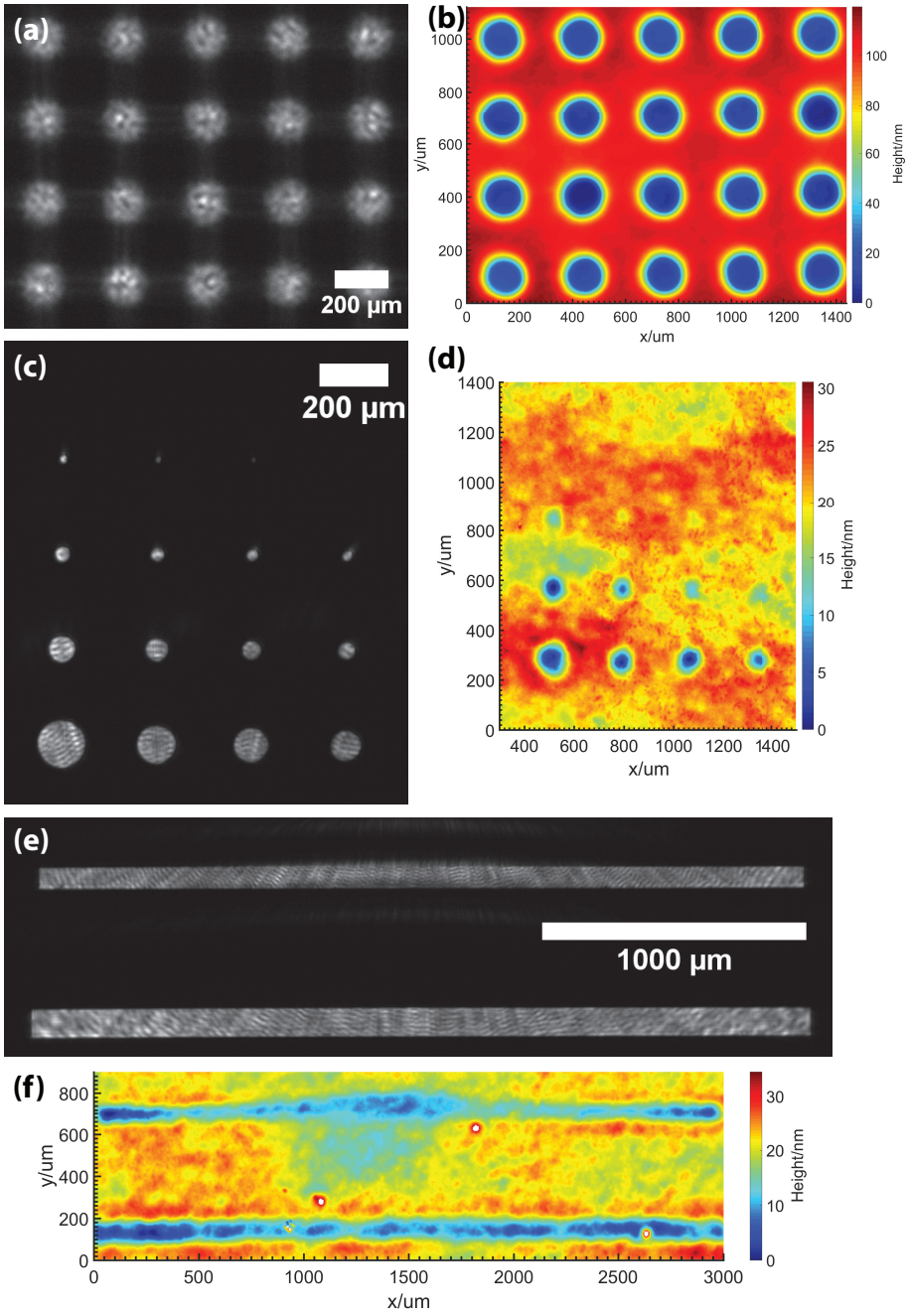

Figure 14.1: (a) Subset of sample L0037 laser light field used in fabrication, obtained by focusing a collimated laser beam through a microlens array in Experimental Setup Alpha. (b) Subset of sample L0037 post-fabrication relative height profile, imaged through scanning white light interferometry (SWLI) (c) Sample L0064 laser light field used in fabrication, obtained by imaging a photomask pattern of a progression of circular holes in Experimental Setup Beta. (d) Sample L0064 post-fabrication relative height profile, imaged through SWLI. (e) Subset of sample L0075A laser light field, obtained by imaging transparent lines in Experiment Setup Beta. (f) Subset of sample L0075A relative height profile, imaged through SWLI.

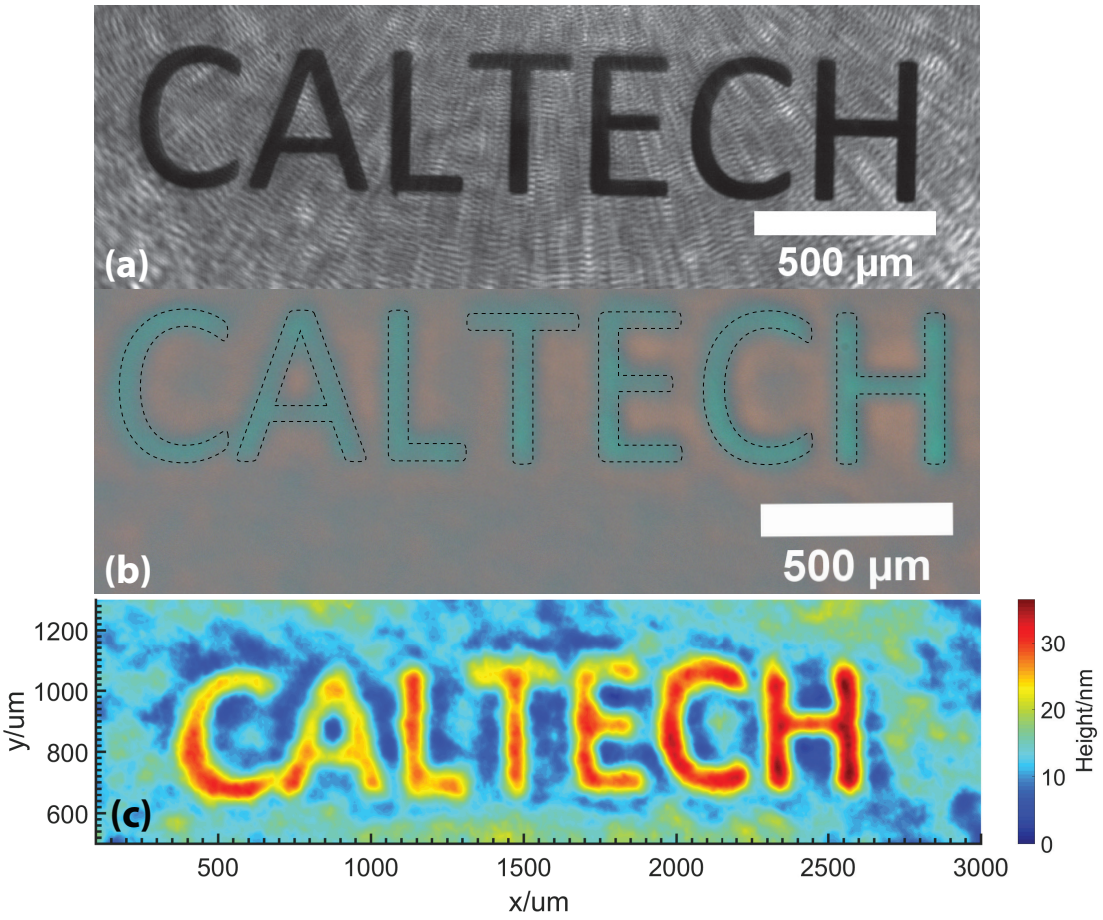

Figure 14.2: Sample L0087, fabricated through Experimental Setup Beta. (a) Laser light field used in fabrication, (b) Light microscopy image post-fabrication. The dotted lines are the outlines of the dark regions in the laser light field. There is very close agreement between the deformed features and the laser light field outlines. (c) Scanning white light interferometry image of the post-fabrication surface.

transmitted shorter wavelengths (containing information about the film topography) towards the sample-viewing camera. Figure 14.3 exhibits the unprocessed and processed images captured by the sample-viewing camera during one fabrication run (Sample L0057). The light microscope image of the same sample post-fabrication is exhibited in Figure 14.4. A video exhibiting the time evolution of both unprocessed and processed images is included as Supplementary Material 1: Air current sensing with Shack-Hartmann Device. The laser light field used is a dark "CALTECH" word against a lighted background (Appendix Figure I.28(a)). This light field hence induced thermocapillary flow towards the less-illuminated regions, thereby creating a protrusion in the shape of "CALTECH".

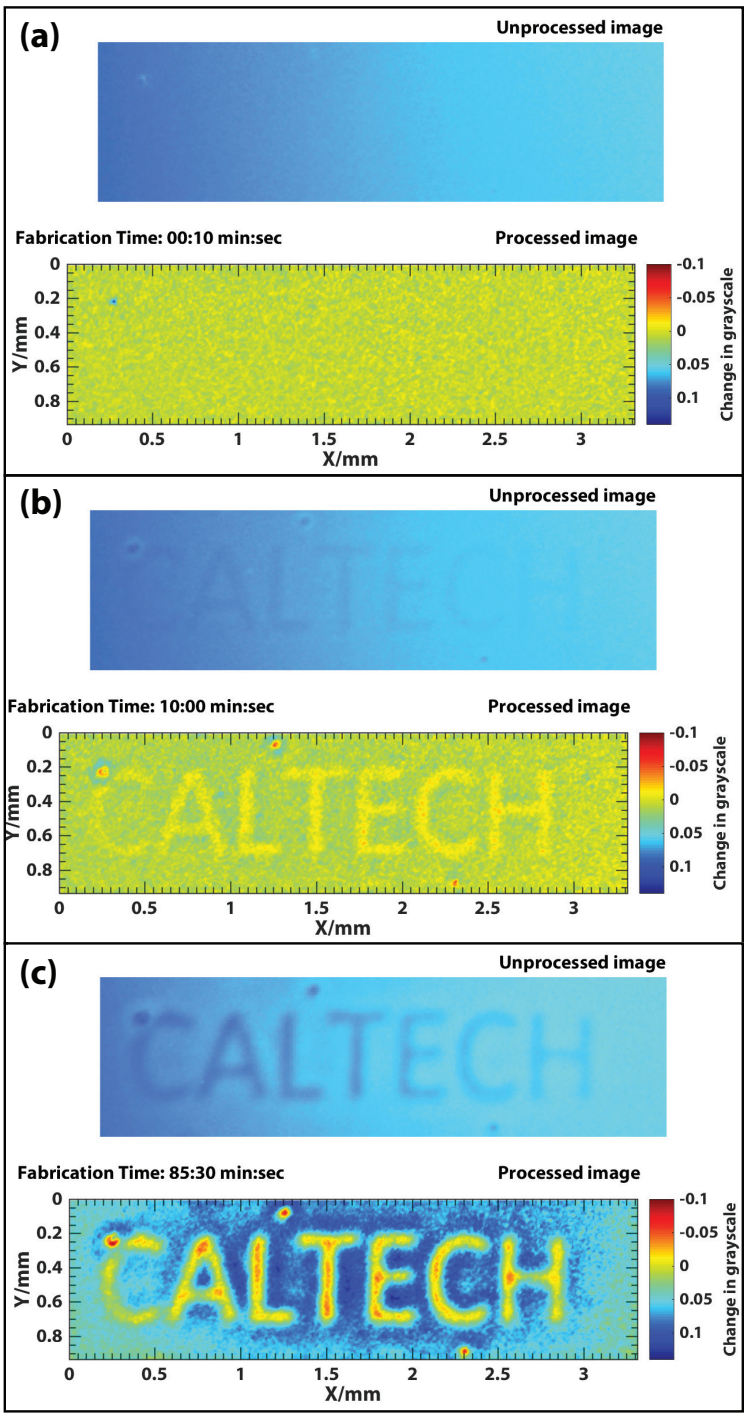

Figure 14.3: Raw images (top of each panel) and processed images (bottom of each panel) of real-time monitoring of the laser-induced film deformation, captured (a) 10 seconds, (b) 10 minutes and (c) 85.5 minutes into the fabrication time. Sample: L0057 in Experimental Setup Beta. The color axis for the processed images represent the grayscale deviation of the captured images (converted to grayscale) from the first captured image at $t = 0$. Note that the color axis is inverted: darker regions (negative changes in grayscale) are generally taller, although this relationship is not necessarily linear. The video of the full fabrication run is available as Supplementary Material 2: Live Viewing of Laser-induced Deformation.

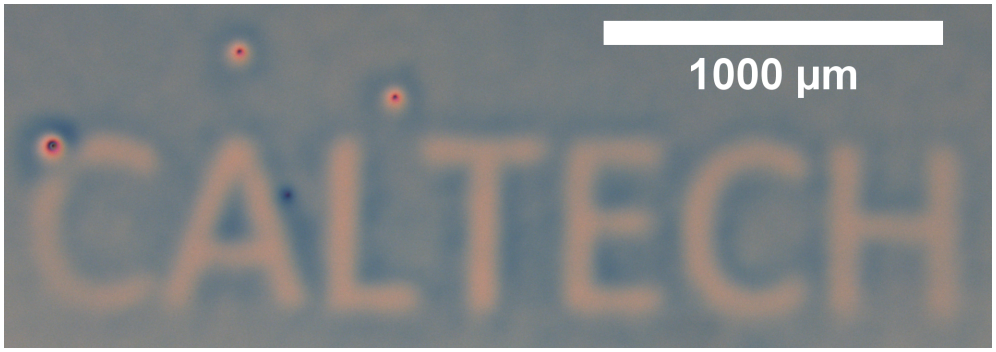

Figure 14.4: Light microscope image of Sample L0057 film deformation. The text protrusions are lighter than the background, as opposed to being darker than the background in Figure 14.3 because this image was captured under full visible light illumination, while that of Figure 14.3 was captured in a range of shorter wavelengths transmitted through the dichroic shortpass filters.

The protrusion in the form of "CALTECH" is visible as a slight darkening of the unprocessed image in the shape of the word. In order to accentuate the contrast, we converted the raw images to grayscale and then subtracted the grayscale contribution due to the first raw image captured at $t = 0$. This process yielded the grayscale change from the initial time to the present fabrication stage, which we plotted as the "Processed Image" surfaces. The processed images show that the changes in grayscale value are approximately uniform over the protrusion pattern, despite the gradient in background illumination. This change in grayscale value can be used as a proxy for local changes in film height; in this particular experimental regime, thicker regions exhibit a lower reflectance and hence appear darker. We verified the monotonically decreasing relationship between the average normal-incidence reflectance of a polystyrene film (equally weighted and averaged over $400 - 520$ nm incident wavelengths) and film thickness (within ± 30 nm of the initial film thickness of 330 nm) using the Filmetrics reflectance calculator and substituting the measured refractive index of the polystyrene used. The monotonically-decreasing dependence of the average normal reflectance on the polystyrene film thickness (averaged over wavelengths that are transmitted through the dichroic filters, $400 - 520$ nm) is plotted as the blue dots in Figure 14.5. We have also plotted the average normal reflectance averaged over the entire visible spectrum ($400 - 700$ nm) as a function of the polystyrene film thickness as the red dots in Figure 14.5. The monotonically increasing average reflectance for the full visible spectrum explains why the thicker protrusions appear lighter under white light illumination in a microscope (Figure 14.4) instead of appearing darker.

However, the reflectance-grayscale relationship (for images captured through the sample-monitoring camera) is not likely to be linear. The light source used to illuminate the sample during sample-viewing does not exhibit a uniform spectrum, and the color camera sensor used also does not have a linear spectral response. The angle made between the light source and the film may also change as the film deforms, which adds an additional degree of uncertainty to the relationship between film darkening and height increases. The relationship between the grayscale value change and the film heights is monotonic at best and hence we do not attempt to interpolate the height measurements as a function of the change in grayscale intensity yet. Nevertheless, we see that the changes in the grayscale value approximate what we would expect for the changes in film height in time. Regions surrounding the protrusion are locally depleted of material and hence are expected to exhibit a slight decrease in thickness. Figure 14.3(c) exhibits that the region surrounding the pattern increases in grayscale value at late times, which is consistent with a decrease in film height. We suspect that the main contributor to the background depletion was not the formation of the "CALTECH" text protrusion, but was the bulk flow of material towards a large (> 5 mm diameter) dewetting center located near the focused laser spot. As material dewets away from a point on the surface, it forms a sharp ring boundary which expands outwards. We believe that the ring boundary does not only contain material from the dewetted region, but also draws in material from outside the dewetted circle. This depletes the surrounding region of polymer material, which reduces the local film thickness and is consistent with an increase in grayscale value (brighter reflections).

14.3 Time evolution of laser-induced depression

In order to examine the effect of changing the total amount of incident radiant energy per unit area (known as the radiant fluence) on the extent of deformation, we performed a time series of fabrication runs in which only the fabrication time was varied (Samples L0034-L0037). All other parameters such as the initial polystyrene film thickness, hotplate temperature and laser beam intensity were kept constant. These fabrication runs were performed in Experiment Setup Alpha and used a microlens array (P = 300 μm) to focus the incident collimated laser light into an array of focused dots. The same light field was used to fabricate each sample and a subset of the camera capture of the light field used is exhibited in Figure 14.1(a). Figure 14.1(b) exhibits a subset of the resultant array of depressions achieved.

We quantified the geometric parameters of the depression arrays by fitting the

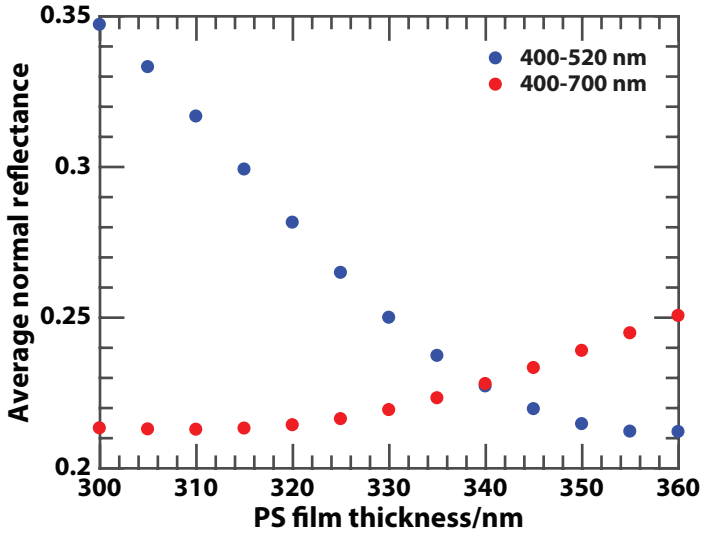

Figure 14.5: Plot of the theoretical average normal reflectance of a polystyrene-on-silicon sample as a function of the polystyrene thickness. The reflectance is averaged over the wavelength range transmitted through the dichroic shortpass filters (blue dots: 400 to 520 nm) and over the entire visible spectrum (red dots: 400 to 700 nm).

depressions to a rotated paraboloid and 1D aspheric profile using the same numerical analysis protocol introduced in Conduction TCL (Section 6.7). This technique was used to compute the effective diameter and height (given by the $z_{\max}$ fitting parameter in the 2D paraboloid fit). We computed the total amount of energy incident on the polystyrene-on-silicon sample per microlens by integrating the power logged by the photodiode beam-monitoring arm, computing the transmitted energy incident on the sample by multiplying the photodiode integrated power by the measured calibration ratio, then scaling the transmitted energy by the ratio of a single microlens area to the total beam area at the sample plane. The depression depths and effective diameters have been plotted in Figure 14.6(a) and b, respectively, as a function of the incident radiant energy per lens. We observed that the depression depth appears to increase approximately linearly up to a radiant energy of around 2 J per lens. Thereafter, the depth appears to stabilize around 70 nm. On the other hand, the effective diameter appears to increase monotonically as a function of radiant energy. These changes can be visualized by examining the cross-sections of depressions superimposed in Figure 14.7. Each cross-section is representative of the depressions within the array in the sense that the depression height and effective diameter parameters for each selected cross-section was the closest to the mean height and diameter computed by sampling at least 25 depressions over each array. It is important to note that these depressions

do not form in isolation; they are part of an array of depressions (P = 300 μm) and hence experience interaction effects with adjacent depressions. We observe that for small incident energies (arising from short fabrication times), the deformed film takes on an approximately Gaussian depression shape. As the energy per lens (and thereby fabrication time) increases, the depression becomes more pronounced, until it becomes to plateau at higher energies per lens. The depression profile at high energies per lens exhibits a flat region in the center of each depression. It is important to note that the film does not break up and dewet from the silicon substrate even when the central region of the depression forms the flat-bottomed plateau. The deformed film remains continuous, while a dewetted film will be expected to form a sharp three-phase boundary along the line of air-polystyrene-silicon contact. Furthermore, since the initial unperturbed polystyrene film thickness of these samples was around 288 nm (to within 2 nm), the flat region of each depression is still more than 150 nm away from the flat silicon substrate beneath. We hence do not believe that frictional effects from the flat substrate are the proximal cause for the bottoming-out of the depressions at high incident laser energies. Instead, the flat bottom appears to be an asymptotic steady state that arises when the lateral thermocapillary flow is no longer able to displace material away from the center of the focused laser beam due to counteracting flows from adjacent depressions doing the same displacement in the opposite direction. The flat profile at the bottom of each depression may indicate that the temperature along the base of the depression is approximately uniform (the film thereby experiencing weak or no thermocapillary forces at the flat locations) since capillary forces have successfully minimized the local surface energy density in producing a flat profile. The action of thermocapillary forces hence appears to be restricted to displacing material at the peripheral regions of the laser heating spot, further increasing the effective diameter of the depression. We expect that the effective depression diameter should eventually asymptote to a constant value as we approach the steady state by increasing the radiant energy per lens.

14.4 Effect of thermal reflow

Thermal reflow is the process in which capillary forces work to induce surface flow to minimize the surface energy and achieve a flat interface (in a uniform gravitational field). During TCL fabrication, thermocapillary forces (arising from temperature gradients and hence surface tension gradients) overwhelm capillary forces (arising from surface tension), thereby enabling the interface to be deformed and increasing the exposed surface energy. In the absence of imposed temperature gradients, a

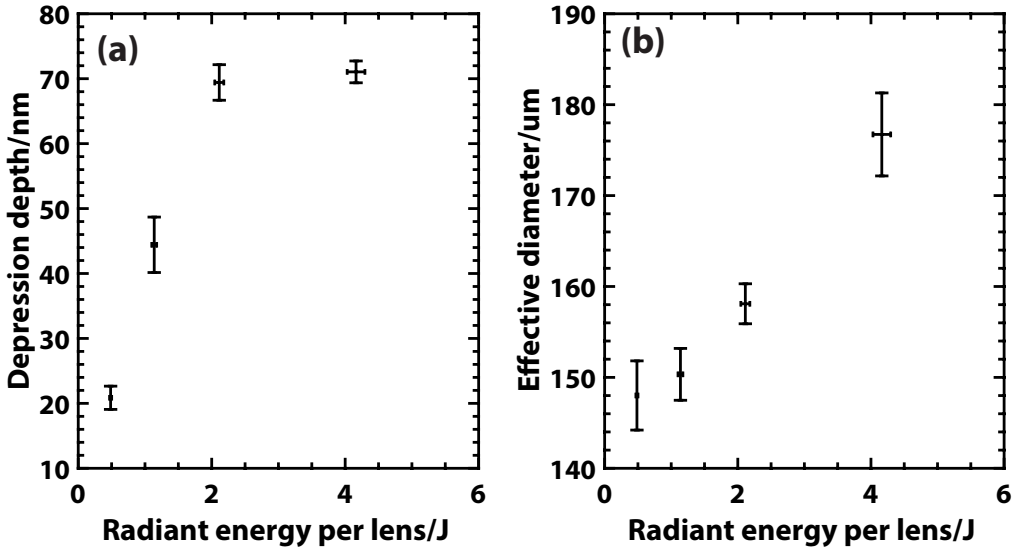

Figure 14.6: Plots of (a) depression heights and (b) characteristic diameters formed under varying radiant energies (per microlens) for depression arrays fabricated by laser focusing through a microlens array (samples L0034-L0037)

deformed surface should reflow under capillary forces to achieve a flat film. This reflow process tends to smooth out high spatial frequency variations in minimizing the surface energy, and has been used as a final processing step to achieve ultrasmooth surfaces. This effect has been known and used for several decades; Popovic *et al.* were the first to propose using thermal reflow to achieve high quality microlens arrays in 1988 [83].

We tested the effect of thermal reflow on the fabricated depression arrays by fabricating two arrays under identical conditions (using a $P = 300$ μm microlens array in Experiment Setup Alpha), then allowing one array to sit at the hotplate temperature for an additional 6 minutes (with the templating laser pattern turned off) to allow thermal reflow to occur. Figure 14.8 exhibits representative cross-sections of the depressions without reflow (Sample L0039 black line) and with the 6 minute reflow (Sample L0040 red line). The cross-sections are representative in the sense that the cross-section plotted belonged to the depression with a measured height and effective diameter closest to the mean values for that array. The reflowed depression exhibits a slightly shorter height, which is consistent with the refilling of material back into the depressions during the reflow process. However, the array-averaged heights are not significantly different (39 ± 2 μm for the reflowed sample and 41 ± 3 μm for the non-reflowed sample), indicating that the 6 minute reflow process may have been too short for significant re-filling to occur. The effective diameters of the

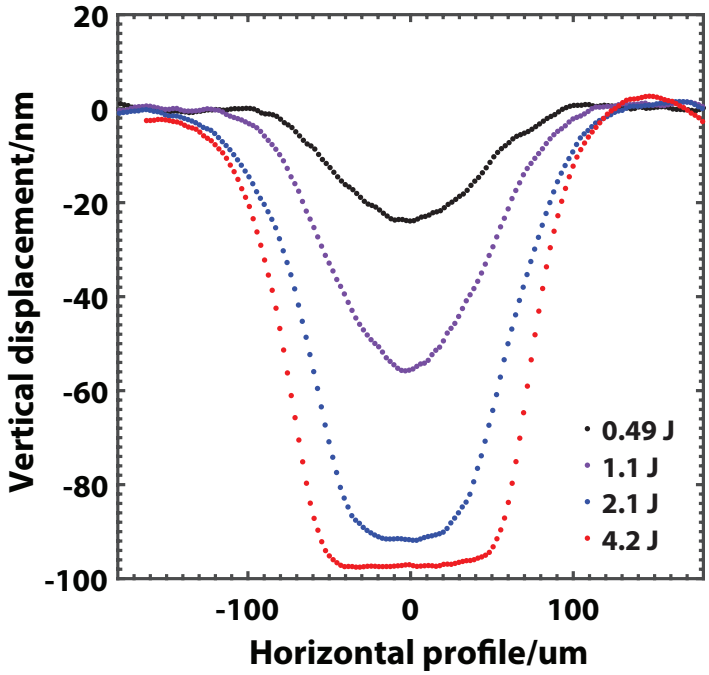

Figure 14.7: Cross-sectional plots of representative depressions within a depression array (P = 300 μm) formed under varying radiant energies per microlens (from the top profile to the bottom, black: 0.49 J/lens, purple: 1.1 J/lens, blue: 2.1 J/lens, and red: 4.2 J/lens). The plots were obtained using scanning white light interferometry. Note that the horizontal scale is in microns while the vertical scale is in nanometers. The film has not broken up or dewetted in the 4.2 J/lens sample; it remains continuous. The original unperturbed polystyrene film thickness is around 288 nm for each sample, hence the flat region was not close to the silicon substrate lying beneath the polystyrene film.

depressions are also not significantly different (217 ± 3 μm for the reflowed depressions and 213 ± 3 μm for the non-reflowed depressions). However, the reflowed depressions do have a slightly smoother surface. The root-mean-square residual for the 2D parabolic fit, which acts as an upper-bound proxy for the true smoothness of the surface, is slightly smaller in the reflowed sample (1.99 ± 0.26 nm) as in the non-reflowed sample (2.54 ± 0.32 nm), where the errors represent the standard deviation across at least 28 depressions measured across each array. This is consistent with the action of capillary forces in smoothing out high spatial frequency variations in the height, which may have been caused by high spatial frequency variations in the incident laser light field.

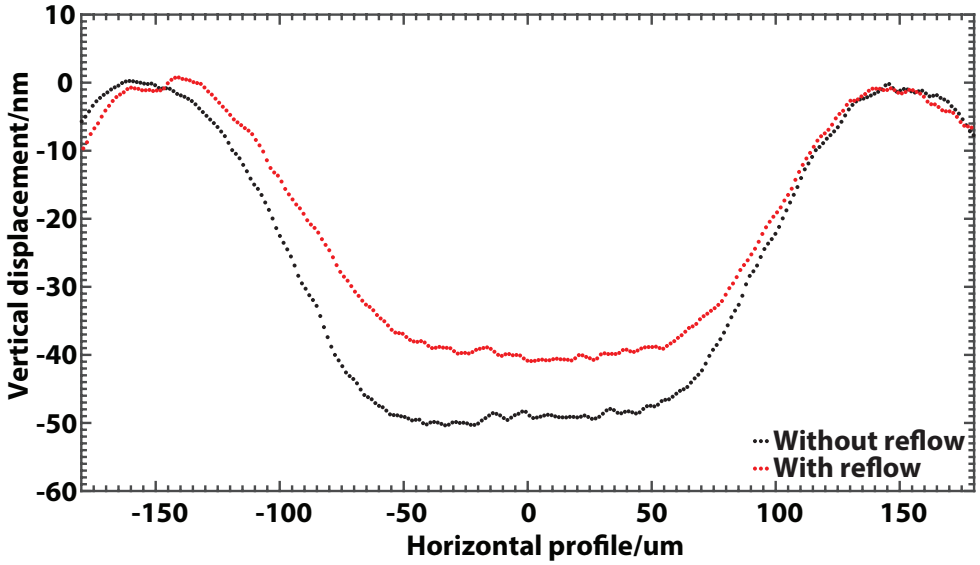

Figure 14.8: Comparison of L0039 (no reflow) to L0040 (additional 6 min reflow).

14.5 Light field feature size relationship to fabricated feature parameters

We examined the relationship between the light field feature size and the fabricated feature parameters by using either a progression of lighted spot sizes (Figure 14.1(c)) or a progression of dark dots against a light background (i.e. the inverse of Figure 14.1(c), displayed in Appendix Figure I.13(a)) as the laser light field. A total of sixteen holes (for the lighted spot pattern) or dots (for the inverted dark dot pattern) of varying sizes were used in each pattern. The samples used were L0064 and L0065, which used the lighted spot pattern against a dark background, but for different fabrication times, and L0067 and L0068, which used a dark spot pattern against a lighted background for different fabrication times. We used the camera image taken of the laser light field to compute the relative amount of radiant fluence transmitted by each lighted spot. Since the light field was captured by a monochrome camera and the exposure time was adjusted so avoid saturated pixels, the pixel grayscale value is proportional to the intensity of light incident on that pixel. The total amount of radiant energy contributed by a single lighted spot (within the same sample) is hence proportional to the sum of the pixel grayscale values making up that lighted spot. This grayscale value sum is known as the integrated density or integrated gray density in ImageJ. We hence use the integrated gray density of each lighted spot as a proxy for the total radiant energy associated with that lighted spot.

However, for light field patterns where the dots were opaque against a lighted background (forming convex protrusions where the dark dots are located), we will

not be able to calculate the radiant energy blocked by that dark spot in the same way. Instead, we estimated the local radiant intensity by taking the average grayscale value of the lighted pixels surrounding the dark spot. We thresholded the laser light field image to select pixels outside the dark spots, then selected a square containing the pixels surrounding the dark spots to be averaged over. This average value was taken as a proxy for the total radiant energy obstructed by the dark spot in a lighted background.

The progression of protrusions or depressions formed using the circle progression laser field patterns were analyzed using the same numerical protocol as described in Section 6.7 for the Conduction TCL microlens arrays. The numerical routine was used to extract the heights and effective diameters of the protrusions or depressions. To afford comparison of these geometric parameters across samples, we normalized the heights and effective diameters to the maximum value within each sample. We then plotted these normalized heights and effective diameters to the normalized integrated gray density values and normalized photomask feature sizes (taken to be the diameter of the circle feature on the photomask itself). The combined plots exhibiting all four samples each plot (two concave depression samples from the lighted spot patterns and two convex protrusion samples from the dark spot patterns) are displayed in Figure 14.9.

The reason why we analyzed the integrated gray value and photomask feature diameter separately was because the background laser light field was not uniform. The integrated gray value was hence not proportional to the photomask feature diameter. This effect can be seen in Figure 14.1(c), where the laser light features on the left of the image are brighter than the features on the right hand side of the image. In particular, the feature in the second-from-bottom position in the leftmost column is brighter than the feature in the bottom right hand corner of the pattern, despite the latter being larger in diameter than the former.

In Figure 14.9(a), we plotted the normalized height against the normalized integrated gray density for each sample. We note that the concave depression samples collapse neatly along a single master curve despite being fabricated with different fabrication times (under the same laser illumination) and hence experiencing different radiant fluences. The convex samples have datapoints that are scattered about the concave master curve but seem to follow a similar pattern. On the other hand, when we plot the normalized heights against the normalized photomask feature size in Figure 14.9(b), we observe a much larger degree of scatter, even within the concave samples.

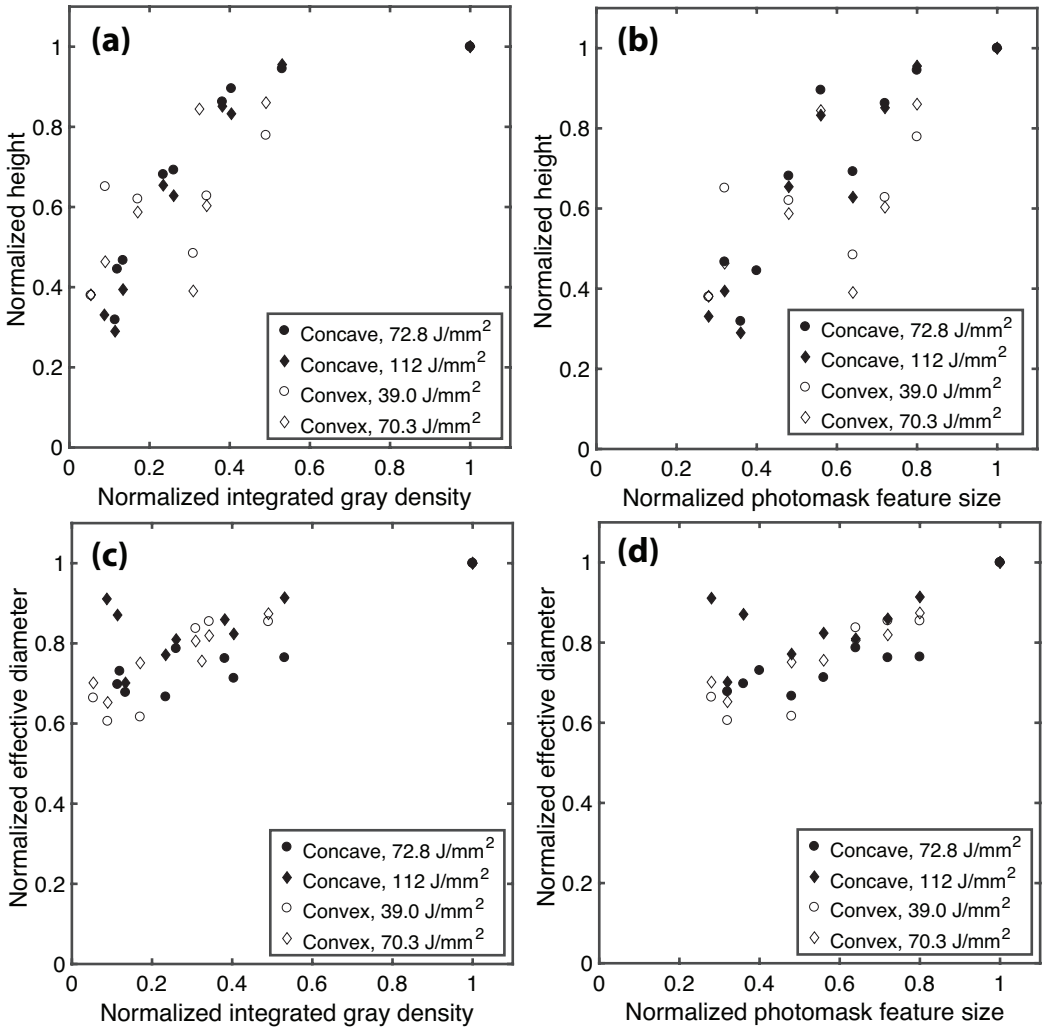

Figure 14.9: Plots of the heights and effective diameter of samples fabricated with the lighted spot/dark spot circle progression. The parameters are normalized to the maximum value in each sample so the results can be compared across samples. Lighted spots in the laser light field produce concave depressions and dark spots produce convex protrusions. Samples shown: L0064 (Concave, fluence = 72.8 J/mm^2), L0065 (Concave, fluence = 112 J/mm^2), L0067 (Convex, fluence = 39.0 J/mm^2), L0068 (Convex, fluence = 70.3 J/mm^2). (a) Plot of feature heights against the integrated grayscale density of the laser light field spot. The concave samples collapse neatly along a master curve, but the convex samples are scattered more widely about the concave sample curve. (b) Plot of feature heights against photomask feature size, (c) Plot of feature effective diameters against integrated grayscale density of the laser light field spot, (d) Plot of feature effective diameters against photomask feature size.

There still appears to be a general increasing trend of depression/protrusion height with photomask feature size, but this dependence is much less pronounced than that observed in the height dependence on integrated gray density. We hence conclude that the amount of radiant energy deposited (or obstructed, assuming a slowly varying illumination pattern in space) is the primary determinant of the height of the fabricated feature, and plays a more significant role than the size of the laser light feature projected onto the target surface. We believe that this biased dependence occurs due to lateral thermal conduction in silicon smearing the effective temperature field out, and thereby reducing the influence of the projected light field feature size.

When we plot the effective diameter of the fabricated features against the normalized integrated gray density (Figure 14.9(c)) and photomask feature size (Figure 14.9(d)), we observe that the diameter does not vary much with the gray density and photomask feature size independent parameters. There appears to be a weak general increasing trend of effective diameter with each of the independent parameters, but this trend is not consistent within individual samples. In effect, the effective diameter of the protrusions/depressions remains approximately constant, independent of the incident radiant energy and projected light field feature size. We believe that this effective diameter is primarily controlled by the geometric parameters of the polystyrene-on-silicon sample itself. The thicker the film, the more smeared the surface temperature field of the polystyrene will be (since it is conductively heated from the silicon surface and does not absorb much incident laser light in the visible), and hence the larger the expected diameter. Similarly, the lower the thermal conductivity of the substrate, the less thermal conduction will occur, and the smaller the effective diameter of the fabricated structures. These considerations can be circumvented if the laser heating occurs primarily at the surface of the deformable fluid itself, and not indirectly through conduction from an absorbing substrate. Two ways to do so are to introduce an absorbing dye into the fluid or to use an incident laser wavelength corresponding to a strong absorption peak of the fluid material.

14.6 Constraints on Laser-induced Thermocapillary Lithography

The main constraint on the Laser-induced TCL setup as it is currently constructed is the spatial inhomogeneity of the laser light field used, even when no photomask pattern is used. Figure 14.10 exhibits the laser light field in the absence of a modulating photomask. It exhibits a high spatial frequency granularity and a concentric ring of slightly lower intensity at the half-radius point. These high spatial frequency perturbations arise because the laser source has a multimode output and the fiber

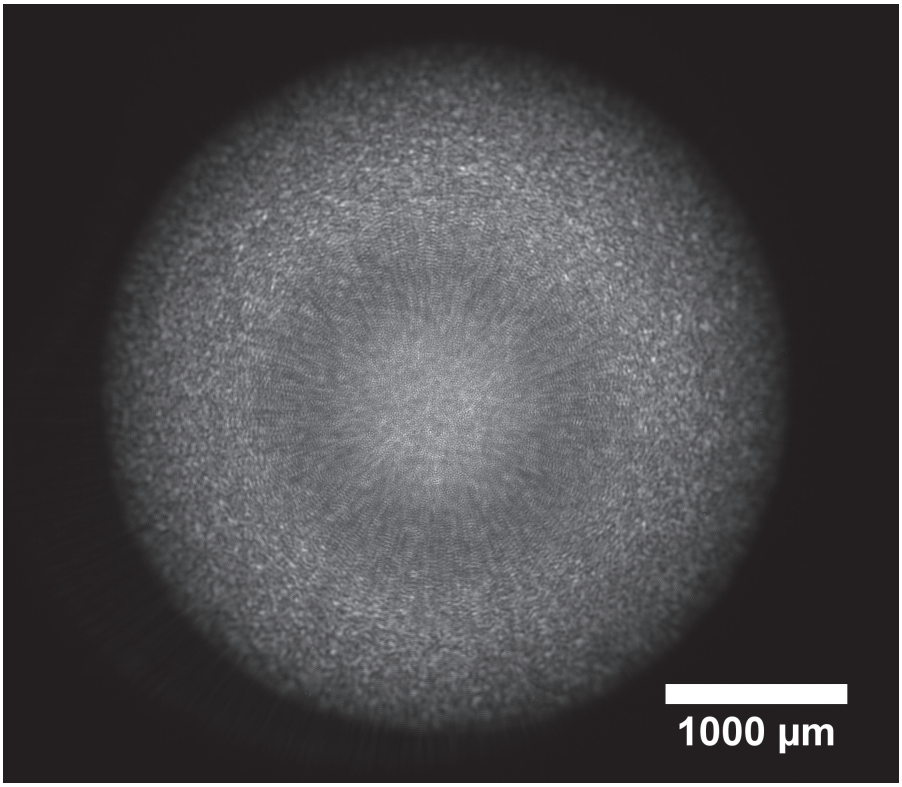

Figure 14.10: The laser light field image without photomask exhibits a spatially inhomogeneous profile with high spatial frequency perturbations. This profile arises because of the multimode output from the laser and the multimode fiber optic used.

optic used to transmit the laser source from the source to the experimental setup is also a multimode fiber. The variable phase difference between propagating spatial modes results in the speckled interference pattern observed in the beam profile as it is incident on the target sample. The speckle patterns reduce the quality of pattern replication on the target sample by introducing unintended fluctuations in film thickness. Ideally, the background laser beam profile should be uniform or slowly varying in space, so that the fabricated sample replicates the photomask patterns exactly. Future implementations of Laser-induced TCL should use a laser source with few spatial modes and a single-mode fiber to achieve a more uniform Gaussian beam. The laser beam can also be spatially filtered by focusing it onto a small pinhole, although this process drastically reduces the amount of power that is incident on the target sample. This loss in energy may need to be circumvented by increasing the input laser power. We also considered homogenizing the beam before passing it through the photomask. However, this process increases the beam divergence, which makes it difficult for the experimenter to achieve sharp projected

image patterns on a surface placed further away.

Another issue faced during fabrication was the spontaneous formation of dewetted holes over the polystyrene film surface. These holes are well known and are extensively studied [84]. We observed that the formation of these dewetting holes can be suppressed significantly by increasing the initial polymer film thickness and by decreasing the hotplate temperature. Increasing the polymer film thickness (from 80 nm to over 200 nm in experiments conducted) also increases the heights of the deformations achieved. Decreasing the hotplate temperature decreases the rate at which the film deforms since the film viscosity is a strong function of temperature. The slower rate of fabrication can be compensated by a higher incident laser power, which establishes larger thermal gradients that can sculpt the interface more rapidly. Practically speaking, the experimenter can also monitor the entire film using the real-time sample-monitoring camera, and halt fabrication if the dewetting defects approach the target pattern area.

We suspected that part of the dewetting hole formation could be due to trapped bubbles of gas which expand to form a dewetting center when heated. To test this hypothesis, we kept two samples (L0083 and L0086) under a low vacuum (-23 to -26 inches of mercury) at room temperature for 40 minutes before fabrication to induce the release of trapped gas. We also kept two controls (L0082 and L0085) at room pressure and fabricated them under similar experimental conditions. There was no consistent change in the number or size of the dewetting spots between the low-vacuum and control samples after fabrication. Future studies may want to investigate if low heating (without allowing the thermocapillary instability to form significantly) and be used as a means to relieve frozen-in stress and trapped air bubbles so as to possibly reduce the incidence of dewetting centers.

Chapter 15

OUTLOOK AND ROADMAP FOR INDUSTRIAL APPLICATION

Laser-induced TCL has been shown to be a truly non-contact means of fabricating surfaces by controlling thermocapillary flow. We have shown that we can control the direction of thermocapillary flow using refractive focusing as well as by projecting an image of a reference photomask pattern onto the target surface, and monitor the film deformation in real-time. Certainly, these are not the only two means of modulating the laser light field spatially. Future experiments should incorporate grayscale masks, in which the patterns can have varying degrees of opacity. This provides an additional degree of control over the temperature profile imposed. The beam can also be modulated temporally by varying the duty cycle of the laser source itself. Importantly, the laser power can be stabilized by feeding the demodulated photodiode voltage (which is proportional to the transmitted power of the main beam) back to adjust the duty cycle of the laser power source in a Proportional-Integral-Derivative (PID) topology. An improved laser power stability increases the reproducibility of the fabricated samples.

In the current iteration of laser-induced TCL, the incident laser energy is absorbed in the silicon substrate volume as opposed being absorbed at the nanofilm surface itself. Ideally, we would like to project a temperature field onto the nanofilm itself without having to rely on additional conduction from the substrate. There are several possible ways to do this. The first is to dope the nanofilm with an absorbing dye with an absorption peak at the laser wavelength. If chemical changes to the nanofilm material are not desired, one can switch the laser to that with a wavelength that corresponds to a strong absorption peak of the nanofilm material itself. This is likely to be in the mid to far infrared for organic polymers like polystyrene, which may be accessible by carbon dioxide gas lasers. The downside to using an infrared laser is that the longer laser wavelength will make it more difficult for one to fabricate small feature sizes with diffraction-limited focusing.

Laser-induced TCL is a versatile concept that has significant manufacturing potential. When optimized, we expect that TCL will be an indispensable means for fabricating curved surfaces in bulk. Its parallel fabrication ability and low equipment requirements makes TCL suitable for rapid prototyping, while its large number of

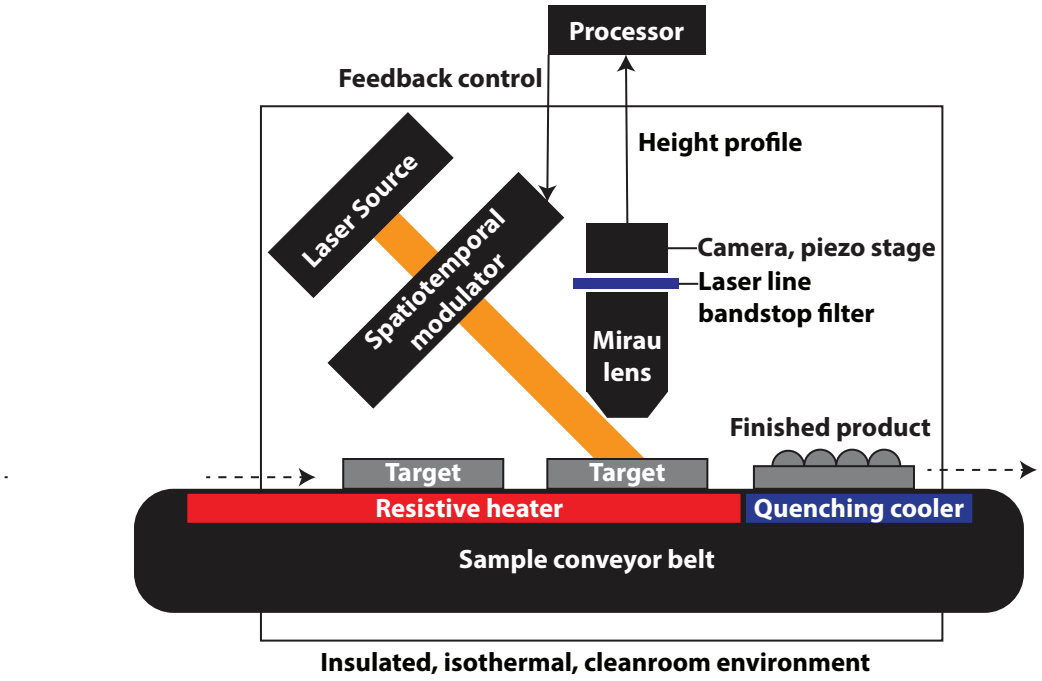

Figure 15.1: A concept drawing of an industrial implementation of Laser-induced TCL.

tunable parameters (especially in tandem with current mature technology in beam-shaping) enables TCL to fabricate complex surfaces with micron-scale control.

15.1 A roadmap for industrial application

Figure 15.1 exhibits a sketch of my concept for an industrial application for laser-induced TCL. In the design concept, the sculpting laser (actively modulated in a spatiotemporal fashion) is incident at an angle to the normal in order for a scanning white light interferometry system to be mounted directly above the sculpting target. One possible interferometry setup is through the use of a Mirau interferometry lens mounted onto a piezoelectric nanometer displacement stage. The output from the Mirau lens is filtered with a laser line bandstop filter (or multiple bandstop filters) to remove the contribution from the sculpting laser before being captured by a camera for height profile reconstruction. The measured height profile can then be compared to a reference profile, and the error signal representing the deviation between the current profile and the desired profile can then be fed back to the laser spatiotemporal modulator. The spatiotemporal modulator can then adjust the intensity or pattern projected so as to let the film evolve towards a desired height profile. One possible way to do this is to use a grayscale mask with a pixel optical density that can be digitally controlled. I believe that an electro-chromic liquid crystal device with a

high-density grid of electrodes will be able to achieve this. If the resolution of the modulator exceeds that required of the target pattern, one may consider expanding the beam, passing the beam through the modulator, and then de-expanding the beam again to obtain the necessary small feature sizes. Once the target surface achieves the desired height profile, it is moved by a conveyor belt system to a cooler quenching stage which halts thermocapillary film evolution. The sample exits the fabrication system afterwards. This simple fabrication system allows for rapid fabrication of arbitrary ultrasmooth surfaces with active height profile control, potentially revolutionizing the precision manufacturing and microstructure fabrication industries.

Part IV

Applications of Thermocapillary Lithography

Chapter 16

ORGANIZATION OF PART IV: APPLICATIONS OF THERMOCAPILLARY LITHOGRAPHY

Having described and evaluated the two main forms of TCL, Conduction TCL and Laser-induced TCL, we now turn to using these techniques to produce functional devices. This Part of the thesis is split into two major topics. First, we use the microlens arrays fabricated through Conduction TCL to perform wavefront sensing. This was done by incorporating the arrays in a Shack-Hartmann geometry. Secondly, we use Conduction TCL to fabricate microcavity arrays: arrays of optical cavities with out-of-plane curvature. In the process, we develop a protocol to coat thermosensitive polymer surfaces with a reflective metallic coating.

Chapter 17

WAVEFRONT SENSING

17.1 Introduction

Microlens arrays have essential applications in wavefront sensors, which are used to measure the shape and intensity distribution of light waves. These wavefront sensors are used in adaptive optics for ground-based astronomical applications [85]. By shining a reference laser beam into the turbulent atmosphere and tracking the scattered light using the wavefront sensor, the ground-based telescope can compensate for atmospheric distortions (usually by deforming a focusing mirror) and achieve stellar images. Wavefront sensors with microlens arrays are also used in ophthalmology to characterize the aberrations of the human eye [86].

Figure 17.1 exhibits a simplified schematic of the Shack-Hartmann wavefront sensor (SHWS). In Figure 17.1(a), an unperturbed beam of light with a uniform wavefront is focused through a convex microlens array to form a regular array of dots on a camera sensor. When the incident beam of light is perturbed by scattering off solid inclusions (Figure 17.1(b), upper lens) or refraction due to regions of varying refractive index (Figure 17.1(b), lower lens), the wavefront is no longer uniform, and upon focusing through a microlens array, the dot array will not be regular. By tracking the positions of the dots within the captured array, one is effectively sampling the local tilt of the wavefront over a regularly spaced 2D grid corresponding to the positions of the microlenses over the microlens array. This tilt information can be used to deduce the incident wavefront geometry.

In our application, we sought to implement a SHWS using a microlens array fabricated through Conduction TCL. However, instead of using a convex microlens array to focus the incident beam into an array of dots, as is commonly done [87], we used a *caldera-like* microlens array that behaved as a concave microlens array. The microlens array was coupled to a microscope objective so that the virtual focal points (located behind the planar face of the microlens array) coincided with the working distance plane of the microscope objective. This allowed the camera sensor coupled to the microscope objective to capture an array of focused dots in real time.

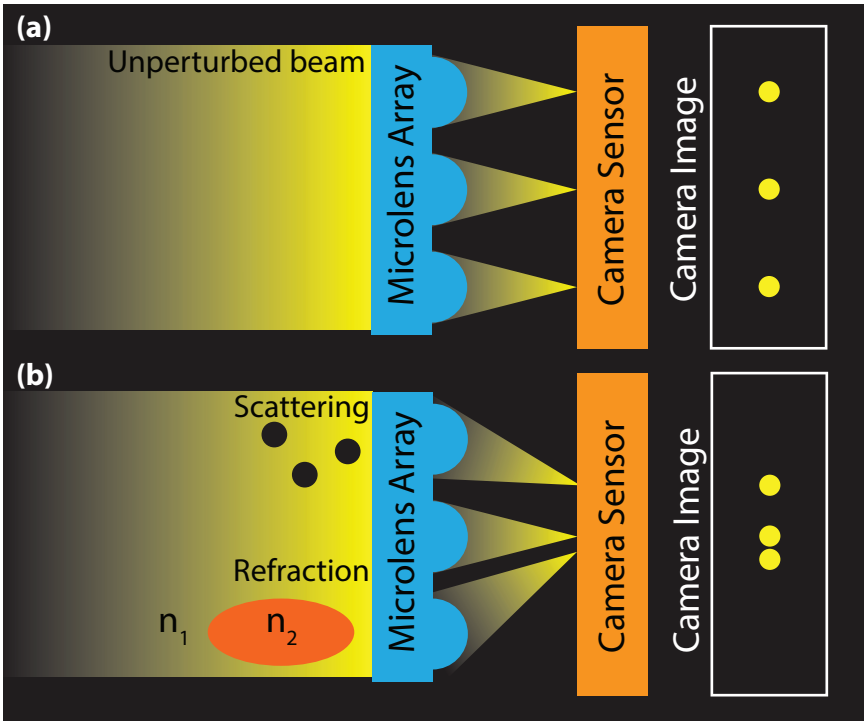

Figure 17.1: Simplified schematic of a Shack-Hartmann wavefront sensor incorporating a microlens array. (a) An unperturbed incident beam is focused by the microlens array to form a regular array of dots on a camera sensor. (b) A beam perturbed by scattering off solid inclusions or refraction produces dots displaced from their equilibrium positions.

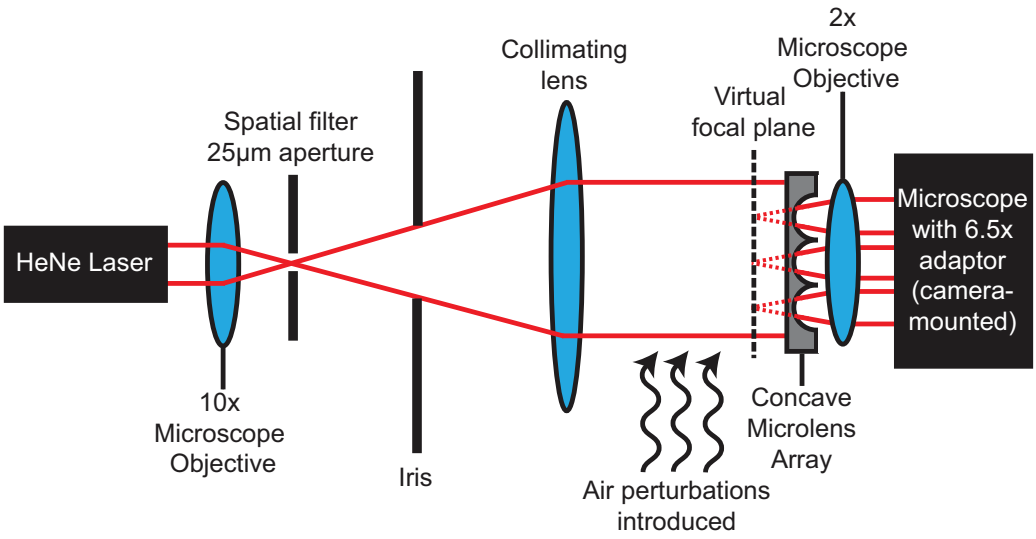

Figure 17.2: Shack-Hartmann wavefront sensor experimental setup for evaluating concave microlens arrays.

17.2 Experimental Setup

Figure 17.2 exhibits the experimental setup for the modified Shack-Hartmann wavefront sensor. A Helium-Neon laser (λ = 632.8 nm, 05-LHP-991, Melles-Griot) was attenuated (ND1.5, 30898, Edmund Optics, to protect the camera sensor), focused through a microscope objective (10x, 0.25 NA, Newport) onto a spatial filter (25 μm diameter, 910PH-25, NewPort) and collimated with a converging lens (KPX115AR.14 plano-convex lens, Newport). An iris was used to transmit only the central Gaussian spot to be normally incident on the planar face of a *caldera-like* MLA quartz substrate (sample Q0026). A 2x microscope objective (Mitotoyo M Plan Apo 2, NA 0.055, working distance 34 mm) was placed after the *caldera-like* MLA. The microscope objective was coupled to a high resolution monochrome CMOS camera (Basler acA2500-14gm, 2592×1944 pixels, 2.2 μm×2.2 μm pixel size) using a Navitar 6.5x ultra-zoom lens. The MLA was mounted onto a micrometer translation stage oriented along the direction of laser propagation and was positioned in front of the virtual focal plane so that the camera recorded an array of focused laser dots. Since the *caldera-like* MLA behaved as a concave (diverging) MLA, the CMOS camera captured a focused dot array when the virtual focal plane located behind the *caldera-like* array coincided with the working plane of the 2x microscope objective.

The air in between the collimating lens and the microlens array was perturbed using short sprays of a canned air duster (Miller-Stephenson MS-222N containing 1,1,1,2-Tetrafluoroethane). The duster sprays were oriented perpendicular to the optical axis to avoid physical movement of the optical components. Since the shifts in dot array position were minuscule, the recorded video of the focused dots evolving under the air perturbation was processed using ImageJ in two steps. Firstly, an image of the dot array positions under stationary experimental conditions was subtracted from each frame in the video to accentuate the spatial displacement of each focused beam. Only focused dots that were displaced from their equilibrium positions were visible after this step. Secondly, the subtracted images were thresholded at the same level and converted into binary masks for improved contrast. The images were then consolidated into a video.

17.3 Results and Discussion

Collimated laser light incident onto the MLA and coupled microscope objective is observed as a well-defined array of dots (Figure 7.4(b)) through the microscope-mounted camera when the virtual focal plane of the MLA is coincident with the

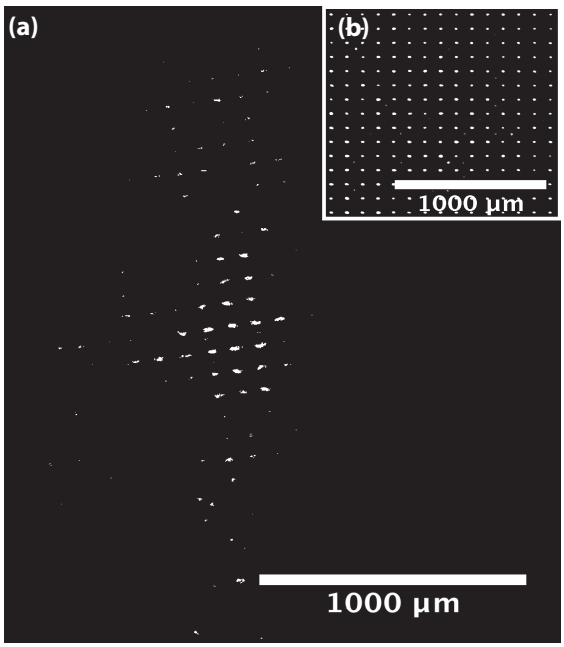

Figure 17.3: Focused dot arrays from a collimated light source transmitted through a concave microlens array. Scale bars refer to distances along the camera sensor. The images have been despeckled once and the contrast has been enhanced. (a) Still frame of an air disturbance proceeding from left to right. The visible dots indicate positions where the focused dot was displaced from the still-air position. (b, inset) The dot array in still air is well-defined and highly regular.

working plane of the microscope objective. When the air between a collimating lens and the microlens array was perturbed using short sprays from a canned air duster, the propagating pulses of cooled air created regions with slightly different refractive indices, thereby tilting the orientation of the collimated laser beam wavefront from the optical axis. This tilt shifted the lateral position of the focused dot array, thereby allowing us to detect the perturbation in real-time by tracking the positions of the individual dots. Figure 7.4(a) exhibits a still frame from a video clip capturing a pulse of air traversing the laser optical path from the left. While the current system contains only a very limited amount of information (the dot array displacement is only around 1-2 pixels, or around 2-4 μm, along the camera sensor), it exhibits the fundamental function of a microlens array in a SHWS sensor. This device is the first functional optical device derived from TCL.

Chapter 18

OPTICAL MICROCAVITY ARRAY FABRICATION

18.1 Introduction

Optical cavities are optical elements in which light forms a steady state field distribution due to confining reflection or interference at the cavity boundaries. Light confined in such a space can build to energy intensities orders of magnitude greater than that of the incident beam. An essential application of these cavities are in lasers, when an active gain medium is placed within the cavity to produce a coherent source. Macroscopic cavities are constructed using highly reflective planar, spherical, or cylindrical mirrors and prisms [88], and range in scale from the optical tabletop to the kilometer-scale arms of the Laser Interferometer Gravitational-Wave Observatory [89]. Increasingly, these cavities have found applications when miniaturized to the micron scale, and these structures are known as optical microcavities. The ultrahigh energy intensities and small cavity volumes in these microcavities allow access to quantum phenomena (studied in cavity quantum electrodynamics) and nonlinear photonic effects [90].

Microcavities generally fall into one of three categories: linear standing-wave resonators, whispering gallery mode resonators, and photonic crystal cavities. Standing-wave resonators are formed when the beam retraces its path through the cavity medium to form a standing wave distribution. Whispering-gallery mode resonators are formed when the mode has azimuthal symmetry and the light beam closes the loop upon itself from the same direction. Photonic crystal cavities are surrounded by submicron periodic structures that suppress the transmission of photonic modes corresponding to the structure periodicity and thereby localize those modes within defects in the array.

At the micron and nanometer scale, it is exceedingly difficult to fabricate curved surfaces that achieve the optical quality demanded for optical manipulation. Standing-wave resonators at the micro-scale hence use flat surfaces and Bragg dielectric stacks to form the cavity walls [91, 92]. Whispering-gallery mode microcavities exploit the volume-minimizing characteristic of surface tension to form closed optical propagation paths along spherical droplets [93] or thermally annealed ultrasmooth racetracks [94]. Whispering-gallery mode microcavities that do not exploit surface

tension are limited to two-dimensional planar structures [95–97].

Recently, a group from IBM proposed and fabricated plano-convex microcavities comprising Gaussian-shaped defects sandwiched between two Bragg mirrors [98–100]. These microcavities were fabricated by approximating an axisymmetric Gaussian using multiple level planes in ion beam milling [99] and can achieve small mode volumes while maintaining a high quality factor Q [98]. Two such cavities can be laterally coupled to achieve cavity polariton mode splitting [100].

In this chapter, we present a refinement of curved microcavity fabrication by using Conduction TCL. We fabricate a large-area array of ultrasmooth curved-surface microcavities made of polystyrene, sandwiched between conformal ultrasmooth reflective gold coats, and characterize it using reflection spectroscopy. In principle, this microcavity array should exhibit resonant behavior in two distinct regimes: one corresponding to standing-wave resonance between the submicron distance between planar surface and the curved reflective surface, and another corresponding to Bragg reflection and intercavity coupling across the micron-scale periodicity of the array. Gold was selected as the reflective material because it exhibited high reflectivity across a broad spectrum from the visible to far infrared. Preliminary results over a narrow range of wavelengths indicate that the fabricated microcavity array exhibits little to no frequency dependence, but further investigation is necessary to achieve a definitive verification of any microcavity behavior.

18.2 Materials and Methods

There were three main steps to form microcavities comprising a sculpted polymer nanofilm sandwiched between two conformal reflective gold surfaces. The first step deposits a uniform planar gold layer, the second coats the gold layer with a polymer coat and sculpts the polymer surface using Conduction TCL, and the third step coats the sculpted surface with a second gold layer. The experimental sample and the controls were then characterized using reflection spectroscopy.

The samples were indexed using the naming convention AU00xx, where the last two digits represent a unique wafer reference.

Four categories of experimental samples were fabricated and are exhibited in Figure 18.1. Three of the experimental sample categories (Figure 18.1(b)-(d)) serve as controls for the actual microcavity array (Figure 18.1(a), called the deformed Au/PS/Au sample, sample name AU0008) so that the behavior of each component of the array can be quantified. The flat Au/PS/Au (Figure 18.1(b), sample name: AU0009) is

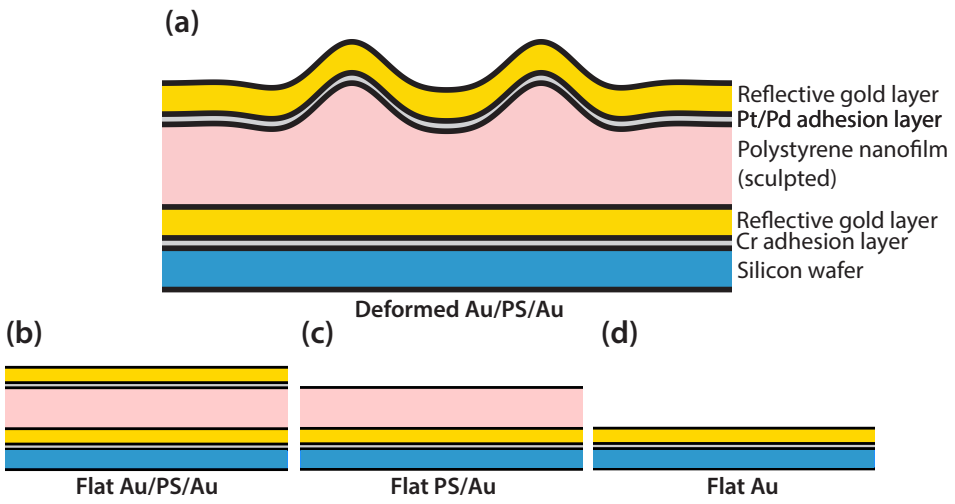

Figure 18.1: Cross-sectional view of the structure of the fabricated microcavity arrays and control samples. (a) The experimental microcavity array (called the deformed Au/PS/Au sample) sandwiches a sculpted polystyrene nanofilm between two reflective gold layers over a silicon wafer substrate. Sample name: AU0008. (b) The flat Au/PS/Au sample is identical to the experimental microcavity array but is not sculpted by the TCL fabrication process. Sample name: AU0009. (c) The flat PS/Au sample consists of an uncoated polystyrene nanofilm spin-coated over a flat gold substrate. Sample name: AU0010. (d) The flat Au sample consists of a flat gold substrate alone. Sample name: AU0005.

identical to the actual microcavity array except that it does not undergo sculpting through the TCL process and hence remains flat. The flat PS/Au sample (Figure 18.1(c), sample name: AU0010) consists of an uncoated PS nanofilm spin-coated onto a flat gold-coated substrate, and the flat Au sample (Figure 18.1(d), sample name: AU0005) just consists of the gold-coated substrate.

Step 1: First gold metallization

Gold could not be sputter-coated directly onto the silicon wafer surface due to the formation of argon bubbles under the deposited gold layer, indicating poor adhesion. This lack of adhesion necessitated a thin chromium adhesion layer. 5.1 ± 0.1 nm of chromium (Ted Pella 8074 sputter target, 99.95% pure) was deposited on a silicon wafer (Diameter 50.8 mm, $\langle 100 \rangle$, Thickness 279 ± 25 μm, Boron doped, Silicon Materials Inc) using a Cressington 208HR sputter coater (constant current sputtering in argon, 80 mA) with MTM-20 high resolution thickness controller to form a thin adhesion layer. 50.0 ± 0.1 nm of gold (Ted Pella 91110 sputter target, 99.99% pure) was sputtered onto the chromium subsequently. The surfaces of the clean silicon

wafer and the deposited gold surface were evaluated using scanning white light interferometry (Zemetrics Zegage) to quantify the effect of sputter coating on the surface roughness. Surface roughness scans were performed on three flat regions over each sample. The complex refractive index of the as-sputtered gold surfaces was evaluating using ellipsometry at source wavelengths of 632.8 nm and 546.1 nm (Rudolph Auto EL III) to establish the substrate parameters for further ellipsometric film measurements to be performed on the gold surface. At 632.8 nm, the refractive index and extinction coefficient was $n = 0.184 \pm 0.002$, $k = 3.599 \pm 0.003$ and at 546.1 nm, it was $n = 0.388 \pm 0.004$, $k = 2.542 \pm 0.005$. These values are consistent with the wide range of optical constants for gold reported in literature.

Step 2: Polymer coating and Conduction TCL

A uniform polystyrene (PS) nanofilm was coated onto the flat gold film by dissolving narrow-distribution PS (M_w = 1100 g/mol, M_n = 990 g/mol, from Scientific Polymer Products Inc.) in toluene to 4% by mass and spin-coating the solution at 1000 RPM for 30 seconds onto the gold-coated silicon wafers. The toluene was filtered through a syringe-mounted filter membrane (Whatman Anodisc, diameter 13 mm, 0.02 μm pore size) prior to mixing with the PS, and the PS solution was filtered again immediately before deposition for spin-coating. The thickness of the resultant nanofilm was measured using ellipsometry with a source wavelength of 632.8 nm. The PS nanofilm thickness for the deformed Au/PS/Au sample (before deformation), the flat Au/PS/Au sample (before second metallization), and the PS/Au sample was 231.7 ± 0.6 nm, 229.3 ± 0.5 nm and 228.9 ± 0.9 nm, respectively. The PS thickness differences between the samples are small and will be neglected.

The PS nanofilm was sculpted using Conduction TCL to form an array of microprotrusions arranged in a hexagonal array. The same experimental setup in Figure 6.1(a) and (b) was used with hexagonal pin arrays (P = 50 μm, D = 25 μm, $s_0 = 1280 \pm 20$ nm, $d_1 = 540 \pm 20$ nm, $T_{\text{stage, cold}} = 30°\text{C}$, $T_{\text{stage, hot}} = 125°\text{C}$, $t = 20$ min) and the resultant arrays were imaged using scanning white light interferometry (Zemetrics Zegage).

Step 3: Second gold metallization

Since the low molecular weight PS used exhibited a large thermal expansion coefficient, the sculpted PS surface could not be metallized directly using the same sputtering protocol used in the first step to form the base gold layer. The hot sputtered material raised the temperature of the PS nanofilm and resulted in significant

thermal expansion. Upon cooling, the nanofilm relaxed more than the metallic coat and undesirable wrinkles formed at the surface. Furthermore, chromium could not be used as an adhesion layer due to its slow sputtering rate and hence long sputtering times. The rate of chromium sputtering at 80 mA constant current was approximately 0.1 nm per 3 seconds. Surface heating and thermal expansion was avoided by repeatedly sputter coating a small amount of material and allowing the sample to cool down in between sputtering runs. The adhesion layer material was chosen to be a platinum/palladium alloy (80:20 ratio, Ted Pella 91115, 99.99% purity) due to its significantly higher sputtering rate than chromium. 3.0 ± 0.1 nm of platinum/palladium was sputter-coated onto the PS surface, then 50 nm of gold was deposited onto the platinum/palladium subsequently in 16 steps, with argon flushing performed in between deposition runs. The first 14 steps deposited 3.0 ± 0.1 nm and the last 2 steps deposited 4.0 ± 0.1 nm to complete 50.0 nm of gold in total. Low vacuum was not broken in between deposition steps. The resultant gold coat was not observed to exhibit any wrinkling. The complete microcavity array was imaged again using scanning white light interferometry (Zemetrics Zegage).

Reflection spectroscopy

The microcavity array and the experimental controls were evaluated by examining the power reflectance as a function of wavelength and incident beam angle. The unpolarized output from a halogen white light source (Fostec 8375) was passed through a pinhole and focused using a long working distance microscopy objective (10x Mitutoyo Plan Apo, NA 0.28) onto the microcavity array surface. The minimum focused spot size was 1.5 mm and the spot was contained entirely within the microcavity array area. The reflected beam was captured using a spectrometer with electric dark correction (Ocean Optics USB4000) calibrated using a mercury-argon plasma lamp. Each sample was evaluated with a sensor exposure time of 100 ms and 200 ms, and each spectrum was averaged 30 times. The experimental sample was then replaced by each control sample under the exact same experimental conditions to obtain the reference spectra. The reflectance spectrum relative to any of the controls was obtained by taking the ratio of the spectrum of the experimental sample to that of the control samples. This process was repeated to obtain the reflectance spectrum for incident angles (measured from the normal) of 20° and 40°. Measurements were performed at several angles of incidence to differentiate systematic detector error from genuine spectral features. These features should exhibit a shift in wavelength as the angle of incidence is increased, which increases optical path

length associated with the sample material.

To obtain the normal incidence reflectance spectrum of the microcavity array, the array was imaged using an Olympus BX60 microscope configured in reflection mode. The array was brought into focus through a 20x microscope objective (Olympus UMPlanFl NA 0.46) and illuminated by a halogen lamp (Olympus U-LH100). The reflected image was directed into a spectrometer and the spectrum was averaged 30 times. This process was repeated for each of the control samples to obtain the reference spectra.

18.3 Results and Discussion

Effect of coating on surface roughness

The white light interferometry scans of each of the control surfaces and bare silicon wafers were used to calculate the root-mean-square surface roughness of each surface. The global curvature of the surface profiles was removed by fitting each surface topology to a surface with constant curvature:

$$z(x, y) = c_0 + c_1 x + c_2 y + c_3 x^2 + c_4 y^2 + c_5 xy \tag{18.1}$$

and subtracting the best fit surface from the surface topology. The root mean square roughness value was obtained by taking the root mean square deviation of the subtracted surface from its mean. The surface roughness of each sample was obtained by taking the arithmetic mean of the roughness measurement at three locations over the sample.

The RMS surface roughness of the clean silicon wafer was 2.19 ± 0.09 nm. Deposition of a PS nanofilm film onto the chromium/gold layer slightly increased the surface roughness to 2.46 ± 0.09 nm (flat PS/Au) and the deposition of the second platinum alloy/gold layer over the PS surface maintained the surface roughness at 2.5 ± 0.4 nm (flat Au/PS/Au). These low surface roughness values indicate that the sputter deposited metallic films and spin-coated PS nanofilms are indeed conformal to the flat silicon wafer surface, and preserve the smoothness of the surface. Since the TCL thermocapillary microfabrication process is sensitive to surface defects, largely due to the dewetting of polymer nanofilm around surface inhomogeneities, the smooth defect-free surfaces of these substrates were optimal for further fabrication.

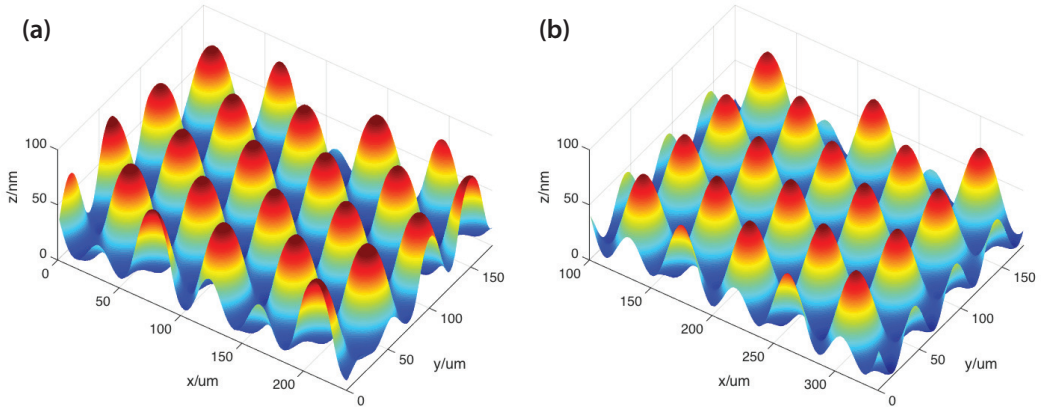

Figure 18.2: Scanning white light interferometry images of the microcavity array surface (a) before and (b) after sputter deposition of the second layer of gold. The vertical scale refers to the relative height differences and not the absolute film thickness. The surface topologies are virtually identical, indicating that the second gold layer formed a good conformal surface coating.

Surface topology of sculpted polymer film

The surface topologies of the microcavity array before and after sputtering the second gold layer are exhibited in Figures 18.2(a) and 18.2(b) respectively. The heights of the individual microcavities are much smaller (tens of nanometers) than the characteristic horizontal sizes of the cavities (tens of micrometers), indicating that the microcavities are shallow and nearly flat. The surfaces are virtually identical and indicate that the second gold layer formed an excellent conformal coat over the polystyrene surface. The lack of surface wrinkling and lack of bubble formation over the second gold coat indicated that the second coating exhibited good adhesion to the PS surface.

The radius of curvature of the fabricated microcavity array was estimated by fitting the central surface topology of each protrusion (prior to the second gold coat) to that of a rotated paraboloid:

$$z(x, y) = z_{\max} - \frac{(x')^2}{2R_1} - \frac{(y')^2}{2R_2} \tag{18.2}$$

$$\begin{pmatrix} x' \\ y' \end{pmatrix} = \begin{pmatrix} \cos\theta & -\sin\theta \\ \sin\theta & \cos\theta \end{pmatrix} \begin{pmatrix} x - x_0 \\ y - y_0 \end{pmatrix} \tag{18.3}$$

where $R_{1,2}$ is the radius of curvature along the lateral principal axes x', y', which are rotated by an angle θ with respect to the raw data axes x, y. (x_0, y_0) is the coordinate

of the microcavity vertex in the raw data coordinates, and $z_{\max}$ is the height of the protrusion at its vertex. 25 microprotrusions at different locations over the entire microcavity array were fitted using this procedure. The radius of curvature of the entire array was taken to be the arithmetic average of the principal radii of curvature for each microprotrusion and was calculated to be 2.8 ± 0.3 mm. The variation in measured curvatures was likely due to small tilts in the cold stage mask over the nanofilm and can be minimized by fabricating cold stage masks with less variation in spacer heights s_0.

The planar face at the base of the PS nanofilm and the sculpted curved surface topology form a standing wave optical resonator. Since the post-sculpting film thickness could not be measured directly (the profiles in Figure 18.2 are relative height differences instead of absolute film thicknesses) we took the initial film thickness to be the resonator length L as a first approximation. The stability parameter g for each of the surfaces is given by:

$$g_i = 1 - \frac{nL}{R_i} \tag{18.4}$$

where L is the resonator geometrical length, n is the refractive index of the medium (taken to be around 1.58 in the visible spectrum), and R_i is the radius of curvature of the ith surface. The stability parameter for the curved surface using the measured value of the radius of curvature is slightly less than unity: $1 - 1.3 \times 10^{-4}$, and the stability parameter for the planar surface is exactly unity. The product of the two stability parameters yields a value slightly less than unity, indicating that the microcavities form strictly stable resonators.

Reflectance spectra studies

We may evaluate the theoretical optical performance of the PS nanofilm by treating it as a plane-parallel Fabry-Perot cavity. The various metallic layers sandwiching the nanofilm can be combined using the Fresnel equations to find the effective reflective behavior of the upper and lower coatings. Figure 18.3(a) exhibits the theoretical reflectance spectrum from the polystyrene nanofilm onto each of the upper and lower metallic films. The reflectance spectra were obtained from the Filmetrics reflectance calculator using the complex-matrix form of the Fresnel equations at normal incidence, and incorporated the thickness of the metallic layers in the experimental microcavity array. The medium in both upper and lower reflectance calculations was taken to have a refractive index of 1.58 at 632.8 nm. The substrate for the lower reflectance calculation was taken to be 50 nm of gold and 5 nm of chromium on a

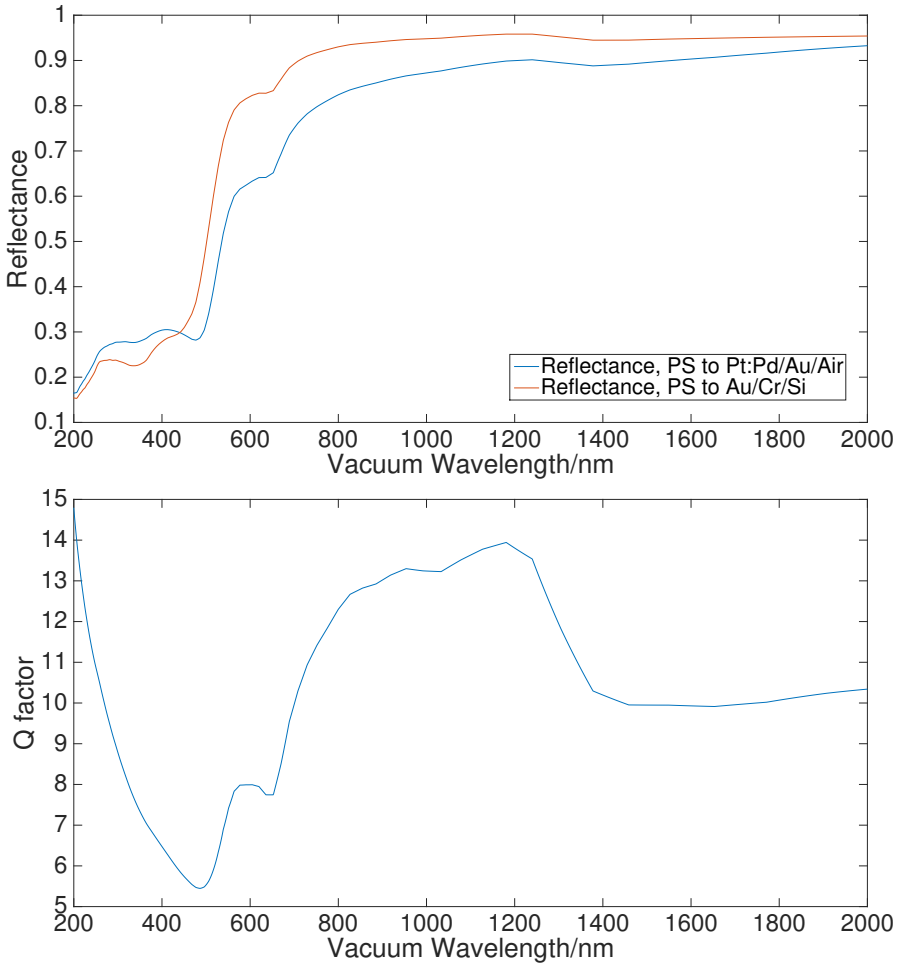

Figure 18.3: (a) Theoretical absolute reflectance spectrum from the PS nanofilm onto the upper (blue line) and lower (orange line) surfaces. (b) Theoretical Q-factor of a Fabry-Perot optical cavity with the reflectance profile in (a) and incorporating the experimental materials and dimensions.

semi-infinite base of silicon. The substrate for the upper reflectance calculation was taken to be 3 nm of platinum and 50 nm of gold on a semi-infinite base of air.

Assuming a lossless polystyrene medium, the reflectances off the upper and lower surfaces can be used to estimate the Q-factors associated with a Fabry-Perot cavity operating at that incident vacuum wavelength. The Q-factor is given by:

$$Q = 2\pi f_0 \frac{E}{-dE/dt} \approx 2\pi f_0 \frac{\Delta t}{-\Delta E/E} \tag{18.5}$$

where f_0 is the resonant frequency of the cavity, E is the stored energy and $-dE/dt$ is the rate of power dissipation from the cavity. In the limit where the round-trip loss $-\Delta E/E = 1 - R_1(\lambda)R_2(\lambda)$ is small, where $R_1(\lambda)$ and $R_2(\lambda)$ are the reflectance

values of each of the effective mirrors as a function of wavelength, the Q-factor can be written in terms of the round-trip loss and the round-trip time Δt. The round trip time is also a wavelength-dependent relation:

$$\Delta t(\lambda) = \frac{2L}{c/n(\lambda)} \tag{18.6}$$

Taking the refractive index of the PS to have the dispersion relation [101]:

$$n(\lambda)^2 - 1 = \frac{1.4435(\lambda/\mu\text{m})^2}{(\lambda/\mu\text{m})^2 - 0.020216} \tag{18.7}$$

the estimated Q-factors as a function of incident vacuum wavelength is exhibited in Figure 18.3(b). The low Q-factors in the visible light range (400 nm - 700 nm) indicate that the microcavity array is expected to behave as a poor optical resonator in the visible and will be expected to have a broad resonant linewidth.

Figure 18.4 exhibits the relative reflectance spectra obtained between pairwise selections of samples, along with the theoretical relative reflectance spectra obtained using the Filmetrics reflectance calculator for flat samples at normal incidence. Figure 18.4(a) exhibits the effect of adding a PS nanofilm over a bare lower gold coat. The absorption at shorter wavelengths is due to thin film interference effects and not due to bulk absorption, since PS is transparent in the visible. The polystyrene acts as an antireflective coating at wavelengths where the optical path length between the air-PS reflection and PS-gold reflection equals a half-integer number of vacuum wavelengths. The minimum does not occur at the expected wavelength corresponding to simple thin film interference due to the large imaginary part of the gold refractive index that changes the reflected wave phase by an angle between 0 and 180°. The phase shift at normal incidence from a medium of real refractive index n_0 onto a medium with complex refractive index $n_1 - ik_1$ is given by [102]:

$$\phi = \pi - \tan^{-1}\left[\frac{2n_0k_1}{n_1^2 + k_1^2 - n_0^2}\right] \tag{18.8}$$

which takes on values between 0 and 180° for nonzero k_1. Simulation of the material stack reflectivity at normal incidence yielded a predicted minimum reflection wavelength of 513 nm in the visible range (Figure 18.4(a) black line), which is close to the measured minimum of 495 nm at normal incidence (Figure 18.4(a) red line). The slight deviation from the theoretical plot may be due to an unobserved slight inclination of the sample on the microscope stage during normal angle incidence measurement. As the angle of incidence increases away from the normal, the

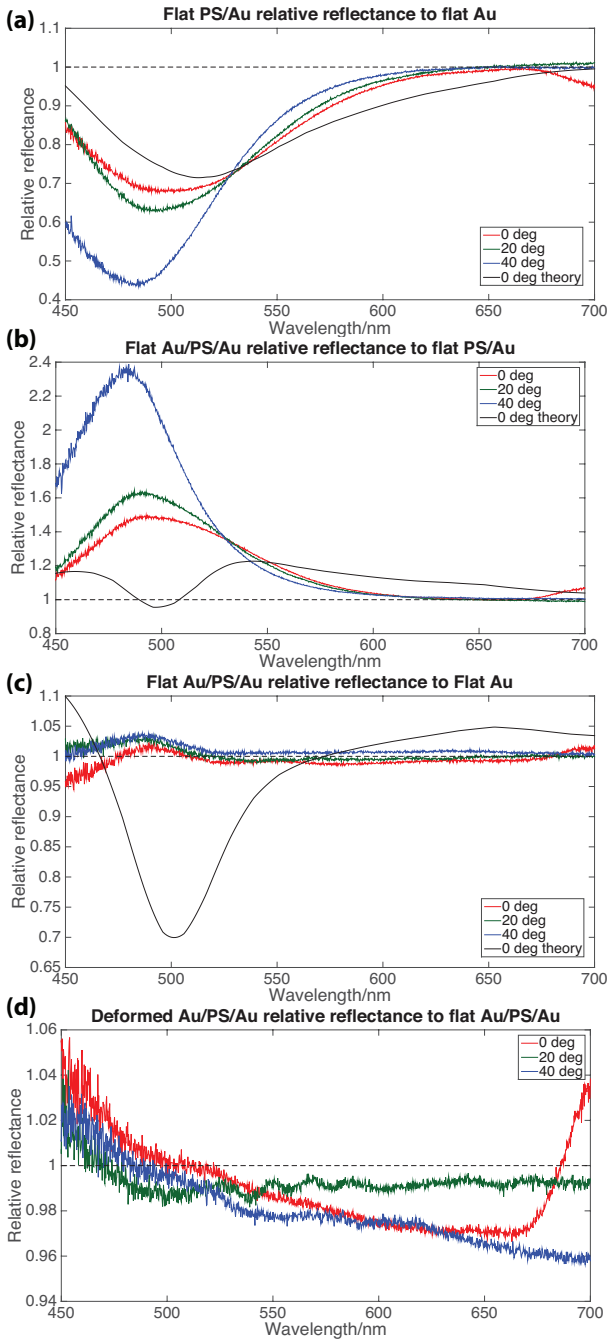

Figure 18.4: Measured relative reflectance values over the visible spectrum with theoretical reflectance spectrum. (a) Reflectance spectrum of the flat PS/Au sample relative to that of the flat Au sample. This relative spectrum arises due to the presence of a PS nanofilm on the former. (b) Reflectance spectrum of the flat Au/PS/Au sample relative to that of the flat PS/Au sample. This relative spectrum arises due to the presence of the second gold coat on the former. (c) Reflectance spectrum of the flat Au/PS/Au sample relative to that of the flat Au sample. This relative spectrum arises due to the presence of a PS layer and second gold layer on the former. (d) Reflectance spectrum of the deformed Au/PS/Au sample relative to that of the flat Au/PS/Au. This relative spectrum arises due to the presence of nanofilm deformation in the former sample.

wavelength of minimum reflectivity decreases and the minimum reflectivity value decreases. The latter corresponds to the greater dissipation at the PS-gold interface.

Figure 18.4(b) exhibits the effect of adding a second gold reflection layer (with the platinum/palladium adhesion layer) over a flat PS nanofilm. The enhanced reflection at the air-gold interface reduces the power dissipated at the lower PS-gold interface, resulting in the largest boost in reflectivity for the 40° angle of incidence sample. The observed relative reflectance spectrum for normal incidence does not match the theoretical relative reflectance spectrum. The observed normal incidence spectrum exhibits a maximum around 500 nm, whereas the theoretical spectrum exhibits a minimum there. The exact reason behind the mismatch is not known. It is possible that the process of sputtering the second gold layer introduced some large-scale redistribution of PS. However, no physical bulges were observed under scanning white light interferometry of the flat Au/PS/Au sample and the sample appeared completely flat under light microscopy. It is also possible that the multiple deposition steps during the formation of the second gold mirror may have introduced additional inhomogeneities between layers and not formed a continuous thick gold layer. This possibility can be explored further using cross-sectional scanning electron microscopy. The observed enhanced reflectivity may also be an artifact of the measurement process. The incident light source had relatively lower intensities at wavelengths less than 500 nm, which may have increased the uncertainty in the measured intensity at those wavelengths. This measurement can be repeated using more accurate instruments at a broader range of wavelengths in the future. Another possibility is that the gold optical parameters used in the Fresnel equation calculation did not match the effective optical parameters for a thin gold film. The Filmetrics reflectance calculator uses a proprietary set of optical parameters that cannot be set externally. Future work should perform the relative reflectance calculation using the measured optical characteristics of the 50 nm gold film instead and investigate if this perturbation is responsible for the deviation between theory and experiment.

The combined effect of the PS nanofilm and the second gold reflection layer is exhibited in Figure 18.4(c), which plots the relative reflectance spectrum for the flat Au/PS/Au sample with respect to the flat Au sample. Despite the uppermost surface being gold in each case, it is evident that the former sample exhibits a slightly enhanced reflectivity at around 500 nm with respect to the latter. This enhanced reflectivity was not expected. Based on the optical characteristics of the materials

used, the flat Au/PS/Au sample is expected to exhibit a decreased reflectivity at 500 nm to around 70% of the reflectivity of the flat Au sample (theoretical black line).

Figure 18.4(d) plots the relative reflectance of the deformed Au/PS/Au array with respect to that of the flat Au/PS/Au sample, and exhibits the effect of sculpting the PS layer before depositing the second reflective gold layer. There are no clear trends as the angle of incidence is increased from 0° to 40° apart from the slight decrease in reflectivity at longer wavelengths. At normal incidence, there appears to be a local minimum in relative reflectivity at 660 nm, but this feature is not observed in the other two angles, possibly due to the inaccessibility of the longer wavelength domain in the instrument used. Nevertheless, the variation of the relative reflectivity with wavelength indicates that the deformation of the surface into an array of microprotrusions did slightly alter the reflective properties of the surface.

18.4 Outlook

We report the successful fabrication of an array of microcavities formed through the metallization of a Conduction TCL-sculpted PS nanofilm through sputter coating. The smoothness of the underlying silicon wafer was preserved under gold sputter deposition, spin-coating of PS, and a second gold sputter deposition. The second coating of gold did not produce the theoretically expected relative reflectance spectrum. Further work is necessary to investigate the effect of metallizing the polymer surface, perhaps through cross-sectional scanning electron microscopy. The sculpting of the PS layer into an array of microprotrusions appeared to slightly decrease the reflectivity of the sculpted surface at longer wavelengths as compared to the unsculpted surface. Further measurement with a wider range of wavelengths is necessary to fully characterize the properties of the fabricated microcavity arrays in view of the small Q-factors and poorly-defined features involved. The far-IR behavior of the microcavity array is particularly relevant since inter-cavity coupling should occur on the length scale of tens of microns. Future work may involve sandwiching the PS nanofilm in between Bragg mirrors so as to achieve greater surface reflectivity from the PS material, larger Q-factors, and better defined resonant spectral features.

BIBLIOGRAPHY

[1]R. F. Probstein, *Physicochemical Hydrodynamics: An Introduction*, 1st (Butterworth Publishers, Massachusetts, 1989).

[2]J. Thomson, "XLII. On certain curious motions observable at the surfaces of wine and other alcoholic liquors", Philos. Mag. 4 **10**, 330–333 (1855).

[3]D. W. G. White, "The surface tensions of Indium and Cadmium", Metall. Trans. **3**, 1933–1936 (1972).

[4]J. W. Nowok, J. P. Hurley, and J. A. Bieber, "The cause of surface tension increase with temperature in multicomponent aluminosilicates derived from coal-ash slags", J. Mater. Sci. **30**, 361–364 (1995).

[5]G. Taylor, "The instability of liquid surfaces when accelerated in a direction perpendicular to their planes. I", P. Roy. Soc. Lond. A Mat. **201**, 192–196 (1950).

[6]J. W. S. Rayleigh, "Investigation of the character of the equilibrium of an incompressible heavy fluid of variable density", in *Scientific Papers*, Vol. 2 (Cambridge University Press, Cambridge, 1899) Chap. 100, pp. 200–207.

[7]E. Schäffer, T. Thurn-Albrecht, T. P. Russell, and U. Steiner, "Electrically induced structure formation and pattern transfer", Nature **403**, 874–877 (2000).

[8]E. Schäffer, T. Thurn-Albrecht, T. P. Russell, and U. Steiner, "Electrohydrodynamic instabilities in polymer films", Europhys. Lett. **53**, 518 (2001).

[9]H. Bénard, "Les tourbillons cellulaires dans une nappe liquide. - méthodes optiques d'observation et d'enregistrement", J. Phys. Theo. Appl. **10**, 254–266 (1901).

[10]M. J. Block, "Surface tension as the cause of benard cells and surface deformation in a liquid film", Nature **178**, 650–651 (1956).

[11]M. Dietzel and S. M. Troian, "Formation of nanopillar arrays in ultrathin viscous films: the critical role of thermocapillary stresses", Phys. Rev. Lett. **103**, 074501 (2009).

[12]M. Dietzel and S. M. Troian, "Mechanism for spontaneous growth of nanopillar arrays in ultrathin films subject to a thermal gradient", J. Appl. Phys. **108**, 074308 (2010).

[13]E. McLeod, Y. Liu, and S. M. Troian, "Experimental verification of the formation mechanism for pillar arrays in nanofilms subject to large thermal gradients", Phys. Rev. Lett. **106**, 175501 (2011).

[14]A. Oron, S. H. Davis, and S. G. Bankoff, "Long-scale evolution of thin liquid films", Rev. Mod. Phys. **69**, 931–980 (1997).

[15]G. Leal, *Advanced transport phenomena: fluid mechanics and convective transport processes* (Cambridge University Press, Cambridge, 2007).

[16]W. Haynes, *CRC Handbook of Chemistry and Physics*, 97th (CRC Press, 2016).

[17]O. Urakawa, S. F. Swallen, M. D. Ediger, and E. D. von Meerwall, "Self-diffusion and viscosity of low molecular weight polystyrene over a wide temperature range", Macromolecules **37**, 1558–1564 (2004).

[18]S. Y. Chou and L. Zhuang, "Lithographically induced self-assembly of periodic polymer micropillar arrays", J. Vac. Sci. Technol. B **17**, 3197–3202 (1999).

[19]C. S. Y., Z. Lei, and G. Linjie, "Lithographically induced self-construction of polymer microstructures for resistless patterning", Appl. Phys. Lett. **75**, 1004–1006 (1999).

[20]K. R. Fiedler and S. M. Troian, "Early time instability in nanofilms exposed to a large transverse thermal gradient: improved image and thermal analysis", J. Appl. Phys. **120**, 205303 (2016).

[21]H. Zappe, *Fundamentals of micro-optics* (Cambridge University Press, 2010).

[22]E. McLeod and S. M. Troian, "One step non-contact fabrication of polymer microlens arrays by thermocapillary lithography", CLEO:2011 - Laser Applications to Photonic Applications, CML3 (2011).

[23]M. D. Dickey, E. Collister, A. Raines, P. Tsiartas, T. Holcombe, S. V. Sreenivasan, R. T. Bonnecaze, and C. G. Willson, "Photocurable pillar arrays formed via electrohydrodynamic instabilities", Chem. Mater. **18**, 2043–2049 (2006).

[24]Y. J. Lee, Y. W. Kim, Y. K. Kim, C. J. Yu, J. S. Gwag, and J. H. Kim, "Microlens array fabricated using electrohydrodynamic instability and surface properties", Opt. Express **19**, 10673–10678 (2011).

[25]P. S. G. Pattader, I. Banerjee, A. Sharma, and D. Bandyopadhyay, "Multiscale pattern generation in viscoelastic polymer films by spatiotemporal modulation of electric field and control of rheology", Adv. Funct. Mater. **21**, 324–335 (2011).

[26]X. Li, H. Tian, Y. Ding, J. Shao, and Y. Wei, "Electrically templated dewetting of a UV-curable prepolymer film for the fabrication of a concave microlens array with well-defined curvature", ACS Appl. Mater. Inter. **5**, 9975–9982 (2013).

[27]H. Tian, Y. Ding, J. Shao, X. Li, and H. Liu, "Formation of irregular micro- or nano-structure with features of varying size by spatial fine-modulation of electric field", Soft Matter **9**, 8033–8040 (2013).

[28]G. Liu, W. Yu, H. Li, J. Gao, D. Flynn, R. W. Kay, S. Cargill, C. Tonry, M. K. Patel, C. Bailey, and M. P. Y. Desmulliez, "Microstructure formation in a thick polymer by electrostatic-induced lithography", J. Micromech. Microeng. **23**, 035018 (2013).

[29]V. Vespini, O. Gennari, S. Coppola, G. Nasti, L. Mecozzi, V. Pagliarulo, S. Grilli, C. Carfagna, and P. Ferraro, "Electrohydrodynamic assembly of multiscale PDMS microlens arrays", IEEE J. Sel. Top. Quant. **21**, 1–8 (2015).

[30]J. Xia, D. Qu, H. Yang, J. Chen, and W. Zhu, "Self assembly polymer microlens array for integral imaging", Displays **31**, 186–190 (2010).

[31]J. M. Katzenstein, D. W. Janes, J. D. Cushen, N. B. Hira, D. L. McGuffin, N. A. Prisco, and C. J. Ellison, "Patterning by photochemically directing the Marangoni effect", ACS Macro Lett. **1**, 1150–1154 (2012).

[32]D. W. Janes, J. M. Katzenstein, K. Shanmuganathan, and C. J. Ellison, "Directing convection to pattern thin polymer films", J. Polym. Sci. Pol. Phys. **51**, 535–545 (2013).

[33]T. A. Arshad, C. B. Kim, N. A. Prisco, J. M. Katzenstein, D. W. Janes, R. T. Bonnecaze, and C. J. Ellison, "Precision Marangoni-driven patterning", Soft Matter **10**, 8043–8050 (2014).

[34]C. Bin Kim, D. W. Janes, D. L. McGuffin, and C. J. Ellison, "Surface energy gradient driven convection for generating nanoscale and microscale patterned polymer films using photosensitizers", J. Polym. Sci. Pol. Phys. **52**, 1195–1202 (2014).

[35]C. B. Kim, S. X. Zhou, D. L. Heilman, D. W. Janes, and C. J. Ellison, "Surface tension driven flow in a low molecular weight photopolymer", J. Photopolym. Sci. Tech. **28**, 67–71 (2015).

[36]E. Schäffer, S. Harkema, M. Roerdink, R. Blossey, and U. Steiner, "Thermo-mechanical lithography: pattern replication using a temperature gradient driven instability", Adv. Mater. **15**, 514–517 (2003).

[37]S. Walheim, M. Böltau, J. Mlynek, G. Krausch, and U. Steiner, "Structure formation via polymer demixing in spin-cast films", Macromolecules **30**, 4995–5003 (1997).

[38]M. Böltau, S. Walheim, J. Mlynek, G. Krausch, and U. Steiner, "Surface-induced structure formation of polymer blends on patterned substrates", Nature **391**, 877–879 (1998).

[39]O. Karthaus, L. Gråsjö, N. Maruyama, and M. Shimomura, "Formation of ordered mesoscopic polymer arrays by dewetting", Chaos **9**, 308–314 (1999).

[40]H. Tze Yang, L. Changqing, P. P. Conway, Y. Weixing, S. Cargill, and M. P. Y. Desmulliez, "Fabrication of a polymeric optical waveguide-on-flex using electrostatic-induced lithography", IEEE Photonic Tech. L. **22**, 957–959 (2010).

[41]I. Nejati, M. Dietzel, and S. Hardt, "Exploiting cellular convection in a thick liquid layer to pattern a thin polymer film", Appl. Phys. Lett. **108**, 051604 (2016).

[42]J. P. Singer, "Thermocapillary approaches to the deliberate patterning of polymers", J. Polym. Sci. Pol. Phys. (2017) 10.1002/polb.24298.

[43]J. R. Melcher, *Field-coupled surface waves* (MIT Press, Cambridge, 1963).

[44]J. M. Reynolds, "Stability of an electrostatically supported fluid column", Phys. Fluids **8**, 161–170 (1965).

[45]A. Corbett and S. Kumar, "Combined thermal and electrohydrodynamic patterning of thin liquid films", J. Eng. Math. **94**, 1–16 (2013).

[46]M. Dietzel and S. M. Troian, "Thermocapillary patterning of nanoscale polymer films", MRS Proc. **1179** (2009) 10.1557/PROC-1179-BB08-02.

[47]S. Troian, *Method and apparatus for the controlled fabrication of micro and nanoscale structures by thermocapillary lithography*, US Patent 8,793,006 B2, 2014.

[48]S. Kedenburg, M. Vieweg, T. Gissibl, and H. Giessen, "Linear refractive index and absorption measurements of nonlinear optical liquids in the visible and near-infrared spectral region", Opt. Mater. Express **2**, 1588–1611 (2012).

[49]J. Rheims, J. Köser, and T. Wriedt, "Refractive-index measurements in the near-IR using an Abbe refractometer", Meas. Sci. Technol. **8**, 601 (1997).

[50]E. Sani and A. Dell'Oro, "Optical constants of ethylene glycol over an extremely wide spectral range", Opt. Mater. **37**, 36–41 (2014).

[51]C. A. Schneider, W. S. Rasband, and K. W. Eliceiri, "NIH Image to ImageJ: 25 years of image analysis", Nat. Methods **9**, 671–675 (2012).

[52]J. Schindelin, I. Arganda-Carreras, E. Frise, V. Kaynig, M. Longair, T. Pietzsch, S. Preibisch, C. Rueden, S. Saalfeld, B. Schmid, J.-Y. Tinevez, D. J. White, V. Hartenstein, K. Eliceiri, P. Tomancak, and A. Cardona, "Fiji: an open-source platform for biological-image analysis", Nat. Methods **9**, 676–682 (2012).

[53]Q. Tseng, "Study of multicellular architecture with controlled microenvironment", Thesis (Université de Grenoble, 2011).

[54]J. Mark, *Physical properties of polymers handbook*, 2nd (Springer New York, New York, 2007).

[55]S. W. Hell and J. Wichmann, "Breaking the diffraction resolution limit by stimulated emission: stimulated-emission-depletion fluorescence microscopy", Opt. Lett. **19**, 780–782 (1994).

[56]G. S. Kino and S. S. C. Chim, "Mirau correlation microscope", Appl. Optics **29**, 3775–3783 (1990).

[57]P. J. De Groot and X. C. de Lega, "Transparent film profiling and analysis by interference microscopy", in *Interferometry xiv: applications*, Vol. 7064 (SPIE, San Diego, 2008), p. 70640I.

[58]J. P. Singer, K. W. Gotrik, J. H. Lee, S. E. Kooi, C. A. Ross, and E. L. Thomas, "Alignment and reordering of a block copolymer by solvent-enhanced thermal laser direct write", Polymer **55**, 1875–1882 (2014).

[59]H. M. J. M. Wedershoven, C. W. J. Berendsen, J. C. H. Zeegers, and A. A. Darhuber, "Infrared laser induced rupture of thin liquid films on stationary substrates", Appl. Phys. Lett. **104**, 054101 (2014).

[60]J.-H. Yoo, J. B. In, C. Zheng, I. Sakellari, R. N. Raman, M. J. Matthews, S. Elhadj, and C. P. Grigoropoulos, "Directed dewetting of amorphous silicon film by a donut-shaped laser pulse", Nanotechnology **26**, 165303 (2015).

[61]P. W. Majewski and K. G. Yager, "Millisecond ordering of block copolymer films via photothermal gradients", ACS Nano **9**, 3896–3906 (2015).

[62]J. P. Singer, S. E. Kooi, and E. L. Thomas, "Focused laser-induced Marangoni dewetting for patterning polymer thin films", J. Polym. Sci. Pol. Phys. **54**, 225–236 (2016).

[63]T. Inagaki, E. T. Arakawa, R. N. Hamm, and M. W. Williams, "Optical properties of polystyrene from the near-infrared to the x-ray region and convergence of optical sum rules", Phys. Rev. B **15**, 3243–3253 (1977).

[64]S. A. Self, "Focusing of spherical gaussian beams", Appl. Optics **22**, 658–661 (1983).

[65]M. A. Green, "Self-consistent optical parameters of intrinsic silicon at 300 K including temperature coefficients", Sol. Energ. Mat. Sol. C. **92**, 1305–1310 (2008).

[66]D. Y. Kim, S. K. Tripathy, L. Li, and J. Kumar, "Laser-induced holographic surface relief gratings on nonlinear optical polymer films", Appl. Phys. Lett. **66**, 1166–1168 (1995).

[67]P. Rochon, E. Batalla, and A. Natansohn, "Optically induced surface gratings on azoaromatic polymer films", Appl. Phys. Lett. **66**, 136–138 (1995).

[68]C. B. Kim, J. C. Wistrom, H. Ha, S. X. Zhou, R. Katsumata, A. R. Jones, D. W. Janes, K. M. Miller, and C. J. Ellison, "Marangoni instability driven surface relief grating in an azobenzene-containing polymer film", Macromolecules **49**, 7069–7076 (2016).

[69]J. P. Singer, S. E. Kooi, and E. L. Thomas, "Focused laser spike (FLaSk) annealing of photoactivated chemically amplified resists for rapid hierarchical patterning", Nanoscale **3**, 2730–2738 (2011).

[70]K. M. Davis, K. Miura, N. Sugimoto, and K. Hirao, "Writing waveguides in glass with a femtosecond laser", Opt. Lett. **21**, 1729–1731 (1996).

[71]B. N. Chichkov, C. Momma, S. Nolte, F. von Alvensleben, and A. Tünnermann, "Femtosecond, picosecond and nanosecond laser ablation of solids", Appl. Phys. A **63**, 109–115 (1996).

[72]S. D. Correa, M. J. Almeida, F. G. Almeida, R. M. Cardoso, L. De Boni, and R. C. Mendonça, "Ultrafast laser pulses for structuring materials at micro/nano scale: from waveguides to superhydrophobic surfaces", Photonics **4** (2017) 10.3390/photonics4010008.

[73]A. Sugar, "Ultrafast (femtosecond) laser refractive surgery", Curr. Opin. Ophthalmol. **13**, 246–249 (2002).

[74]J. Kuryan, A. Cheema, and R. S. Chuck, "Laser-assisted subepithelial keratectomy (LASEK) versus laser-assisted in-situ keratomileusis (LASIK) for correcting myopia", Cochrane Db. Syst. Rev. **2**, CD011080 (2017).

[75]D. D. Gu, W. Meiners, K. Wissenbach, and R. Poprawe, "Laser additive manufacturing of metallic components: materials, processes and mechanisms", Int. Mater. Rev. **57**, 133–164 (2012).

[76]I. Mingareev and M. Richardson, "Laser additive manufacturing: going mainstream", Opt. Phot. News **28**, 24–31 (2017).

[77]G. D. Costa and J. Calatroni, "Transient deformation of liquid surfaces by laser-induced thermocapillarity", Appl. Optics **18**, 233–235 (1979).

[78]G. Da Costa, "Self-focusing of a Gaussian laser beam reflected from a thermocapillary liquid surface", Phys. Lett. A **80**, 320–322 (1980).

[79]J. Hartikainen, J. Jaarinen, and M. Luukkala, "Deformation of a liquid surface by laser heating: laser-beam self-focusing and generation of capillary waves", Can. J. Phys. **64**, 1341–1344 (1986).

[80]T. R. Anthony and H. E. Cline, "Surface rippling induced by surface-tension gradients during laser surface melting and alloying", J. Appl. Phys. **48**, 3888–3894 (1977).

[81]D. Gentili, G. Foschi, F. Valle, M. Cavallini, and F. Biscarini, "Applications of dewetting in micro and nanotechnology", Chem. Soc. Rev. **41**, 4430–4443 (2012).

[82]J. P. Singer, P.-T. Lin, S. E. Kooi, L. C. Kimerling, J. Michel, and E. L. Thomas, "Direct-write thermocapillary dewetting of polymer thin films by a laser-induced thermal gradient", Adv. Mater. **25**, 6100–6105 (2013).

[83]Z. D. Popovic, R. A. Sprague, and G. A. Neville Connell, "Technique for monolithic fabrication of microlens arrays", Appl. Optics **27**, 1281–1284 (1988).

[84]A. Sharma and G. Reiter, "Instability of thin polymer films on coated substrates: rupture, dewetting, and drop formation", J. Colloid Interf. Sci. **178**, 383–399 (1996).

[85]G. E. Artzner, "Microlens arrays for Shack-Hartmann wavefront sensors", Opt. Eng. **31**, 1311–1322 (1992).

[86]J. Liang and D. R. Williams, "Aberrations and retinal image quality of the normal human eye", J. Opt. Soc. Am. A **14**, 2873–2883 (1997).

[87]B. Platt and R. Shack, "History and principles of Shack-Hartmann wavefront sensing", J. Refract. Surg. **17**, S573–S577 (2001).

[88]N. Hodgson and H. Weber, *Optical resonators: fundamentals, advanced concepts and applications* (Springer, United Kingdom, 1997).

[89]M. H. Gregory and L. S. Collaboration, "Advanced LIGO: the next generation of gravitational wave detectors", Classical Quant. Grav. **27**, 084006 (2010).

[90]K. Vahala, "Optical microcavities", Nature **424**, 839–846 (2003).

[91]J. M. Gérard, D. Barrier, J. Y. Marzin, R. Kuszelewicz, L. Manin, E. Costard, V. Thierry-Mieg, and T. Rivera, "Quantum boxes as active probes for photonic microstructures: the pillar microcavity case", Appl. Phys. Lett. **69**, 449–451 (1996).

[92]G. S. Solomon, M. Pelton, and Y. Yamamoto, "Modification of spontaneous emission of a single quantum dot", Phys. Status Solidi A **178**, 341–344 (2000).

[93]J. Buck and H. Kimble, "Optimal sizes of dielectric microspheres for cavity QED with strong coupling", Phys. Rev. A **67**, 033806 (2003).

[94]D. K. Armani, T. J. Kippenberg, S. M. Spillane, and K. J. Vahala, "Ultra-high-Q toroid microcavity on a chip", Nature **421**, 925–928 (2003).

[95]S. McCall, A. Levi, R. Slusher, S. Pearton, and R. Logan, "Whispering-gallery mode microdisk lasers", Appl. Phys. Lett. **60**, 289–291 (1992).

[96]B. Gayral, J. Gérard, A. Lemaître, C. Dupuis, L. Manin, and J. Pelouard, "High-Q wet-etched GaAs microdisks containing InAs quantum boxes", Appl. Phys. Lett. **75**, 1908–1910 (1999).

[97]S. T. Chu, B. E. Little, W. Pan, T. Kaneko, S. Sato, and Y. Kokubun, "An eight-channel add-drop filter using vertically coupled microring resonators over a cross grid", IEEE Photonic Tech. L. **11**, 691–693 (1999).

[98]F. Ding, T. Stöferle, L. Mai, A. Knoll, and R. F. Mahrt, "Vertical microcavities with high Q and strong lateral mode confinement", Phys. Rev. B **87**, 161116 (2013).

[99]L. Mai, F. Ding, T. Stöferle, A. Knoll, B. Jan Offrein, and R. F. Mahrt, "Integrated vertical microcavity using a nano-scale deformation for strong lateral confinement", Appl. Phys. Lett. **103**, 243305 (2013).

[100]D. Urbonas, T. Stöferle, F. Scafirimuto, U. Scherf, and R. F. Mahrt, "Zero-dimensional organic exciton–polaritons in tunable coupled Gaussian defect microcavities at room temperature", ACS Photonics **3**, 1542–1545 (2016).

[101]N. Sultanova, S. Kasarova, and I. Nikolov, "Dispersion properties of optical polymers", Acta Phys. Pol. A **116**, 585–587 (2009).

[102]T. Doi, K. Toyoda, and Y. Tanimura, "Effects of phase changes on reflection and their wavelength dependence in optical profilometry", Appl. Optics **36**, 7157–7161 (1997).

Appendix A

DRAWINGS OF CONDUCTION THERMOCAPILLARY LITHOGRAPHY HOT RESERVOIR

Included in the following pages are the CAD drawings of the lower and upper halves (in order) of the Conduction TCL hot reservoir. The rectangular crevice in the lower half accommodates the square ceramic heating element. These components were fabricated by the Instrument Shop in Caltech.

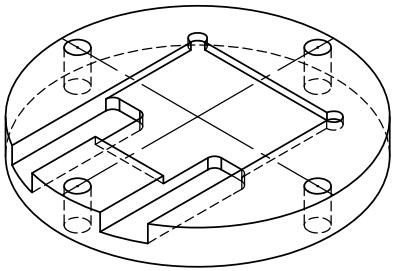

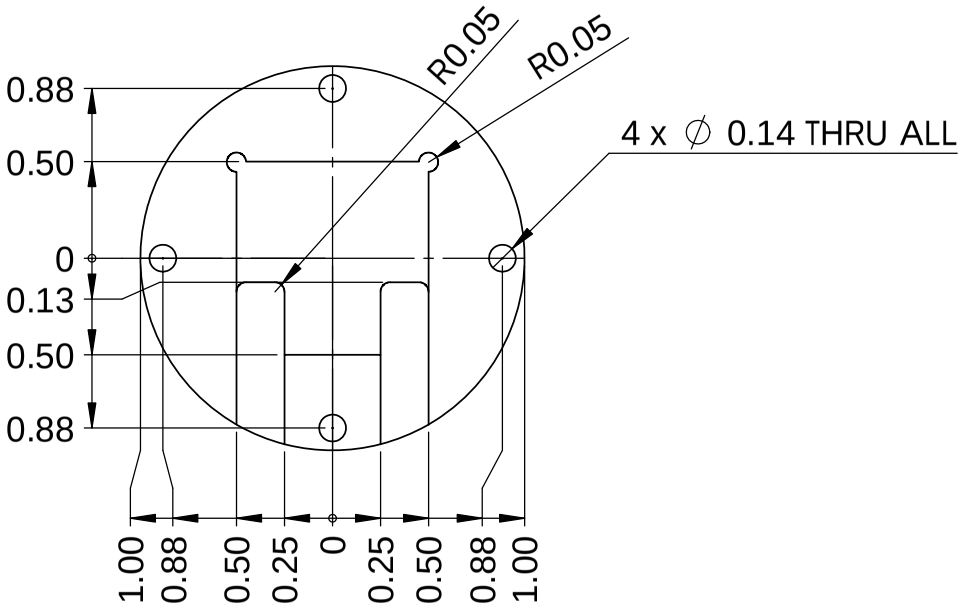

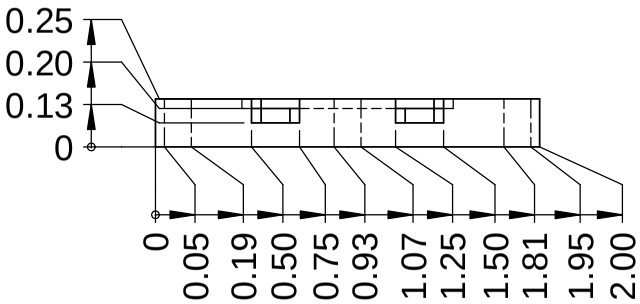

UNLESS OTHERWISE SPECIFIED:		NAME	DATE
DIMENSIONS ARE IN INCHES TOLERANCES: FRACTIONAL ± ANGULAR: MACH ± BEND ± TWO PLACE DECIMAL ± THREE PLACE DECIMAL ±	DRAWN		
	CHECKED		
	ENG APPR.		
	MFG APPR.		
	Q.A.		
INTERPRET GEOMETRIC TOLERANCING PER:	COMMENTS:		
MATERIAL: Aluminum			
FINISH: Hand Polish			
DO NOT SCALE DRAWING			

TITLE:

Daniel Lim
danlimsw@caltech.edu

140

SIZE	DWG. NO.	REV
A	TCSetup_CircularHolder_Bottom_v1	

SCALE: 1:1	WEIGHT:	SHEET 1 OF 1

5 4 3 2 1

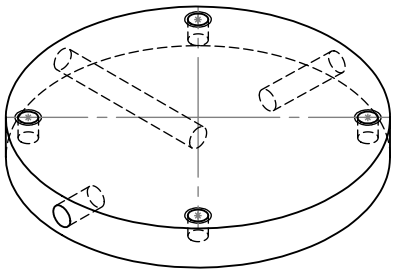

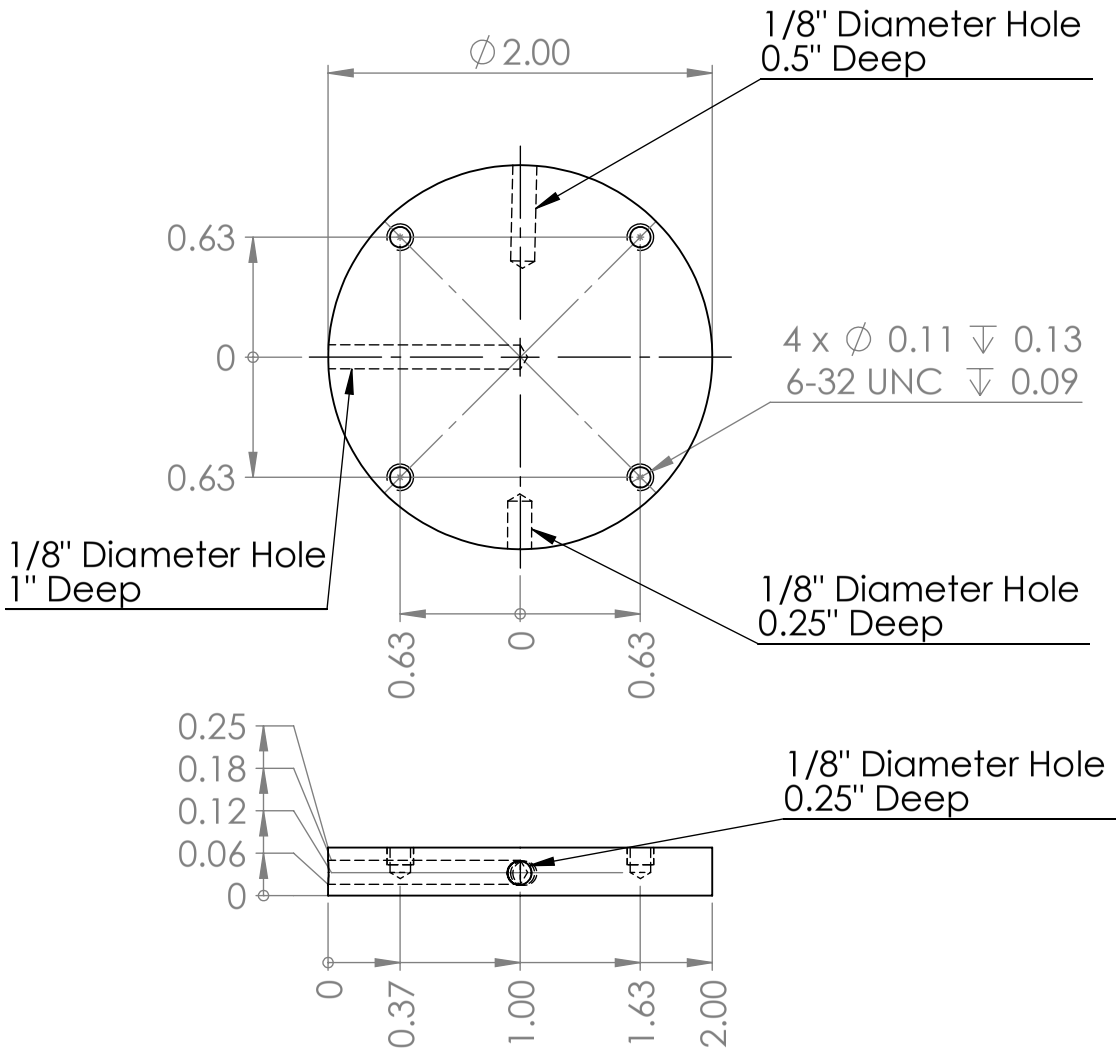

UNLESS OTHERWISE SPECIFIED:		NAME	DATE
DIMENSIONS ARE IN INCHES TOLERANCES: FRACTIONAL ± ANGULAR: MACH ± BEND ± TWO PLACE DECIMAL ± THREE PLACE DECIMAL ±	DRAWN		
	CHECKED		
	ENG APPR.		
	MFG APPR.		
	Q.A.		
INTERPRET GEOMETRIC TOLERANCING PER:	COMMENTS:		
MATERIAL Aluminum			
FINISH Hand Polish			
DO NOT SCALE DRAWING			

TITLE:
Daniel Lim
danlimsw@caltech.edu
141

SIZE	DWG. NO.	REV
A	TCSetup_CircularHolder_Top_v2	

SCALE: 1:1	WEIGHT:	SHEET 1 OF 1

5 4 3 2 1

Appendix B

DRAWINGS OF LASER-INDUCED THERMOCAPILLARY LITHOGRAPHY CAMERA MOUNT AND SAMPLE HOLDER

Included in the following pages are the CAD drawings of the precision-height camera mount (for the Basler dart board camera) and cylindrical sample holder used in the Laser-induced TCL setup. These components were fabricated by Graduate Aerospace Laboratories in Caltech (GALCIT) Precision Machining shop.

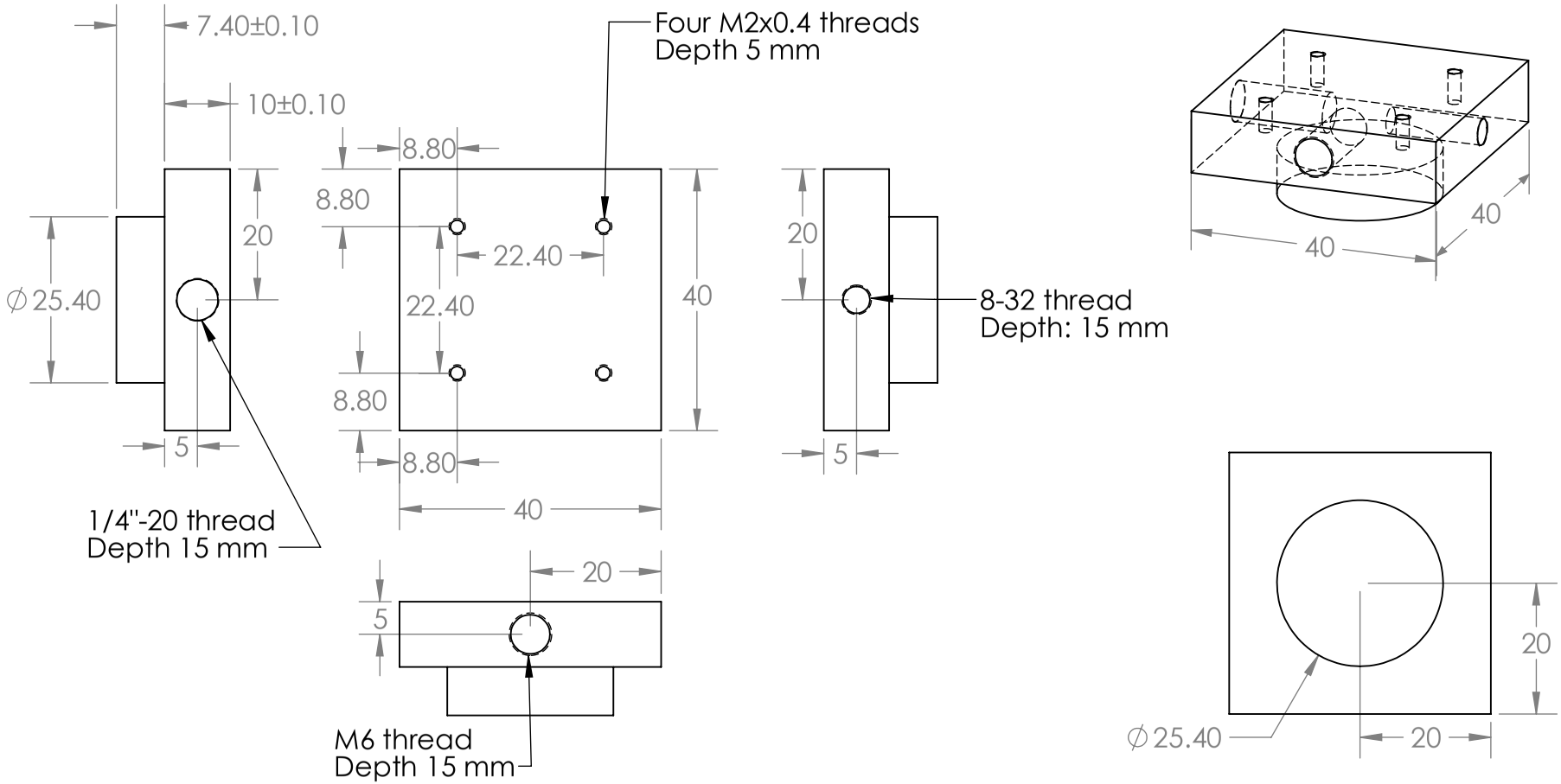

		UNLESS OTHERWISE SPECIFIED:		NAME	DATE
		DIMENSIONS ARE IN MM TOLERANCES: 0.1 MM (vertical) FRACTIONAL ± ANGULAR: MACH ± BEND ± TWO PLACE DECIMAL ± THREE PLACE DECIMAL ±	DRAWN		
			CHECKED		
			ENG APPR.		
			MFG APPR.		
		INTERPRET GEOMETRIC TOLERANCING PER:	Q.A.		
		MATERIAL Aluminum	COMMENTS: Vertical dimension tolerance (10mm and 7.1 mm) is <0.1 mm. Relative positioning tolerance for the four M2 holes (22.4 mm apart) is also <0.1 mm.		
NEXT ASSY	USED ON	FINISH Hand polish			
APPLICATION		DO NOT SCALE DRAWING			

TITLE:

Basler Dart Adaptor v1
Soon Wei Daniel Lim (Troian Lab, APh)

143

SIZE	DWG. NO.	REV
A	20161022_DL_BaslerDartAdaptor	
SCALE: 1:1	WEIGHT:	SHEET 1 OF 1

5 4 3 2 1

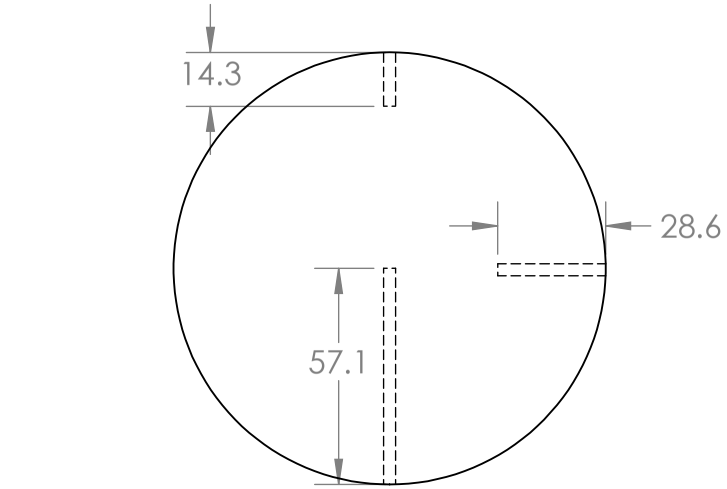

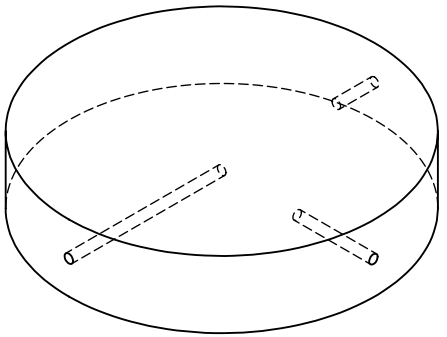

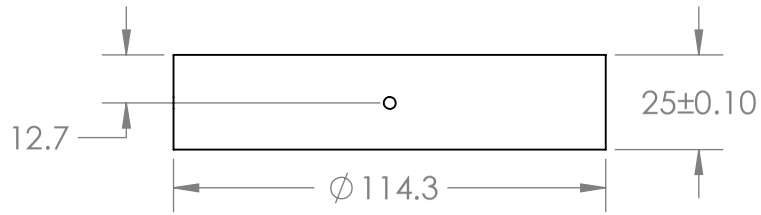

		UNLESS OTHERWISE SPECIFIED:		NAME	DATE
		DIMENSIONS ARE IN MM TOLERANCES: 0.1 mm (vertical) FRACTIONAL ± ANGULAR: MACH ± BEND ± TWO PLACE DECIMAL ± THREE PLACE DECIMAL ±	DRAWN		
			CHECKED		
			ENG APPR.		
			MFG APPR.		
		INTERPRET GEOMETRIC TOLERANCING PER:	Q.A.		
		MATERIAL Aluminum	COMMENTS: Hole depth tolerance: 1 mm Disc diameter tolerance: 1 mm Disc height tolerance: <0.1 mm		
NEXT ASSY	USED ON	FINISH Top: specular			
APPLICATION		DO NOT SCALE DRAWING			

TITLE:

Wafer holder (precision height)
Soon Wei Daniel Lim (Troian lab, APh)

SIZE	DWG. NO.	REV
A	20161022_DL_WaferHolder	
SCALE: 1:2	WEIGHT:	SHEET 1 OF 1

5 4 3 2 1

Appendix C

FABRICATION PROTOCOL FOR SAPPHIRE COLD STAGES

1. Prerequisites

    a) Sapphire Window, cleaned with piranha solution and dried with Techni-wipe

    b) SU-8 Developer solution

    c) SU-8 in appropriate concentration, diluted with isopropanone

    d) 2N clean cut microscope slides, where N is the number of windows to fabricate

    e) S1813 photoresist

2. Using a glass pipette tip, drop a small drop of S1813 onto a microscope slide, then put the sapphire window on top. Ensure that the coloration of the S1813 layer is uniform so that the sapphire window sits parallel to the slide surface.

3. Bake the slides and windows for 10 min at 95°C to attach the sapphire window to the microscope slide.

4. Fill a glass syringe with SU-8 solution completely, then discharge it back into the SU-8 container.

5. Fill the syringe completely again, then cover the sapphire window completely. Spin-coat the SU-8 at 3000 RPM for 60 seconds.

6. Soft bake the spin-coated sample for 1 minute at 65°C and then 2 minutes at 95°C.

7. Mount the window onto the MJB3 mask aligner and hold it in place using green paper tape on the microscope slide edges.

8. Align the mask so that its spacer pattern (six 1 mm diameter holes) is coincident with the central position of the sapphire window.

9. Expose the sample to UV light for 60 seconds.

10. Soft bake the spin-coated sample for 1 minute at 65°C and then 2 minutes at 95°C.

11. Allow the samples to cool down to room temperature.

12. Develop the windows for 20 sec in SU-8 developer, swirling thoroughly. Wash the developed windows for 20 sec in fresh isopropyl alcohol.

13. Fill a container with a shallow layer of acetone. Place the developed window (with microscope slide still attached) into the acetone. The acetone dissolves the S1813 adhesion layer. Immediately use tweezers to dislodge and remove the sapphire window.

14. Rinse both sides of the sapphire window with bottled acetone. Scratch any unwanted SU-8 residue off and rinse in acetone if necessary.

15. Dry the sapphire window gently with dry nitrogen.

16. Perform steps 2 to 15 to deposit the central pin pattern.

17. Hard bake the windows at 200°C for 120 minutes on a hotplate. After the 120 minutes have elapsed, switch the hotplate off and allow the windows to come to room temperature.

18. Place the windows in an evacuated desiccator. Use a glass pipette to drop five drops of PFOTS in an adjacent beaker in the desiccator. Evacuate the desiccator and the silanization proceed for at least one hour.

19. Measure the SU-8 pin and spacer heights using an Ambios XP2 profilometer.

20. Wash the window in fresh toluene and dry with nitrogen immediately before use.

Appendix D

FABRICATION PROTOCOL FOR CONDUCTION THERMOCAPILLARY LITHOGRAPHY

1. Set the temperature on the Fisher Scientific Model 910 cooling pump and switch it on. It takes about 30 min to stabilize at 60°C.
2. Switch on the Keithley power supply, MATLAB R2013a 32-bit, Omega Logging Software and connect the PT104A.
3. Use a metal spatula to place a drop of thermal paste onto the heater surface.
4. Place the quartz window onto the thermal paste. Pressing down along the sides so that the thermal paste fills the underside of the window.
5. Place the sapphire window face down onto the quartz window. There should be visible concentric interference fringes to show that the surfaces are flat relative to each other.
6. Push the assembly under the aluminum cold reservoir, locking the horizontal translation stage in position.
7. Use the motorized dovetail Z-axis motor to raise the assembly. Stop when the sapphire window makes contact with the cold reservoir and the Z-axis motor emits a clicking sound.
8. Start "tempController" on Matlab and enter the fabrication duration and desired heater temperature.
9. Click "Prepare for Liftoff", then "Start".
10. When the fabrication duration ends, the heater will switch off and the setup will be allowed to cool.
11. When the central temperature decreases to within 10°C of the cold reservoir temperature, click the "Stop" checkbox.
12. Click "Export Data" to save the logged temperature, voltage, and current values.

13. Lower the stage using the Z-axis motor.
14. Remove the sapphire window with tweezers.
15. Re-silanize the sapphire window in the evacuated desiccator.

Appendix E

USAGE INSTRUCTIONS FOR ZEMETRICS ZEGAGE SYSTEM

1. With the computer at the Desktop (and without the Zemaps software running), switch on the scan head and the control panel.

2. Run the file "1.15.46", which is the Zemaps program. The system will run an automatic diagnostic. All the tests should be green and show "PASS".

    - If there are error messages, proceed with the following debugging steps:

        a) Close Zemaps, switch the Zemetrics off, and restart the computer. Then try again.

        b) If 2a fails, close Zemaps, switch the Zegage off, unplug the two silver USB cables (connected to the scan head USB hub) from the rear of the white Dell system, wait a few seconds, then plug it back in and restart the computer.

        c) If 2b fails as well, seek help from Zygo representatives online.

3. "Your stage can optionally be homed" $\rightarrow$ No

4. "Do you want to open the last recipe you used (20160812_recipe)?" $\rightarrow$ Yes

    - This uses the configuration and calibration performed by me on all three microscope objectives and magnification settings. The calibration was performed using an NIST-traceable VLSI SHS-880 QC 88 nm step height standard.

5. Go to the main ZeMaps window.

6. In the lower left corner, you will see three objective icons (20x, 5x and 2.5x). If you are using the single Zygo CF Plan 2.5x/0.075 TI $\infty/0$ EPI Michelson objective, click the 2.5x icon and select the icon with the minus (-) sign in the bottom right hand corner. Otherwise, if you are using the Zygo CF Plan 5x/0.13 TI $\infty/0$ EPI Michelson or Zemetrics 20x/0.40 Mirau objectives mounted on the six-objective rotating stage, select the corresponding icon and pick the option with the (-) sign.

7. There are several internal lenses within the scan head which allow access to additional magnifications beyond that provided by the objectives. The plus (+) option adds optics to increase magnification and the minus (-) option adds optics to demagnify.

8. Check that the z position (top right corner of the bottom left hand panel) is around 122 mm. This indicates that the scan head is about 55 mm from the surface of the sample.

9. Load the sample onto the stage.

10. To bring the scan head down, click the "Z" button on the left hand side of the bottom left hand panel. This adjusts the vertical movement speed of the scan head. Set this to maximum (speedometer to the right). Use the Z control on the control panel to bring the scan head down while monitoring the camera (bottom left hand panel) and ensuring that the objective does not touch the sample. The 2.5x objective comes into focus when z = 177 mm (for a flat silicon wafer sample). Use the lighting panel on the left of the bottom left hand panel to adjust the light intensity to make focusing easier.

11. Use the XY control to find the region of interest and center it in the camera view (bottom left panel). Since the XY stage starts out at a corner of the accessible range, it may be useful to bring the stage to the middle of its accessible range before loading the sample directly under the microscope objective.

12. Switch the Z speed to slow (speedometer to the left) and continue to adjust the focus until alternating dark-light fringes come into view. Set the XY speed to slow and use the Tip/Tilt control on the control panel to null the fringes.

    - Nulling the fringes refers to adjusting the tip/tilt position until the fringes are maximized in size. This ensures that the sample surface is flat relative to the reference optics in the objective. To do this, move the tip/tilt joystick in the direction orthogonal to the fringe lines. Since there are two orthogonal directions, one of these directions will shrink the fringes (bring them closer) and the other will increase the spacing between fringes. Find the appropriate direction and increase the fringe spacing. Use the z-control to bring the fringes back into view when they leave the screen. It may be useful to modulate the z and tip/tilt joysticks

at the same time to keep the fringes in view. When nulling is complete, one fringe should fill the entire image.

- If no fringes are visible, check that the Michelson window is open (for Michelson objectives). To do this, change the position of the rectangular panel on the side arm of the microscope objective to the other extreme end.

13. Select the ”Acquire recipe options” logo in the camera panel. A good first selection of settings are the following (these can be adjusted based on one’s needs):

    - Surface: Smooth scan
    - Environment: Good
    - Auto light level: On
    - Auto focus: On, 20 um
    - Auto calculate scan length: Off
    - Data averages: Off
    - Scan levels: 1 Level standard scan
    - Scan length: 10 um
    - Subtract objective reference: Off
    - Subtract retrace reference: Off
    - Signal threshold: 5.0%
    - Saturation threshold: 20.0%
    - RMS threshold: Off
    - Save single intensity: Off
    - Save fringe-free image: Off
    - Save confocal image: Off
    - Save stage view image: Off

14. Acquire an image by pressing F2 or the “Start Acquire” button. Press “Start” in the panel that pops up.

15. The height profile should show up in the top right hand panel. Examine the profile using the cross-section profile tool. The 1D cross section will show up at the bottom left hand panel. Drag the white arrows to set the scale in the 1D cross section plot.

16. If necessary, level the height profile. Select the "Show/hide level map tool" button in the top right panel. Move the rectangle bounds around until it encompasses a region which is known to be flat. Click the center button beneath the rectangle until it shows "Tilt" (or "Cylinder" or "Sphere", depending on use). Click the left button "Remove".

17. Export the height profile. Go to File→Save Map→Save as type = SDL file.

18. Repeat steps 9-17 for other magnifications, positions on the sample, or other samples.

19. To shut the machine down, first exit Zemaps. Agree to move the stage 55 mm from the surface before exiting. Switch both the scan head and control panel off.

Appendix F

ANALYSIS PROTOCOL FOR ZYGOCRUNCHER LENS CHARACTERIZATION

Pre-requisites: MATLAB R2016a or later, zygocruncher.m script, zygocruncher.fig figure file.

1. Run MATLAB R2016a or later, and call zygocruncher in the command line.
2. Click "Pick Save Folder" and select a folder for the fitting results to be saved. If the results do not need to be saved, just press Cancel.
3. Press "Load Input File" and select the raw data file to be analyzed. The accepted file formats are:
    - ASCII (.asc) files exported from the Zygo NewView 600 software.
    - Igor Text (.itx) files exported from the Wavemetrics Igor Pro software.
    - SDF (.sdf) files exported from the Zegage Zemaps software.
4. The Full Plot frame should display a 3D image of the surface topology. Click and drag on the plot to pan around. If 3D panning is not enabled, click the "Rotate 3D" button on the top left hand corner of the window.
    - To take a picture of the Full Plot by itself, click "Open Full Plot in new window". The plot can then be annotated and adjusted by inputting commands from the Matlab command line.
    - If the 3D full plot is not rotating as you like it, relax the axis constraint by entering "axis normal" in the Matlab command line.
5. Pick subset of points. Enter the desired start and end points in the X and Y axes and click "Show subset". The Selected Plot frame should show a 3D image of the selected surface subset.
    - To take a picture of the Selected Plot by itself, click "Open Selected Plot in new window". The plot can then be annotated and adjusted by inputting commands from the Matlab command line.

- If the 3D full plot is not rotating as you like it, relax the axis constraint by entering "axis normal" in the Matlab command line.
- Note that if you enter a value exceeding the maximum or minimum values allowed by the data file, the script will only consider the maximum or minimum values respectively.

6. Threshold region. This step allows you to pick a Z subset of the surface, and is especially useful when Zygo gives error pixels. Enter the desired bottom and top Z-values and click "Update subset".

   - If you want to expand the Z-range from a shorter range, you will need to click "Show subset" from "Step 3: Pick subset of points" to pull in the original data before pressing "Update subset".

7. (Optional, depending on scale) Remove an overall plane by clicking "Remove Plane" in the "RMS Calculator" panel. This fits a plane through the data and subtracts it.

8. (Optional, depending on scale) Remove the overall curvature (quadratic terms) by clicking "Remove curvature" in the "RMS Calculator" panel. This fits a generalized quadratic through the data and subtracts it. Note that this step will automatically remove the plane (linear terms) as well.

9. Calculate the curvature everywhere to select the fitting domain:

   a) Enter the appropriate smoothing factor (a typical value is 1e-4) into the textbox labeled "Smoothing".

   b) Click "Cubic Spline Smoothing". This function fits a cubic spline to the data points selected in "Selected Plot" and displays it there.

   c) Click "Surface Curvature Plot". This calculates the curvature everywhere using the cubic spline and displays the result in a new window.

   d) For analysis of protrusions, select "-ve (Convex)" and for depressions, "+ve (Concave)"

   e) Click "Filter curv.". This function deletes all points with the opposite sign of the mean curvature based on the previous selection. Note that the smoothed surface is replaced with the original data points at this step.

f) Click "Click central region". Use the cross-hairs to select the protrusion/depression of interest. This function restricts the domain to the contiguous region containing the clicked point.

g) If the region of interest has points of opposite curvature that have been removed in the previous step, but are necessary for further analysis (e.g. calculation of feature area), click "Add enclosed region". Use the cross-hairs to select an empty, closed region that needs to be added to the current domain.

h) Click "Shift to zero". This function moves the minimum (maximum) of the selected protrusion (depression) to zero, so that the calculated z-displacement will be equal to the height of the feature above (below) the zero-curvature contour.

10. Enter estimated fitting parameter values into the panel labelled "Step 5: Perform Paraboloid Fit". Several useful starting values have already been populated: $b_1 = -8.7e-5, b_2 = 7.6e-5, b_3 = 0.05, b_4 = 10, b_5 = 10, b_6 = 0$. The fitting equation is:

$$z(x, y) = z_{max} - \frac{(x')^2}{2R_1} - \frac{(y')^2}{2R_2} \tag{F.1}$$

$$\begin{pmatrix} x' \\ y' \end{pmatrix} = \begin{pmatrix} \cos\theta & -\sin\theta \\ \sin\theta & \cos\theta \end{pmatrix} \begin{pmatrix} x - x_o \\ y - y_o \end{pmatrix} \tag{F.2}$$

and the correspondence to the fitting parameter values is:

$$b_1 = -\frac{1}{2R_1}, \quad b_2 = -\frac{1}{2R_2}, \quad b_3 = z_{max}, \quad b_4 = x_0, \quad b_5 = y_0, \quad b_6 = \theta \tag{F.3}$$

For fitting depressions, start with positive values for b_1 and b_2 instead.

The fit results will appear in the panel "Step 6: View paraboloid fit parameters".

- To calculate the focal length with a different refractive index, update the textbox labelled "Refractive index" and click "Recalculate focal length".

11. Click "Fit 1D Asphere (equal spacing)" in the "Step 7: Aspheric Fit (Perform parabolic fit first!)" panel. This function takes the principal axes cross-sections determined by the parabolic fit and fits the cross-sections to the 1D

aspheric equation. The starting guesses for the nonlinear fit can be adjusted in the textboxes above the table. The fitting results will appear in the table. The aspheric fitting equation is:

$$z(r) = z_{max} - \left[\frac{(r - r_{cent})^2}{R\left(1 + \sqrt{1 - (r - r_{cent})^2/R^2}\right)} + \alpha_1 r^4 \right] \tag{F.4}$$

12. (Optional) Save the data by clicking "Step 8: Save fits to Workspace file". Enter a comment if necessary. The processing parameters, fitting parameters and results will be saved to a text file located within the Workspace file chosen in Step 2.

Appendix G

FABRICATION PROTOCOL FOR LASER-INDUCED THERMOCAPILLARY LITHOGRAPHY: SETUP ALPHA

1. With the hotplate cool, switch on the laser and set it to 1.45 amperes, the lowest setting with a visible emission.

2. Place the sample mount on the hotplate and measure the size of the laser spot on the sample mount using vernier calipers. Verify that the sample holder is horizontal using a liquid level. Adjust the hotplate leveling otherwise.

3. Remove the sample mount and replace it with the bare-board camera and mount. Align the camera sensor so that it is centered on the laser spot. Connect the camera to the computer and open "pylon Viewer (x64)". Select the camera and open the live view.

4. Mount the microlens array above the bare-board camera. Adjust the tip/tilt of the microlens array holder using the liquid level so that it is horizontal. Adjust the vertical micrometer translation stage on the holder while monitoring the bare-board camera live view.

5. Adjust the live view exposure so that no pixels are saturated. Take an uncompressed camera image.

6. Unplug the bare-board camera and replace the camera and its mount with the sample holder. Do so carefully, ensuring that nothing comes into contact with the photomask at any point in time.

7. Set the hotplate to the desired temperature and begin heating.

8. While the hotplate is heating up, ensure that all two thermocouples are connected to the DT9805 DAQ and that the photodiode, beam chopper, and lock-in amplifier are switched on.

9. Open "QuickDAQ" on the computer and monitor the readings of the two thermocouples and the photodiode, verifying that they are connected and readable.

10. When the thermocouple readings stabilize, the fabrication process can begin. Obtain a polystyrene-on-silicon sample and rinse it in dry nitrogen. Use a pair of wafer tweezers to place the wafer gently onto the hot sample holder and nudge the sample into place in the path of the laser beam.

11. Begin recording in QuickDAQ. Close the laser curtain around the setup and ensure that all four sides are held down by velcro. Ramp the laser current up to the target value.

12. After the requisite length of time, ramp the laser current down to zero and switch the laser off. Stop recording in QuickDAQ. Raise the laser curtain and use a pair of wafer tweezers to remove the wafer sample. Place the sample immediately onto a copper plate held at room temperature. Wait at least 10 seconds, then transfer the sample to a wafer carrier. The fabrication is complete.

Appendix H

FABRICATION PROTOCOL FOR LASER-INDUCED THERMOCAPILLARY LITHOGRAPHY: SETUP BETA

1. With the hotplate cool, switch on the laser and set it to 1.45 amperes, the lowest setting with a visible emission.
2. Place the sample mount on the hotplate and measure the size of the laser spot on the sample mount using vernier calipers. Verify that the sample holder is horizontal using a liquid level. Adjust the hotplate leveling otherwise.
3. Remove the sample mount and replace it with the bare-board camera and mount. Align the bare-board camera sensor so that it is centered on the laser spot. Connect the camera to the computer and open "pylon Viewer (x64)". Select the camera and open the live view.
4. Mount the photomask vertically on the horizontal translation stage. Use the XY mount adjustments to select the pattern for the laser to pass through. Use the horizontal translation stage to bring the camera image into focus.
5. Adjust the camera exposure so that no pixels are saturated. Take an uncompressed camera image.
6. Unplug the bare-board camera and replace the camera and its mount with the sample holder.
7. Set the hotplate to the desired temperature and begin heating.
8. While the hotplate is heating up, ensure that all three thermocouples are connected to the DT9805 DAQ and that the photodiode, beam chopper, and lock-in amplifier are switched on.
9. Open "QuickDAQ" on the computer and monitor the readings of the three thermocouples and the photodiode, verifying that they are connected and readable.
10. Connect the sample-viewing camera to the computer and bring the holder surface into focus by adjusting the vertical micrometer translation stage holding the sample-viewing camera.

11. When the thermocouple readings stabilize, the fabrication process can begin. Obtain a polystyrene-on-silicon sample and rinse it in dry nitrogen. Use a pair of wafer tweezers to place the wafer gently onto the hot sample holder and nudge the sample into place in the path of the laser beam.

12. Begin recording in QuickDAQ. Start the sample-viewing camera capture sequence. Close the laser curtain around the setup and ensure that all four sides are held down by velcro. Ramp the laser current up to the target value.

13. After the requisite length of time, ramp the laser current down to zero and switch the laser off. Stop recording in QuickDAQ and in pylon viewer (for the sample-viewing camera). Raise the laser curtain and use a pair of wafer tweezers to remove the wafer sample. Place the sample immediately onto a copper plate held at room temperature. Wait at least 10 seconds, then transfer the sample to a wafer carrier. The fabrication is complete.

Appendix I

FABRICATED LASER-INDUCED THERMOCAPILLARY LITHOGRAPHY SAMPLE PARAMETERS AND PROFILES

This chapter lists the fabrication parameters, displays the laser light field, light microscope profile, and scanning white light interferometry profile for each deformed Laser-induced TCL sample. Each sample is indexed with the reference number L00xx. The relative ordering of the reference numbers indicates the relative order in which the sample polymer nanofilms were spin-coated. The samples in this appendix have been listed in chronological order of laser-induced fabrication and not spin-coating. Samples that share the same laser light field are hence listed in close proximity in this Chapter.

I.1 L0034

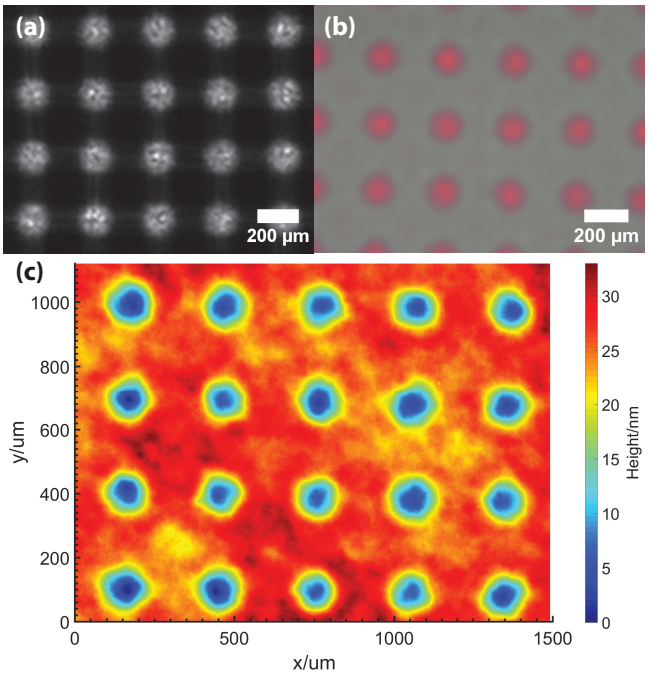

Figure I.1: Sample L0034, fabricated in laser-induced experimental setup Alpha. (a) Camera image of subset of laser light field used in fabrication, (b) Light microscope image of fabricated sample and (c) Scanning white light interferometry profile of fabricated sample. These images may not be of the same location on the fabricated sample.

Table I.1: List of experimental parameters used to fabricate sample L0034 in Experimental Setup Alpha.

Parameter	Value
t_{PS}	286 ± 0.2 nm
T_H	120.0 ± 0.1 °C
Wafer temperature	114.3 ± 0.7 °C
Heating and irradiation time	14.0 ± 0.2 min
Total fluence	5.4 ± 0.2 J/mm^2
Total radiant energy per lens	0.49 ± 0.02 J
Pattern	Thorlabs MLA300-14AR-M
Polarity	–

I.2 L0035

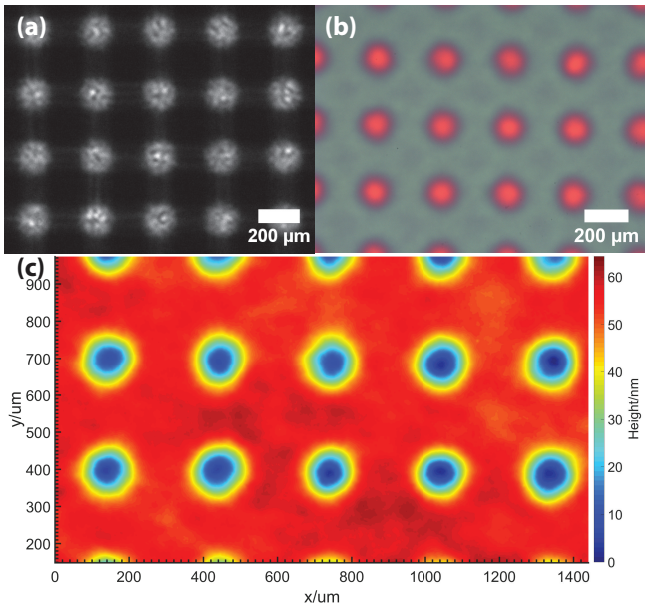

Figure I.2: Sample L0035, fabricated in laser-induced experimental setup Alpha. (a) Camera image of subset of laser light field used in fabrication, (b) Light microscope image of fabricated sample and (c) Scanning white light interferometry profile of fabricated sample. These images may not be of the same location on the fabricated sample.

Table I.2: List of experimental parameters used to fabricate sample L0035 in Experimental Setup Alpha.

Parameter	Value
t_{PS}	289 ± 1 nm
T_H	120.0 ± 0.1 °C
Wafer temperature	115.0 ± 0.6 °C
Heating and irradiation time	33.2 ± 0.2 min
Total fluence	12.7 ± 0.4 J/mm^2
Total radiant energy per lens	1.14 ± 0.04 J
Pattern	Thorlabs MLA300-14AR-M
Polarity	–

I.3 L0036

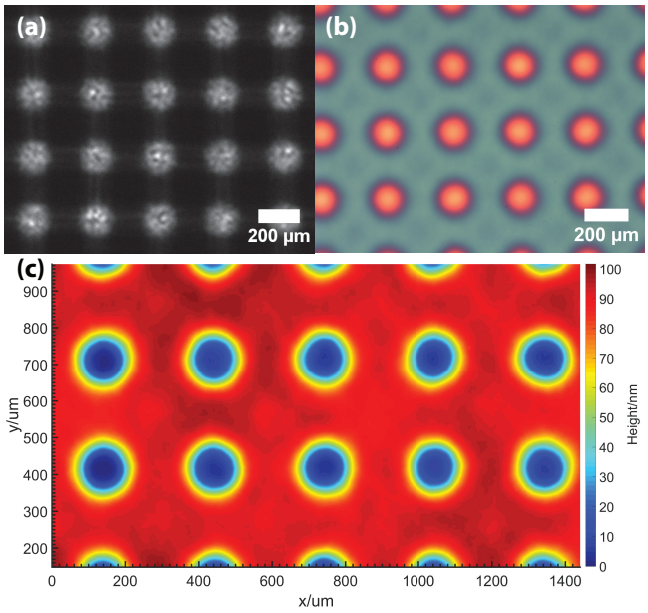

Figure I.3: Sample L0036, fabricated in laser-induced experimental setup Alpha. (a) Camera image of subset of laser light field used in fabrication, (b) Light microscope image of fabricated sample and (c) Scanning white light interferometry profile of fabricated sample. These images may not be of the same location on the fabricated sample.

Table I.3: List of experimental parameters used to fabricate sample L0036 in Experimental Setup Alpha.

Parameter	Value
t_{PS}	288.3 ± 0.6 nm
T_H	120.0 ± 0.1 °C
Wafer temperature	115.6 ± 0.6 °C
Heating and irradiation time	59.3 ± 0.2 min
Total fluence	23.5 ± 0.7 J/mm^2
Total radiant energy per lens	2.11 ± 0.07 J
Pattern	Thorlabs MLA300-14AR-M
Polarity	–

I.4 L0037

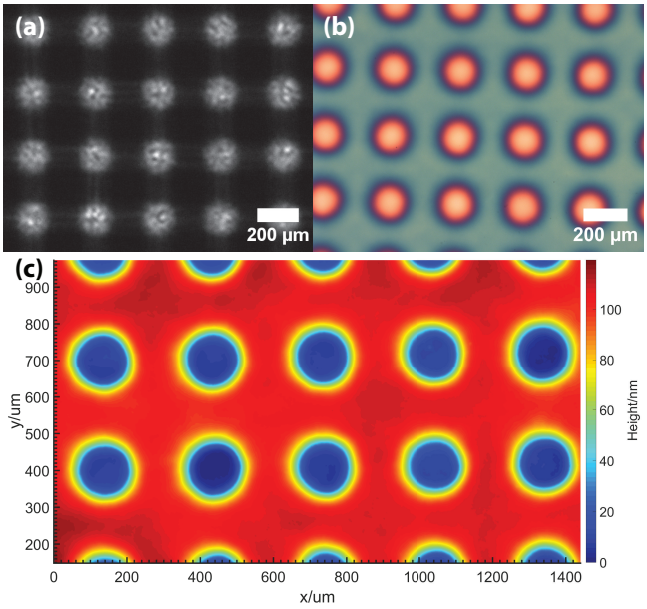

Figure I.4: Sample L0037, fabricated in laser-induced experimental setup Alpha. (a) Camera image of subset of laser light field used in fabrication, (b) Light microscope image of fabricated sample and (c) Scanning white light interferometry profile of fabricated sample. These images may not be of the same location on the fabricated sample.

Table I.4: List of experimental parameters used to fabricate sample L0037 in Experimental Setup Alpha.

Parameter	Value
t_{PS}	290.2 ± 0.7 nm
T_H	120.0 ± 0.1 °C
Wafer temperature	115.9 ± 0.5 °C
Heating and irradiation time	119.7 ± 0.2 min
Total fluence	46 ± 1 J/mm^2
Total radiant energy per lens	4.2 ± 0.1 J
Pattern	Thorlabs MLA300-14AR-M
Polarity	–

I.5 L0039

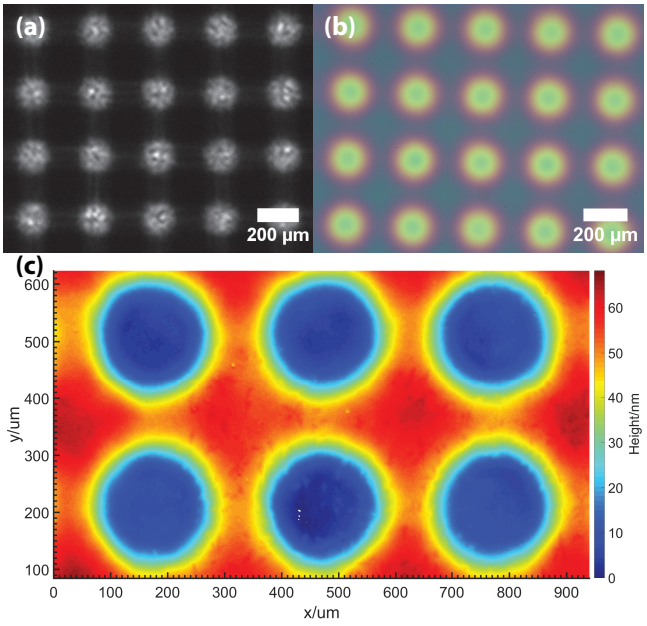

Figure I.5: Sample L0039, fabricated in laser-induced experimental setup Alpha. (a) Camera image of subset of laser light field used in fabrication, (b) Light microscope image of fabricated sample and (c) Scanning white light interferometry profile of fabricated sample. These images may not be of the same location on the fabricated sample.

Table I.5: List of experimental parameters used to fabricate sample L0039 in Experimental Setup Alpha.

Parameter	Value
t_{PS}	434 ± 3 nm
T_H	140.0 ± 0.1 °C
Wafer temperature	132.0 ± 0.1 °C
Heating and irradiation time	15.2 ± 0.2 min
Total fluence	5.7 ± 0.2 J/mm^2
Total radiant energy per lens	0.51 ± 0.02 J
Pattern	Thorlabs MLA300-14AR-M
Polarity	–

I.6 L0040

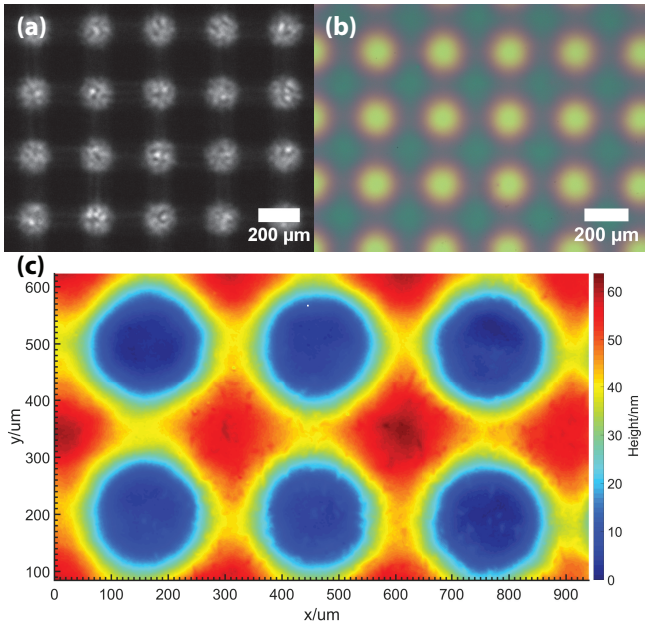

Figure I.6: Sample L0040, fabricated in laser-induced experimental setup Alpha. (a) Camera image of subset of laser light field used in fabrication, (b) Light microscope image of fabricated sample and (c) Scanning white light interferometry profile of fabricated sample. These images may not be of the same location on the fabricated sample.

Table I.6: List of experimental parameters used to fabricate sample L0040 in Experimental Setup Alpha.

Parameter	Value
t_{PS}	436 ± 3 nm
T_H	140.0 ± 0.1 °C
Wafer temperature	131.9 ± 0.2 °C
Irradiation time	15.5 ± 0.2 min
Heating time	21.5 ± 0.2 min
Total fluence	5.8 ± 0.2 J/mm^2
Total radiant energy per lens	0.52 ± 0.02 J
Pattern	Thorlabs MLA300-14AR-M
Polarity	–

Sample L0040 was fabricated under the same conditions as that of L0039, except that it was subject to an additional 6 minutes of thermal reflow time (hotplate heating without laser heating) at the end of the laser fabrication duration.

I.7 L0042

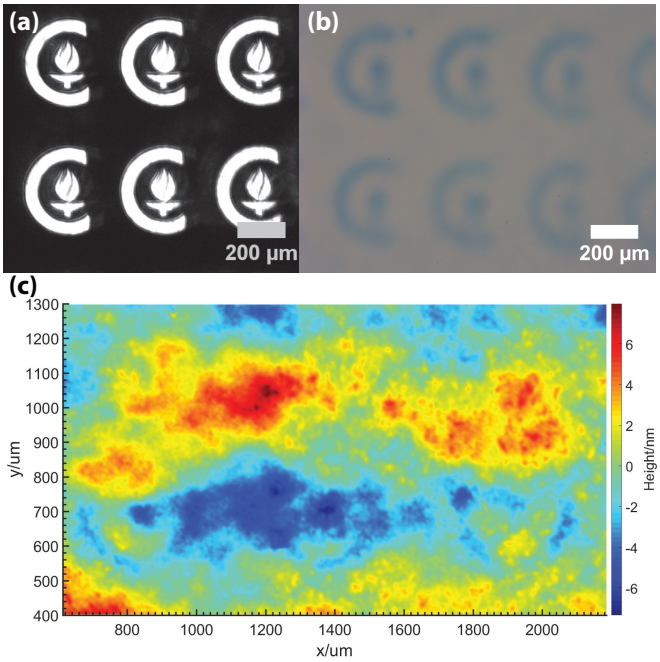

Figure I.7: Sample L0042, fabricated in laser-induced experimental setup Beta. (a) Camera image of subset of laser light field used in fabrication, (b) Light microscope image of fabricated sample and (c) Scanning white light interferometry profile of fabricated sample. These images may not be of the same location on the fabricated sample.

Table I.7: List of experimental parameters used to fabricate sample L0042 in Experimental Setup Beta.

Parameter	Value
t_{PS}	333.4 ± 0.7 nm
T_H	120.0 ± 0.1 °C
Wafer temperature	111.0 ± 0.4 °C
Irradiation and heating time	33.5 ± 0.2 min
Total fluence	38.9 ± 0.3 J/mm^2
Pattern	Caltech Logo (Lasermask Pattern D2)
Array size	8×10
Polarity	Light pattern on dark background

I.8 L0061

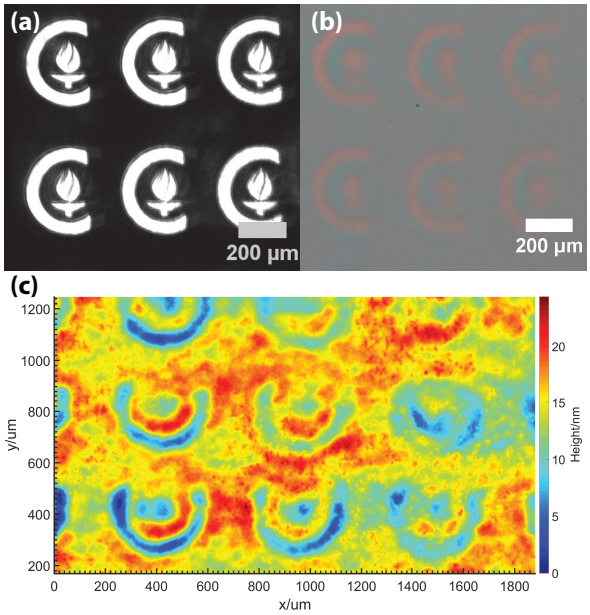

Figure I.8: Sample L0061, fabricated in laser-induced experimental setup Beta. (a) Camera image of subset of laser light field used in fabrication, (b) Light microscope image of fabricated sample and (c) Scanning white light interferometry profile of fabricated sample. These images may not be of the same location on the fabricated sample.

Table I.8: List of experimental parameters used to fabricate sample L0061 in Experimental Setup Beta.

Parameter	Value
t_{PS}	267.1 ± 0.4 nm
T_H	110.0 ± 0.1 °C
Wafer temperature	99.6 ± 0.4 °C
Irradiation and heating time	30.0 ± 0.2 min
Total fluence	33.4 ± 0.3 J/mm^2
Pattern	Caltech Logo (Lasermask Pattern D2)
Array size	8 × 10
Polarity	Light pattern on dark background

I.9 L0060

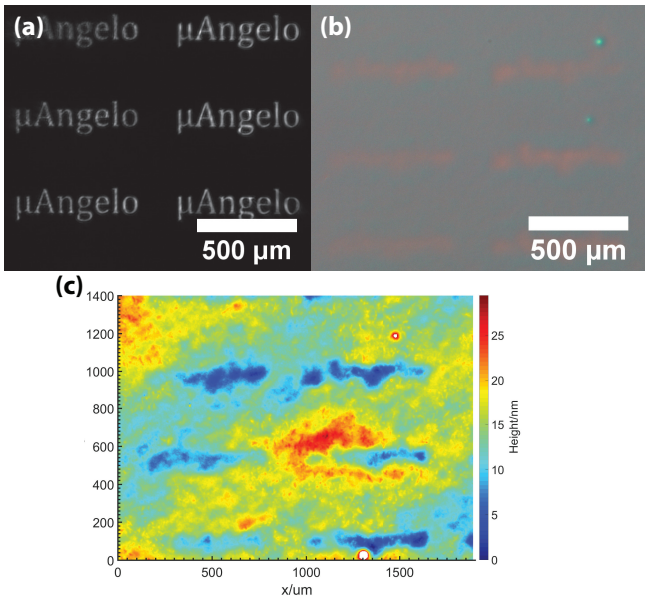

Figure I.9: Sample L0060, fabricated in laser-induced experimental setup Beta. (a) Camera image of subset of laser light field used in fabrication, (b) Light microscope image of fabricated sample and (c) Scanning white light interferometry profile of fabricated sample. These images may not be of the same location on the fabricated sample.

Table I.9: List of experimental parameters used to fabricate sample L0060 in Experimental Setup Beta.

Parameter	Value
t_{PS}	267.2 ± 0.3 nm
T_H	110.0 ± 0.1 °C
Wafer temperature	100.9 ± 0.2 °C
Irradiation and heating time	72.3 ± 0.2 min
Total fluence	79.1 ± 0.7 J/mm^2
Pattern	"μAngelo" (Lasermask Pattern C3)
Array size	15×7
Polarity	Light pattern on dark background

I.10 L0064

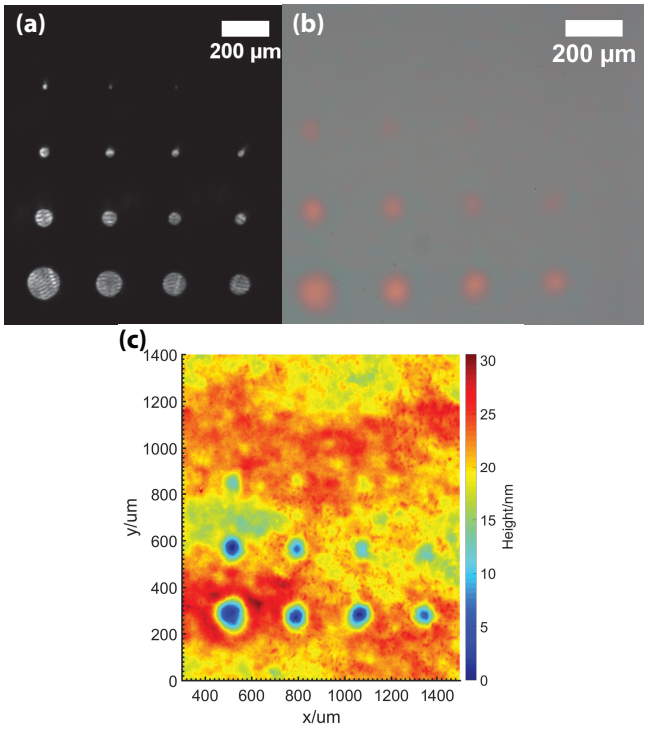

Figure I.10: Sample L0064, fabricated in laser-induced experimental setup Beta. (a) Camera image of subset of laser light field used in fabrication, (b) Light microscope image of fabricated sample and (c) Scanning white light interferometry profile of fabricated sample.

Table I.10: List of experimental parameters used to fabricate sample L0064 in Experimental Setup Beta.

Parameter	Value
t_{PS}	271.7 ± 0.9 nm
T_H	110.0 ± 0.1 °C
Wafer temperature	100.2 ± 0.1 °C
Irradiation and heating time	66.2 ± 0.2 min
Total fluence	72.8 ± 0.6 J/mm^2
Pattern	Circle progression (Lasermask Pattern A4)
Array size	4×4
Polarity	Light pattern on dark background

I.11 L0065

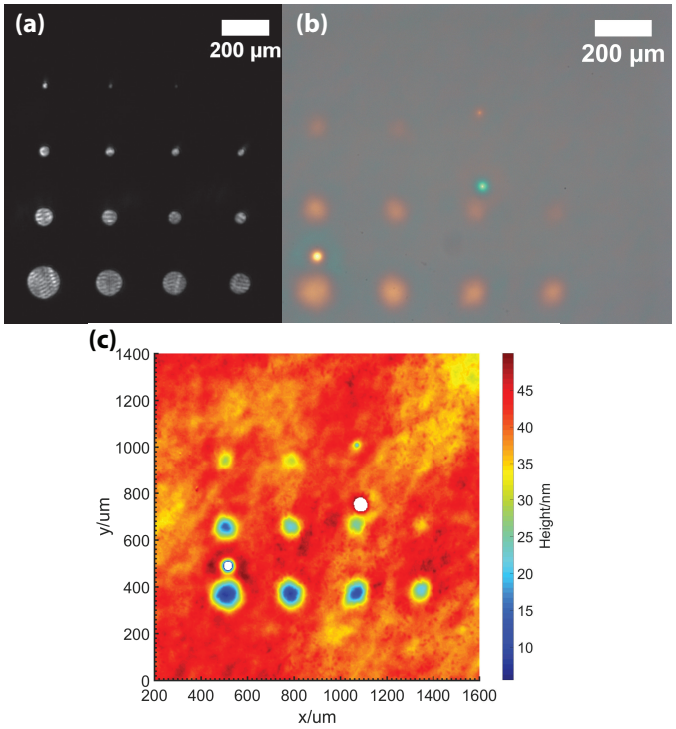

Figure I.11: Sample L0065, fabricated in laser-induced experimental setup Beta. (a) Camera image of subset of laser light field used in fabrication, (b) Light microscope image of fabricated sample and (c) Scanning white light interferometry profile of fabricated sample.

Table I.11: List of experimental parameters used to fabricate sample L0065 in Experimental Setup Beta.

Parameter	Value
t_{PS}	265.8 ± 0.3 nm
T_H	110.0 ± 0.1 °C
Wafer temperature	100.6 ± 0.1 °C
Irradiation and heating time	100.7 ± 0.2 min
Total fluence	112 ± 1 J/mm^2
Pattern	Circle progression (Lasermask Pattern A4)
Array size	4×4
Polarity	Light pattern on dark background

I.12 L0067

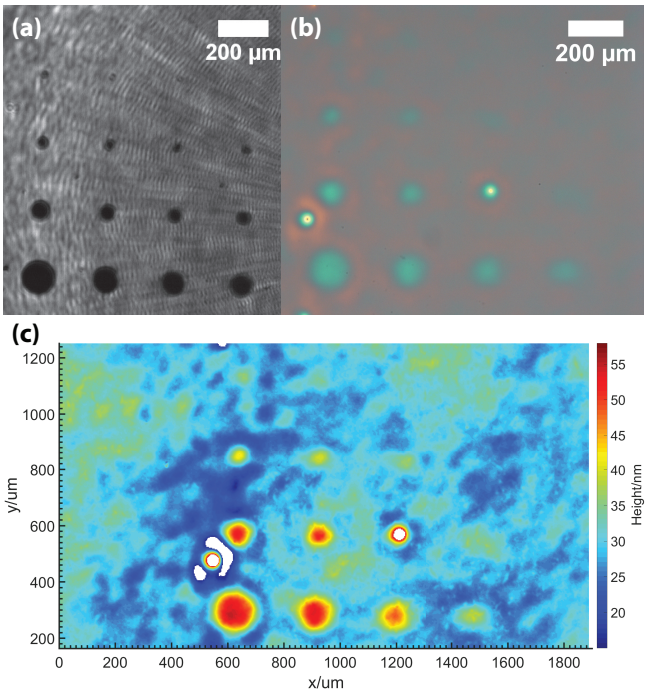

Figure I.12: Sample L0067, fabricated in laser-induced experimental setup Beta. (a) Camera image of subset of laser light field used in fabrication, (b) Light microscope image of fabricated sample and (c) Scanning white light interferometry profile of fabricated sample.

Table I.12: List of experimental parameters used to fabricate sample L0067 in Experimental Setup Beta.

Parameter	Value
t_{PS}	270.5 ± 0.4 nm
T_H	110.0 ± 0.1 °C
Wafer temperature	100.7 ± 0.2 °C
Irradiation and heating time	34.3 ± 0.2 min
Total fluence	39.0 ± 0.3 J/mm^2
Pattern	Circle progression (Lasermask Pattern B4)
Array size	4×4
Polarity	Dark pattern on light background

I.13 L0068

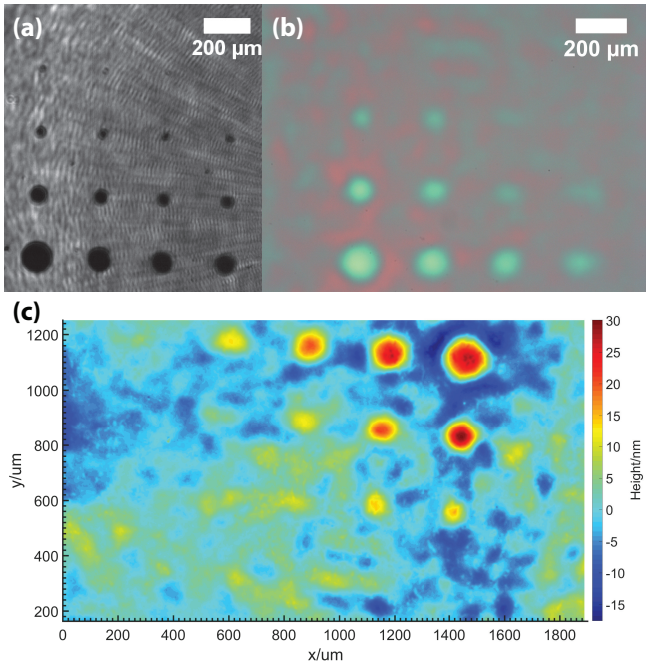

Figure I.13: Sample L0068, fabricated in laser-induced experimental setup Beta. (a) Camera image of subset of laser light field used in fabrication, (b) Light microscope image of fabricated sample and (c) Scanning white light interferometry profile of fabricated sample.

Table I.13: List of experimental parameters used to fabricate sample L0068 in Experimental Setup Beta.

Parameter	Value
t_{PS}	278.0 ± 0.7 nm
T_H	110.0 ± 0.1 °C
Wafer temperature	100.8 ± 0.1 °C
Irradiation and heating time	63.7 ± 0.2 min
Total fluence	70.3 ± 0.6 J/mm^2
Pattern	Circle progression (Lasermask Pattern B4)
Array size	4×4
Polarity	Dark pattern on light background

I.14 L0069

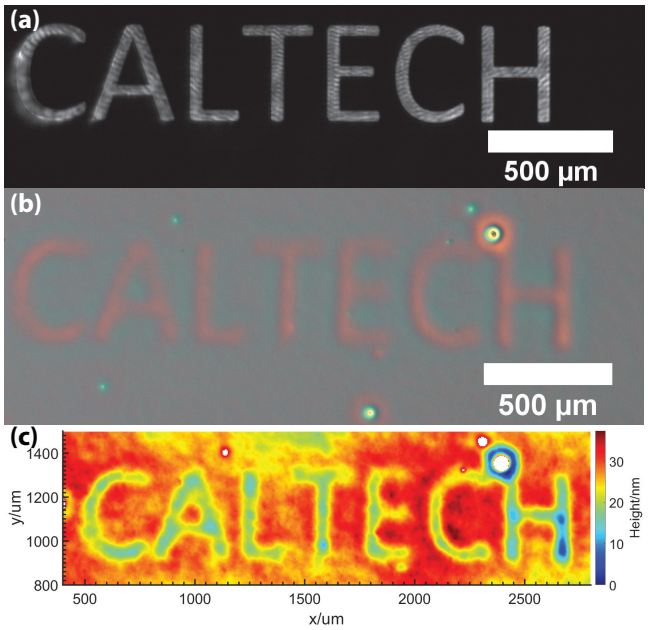

Figure I.14: Sample L0069, fabricated in laser-induced experimental setup Beta. (a) Camera image of subset of laser light field used in fabrication, (b) Light microscope image of fabricated sample and (c) Scanning white light interferometry profile of fabricated sample.

Table I.14: List of experimental parameters used to fabricate sample L0069 in Experimental Setup Beta.

Parameter	Value
t_{PS}	270.9 ± 0.5 nm
T_H	110.0 ± 0.1 °C
Wafer temperature	102 ± 2 °C
Irradiation and heating time	60.2 ± 0.2 min
Total fluence	69.6 ± 0.6 J/mm^2
Pattern	“CALTECH” (Lasermask Pattern A5)
Array size	1×1
Polarity	Light pattern on dark background

I.15 L0075

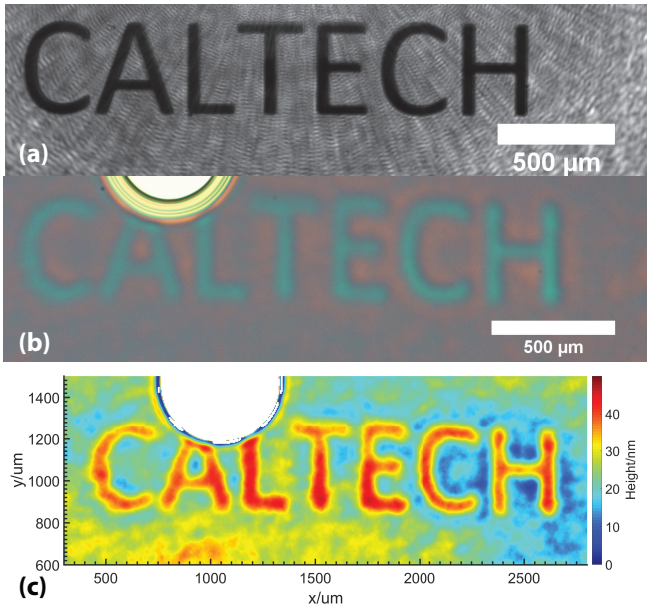

Figure I.15: Sample L0075, fabricated in laser-induced experimental setup Beta. (a) Camera image of subset of laser light field used in fabrication, (b) Light microscope image of fabricated sample and (c) Scanning white light interferometry profile of fabricated sample.

Table I.15: List of experimental parameters used to fabricate sample L0075 in Experimental Setup Beta.

Parameter	Value
t_{PS}	268.7 ± 0.5 nm
T_H	110.0 ± 0.1 °C
Wafer temperature	100.7 ± 0.2 °C
Irradiation and heating time	58.8 ± 0.2 min
Total fluence	64.1 ± 0.6 J/mm^2
Pattern	“CALTECH” (Lasermask Pattern B5)
Array size	1×1
Polarity	Dark pattern on light background

I.16 L0071

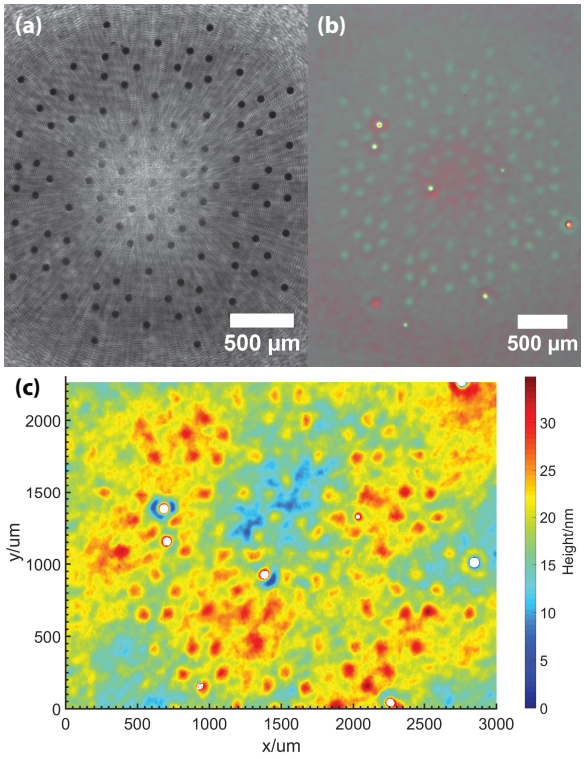

Figure I.16: Sample L0071, fabricated in laser-induced experimental setup Beta. (a) Camera image of subset of laser light field used in fabrication, (b) Light microscope image of fabricated sample and (c) Scanning white light interferometry profile of fabricated sample.

Table I.16: List of experimental parameters used to fabricate sample L0071 in Experimental Setup Beta.

Parameter	Value
t_{PS}	284.8 ± 0.4 nm
T_H	110.0 ± 0.1 °C
Wafer temperature	100.3 ± 0.2 °C
Irradiation and heating time	61.2 ± 0.2 min
Total fluence	66.0 ± 0.6 J/mm^2
Pattern	10-fold symmetric array (Lasermask Pattern D5)
Array size	–
Polarity	Dark pattern on light background

I.17 L0073

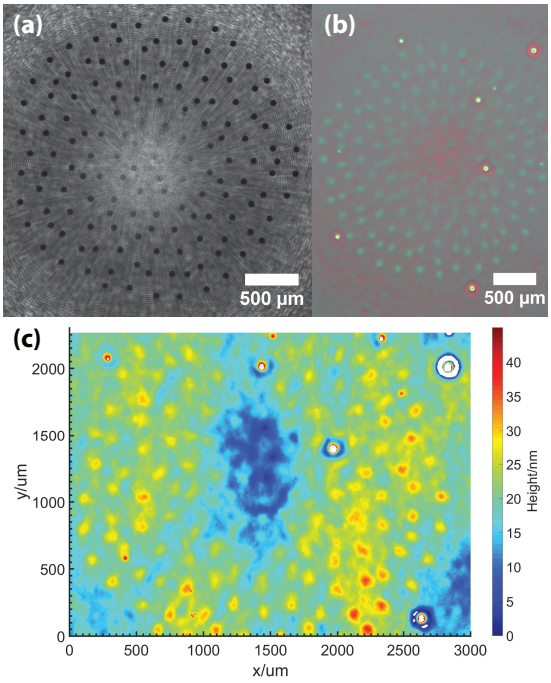

Figure I.17: Sample L0073, fabricated in laser-induced experimental setup Beta. (a) Camera image of subset of laser light field used in fabrication, (b) Light microscope image of fabricated sample and (c) Scanning white light interferometry profile of fabricated sample.

Table I.17: List of experimental parameters used to fabricate sample L0073 in Experimental Setup Beta.

Parameter	Value
t_{PS}	282.0 ± 0.3 nm
T_H	110.0 ± 0.1 °C
Wafer temperature	100.9 ± 0.1 °C
Irradiation and heating time	59.8 ± 0.2 min
Total fluence	63.3 ± 0.5 J/mm^2
Pattern	5-fold symmetric array (Lasermask Pattern E5)
Array size	–
Polarity	Dark pattern on light background

I.18 L0066

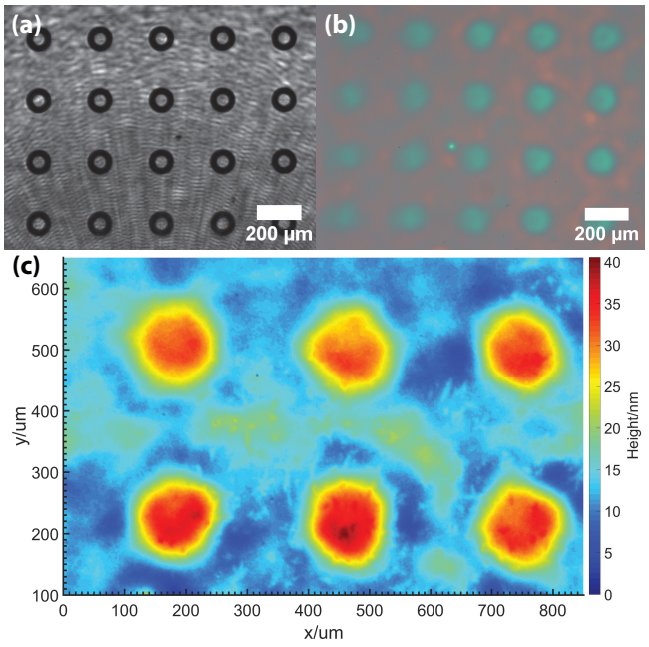

Figure I.18: Sample L0066, fabricated in laser-induced experimental setup Beta. (a) Camera image of subset of laser light field used in fabrication, (b) Light microscope image of fabricated sample and (c) Scanning white light interferometry profile of fabricated sample. These images may not be of the same location on the fabricated sample.

Table I.18: List of experimental parameters used to fabricate sample L0066 in Experimental Setup Beta.

Parameter	Value
t_{PS}	270.7 ± 0.4 nm
T_H	110.0 ± 0.1 °C
Wafer temperature	100.8 ± 0.2 °C
Irradiation and heating time	62.2 ± 0.2 min
Total fluence	66.7 ± 0.6 J/mm^2
Pattern	Annuli array (Lasermask Pattern D4)
Array size	20×20
Polarity	Dark pattern on light background

I.19 L0072

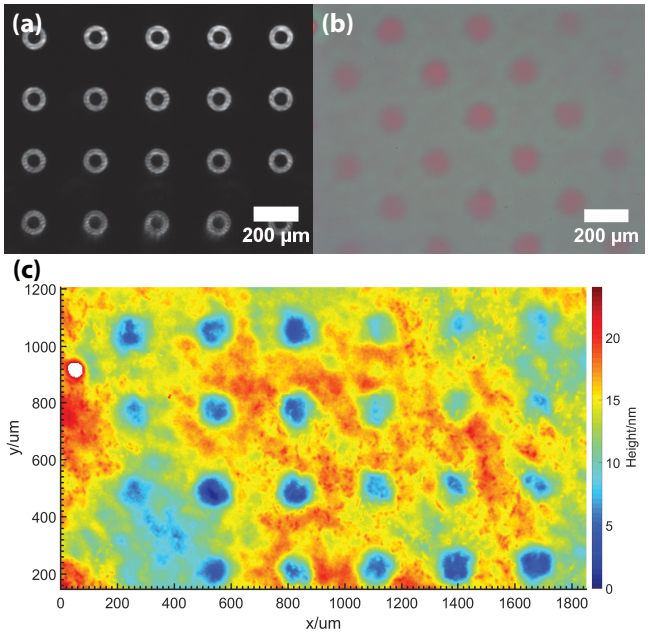

Figure I.19: Sample L0072, fabricated in laser-induced experimental setup Beta. (a) Camera image of subset of laser light field used in fabrication, (b) Light microscope image of fabricated sample and (c) Scanning white light interferometry profile of fabricated sample. These images may not be of the same location on the fabricated sample.

Table I.19: List of experimental parameters used to fabricate sample L0072 in Experimental Setup Beta.

Parameter	Value
t_{PS}	283.5 ± 0.4 nm
T_H	110.0 ± 0.1 °C
Wafer temperature	100.2 ± 0.2 °C
Irradiation and heating time	59.5 ± 0.2 min
Total fluence	64.3 ± 0.6 J/mm^2
Pattern	Annuli Array (Lasermask Pattern C4)
Array size	20×20
Polarity	Light pattern on dark background

I.20 L0074

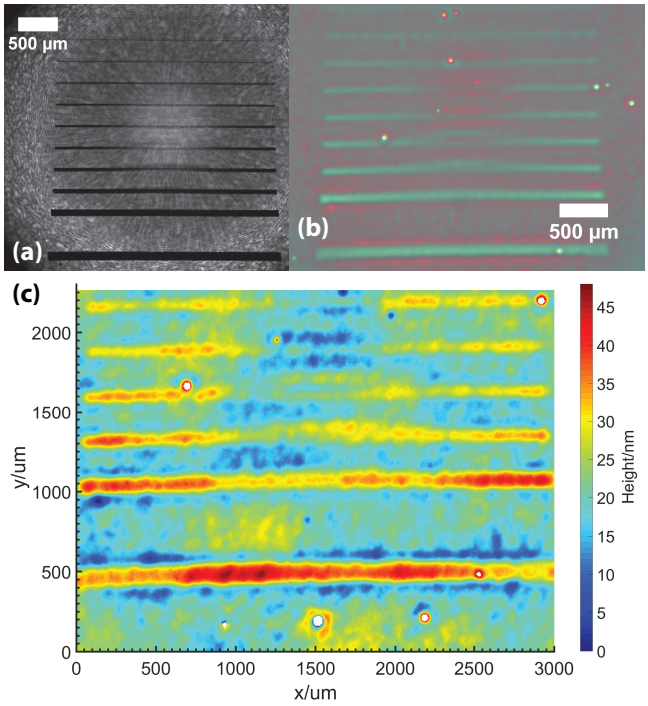

Figure I.20: Sample L0074, fabricated in laser-induced experimental setup Beta. (a) Camera image of subset of laser light field used in fabrication, (b) Light microscope image of fabricated sample and (c) Scanning white light interferometry profile of fabricated sample.

Table I.20: List of experimental parameters used to fabricate sample L0074 in Experimental Setup Beta.

Parameter	Value
t_{PS}	280.4 ± 0.8 nm
T_H	110.0 ± 0.1 °C
Wafer temperature	100.9 ± 0.1 °C
Irradiation and heating time	59.8 ± 0.2 min
Total fluence	64.7 ± 0.6 J/mm^2
Pattern	Waveguide size progression (Lasermask Pattern B3)
Array size	12×1
Polarity	Dark pattern on light background

I.21 L0075A

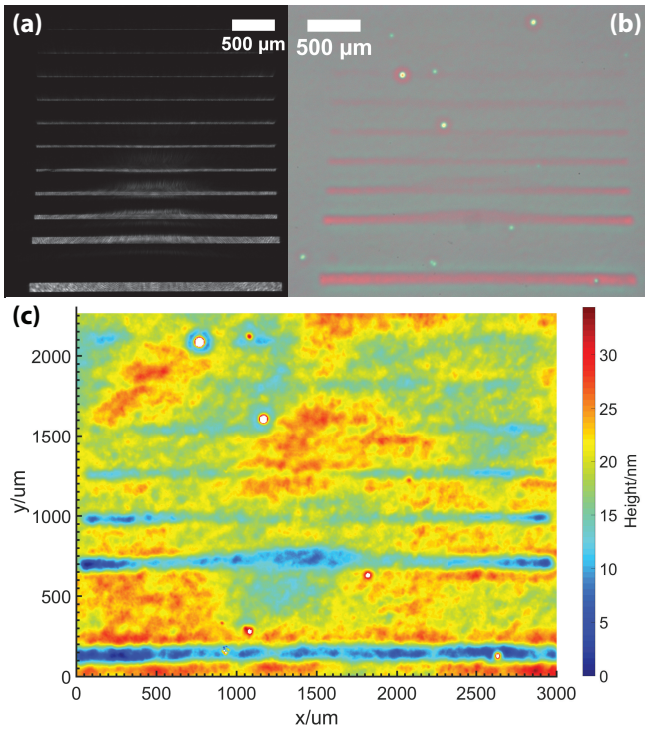

Figure I.21: Sample L0075A, fabricated in laser-induced experimental setup Beta. (a) Camera image of subset of laser light field used in fabrication, (b) Light microscope image of fabricated sample and (c) Scanning white light interferometry profile of fabricated sample.

Table I.21: List of experimental parameters used to fabricate sample L0075A in Experimental Setup Beta.

Parameter	Value
t_{PS}	279.3 ± 0.4 nm
T_H	110.0 ± 0.1 °C
Wafer temperature	99.8 ± 0.2 °C
Irradiation and heating time	59.7 ± 0.2 min
Total fluence	63.5 ± 0.5 J/mm^2
Pattern	Waveguide size progression (Lasermask Pattern A3)
Array size	12 × 1
Polarity	Light pattern on dark background

I.22 L0078

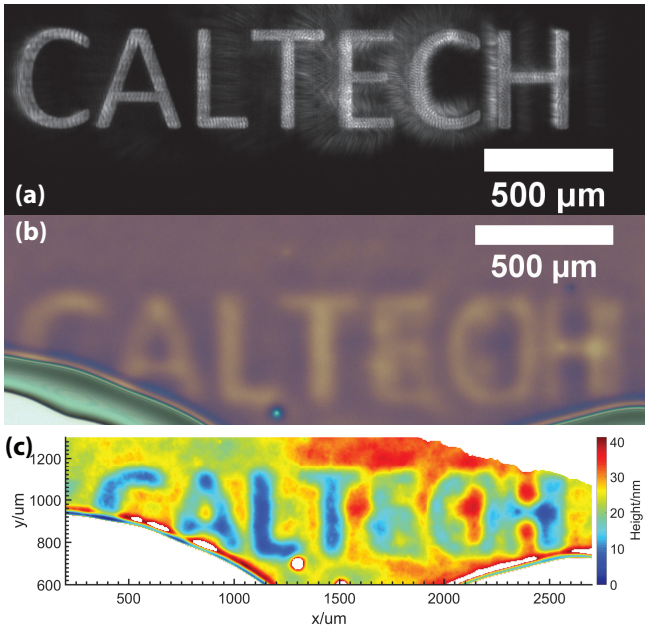

Figure I.22: Sample L0078, fabricated in laser-induced experimental setup Beta. (a) Camera image of subset of laser light field used in fabrication, (b) Light microscope image of fabricated sample and (c) Scanning white light interferometry profile of fabricated sample.

Table I.22: List of experimental parameters used to fabricate sample L0078 in Experimental Setup Beta.

Parameter	Value
t_{PS}	246.6 ± 0.4 nm
T_H	120.0 ± 0.1 °C
Wafer temperature	112.1 ± 0.2 °C
Irradiation and heating time	60.0 ± 0.2 min
Total fluence	66.8 ± 0.6 J/mm^2
Pattern	“CALTECH” (Lasermask Pattern A5)
Array size	1×1
Polarity	Light pattern on dark background

I.23 L0081

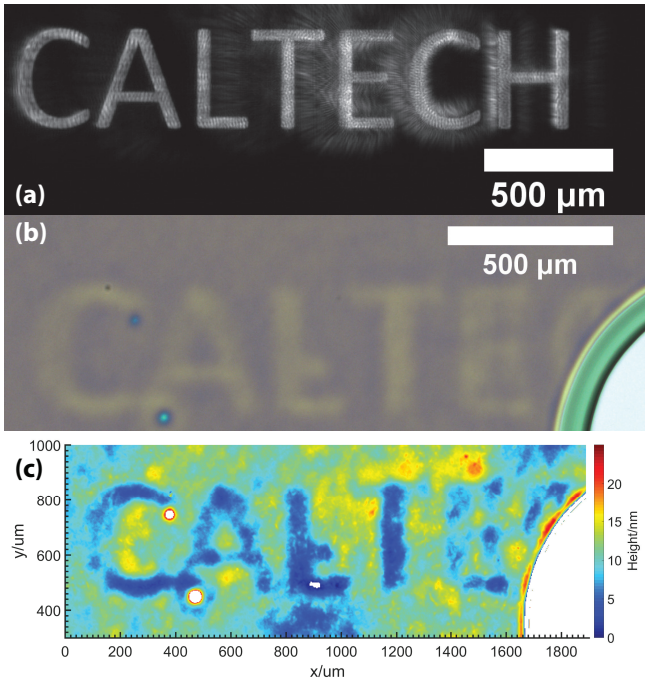

Figure I.23: Sample L0081, fabricated in laser-induced experimental setup Beta. (a) Camera image of subset of laser light field used in fabrication, (b) Light microscope image of fabricated sample and (c) Scanning white light interferometry profile of fabricated sample.

Table I.23: List of experimental parameters used to fabricate sample L0081 in Experimental Setup Beta.

Parameter	Value
t_{PS}	246.2 ± 0.4 nm
T_H	110.0 ± 0.1 °C
Wafer temperature	100.0 ± 0.2 °C
Irradiation and heating time	59.2 ± 0.2 min
Total fluence	68.1 ± 0.6 J/mm^2
Pattern	“CALTECH” (Lasermask Pattern A5)
Array size	1×1
Polarity	Light pattern on dark background

I.24 L0083

Sample L0083 was placed in a low vacuum (-26 inHg) for 40 minutes prior to fabrication to remove trapped air bubbles.

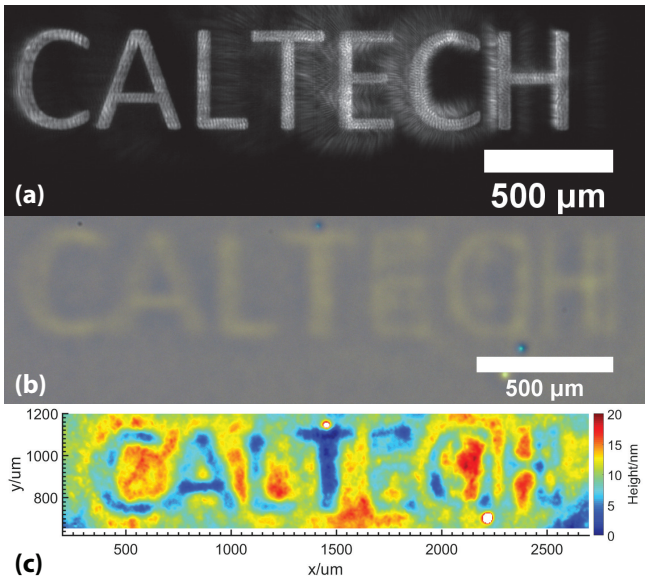

Figure I.24: Sample L0083, fabricated in laser-induced experimental setup Beta. (a) Camera image of subset of laser light field used in fabrication, (b) Light microscope image of fabricated sample and (c) Scanning white light interferometry profile of fabricated sample.

Table I.24: List of experimental parameters used to fabricate sample L0083 in Experimental Setup Beta.

Parameter	Value
t_{PS}	251.6 ± 0.5 nm
T_H	110.0 ± 0.1 °C
Wafer temperature	99.8 ± 0.2 °C
Irradiation and heating time	59.7 ± 0.2 min
Total fluence	64.7 ± 0.6 J/mm^2
Pattern	“CALTECH” (Lasermask Pattern A5)
Array size	1×1
Polarity	Light pattern on dark background

I.25 L0085

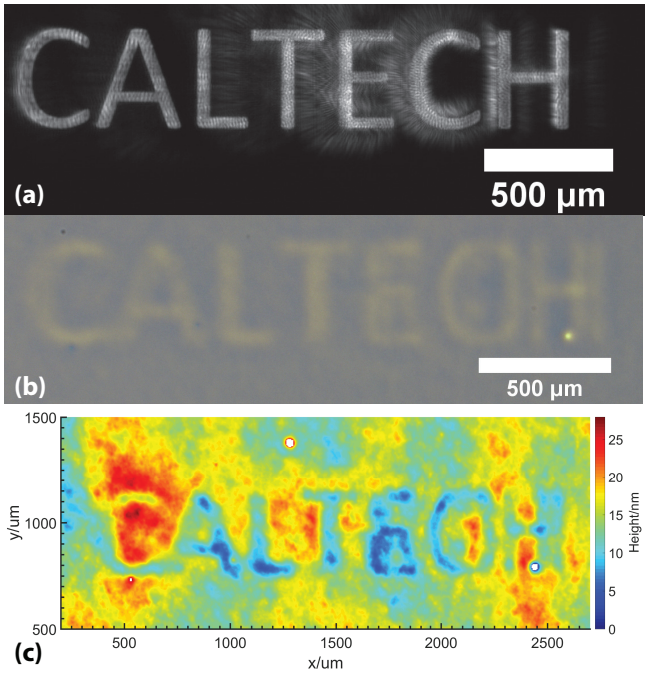

Figure I.25: Sample L0085, fabricated in laser-induced experimental setup Beta. (a) Camera image of subset of laser light field used in fabrication, (b) Light microscope image of fabricated sample and (c) Scanning white light interferometry profile of fabricated sample.

Table I.25: List of experimental parameters used to fabricate sample L0085 in Experimental Setup Beta.

Parameter	Value
t_{PS}	250.5 ± 0.8 nm
T_H	110.0 ± 0.1 °C
Wafer temperature	100.1 ± 0.3 °C
Irradiation and heating time	59.2 ± 0.2 min
Total fluence	65.4 ± 0.6 J/mm^2
Pattern	“CALTECH” (Lasermask Pattern A5)
Array size	1×1
Polarity	Light pattern on dark background

I.26 L0086

Sample L0086 was placed in a low vacuum (-23 inHg) for 40 minutes prior to fabrication to remove trapped air bubbles.

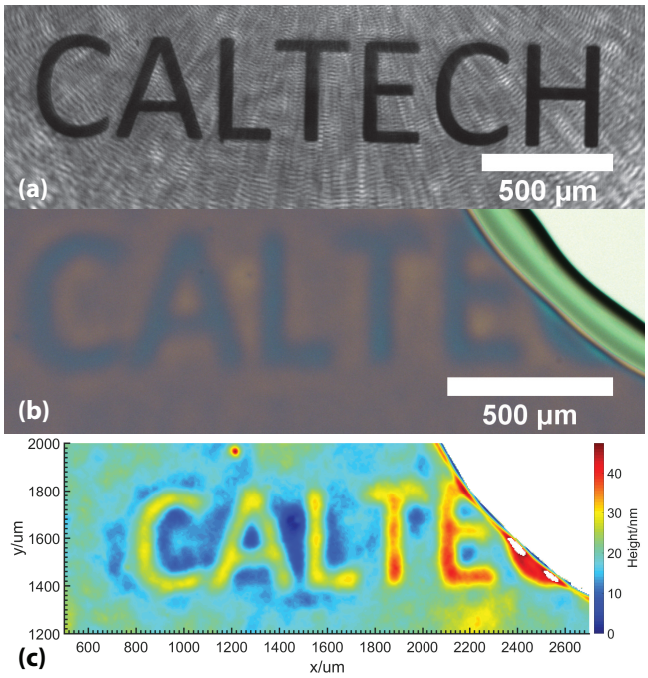

Figure I.26: Sample L0086, fabricated in laser-induced experimental setup Beta. (a) Camera image of subset of laser light field used in fabrication, (b) Light microscope image of fabricated sample and (c) Scanning white light interferometry profile of fabricated sample.

Table I.26: List of experimental parameters used to fabricate sample L0086 in Experimental Setup Beta.

Parameter	Value
t_{PS}	259.1 ± 0.5 nm
T_H	110.0 ± 0.1 °C
Wafer temperature	101.0 ± 0.3 °C
Irradiation and heating time	59.5 ± 0.2 min
Total fluence	65.4 ± 0.6 J/mm^2
Pattern	“CALTECH” (Lasermask Pattern B5)
Array size	1×1
Polarity	Dark pattern on light background

I.27 L0087

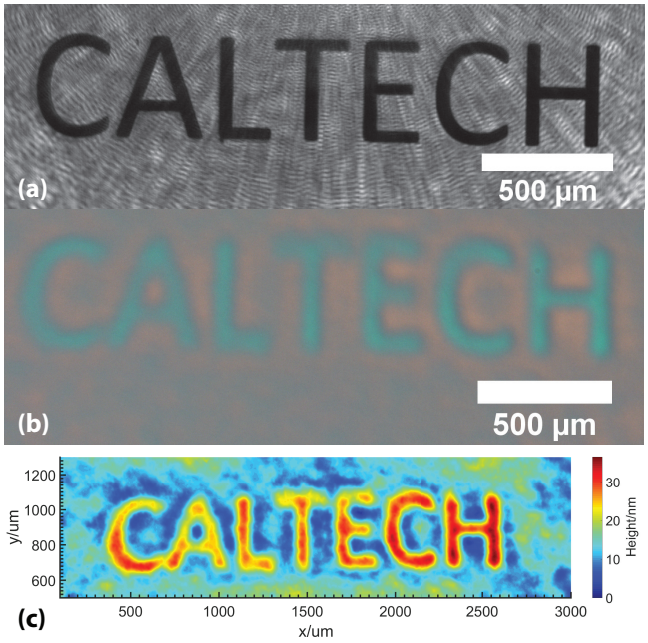

Figure I.27: Sample L0087, fabricated in laser-induced experimental setup Beta. (a) Camera image of subset of laser light field used in fabrication, (b) Light microscope image of fabricated sample and (c) Scanning white light interferometry profile of fabricated sample.

Table I.27: List of experimental parameters used to fabricate sample L0087 in Experimental Setup Beta.

Parameter	Value
t_{PS}	265 ± 2 nm
T_H	110.0 ± 0.1 °C
Wafer temperature	101.3 ± 0.3 °C
Irradiation and heating time	68.8 ± 0.2 min
Total fluence	74.2 ± 0.6 J/mm^2
Pattern	“CALTECH” (Lasermask Pattern B5)
Array size	1×1
Polarity	Dark pattern on light background

I.28 L0057

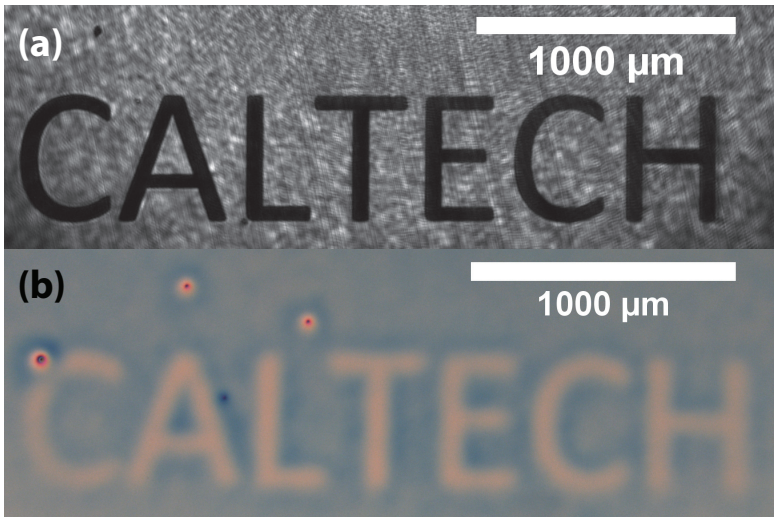

Figure I.28: Sample L0057, fabricated in laser-induced experimental setup Beta. (a) Camera image of subset of laser light field used in fabrication and (b) Light microscope image of fabricated sample. Scanning white light interferometry data was not available due to equipment malfunction.

Table I.28: List of experimental parameters used to fabricate sample L0057 in Experimental Setup Beta.

Parameter	Value
t_{PS}	330.4 ± 0.6 nm
T_H	110.0 ± 0.1 °C
Wafer temperature	98.8 ± 0.6 °C
Irradiation and heating time	85.0 ± 0.2 min
Total fluence	161 ± 1 J/mm^2
Pattern	“CALTECH” (Lasermask Pattern B5)
Array size	1×1
Polarity	Dark pattern on light background